Analysis and Design of Nickel-Based Single Crystal Superalloys



Zailing Zhu

St Anne's College

Department of Materials

University of Oxford

A thesis submitted for the degree of

Doctor of Philosophy

Trinity Term 2014

Analysis and Design of Nickel-Based Single Crystal Superalloys

Zailing Zhu, St Anne's College, University of Oxford
For the degree of D.Phil. in Materials, Trinity Term 2014

Abstract

This thesis provides a research into properties of nickel-based single crystal superalloys. The underlying quantitative relationship between alloy chemistry and the important properties have been studied. To design new grade of single crystal superalloys, computational modelling methods have been proposed which build on the findings of composition-microstructure-property relationships.

A physical model for the creep deformation of single crystal superalloys is presented, in which the dependence of the kinetics of creep deformation on alloy chemistry is rationalised. The rate-controlling step is considered to be climb of dislocations at the matrix/particle interfaces and their rate of escape from trapped configurations. The effects of microstructural scale precipitate size, geometry and spacing are also studied. A first order estimate for the rate of creep deformation emerges from the model, which is useful for the purposes of alloy design.

Three new single crystal superalloys have been isolated using theory-based computational modelling approaches, termed Alloys-By-Design methods. They are (i) an oxidation-resistant low Re-containing alloy with balanced properties, intended for general-purpose gas turbine applications; (ii) an alloy containing 5.6 wt.% Re and 2.6 wt.% Ru suitable for high performance jet engine applications, and (iii) a cheap, corrosion-resistant alloy for power generation applications. The new alloys have been manufactured using investment casting techniques, and their creep and oxidation behaviour evaluated.

The multicomponent composition space pertinent to the single crystal nickel-based superalloys has been mapped and searched, by using newly developed numerical algorithms. This allowed compositions of alloys conferring the microstructures needed for optimal properties to be identified, at a resolution of 0.1 wt.%. Databases have been constructed which contain all appropriate compositions available in these systems. When coupled with composition- and microstructure-dependent property models, the databases can be searched to identify new alloys predicted to exhibit the very best properties or combinations of them.

To my parents

Acknowledgements

I would like to thank my supervisor Prof. Roger Reed, for all the help and guidance throughout my D.Phil study. Without his great patience and encouragement, this work could not have been accomplished. I am deeply impressed by his enthusiasm and hard-working, and this will be an inspiration throughout my future life.

I would also like to express my thanks to Dr. Robert Broomfiled, for his supervision and assistance on the experimental work during my first year. My thanks go to Dr. Nils Warnken for his insight into my project and Dr. Jean-Christophe Gebelin for his support on the modelling side. I thank Dr. Hector Basoalto for the discussions on creep modelling, and Dr. Lars Höglund and Dr. Henrik Larsson for their helpful suggestions on the alloy mapping work.

My experimental work could not have been successful without the assistance of Mr Mick Wickins, who helped me create wax parts and casting moulds, and Mr Peter Cranmer, who helped with the investment casting. I acknowledge too the assistance of Mr Chris Salter for EPMA analysis on oxidation samples.

I am highly appreciated of the support from my colleagues, Dr. Jianglin Huang and Dr. Atsushi Sato, for their valuable discussions on oxidation experiments and computational programming. Many thanks go to all the friends I met in Oxford, who make my life more enjoyable during this work.

Last but not least, I am very grateful to my parents, for their endless love, support and encouragement.

Preface

Parts of this thesis have been published or submitted for publication in:

- Z. Zhu, H. Basoalto, N. Warnken, R.C. Reed. A Model for the Creep Deformation Behaviour of Nickel-Based Single Crystal Ssuperalloys. Acta Materialia, vol.60, 2012, p4888-4900.
- Z. Zhu, L. Höglund, H. Larsson, R.C. Reed. Isolation of Optimal Compositions of Single Crystal Superalloys by Mapping of a Material's Genome. Acta Materialia, vol.90, 2015, p330-343.

Contents

Contents **v**

List of Figures **ix**

List of Tables **xvii**

1 Introduction **1**

1.1 Gas Turbines 2

1.2 Aims and Scope of This Work 3

2 Literature Review **5**

2.1 Nickel-Based Superalloys 5

2.1.1 Composition Microstructure Relationships in Nickel-Based Superalloys 5

2.1.2 Strengthening Mechanisms in Nickel-Based Superalloys 7

2.1.3 Historical Development of The Superalloys 11

2.1.4 Superalloys for Turbine Blades Applications 16

2.2 High Temperature Creep Deformation 17

2.2.1 Creep Behaviour of Nickel-Based Superalloys 17

2.2.2 Creep Modelling in Nickel-Based Single Crystal Superalloys . . 24

2.3 High Temperature Oxidation 30

2.3.1 Fundamental Principles of Oxidation 30

2.3.2 Wagner Theory of Parabolic Oxidation 32

2.3.3 Oxidation of Ni-Cr-Al Alloy System 35
2.3.4 The Gettering Effect 37
2.3.5 Oxidation of Nickel-Based Superalloys 37
2.3.6 Oxidation Modelling in Nickel-Based Single Crystal Superalloys 43
2.4 Design Of New Single Crystal Superalloys 45

3 A Model for The Creep Deformation Behaviour of Nickel-Based Single Crystal Superalloys 46

3.1 Summary 46
3.2 Introduction 47
3.3 Background 48
3.4 The Model 52
3.4.1 Estimation of Shear Strain Rate 54
3.4.2 Constitutive Equations for Relating Microscopic and Macroscopic Behaviour 57
3.4.3 Estimation of Effective Diffusivity of Multicomponent Alloys . 58
3.5 Results and Discussion 60
3.5.1 On The Effective Diffusivity For Climb-Assisted Creep Deformation 60
3.5.2 On The Creep Deformation Behaviour of the CMSX-4 Superalloy 63
3.5.3 On The Dependence of Creep Deformation on Alloy Composition 70
3.5.4 Adaptation To Account For Effect of Rafting 73
3.6 Summary and Conclusions 79

4 Isolation and Testing of New Single Crystal Superalloys Using Alloys-By-Design Method 80

4.1 Summary 80

4.2 Introduction 81
4.3 Description of Alloy-By-Design Method for Single Crystal Superalloys 82
4.3.1 Description of Alloy Isolation Procedure 83
4.3.2 Model for Creep Resistance 89
4.3.3 Model for Oxidation Resistance 90
4.3.4 Models for Density 92
4.3.5 Models for Cost 94
4.4 Isolation of Three New Single Crystal Superalloys 94
4.4.1 Design of alloys for jet propulsion – comparable to current second-generation superalloys 97
4.4.2 Design of alloys for high performance jet engine – comparable to current fourth-generation superalloys 99
4.4.3 Design of alloys for industrial gas turbines – appreciable creep strength and adequate corrosion resistance 105
4.5 Experimental Methods 110
4.5.1 Investment Casting 110
4.5.2 Heat Treatment 111
4.5.3 Creep Testing 113
4.5.4 Cyclic Oxidation Testing 115
4.5.5 Determination of Density 115
4.5.6 Hot Mounting Sample Preparation 115
4.5.7 Cold Mounting Sample Preparation 116
4.5.8 Scanning Electron Microscopy (SEM) 116
4.5.9 Electron Probe Microanalysis (EPMA) 116
4.6 Results 117
4.6.1 Cyclic Oxidation 117
4.6.2 Creep Behaviour 122
4.7 Discussion: Future Direction for Alloy Design 129

4.7.1 Design of alloys for better microstructural stability 129
4.7.2 Design of alloys for low density 136
4.8 Summary and Conclusions 138

5 Mapping of Alloy Design Space for Single Crystal Superalloys 141
5.1 Summary 141
5.2 Introduction 142
5.3 Computational Modelling: The Challenge and Approach Taken . . . 142
5.3.1 Example of Ternary System: Ni-Al-Cr 144
5.3.2 Extension to Quaternary and Multicomponent Systems 151
5.4 Results 158
5.4.1 Ternary Systems Ni-Al-X: Identification of Alloys of Optimum Architecture 158
5.4.2 Extension to Quaternary Systems: Ni-Al-X-Y 163
5.4.3 Multicomponent Systems 168
5.5 Application: Isolation of Optimal Alloys 170
5.5.1 Design of Creep Resistant Alloys with Density Limit 171
5.5.2 Design of Creep Resistant Alloys with Microstructure Stability and Cost Limit 176
5.5.3 Design of Creep Resistant Alloys with Oxidation Resistance Combined 179
5.6 Summary and Conclusions 182

6 Conclusions and Future Work 183
6.1 Summary and Conclusions 183
6.2 Suggestions for Future Work 185

References 187

List of Figures

1.1 A schematic diagram of the basic features of a gas turbine engine: the turbo jet. 2

1.2 Illustration of material usage in the Trent 800 engine, in which nickel-based superalloys are used extensively in the combustor and turbine sections. (Courtesy of Rolls-Royce.) 3

2.1 Size factors of elements for solid solutions with nickel. 8

2.2 Variation of the creep rupture lives of the single-crystal superalloys, as a function of the amount of γ' phase. The creep rupture life is largest when the γ' fraction is about 70%. 10

2.3 Variation of the yield stress of a number of single crystal superalloys at different temperatures. 12

2.4 Evolution of the high-temperature performance of the superalloys since their emergence in the 1940s. 14

2.5 Creep data for single crystal superalloy CMSX-4 at various temperatures and stresses: (a) 750°C and 750MPa, (b) 950°C and 185MPa, (c) 1150°C and 100MPa. 18

2.6 Creep curves for CMSX-4 at low temperatures and high stresses, i.e. in the primary creep regime. (a)750°C; (b)850°C. 20

2.7 Illustration of the mechanism of shearing of the γ' by an $a\langle 11\bar{2}\rangle$ during primary creep. 20

2.8 Rafted γ/γ' structure of single crystal superalloy CMSX-4 after creep loading to 0.39% strain in 10h at 1150°C and 100MPa. 23
2.9 Ellingham diagram for the formation of selected oxides. 33
2.10 Classification of Ni-Cr-Al alloys based on the oxidation mechanism at 1000°C. 35
2.11 Oxide morphology formed on Ni-Al-Cr alloys exposed at temperature between 1000°C to 1200°C. (a) Group I, (b) Group II and (c) Group III. 38
2.12 Schematic illustration of the oxidation mechanisms occurring in Ni-Cr-Al alloys. 39
2.13 Temperature dependence of the parabolic rate constants obtained for the oxidation of a typical Group I alloy (Ni-5Cr-1Al), Group II alloys (Ni-20Cr-2Al, Ni-30Cr-2Al), and Group III alloys. Parabolic rate constants for the growth of NiO on pure nickel, Cr_2O_3 on Ni-30Cr, and Al_2O_3 on Ni-25Al are included for comparison. 40
2.14 Data for the rate of weight loss during oxidation of the PWA1480 and PWA1484 single crystal superalloys, confirming the improved oxidation behaviour of the second-generation alloy. 42

3.1 Basic geometry of climb/glide events in a nickel-based single crystal superalloy. 50
3.2 Dislocation configurations during dislocation creep in a nickel-based single crystal superalloy. 53
3.3 Variation of the dependence of creep strain rate on volume fraction of γ' and matrix channel width. 64
3.4 Comparisons of simulated creep curves with experimental data for CMSX-4 at 900°C. 65
3.5 Comparisons of simulated creep 1% strain life and rupture life with experimental data for CMSX-4. 66

3.6 Temperature dependence of the γ' volume fraction for the CMSX-4 single crystal superalloy. 67

3.7 Simulated creep curves for CMSX4 at 900°C/400MPa with various assumed values of microstructural parameters: (a) volume fraction of γ', (b) γ' particle size, (c) initial dislocation densities, (d) dislocation multiplication parameter. 69

3.8 Comparisons of simulated Larson-Miller plots with experimental data. (a) and (b): Calculations by using mean concentrations; (c) and (d): Calculations by using concentrations in gamma phase. The data are derived from LM plots in. 71

3.9 Simulated creep curves for different generations of single crystal nickel based superalloy at 900°C/400MPa. 72

3.10 Comparison of predicted $1/D_{\text{eff}}$ with experimentally measured time to 1% strain for various nickel-based single crystal superalloys. 73

3.11 Schematic illustration of the changes in microstructural dimensions during rafting by a simple flow of matrix material from the vertical channels to the horizontal channels. From (a) to (c) the γ' precipitates are assumed to retain their cuboidal shape and will coalese along their vertical interfaces. 75

3.12 Schematic illustration of the changes in microstructural dimensions during rafting by a more complex preferential flow of γ and γ' forming elements within the matrix channels: (a) initial state; (b) microstructure in a rafted state, no coalescence of γ' particles; (c) fully rafted structure. 'A' indicates the flux of γ' forming elements; 'B' indicates the flux of γ stabilising elements. 76

3.13 Comparisons of simulated thinning rate of γ matrix vertical channel with experimental data for CMSX-4. 77

3.14 Comparisons of simulated time to 1% strain with experimental data for CMSX-4, dashed curves demonstrate the predictions with rafting. 78

4.1 Illustrations of microstructure-property relationships in nickel-based single crystal superalloys.. 84
4.2 Typical procedures of an alloy design system. 85
4.3 Oxidation diagram for well-known nickel-based single crystal superalloys, in which the predicted Gibbs free energy of Al_2O_3 formation is plotted against the total effective valence in Al_2O_3 scale. Below the dashed line indicates that the Al_2O_3 layer becomes continuous. 93
4.4 Variation of the maximum predicted Creep Merit Index as a function of Cr content, for different misfit ranges. Also plotted is a dotted line corresponding to the best creep merit index in the original dataset. . 98
4.5 Variation of the stability number Md of the alloys predicted to be the most stable as a function of Cr content, for different misfit ranges. . . 99
4.6 Scatter diagram (Creep Merit Index vs. Oxidation Merit Index) for original 161280 alloys dataset. 100
4.7 Comparison of histograms for predicted lattice misfit in different design systems: (a) Previous design in Ni-Cr-Co-Re-W-Al-Ta system; (b) Present design in Ni-Cr-Co-Re-Ru-W-Al-Ta system. 102
4.8 Definition of different lattice misfit range: zero, negative and very negative. 103
4.9 Scatter diagrams (Creep Merit Index vs. Oxidation Index) for different density ranges: (a) density less than 9.0g/cm^3; (b) density less than 8.8g/cm^3; (c) density less than 8.6g/cm^3. 104
4.10 (a) Variation of maximum predicted Creep Merit Index as a function of Cr content for different density ranges; (b) Corresponding Stability Number Md values of these alloys. 106

4.11 (a) Variation of maximum predicted ratio of Creep Merit Index/(Density×Cost) as a function of Cr content for different density ranges; (b) Corresponding Stability Number Md of these alloys. 107
4.12 Variation of maximum predicted creep merit index as a function of Cr content, for alloys with various values of the stability index. 108
4.13 Scatter diagram (Creep Merit Index vs. Oxidation Merit Index) for selected compositions of IGT Alloy 70-81. 110
4.14 (a) Casting furnace in University of Birmingham; (b) Typical mould used for single crystal bars in this study. 111
4.15 Schematic illustration of specimen geometry for creep testing. 114
4.16 The heat treated microstructures of ABD alloys, with cuboidal γ' particles and γ matrix,(a) ABD-1, (b) ABD-2, (c) ABD-3. 118
4.17 Weight change of ABD alloys at different temperatures (a)1000°C and (b)1100°C. Also shown are tests of current employed alloys CMSX-4 and TMS-138A. 120
4.18 Parabolic oxidation constants k_{p} of ABD alloys at 1000°C. Also shown kp of pure oxides from literatures. 121
4.19 Microstructures of cross-sections of oxidized superalloys after 10 hours exposure at 1000°C, (a) ABD-1, (b) ABD-2, (c) ABD-3. 123
4.20 EPMA chemical mapping of oxidized superalloys after 10 hours exposure at 1000°C, (a) ABD-1, (b) ABD-2, (c) ABD-3. 124
4.21 Larson-Miller curves of ABD-1 and 2 for time to 1% strain and rupture life. 126
4.22 Larson-Miller curves of ABD-3 for time to 1% strain and rupture life. 127
4.23 Microstructures of interrupted creep tests of ABD-1, (a) 900°C/400MPa, (b) 1050°C/135MPa. 128

4.24 (a) Histogram of 106920 alloys in Ni-Cr-Co-Re-W-Al-Ta system showing statistic spread of alloys that are TCP-prone or TCP-free as a function of their corresponding Md values. (b) Structure map ($\overline{\text{Md}}$, $\overline{\Delta V/V}$) of 106920 alloys in Ni-Cr-Co-Re-W-Al-Ta system. 131

4.25 Structure map ($\overline{\text{Md}}$, $\overline{\Delta V/V}$) of final selection 38 alloys for refinement design. 134

4.26 Scatter diagrams (Creep Merit Index vs. Md values) for final selected 14 alloys. 135

4.27 The effect of altering alloying element concentration on properties of creep and density. 137

4.28 Mapping of creep merit index vs. density for alloys with 60-70% γ' volume fraction. 138

5.1 Illustrations of composition-microstructure-property relationships in nickel-based single crystal superalloys. 143

5.2 (a) Ni-Al-Cr ternary phase diagram at 900°C (generated by the Thermo-Calc software; (b) enlarged view of γ+γ' region on which tie-lines are superimposed. 146

5.3 Schematic illustration of all compositions in the Ni-Al-Cr ternary system, at a resolution of 1 wt.%. Trial compositions x_i^{trial} located in the γ and γ' two-phase region can be identified, shown as the black points. White points represent all the other compositions located in the single phase region, either γ or γ'. Also plotted are the corresponding tie-lines of some trial compositions. 148

5.4 Schematic illustration of method to adjust the trial compositions along the γ/γ' tie-lines in the Ni-Al-Cr ternary system, for compositions with correct fractions of phases, x_i^{correct}. 149

5.5 Schematic illustration of mapping compositions between x_i^{correct} and x_{i+1}^{correct} in the Ni-Al-Cr ternary system. 152

5.6 Schematic illustration of method to adjust the trial compositions along the γ/γ' tie-lines in the Ni-Al-Cr-Ta quaternary system. 154
5.7 Schematic illustration of mapping compositions in the Ni-Al-Cr-Ta quaternary system. Two directions should be considered each time during mapping process. 155
5.8 Procedures of mapping of an alloy design space. 157
5.9 Trial compositions which have mixture of γ and γ' two phases in the Ni-Al-Cr ternary system. 159
5.10 Correct compositions which have 50% γ' phase in the Ni-Al-Cr ternary system. 160
5.11 Spacing between correct compositions in the Ni-Al-Cr ternary system. 160
5.12 Mapped compositions which correspond to 50% γ' phase in the Ni-Al-Cr ternary system. 161
5.13 Spacing between mapped compositions in the Ni-Al-Cr ternary system.161
5.14 Mapped compositions which corresponds to different fractions of γ' phase, 50%–70%, in the Ni-Al-Cr ternary system. 162
5.15 Mapped compositions which correspond to 50% γ' phase in the possible Ni-Al-X ternary system: (a) Ni-Al-Co; (b) Ni-Al-Re; (c) Ni-Al-Ta; (d) Ni-Al-W. 164
5.16 Number of mapped compositions in each Ni-Al-X ternary system. . . 165
5.17 Correct compositions which have 50% γ' phase in the Ni-Al-Cr-Ta quaternary system. 166
5.18 Spacing between correct compositions in the Ni-Al-Cr-Ta quaternary system. 166
5.19 Mapped compositions which have 50% γ' phase in the Ni-Al-Cr-Ta quaternary system. 167
5.20 Spacing between mapped compositions in the Ni-Al-Cr-Ta quaternary system. 167

5.21 Number of mapped compositions in each Ni-Al-X-Y quaternary system. 168
5.22 Spacing between correct compositions in the Ni-Cr-Co-Re-W-Al-Ta system. 169
5.23 Spacing calculated from random migrations in the Ni-Cr-Co-Re-W-Al-Ta system. 170
5.24 Scatter diagram (Creep Merit Index vs. Density) for the mapped 357636 alloys in the Ni-Cr-Co-Re-W-Al-Ta system. 172
5.25 Scatter diagrams (Creep Merit Index vs. Density) for the mapped alloys corresponding to different Al concentrations: (a) 4.0∼4.5 wt.%; (b) 4.5∼5.0 wt.%; (c) 5.0∼5.5 wt.%; (d) 5.5∼6.0 wt.%; 174
5.26 Scatter diagrams (Creep Merit Index vs. Density) which illustrate the compositional effects on creep and density. (a) different Al concentrations; (b) different Re concentrations; (c) different W concentrations; (d) different Ta concentrations. 175
5.27 Scatter diagram (Creep Merit Index vs. Density) for the mapped alloys in the Ni-Cr-Co-Re-W-Al-Ta system. Also plotted are the limits of different Md values. 177
5.28 Scatter diagram (Creep Merit Index vs. Density) for the mapped alloys in the Ni-Cr-Co-Re-W-Al-Ta system. Also plotted are the limits of different cost. 179
5.29 Scatter diagram (Creep Merit Index vs. Oxidation Merit Index) for the mapped alloys in the Ni-Cr-Co-Re-W-Al-Ta system. 180
5.30 Scatter diagram (Creep Merit Index vs. Oxidation Merit Index) which illustrates the effect of Al on creep and oxidation. 181

List of Tables

2.1 Nominal chemical compositions (wt.%) of typical nickel-based superalloys. 15

3.1 Nominal chemical compositions (wt.%) of different generations of nickel-based single crystal superalloys. 61

3.2 Pre-exponential factors and activation energies for solutal diffusion in nickel. 62

3.3 Calculated effective pre-exponential factors and effective activation energies for different generations of superalloys. 62

3.4 Initial microstructural model parameters and physical constant used for CMSX-4. 63

4.1 Nominal chemical compositions (wt.%) of some common superalloys. 86

4.2 Design target and design criteria of three ABD alloys. 96

4.3 The compositions of IGT alloys designed in this study. 109

4.4 Impurity levels (unit: ppm) in bar stocks of each alloy. 112

4.5 Nominal compositions, barstock compositions and casting compositions for ABD alloys (wt.%). 112

4.6 Creep test conditions of ABD alloys. 114

4.7 Measured densities of ABD alloys. 115

4.8 The 38 compositions selected in ABD-1 design system for improvement design of TCP susceptibility. 132

4.9 The 14 compositions selected form refinement results. 134

5.1 Numbers of possible combinations for given alloying elements and resolutions, which indicate the numbers of compositions in their corresponding alloy systems. 145

5.2 Numbers of correct compositions and their average spacings in all possible Ni-Al-X ternary systems. 163

5.3 Optimal compositions (wt.%) with the best creep resistance for different density limits. 171

5.4 Optimal compositions (wt.%) with the best creep resistance for different density limits, with stability number Md being considered. . . . 178

5.5 Optimal compositions (wt.%) with the best creep resistance for different cost limits. 178

5.6 Optimal compositions (wt.%) with the best combinations of creep and oxidation resistances. 181

Chapter 1

Introduction

Superalloys are unique high temperature materials which have been used for gas turbine applications, due to their outstanding resistance to mechanical and chemical degradation. The increasing demand for improvements in engine efficiency in recent years has provided significant momentum for the research and development of these materials. The gas turbine consists of many different parts of turbomachinary, where turbine blades are the greatest importance since many engine characteristics, such as fuel economy and thrust, depend very strongly on the operating conditions which can be withstood by them. The severe temperature and stress conditions have almost pushed the materials to the limits of their capability.

So far the existing nickel-based superalloys used in service have been designed empirically, but nowadays the better understanding of these metal systems and their underlying physics make it possible to attempt modelling-based design approaches to assist in their future development. This thesis aims to develop the computational modelling tools which can be used to isolate optimal compositions of these alloys, on the basis of composition-property relationships.

1.1 Gas Turbines

Gas turbines are used extensively for applications in jet propulsion and industrial electricity generation. The operation of a modern turbojet engine can be illustrated in Figure 1.1. Three main sections can be identified: the compressor, the combustion chamber and the turbines. At the first section, the compressor, consisting of compressor blades and discs, squeezes the incoming air, thus increasing its pressure. The compressed air is delivered into the combustion chamber, where it is mixed with fuel and ignited. Hot gases leaving the combustor are allowed to expand through the turbine. The turbine blades and discs extract the energy stored within the gas to drive the compressor, which is transmitted by a shaft. After the turbine, the accelerated gases expand through the exhaust nozzle to atmospheric pressure, producing a high velocity jet in the exhaust plume. Figure 1.2 illustrates the usage of materials in the various parts of the Trent 800 engine. One can see that nickel-based superalloys are used extensively in the combustor and turbine sections, due to their remarkable high temperature properties.

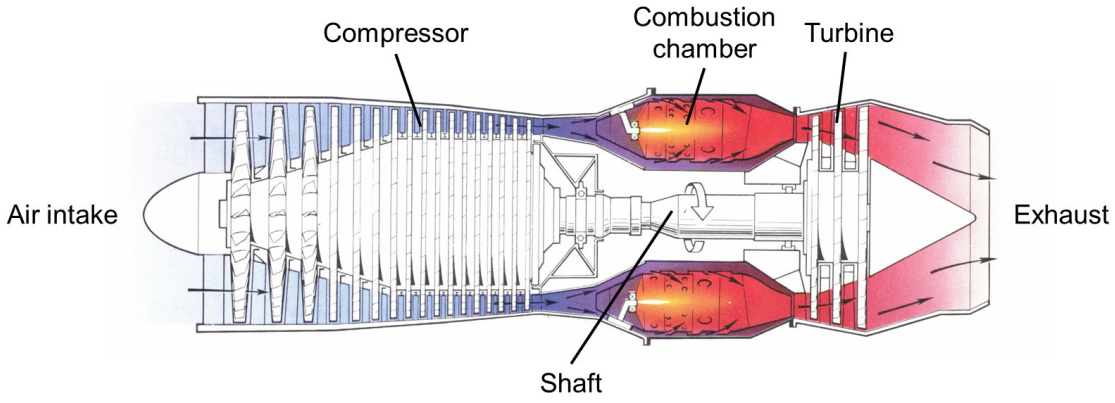

Figure 1.1: A schematic diagram of the basic features of a gas turbine engine: the turbo jet [1].

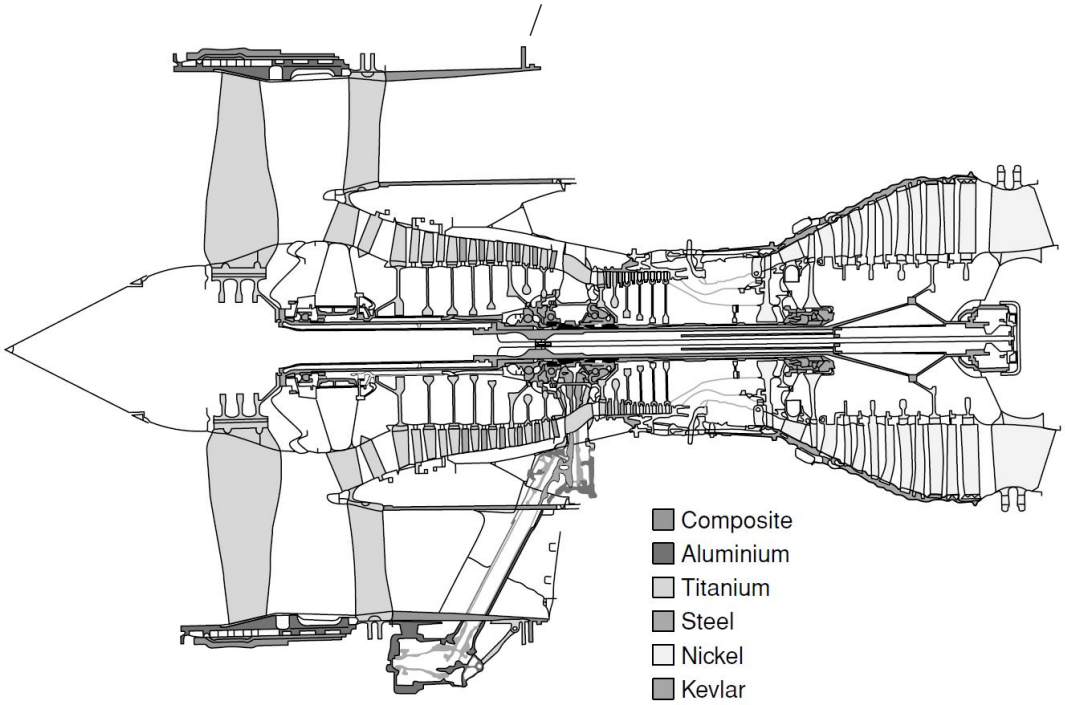

Figure 1.2: Illustration of material usage in the Trent 800 engine, in which nickel-based superalloys are used extensively in the combustor and turbine sections. (Courtesy of Rolls-Royce.)

1.2 Aims and Scope of This Work

As the turbine entry temperature of these engines increases, there is a continuous demand for improvements of these materials. To date, the existing single crystal superalloys used for turbine blade have been designed empirically. Their compositions have been chosen by carrying out many trial tests, on the basis of statistical analysis of existing experimental data, or some metallurgical rules-of-thumb derived from experience. Thus it is unlikely that these alloys have been entirely optimised, and there are compositions waiting to be discovered, which are superior to the current empirically designed ones. In this research, we set the goal to determine the possible underlying quantitative relationship between alloy chemistry and the important properties of nickel-based single crystal superalloys. Composition-microstructure-property relationships will be employed to execute theory-based computational modelling for predictive purposes. The procedures of isolation of optimal alloy compositions will

also be developed in various ways to study the different trade-offs between the important properties.

Chapter 2

Literature Review

2.1 Nickel-Based Superalloys

2.1.1 Composition Microstructure Relationships in Nickel-Based Superalloys

The nickel-based superalloys usually contain ten or more alloying elements, and thus can be considered as one of the most complex alloy systems amongst current engineering materials. Although a wide range of elements are used, some common rules are followed. Most of the superalloys have 10-20 wt.% chromium, up to about 8 wt.% aluminium and titanium, and 5-10 wt.% cobalt. Small amounts of boron, zirconium and carbon are often added. Other optional additions include rhenium, tungsten, tantalum and hafnium, from the 5d block of transition metals, and ruthenium, molybdenum, niobium and zirconium from the 4d block [2]. The behaviour and influence of each alloying elements can be summarised as follows. A first group of elements, cobalt, chromium, molybdenum, rhenium, ruthenium and tungsten, prefer to partition to the austenitic γ matrix. The atomic radii of these elements are very similar to that of nickel. A second group of elements, aluminium, titanium, niobium and tantalum, promote the formation of ordered $Ni_3(Al, Ta, Ti)$, known

as γ'. Boron, carbon and zirconium make up a third class of elements that tend to segregate to the grain boundaries. There are also two subclassifications beyond these. One is the carbide formers: chromium, molybdenum, tungsten, tantalum and titanium. The second consists of the chromium and aluminium, which aid the formation of protective oxide films.

The phases presented in the microstructure of a typical superalloy are summarised in the following list [3]:

(i) The gamma phase, denoted γ. This forms a continuous matrix phase which has the FCC structure. Significant concentrations of elements such as cobalt, chromium, molybdenum, ruthenium and rhenium are present in this phase.

(ii) The gamma prime precipitate, denoted γ'. This precipitate phase exhibits the $L1_2$ ordered structure, which is often coherent with the γ matrix. Elements such as aluminium, titanium and tantalum partition to this phase.

(iii) Carbides and borides. The small amount of carbon present in the alloy react with elements such as titanium, tantalum and hafnium to form MC carbides. During processing or service, these can decompose to form other types of carbides, $M_{23}C_6$ and M_6C, which tend to reside on the γ grain boundaries. These carbides are usually rich in chromium, molybdenum and tungsten. Boron can combine with elements such as chromium or molybdenum to form borides.

(iv) Topologically close-packed (TCP) phases (μ, σ, Laves, etc.). These phases appear in certain superalloys, particularly in the service-aged condition. TCPs usually form as needle-like or round structures and are detrimental to the mechanical properties of the alloy.

2.1.2 Strengthening Mechanisms in Nickel-Based Superalloys

Strengthening in modern nickel-based superalloys arises from a combination of solid solution strengthening and precipitation hardening. Typical nickel-based superalloys consist of a solid solution strengthened FCC γ matrix, further hardened by coherent particles of γ' (Ni_3Al, Ti, Ta). It is important to understand the role of alloying elements as solid solution strengtheners and precipitate formers. This is particularly the case for alloy design purposes.

Solid Solution Strengthening

Solutes with reasonable solid solubility and high hardening coefficients can provide appreciable solid solution hardening to the γ matrix and improve the creep strength of the alloys. The solubility of various elements in nickel can be assessed by a size factor that has the expression $100(d_i - d_{\mathrm{Ni}})/d_{\mathrm{Ni}}$. d_i is the atomic diameter of element i. Elements falling within the shaded zone (± 15 size factor) in Figure 2.1 are expected to exhibit good solid solubility in nickel [4, 5]. The solid solution strengthening primarily improves the resistance to the movement of dislocations in the alloy. Solute atoms cause distortions and shear modulus changes in the lattice, and make it more difficult for cross slip of dissociated dislocations in solid solutions where the stacking fault energy has been lowered due to alloying [6]. The amount of lattice distortion due to atomic size differences between nickel and the solute is given by the change in lattice parameters due to alloying. It is found that the amount of lattice distortion and decrease of stacking fault energy is greater when the separation between the groups for nickel and the solute in the Periodic Table is greater [6, 7, 8]. Therefore, solutes with large atomic diameters and from groups in the Periodic Table well separated from nickel are more likely to strengthen the matrix.

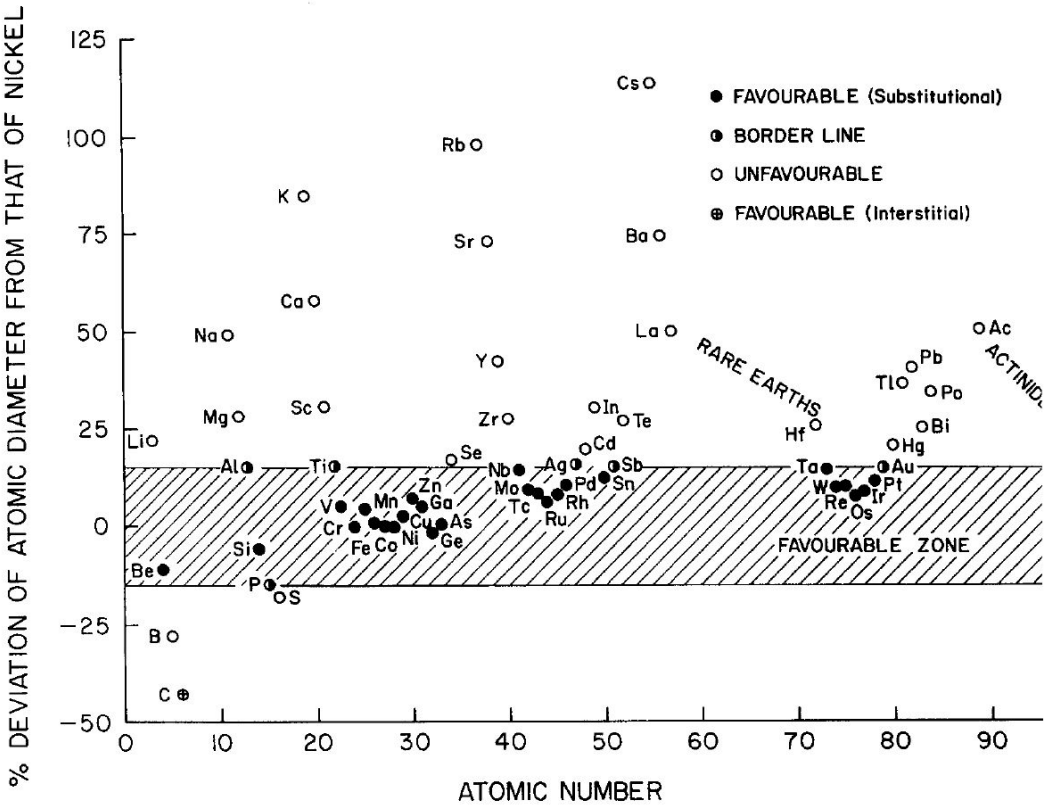

Figure 2.1: Size factors of elements for solid solutions with nickel [5].

Precipitation Hardening

The precipitation phase γ' contributes the major strengthening in nickel-based superalloys, which is provided by coherent stable intermetallic compounds (Ni_3Al, Ti, Ta). The strengthening effects strongly depend on the volume fraction and size of the γ'. For the single crystal superalloys, the creep performance is best when the volume fraction of γ' phase is about 70% (see Figure 2.2) [9]. Creep deformation is restricted to the γ matrix across a wide range of operating temperatures and stresses, with no cutting of the γ' precipitates. Therefore the optimum microstructure of a nickel-based superalloy is fine γ' precipitates, uniformly dispersed, with small γ matrix channel between the precipitates. Beyond the volume fraction of 70%, the strengthening effect starts to fall off resulting in a decrease in creep rupture life. The dislocations may either bow around the precipitates or cut through them, depending on the size of the precipitate particles. The stress τ for dislocation bowing is given by $\tau = Gb/L$ where G is the shear modulus, b is the Burgers vector and L is the center distance between two particles. The stress is found to be inversely proportional to the inter-particle spacing. For dislocation cutting through the particle, the stress required is proportional to the square root of its size, $\tau \propto R^{1/2}$, where R is the particle radius.

In the γ matrix, slip is due to the glide of $a/2\langle 110\rangle\{\bar{1}11\}$ dislocations, where $a/2\langle 110\rangle$ is the shortest lattice vector, and it lies in the close-packed plane. However, in the $L1_2$ structure, the close-packed planes are also $\{\bar{1}11\}$, but the shortest lattice vectors become $a\langle 100\rangle$, which do not reside in them. Therefore, a single $a/2\langle 110\rangle\{\bar{1}11\}$ dislocation travelling in γ cannot enter the γ' phase without formation of an anti-phase boundary (APB). Two $a/2\langle 110\rangle\{\bar{1}11\}$ travel through the γ in pairs to restore the $L1_2$ structure and remove the anti-phase boundary produced by the first dislocation [10]. The associated anti-phase boundary energy, γ_{APB}, represents a barrier which must be overcome for the dislocation cutting to occur. Each dislocation is called a superpartial and a pair of two such dislocations is called a

superdislocation, linked by an APB.

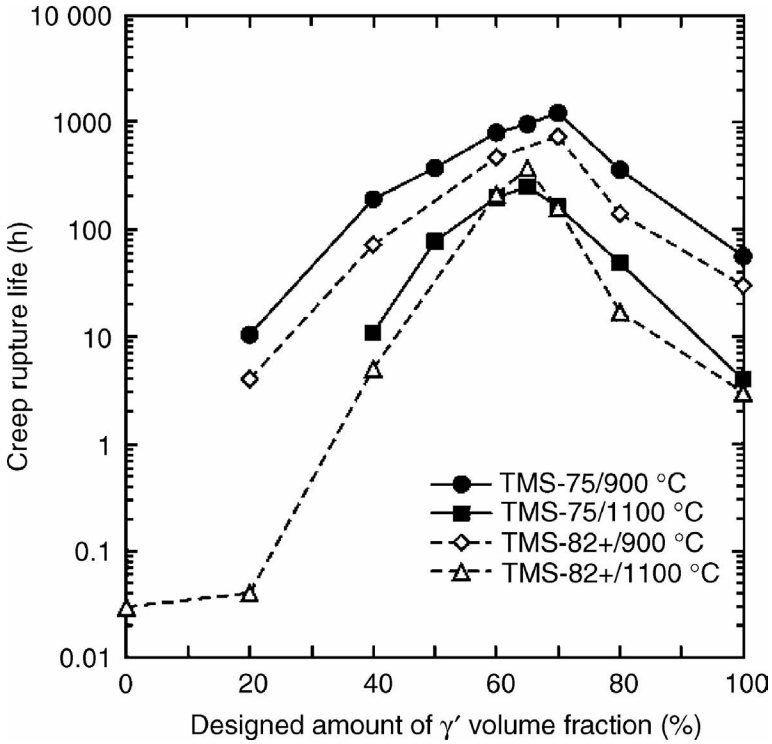

Figure 2.2: Variation of the creep rupture lives of the single-crystal superalloys, as a function of the amount of γ' phase. The creep rupture life is largest when the γ' fraction is about 70% [9].

Misfit Strengthening

Because a slight difference in lattice parameters between the coherent γ and γ' phases, a strain field is produced which could hinder the dislocation motion, hence strengthening the alloy. The lattice misfit δ, is defined as

$$\delta = \frac{2(a_{\gamma'} - a_{\gamma})}{a_{\gamma'} + a_{\gamma}} \tag{2.1}$$

where a_{γ} and $a_{\gamma'}$ represent the lattice parameters of the γ and γ' phases, respectively. Small lattice misfits ($\delta \sim \pm 0.15\%$) are associated with the formation of coherent cuboidal γ' precipitates that provide optimum mechanical properties. Large lattice misfits result in spherical particles and coherency is lost. Values of δ can be adjusted by changing the concentrations of γ and γ' forming elements [11].

Temperature Dependence of Strengthening

The nickel-based superalloys exhibit a remarkable property: the yield stress does not decrease markedly with increasing temperature, as is the case for most of the metallic alloy systems. In fact, for many superalloys the yield stress increases with increasing temperature. Figure 2.3 illustrates the change of yield stress are different temperatures, for a number of single crystal superalloys [10]. The yield stress increases until the temperatures approach to 800°C. After this, the yield stress decrease quickly; at about 1200°C little resistance to plastic deformation is displayed. The anomalous yielding behaviour can be explained as follows. During deformation, the applied stress, together with the anisotropy of the APB energy and further contribution from the elastic anisotropy combine to promote the cross-slip of segments of the γ' superpartial dislocations from the $\{111\}$ slip plane to the cross-slip plane $\{001\}$ [12]. The cross-slipped segments represent microstructural locks, known as Kear-Wilsdorf locks, which resist deformation and cannot move without overcoming the barriers of APBs [13]. The strengthening gradually increases as the temperature rises, since the cross-slip process is thermally activated. Beyond the peak stress, which usually occurs around 800°C, the mode of slip deformation changes to $a/2\,\langle 110\rangle\,\{001\}$; so-called cube slip dominates [14].

2.1.3 Historical Development of The Superalloys

Over the second half of the twentieth century, the story of the evolution of nickel-based superalloys demonstrates a perfect example of the parallel development of a material and its processing method, thus enabling the performance to be improved dramatically. Figure 2.4 provides a perspective for the alloy and process development which has occurred since the first superalloy began to appear in the 1940s [10]. The first superalloys were Ni-Cr wrought alloys. Sufficient chromium additions form stable protective oxides, Cr_2O_3, protecting the alloy from damage by high temper-

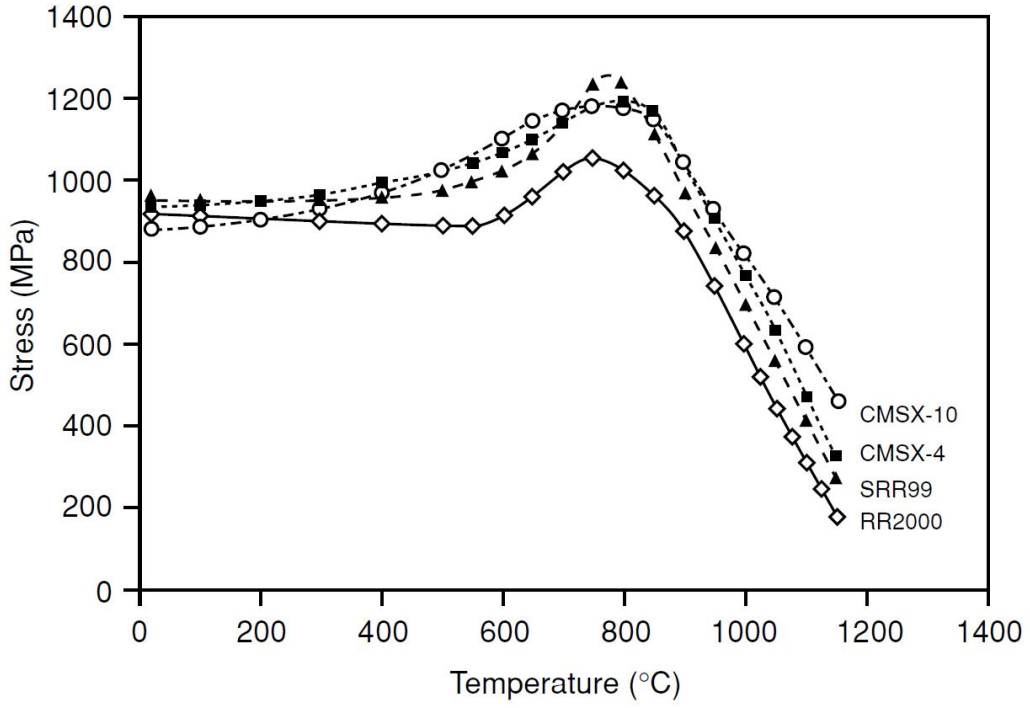

Figure 2.3: Variation of the yield stress of a number of single crystal superalloys at different temperatures [10].

ature oxidation. Carbon and titanium were added, forming carbides at the grain boundary. Aluminium was also added to produce the coherent γ' phase. The very first alloys in this time were commercialised by the Mond Nickel Co. as Nimonic 75 and Nimonic 80 [15]. Two methods were attempted to have further improvement of the high temperature strength: (i) increasing volume fraction of γ' and (ii) increasing solid solution strengthening elements. Beardmore et al. [16] proved that a good balance of mechanical properties was achieved at 40-60% γ' in a series of ternary Ni-Cr-Al alloys. Under this conditions, dislocations cut the precipitate particles so solid solution strengthening is necessary for both phases. This principle was applied successfully to develop Nimonic 105 which contains 5% molybdenum to strengthen the matrix and 4.7% aluminium to form the precipitates [17]. Further wrought alloy development beyond Nimonic 105 was caused by the problems during manufacturing. It is very difficult to forge alloys with more than 40% γ' phase since the high temperature strength of the alloys places a practical limit on

the processing. Therefore, in 1950s the investment casting technologies were introduced to help with the limitation of the forging process. With the removal of the requirement to hot-work process, the volume fraction of γ' in the cast polycrystal superalloys could be increased up to 60% by increasing the aluminium content. A typical cast alloy developed in this time is IN738LC. A significant step forward in the development of cast superalloys was the introduction of the Mar-M series alloys in 1965 [17]. These alloys contained high concentration of tungsten to strengthen the γ matrix and small additions of tantalum or niobium to strengthen the γ' phase. Subsequently, the ductility of these alloys were improved by additions of hafnium [18]. Hafnium could react with residual sulphur, forming carbonsulphide particles [19, 20]. It also enters the carbides and modifies the γ' morphology. Blocky particles are found at grain boundaries which retard grain boundary sliding [20, 21]. Later in 1970s introduction of directional solidification resulted in significant improvements of creep performance of these alloys [22]. This technology produced the columnar microstructure in which the transverse grain boundaries were removed. The final major improvement was the introduction of single crystal casting by using pig-tail or grain selector. The single crystal superalloys allowed the removal of grain boundary strengtheners (C, B, Zr), which enabled better heat treatment to reduce microsegregation.

The first generation single crystal superalloys, for example SRR99 and PWA1480, contain appreciable quantities of γ' forming elements, aluminium, titanium and tantalum. It was recognised in the late 1980s that a further increment in high temperature creep performance can be achieved by decreasing the tungsten and molybdenmum content and adding rhenium. The best known second generation superalloy is CMSX-4, which is characterised by 3 wt.% concentration of rhenium. The third generation increased the rhenium content to about 6 wt.%, e.g. CMSX-10, providing a further improvement to the high temperature capability. It has been suggested that rhenium clusters in the γ, thus offering an explanation of the rhenium-effect [23].

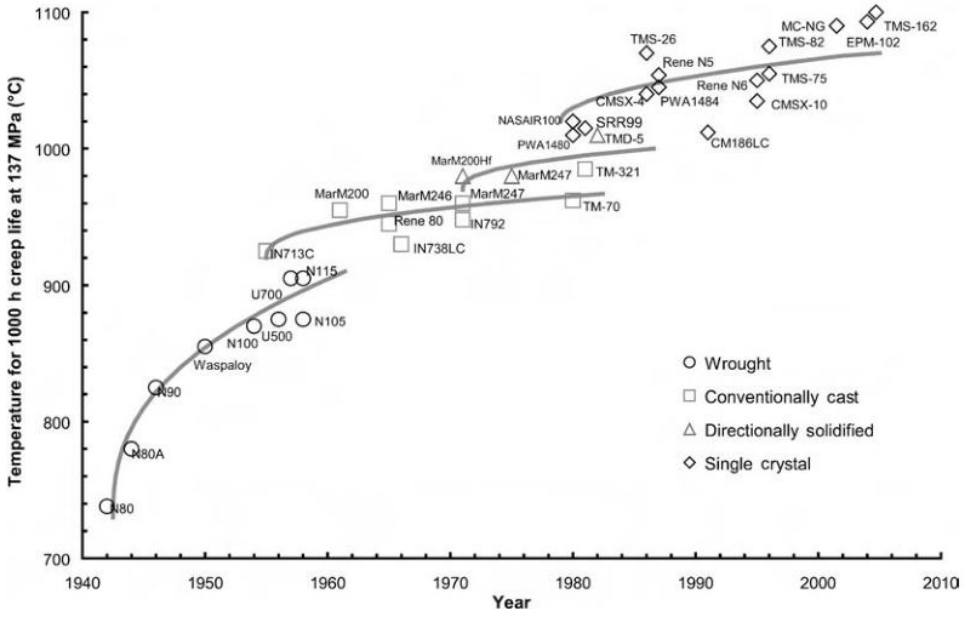

Figure 2.4: Evolution of the high-temperature performance of the superalloys since their emergence in the 1940s [10].

However, recent research shown that rhenium does not cluster [24]. An alternative explanation is that rhenium exists as a solid solution strengthener in the γ and retards all diffusion-driven processes since the vacancy exchange energy of rhenium is remarkably high [25]. Since 2000, the fourth generation single crystal superalloys, such as TMS-138 and TMS-162, are characterised by additions of ruthenium, which hinder vacancy migration in a similar manner to rhenium [26]. The compositions of these typical nickel-based superalloys are summarised in Table 2.1.

Table 2.1: Nominal chemical compositions (wt.%) of typical nickel-based superalloys.

Alloy	Cr	Co	Mo	W	Nb	Al	Ti	Ta	Re	Ru	Hf	C	B	Zr	Ni
Nimonic 75	19.5	-	-	-	-	-	0.4	-	-	-	-	0.10	-	-	Bal
Nimonic 80A	19.5	-	-	-	-	1.4	2.4	-	-	-	-	0.06	0.003	0.06	Bal
Nimonic 105	15.0	20.0	5.0	-	-	4.7	1.2	-	-	-	-	0.13	0.005	0.10	Bal
IN738LC	16.0	8.5	1.75	2.6	0.9	3.4	3.4	1.75	-	-	-	0.11	0.01	0.04	Bal
Mar-M200Hf	8.0	9.0	-	12.0	1.0	5.0	1.9	-	-	-	2.0	0.13	0.015	0.03	Bal
SRR99	8.0	5.0	-	10.0	-	5.5	2.2	3	-	-	-	-	-	-	Bal
PWA1480	10.0	5.0	-	4.0	-	5.0	1.5	12.0	-	-	-	-	-	-	Bal
CMSX-4	6.5	9.0	0.6	6.0	-	5.6	1.0	6.5	3.0	-	0.1	-	-	-	Bal
CMSX-10	2.0	3.0	0.4	5.0	0.1	5.7	0.2	8.0	6.0	-	0.03	-	-	-	Bal
TMS-138	2.8	5.8	2.9	6.1	-	5.8	-	5.6	5.1	1.9	0.05	-	-	-	Bal
TMS-162	2.9	5.8	3.9	5.8	-	5.8	-	5.6	4.9	6.0	0.09	-	-	-	Bal

2.1.4 Superalloys for Turbine Blades Applications

The first gas-turbines blades were produced by extrusion and forging. Nowadays turbine blades are produced by investment casting [27]. Investment casting makes it possible to introduce cooling channels within the blades, and the mechanical strength can be improved without concerns of forging limitations. The investment casting or so-called 'lost-wax' process to produce single crystal casting involves the following steps. First, a wax model is produced by injecting molten wax into a metallic master mould. For blades with cooling passages, ceramic replicas are placed in the master mould, allowing wax to set around them. These moulds are placed on a wax assembly tree, to produce several blades in a single casting. The investment shell is produced by dipping the model into ceramic slurries (mixtures of zircon, alumina and silica), followed by stuccoing with particles of these ceramics. This operation is usually repeated three or four times until the shell thickness is adequate. Finally, the mould is baked to build up its strength. After this, a steam autoclave is used to melt out the wax. Further steps at higher temperatures are employed to fire the ceramic mould. The furnace for producing single crystal castings consists of three parts. The upper melting chamber is used to melt the charge by using high frequency induction melting in a disposable, refractory-fibre crucible. Below this is the central mould chamber, a furnace within which the investment mould sits on a chill plate, and below this is the withdrawal chamber. Each chamber is degassed, the central mould chamber is preheated, and the charge is melted in the melting chamber. The liquid superalloy is poured into the mould which is maintained at a temperature above the liquidus. Immediately after pouring, the mould is withdrawn at the programmed rate. This method will produce a columnar-grained structure; however for a single crystal structure, a grain selector or a seed is placed to the base of the mould.

2.2 High Temperature Creep Deformation

2.2.1 Creep Behaviour of Nickel-Based Superalloys

Creep is the time-dependent permanent deformation of a material which is subjected to a constant stress or load. The high temperatures and stresses experienced by turbine blades result in creep deformation on the nickel-based superalloys employed. The mechanism of creep deformation in nickel-based single crystal superalloys along $\langle 001 \rangle$ direction varies strongly with the conditions of temperature and stress that are applied. Data of creep performance for CMSX-4 superalloys confirms three different regimes can be identified, see Figure 2.5. Consider the first data at low temperature high stress (750°C/750MPa). A phenomena called 'primary' creep occurs, in which creep strain rate first increases and then decreases with increasing creep strain. After this, the primary creep gives way to a 'secondary' creep regime, with a constant creep strain rate to a first approximation. It is found that such 'secondary' creep occurs only after a substantial period of primary creep. Consider the intermediate conditions of 950°C and 185MPa. The 'tertiary' creep deformation is observed in which creep strain rate increases monotonically with creep strain. The primary creep and steady-state secondary creep regimes are absent in these temperatures and stress levels. Finally, at temperatures beyond about 1050°C, the creep curve shows a distinct plateau before the creep strain increases dramatically to a rupture occurring almost immediately. At these high temperatures, creep performance is affected by the evolution of γ/γ' microstructure, which results in a 'rafted' structure, the so-called 'rafting regime'. The mechanisms of deformation in different regimes are discussed in the following sections in detail.

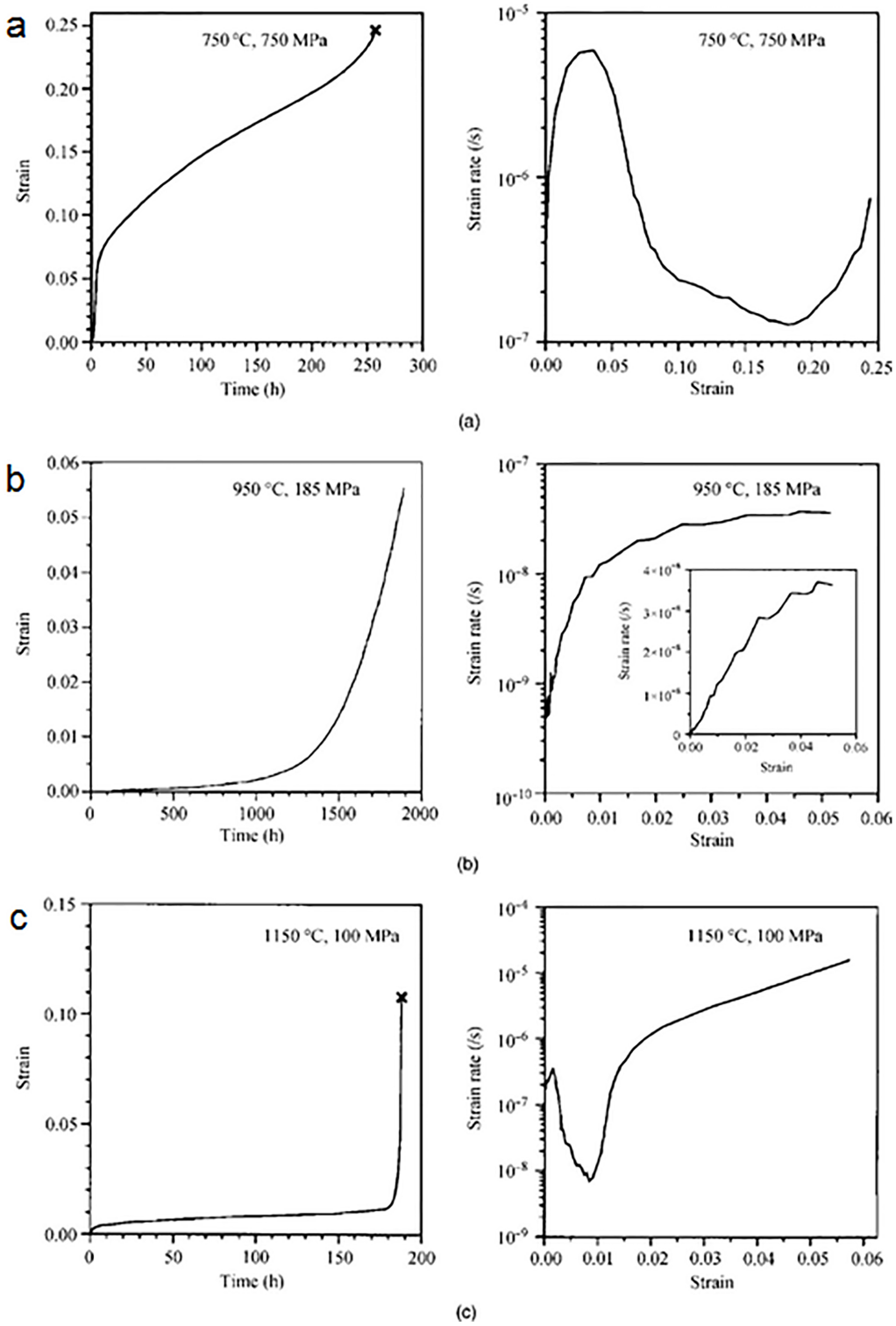

Figure 2.5: Creep data [28, 29] for single crystal superalloy CMSX-4 at various temperatures and stresses: (a) 750°C and 750MPa, (b) 950°C and 185MPa, (c) 1150°C and 100MPa.

Primary Creep Regime

At low temperature and high stress conditions, primary creep deformation occurs in the ⟨001⟩-oriented single crystal superalloys. Creep curves for CMSX-4 are plotted at temperatures of 750°C and 850°C in Figure 2.6. It can be observed that the primary creep strain increases with applied stress, with primary creep eventually giving way to a steady-state secondary creep. The behaviour also indicates primary creep happens only when the applied stress is greater than a critical value of about 500 MPa. Before the onset of primary creep, dislocation motion is often confined within the γ matrix, on the usual $\langle 1\bar{1}0\rangle \{111\}$ slip system. Observations of primary creep in single crystal superalloys were first made by Leverant and Kear [30], where shearing of γ' occurs via pairs of $\langle 11\bar{2}\rangle$ type of dislocations cutting through the γ' particles. There has been considerable controversy about the mechanism of formation of the $\langle 11\bar{2}\rangle$ dislocation ribbons, but it is now known as the dissociation of $a/2\,\langle 1\bar{1}0\rangle \{111\}$ dislocations into their Shockley partials. The reaction can be given by [31]

$$a/2\,[011] + a/2\,[\bar{1}01] \rightarrow a/3\,[\bar{1}12] + a/6\,[\bar{1}12] \tag{2.2}$$

If the applied stress is sufficient, the $a/3\,[\bar{1}12]$ dislocation is able to penetrate into the precipitate, leaving a superlattice intrinsic stacking fault (SISF) behind it and remaining the partial $a/6\,[\bar{1}12]$ at the interface. The further reactions between the $a/2\,\langle 1\bar{1}0\rangle \{111\}$ type dislocations will introduce a second pair of $a/3\,[\bar{1}12]$ and $a/6\,[\bar{1}12]$, see Figure 2.7. An anti-phase boundary (APB) separates the two $a/6\,[\bar{1}12]$ dislocations, leaving a superlattice extrinsic stacking fault (SESF) within and the final $a/3\,[\bar{1}12]$ at the interface.

Tertiary Creep Regime

At high temperature and moderate applied stress conditions, it is observed that creep of nickel-based superalloys can occur without any noticeable primary stage.

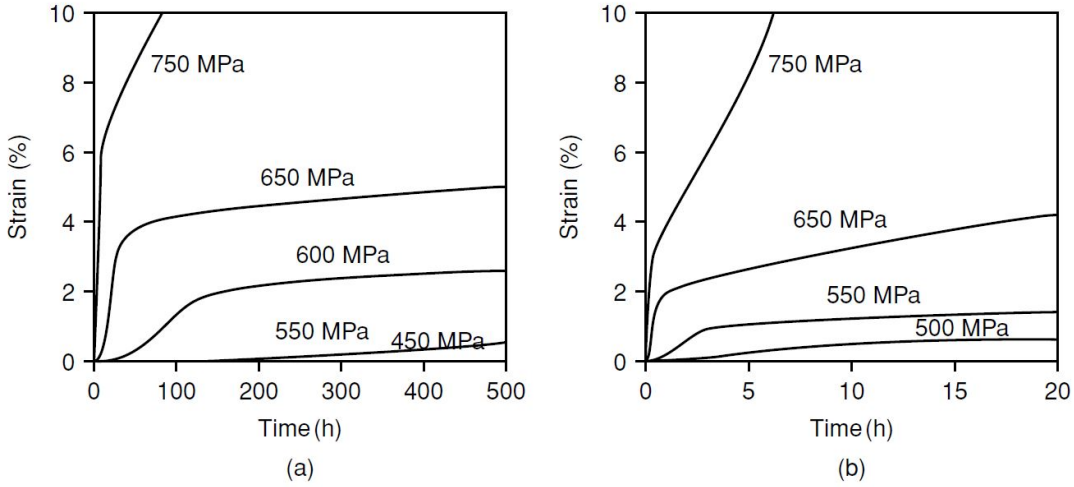

Figure 2.6: Creep curves for CMSX-4 at low temperatures and high stresses, i.e. in the primary creep regime. (a)750°C; (b)850°C [28, 29].

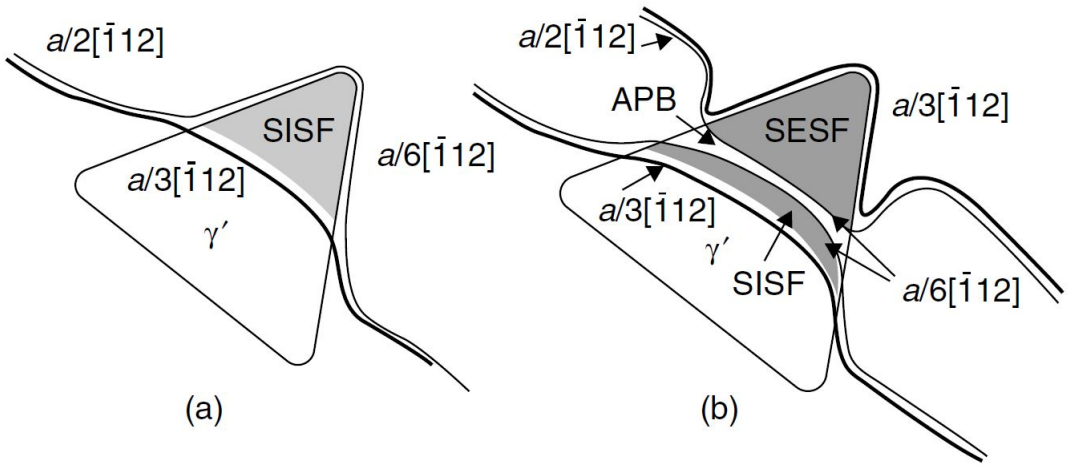

Figure 2.7: Illustration of the mechanism of shearing of the γ' by an $a\langle 11\bar{2}\rangle$ during primary creep [10].

Figure 2.5 illustrates that creep strain increases monotonically from the initial stage to rupture. In the intermediate tertiary creep regime, evidence from TEM work [28, 32, 33, 34] indicates that dislocation activity is of the $a/2\langle 1\bar{1}0\rangle\{111\}$ and restricted to the γ matrix channels. The density of dislocations is found to increase with increasing creep strain, while no microstructural degradation occurs. Since the γ' particles are not sheared by the dislocations, cross-slip is required for substantial deformation to occur. The leading dislocation loops are screw expanded throughout the matrix; later segments of mixed or edge dislocations will be deposited at the γ/γ' interfaces [35]. This part of creep curve suggests an exponential interpretation for the strain growth with time. This has been developed on the basis of that the creep strain rate, $\dot{\epsilon}$ is proportional to the accumulated macroscopic creep strain, ϵ. It has been assumed that the mobile dislocation density ρ_{m} varies with the macroscopic creep strain rate, according to [36]

$$\rho_{\mathrm{m}} = (\rho_0 + M\epsilon)\exp\{-\phi\epsilon\} \tag{2.3}$$

where ρ_0 is the initial dislocation density, M is a dislocation multiplication rate and ϕ is a dislocation attrition coefficient. The macroscopic creep strain rate $\dot{\epsilon}$ is given by Orowan's equation

$$\dot{\epsilon} = \rho_{\mathrm{m}} b v \tag{2.4}$$

where b is the Burgers vector and v is the dislocation velocity. Assuming that the provided v is constant, one has

$$\dot{\epsilon} = (\dot{\Gamma} + \Omega\epsilon)\exp\{-\phi\epsilon\} \tag{2.5}$$

where $\dot{\Gamma} = \rho_0 b v$ is the initial creep rate and $\Omega = Mbv$ is a softening coefficient which is proportional to the rate of dislocation multiplication. It has been confirmed that

the attrition term ϕ is orientation dependent and Ω has an exponential function of the applied stress [28]. The latter stage of tertiary creep is associated with the damage mechanisms of active creep cavitation and γ' coarsening, which gives a dramatic increase of creep rate.

Rafting Regime

In the rafting regime, degradation of γ/γ' microstructure becomes faster since the thermally activated processes are favoured by high temperatures. Two effects have been found at the very early stages of deformation: (i) the formation of equilibrium interfacial dislocation networks at the γ/γ' interfaces [37], and (ii) the directional coarsening process of γ' particles known as the rafting effect. Figure 2.8 shows the rafted γ/γ' structure of single crystal superalloy CMSX-4 after creep loading to 0.39% strain in 10h at 1150°C and 100MPa [38]. The external loading lies in the plane of the micrograph in the vertical direction; thus the plated-shaped rafts formed perpendicular to the axis of loading. This is always found to be case for superalloys with negative misfit, such as the commercially developed CMSX-4. When the misfit is positive, rafts are found to lie parallel to the direction of loading.

In Figure 2.5, the following observations can be made for creep when rafting happens: (i) at initial stage, a small amount of strain is accumulated and then a plateau occurs in which the creep strain almost remains constant with time; (ii) at later time, the creep strain increases dramatically, with rupture eventually occurring. The observations in [38] support the view that the initial reduction of creep rate arises as a consequence of the rafting effect. Figure 2.8 shows that more than ten γ' precipitates coalesce in the transverse direction to form the fully rafted structure. It proves that the rafting and the eventual inversion of the γ/γ' structure reduces the activity of $\langle 1\bar{1}0\rangle\,\{111\}$ dislocations and prevents the dislocation glide/climb process. The later rapid increase of creep strain is associated with extensive creep cavitation occurring at either the casting porosity from interdendritic regions, or alternatively

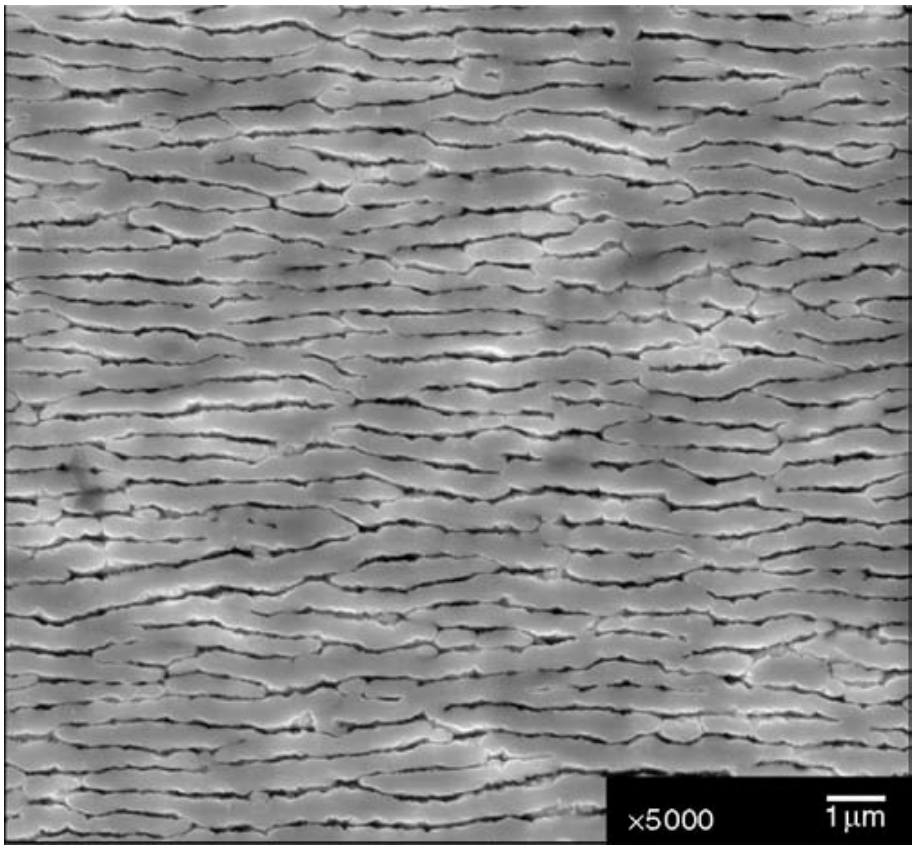

Figure 2.8: Rafted γ/γ' structure of single crystal superalloy CMSX-4 after creep loading to 0.39% strain in 10h at 1150°C and 100MPa [38].

at pores from around TCP phases forming at these elevated temperatures.

2.2.2 Creep Modelling in Nickel-Based Single Crystal Superalloys

The significance of creep behaviour for superalloys in gas turbine engine applications has resulted in extensive research in creep mechanics and creep life predictions. Past approaches of creep modelling have largely been empirical, in which parameters are numerically fitted to a limited creep database to interpolate behaviour. The creep predictions of empirical equations are not ideal for the complex engineering alloys. Firstly, the creep curves of superalloys do not have a distinct steady state regime where the microstructure does not change, and secondly the extrapolation of short time creep data might not be valid for the prediction of long term behaviour. Until now, the empirical fitting methods still remain as a common practice for creep prediction despite the problems of accuracy with the extrapolation method.

Steady State Power-Law Creep

The power law creep equations are the most widely used to explain the steady state creep of pure metals and simple alloys [34]. The constant creep strain rate, $\dot{\epsilon}_{ss}$ is given by

$$\dot{\epsilon}_{ss} = A\sigma^n \exp\left\{-\frac{Q}{RT}\right\} \tag{2.6}$$

where σ is the applied stress, n is the stress exponent, A is a constant and Q is an activation energy. From the analysis of the experimental creep data, the activation energy is found to be correlated to the value of self diffusion [39]. It indicates that some of the mass transport on the microstructural scale is rate-controlling. The classic work of Ansell and Weertman [40] made the first attempt to derive a steady-state creep equation for a particle-strengthened alloy. In this model, they assumed

that creep behaviour of these alloys was controlled by the climb-glide movement of dislocations passing over second-phase particles. When a gliding dislocation become pinned, climb is required to release it for further glide. Therefore the gliding process is responsible for creep deformation, but the creep rate is determined by the climb process. Based on this assumption, Ansell and Weertman's model predicts that the larger the particle size the more climb is required, so that creep rate is proportional to particle size. Although the model clearly demonstrates most of the creep physics but it predicts only a linear relationship between creep rate and stress for stresses below the Orowan stress. When using power-law function to explain the creep of particle-strengthened alloys, it is obvious that the stress exponent n is not a constant; it varies between approximately two and twenty. The activation energy employed in power-law models increases with stress and are always greater than that for diffusion.

It is known that the steady state creep models do not account for the microstructure changing during creep. For nickel-based superalloys, these microstructure evolutions have an effect on creep rate and rupture lifetimes. Therefore, the Dyson model [41, 42] is developed as a microstructure-based kinetic creep equation to overcome the insufficiency of the power-law, which incorporates the continuum damage mechanics (CDM) [41, 43] to account for the kinetics of microstructural evolution. Both the Dyson model and CDM are described in the following sections.

Larson-Miller Prediction

The Larson-Miller parameter was introduced for life time prediction of materials based on the Arrhenius relation, which is functionally related to time and temperature [44]. Larson and Miller assumed that creep rate could be explained by the Arrhenius type equation

$$\dot{\epsilon} = A \exp\left\{-\frac{Q}{RT}\right\} \tag{2.7}$$

where $\dot{\epsilon}$ is the creep rate, A is a constant, R is the gas constant, T is the temperature and Q is the activation energy for the creep process. Assuming that the creep strain to rupture ϵ_{r} is constant over the temperature range of interest, and steady state creep is dominant in the major part of creep, then the average creep strain rate is $\dot{\epsilon} = \epsilon_{\mathrm{r}}/t_{\mathrm{r}}$. Substituting this into Equation 2.7,

$$P = T(C + \ln t_{\mathrm{r}}) \tag{2.8}$$

where C is the Larson-Miller constant, which is usually taken to be 20. As already stated, the Larson-Miller parameter is derived with the assumption that the majority of creep is controlled by steady state creep and no microstructural changings occur before rupture. However, it is contradictory to the nature of creep in complex particle-strengthened alloy. Therefore, it is not surprising that Larson-Miller prediction is sometimes inaccurate.

Continuum Damage Mechanics of Creep

Continuum Damage Mechanics (CDM) can describe the tertiary creep behaviour during a constant loading test. The CDM was originally introduced by Kachanov in his seminal work of 1958 [45], and subsequently extended by Rabotnov [46] and Leckie and Hayhurst [47]. Although the damage can arise from numerous mechanisms of dagadation, Kachanov and Rabotnov decided to use a single damage parameter ω, representing a state variable ranging from an initial value of 0 to final value of 1 when failure is assumed to occur. The evolution of creep strain and damage are assumed to depend on stress σ, temperature T and current condition of damage within the material. Thus a simple set of equations can be given as

$$\dot{\epsilon} = f(\sigma, T, \omega) \tag{2.9}$$

$$\dot{\omega} = g(\sigma, T, \omega) \tag{2.10}$$

In the concept of empirical CDM, a power-law creep rate equation is coupled with a similar power-law dependence of the damage evolution equation, according to

$$\dot{\epsilon} = \dot{\epsilon}_0 \left(\frac{\sigma}{\sigma_0(1-\omega)} \right)^n \tag{2.11}$$

$$\dot{\epsilon} = \dot{\omega}_0 \left(\frac{\sigma}{\sigma_0(1-\omega)} \right)^m \tag{2.12}$$

where $\dot{\epsilon}_0$, $\dot{\omega}_0$ and σ_0 are constants. These equations can be fitted to empirical data for predictive purposes. However, the use of single damage parameter can lead to poor extrapolation when more than one damage mechanism is operating. Thus, it is inevitable that more parameters are required to describe the creep behaviour of engineering alloys in complex service conditions.

The Dyson Model

The shortcomings of the empirical fitting methods and power-law creep equations have led to the development of a microstructure-based creep constitutive model. This generic microstructure-explicit model consists of two parts. Firstly, a creep rate equation is developed to overcome the shortcomings of power-law relations. The creep rate is explained not only as a function of stress and temperature, but also of the underlying microstructural characteristics (particle size, volume fraction of γ', dislocation density etc.). Secondly, the physically-based continuum damage mechanics are coupled to describe the microstructure evolution, which accounts for the damage variable such as cavitation growth, particle coarsening and dislocation multiplication.

The Dyson model was built upon the traditional continuum damage mechanics, where several categories of damages have been specified. Williams and Cane [48] and Dyson and Meclean [49] proposed that particle coarsening results in a progressive increasing of creep strain rate (tertiary creep). Ashby and Dyson reviewed the presumable microstructural features that would affect the creep behaviour and lifetime.

The principal categories of damage can be [50]:

(i) intrinsic softening of material due to multiplication of dislocation and particle coarsening.

(ii) intrinsic softening of material due to cavitation and crack initiation at grain boundaries.

(iii) change of applied stress due to the reduction of cross-section area under constant load.

The work accomplished by Ion et al. incorporates those specific categories of damage into a software package, which can be applied for particular engineering alloys creep modelling, e.g. nickel-based superalloys [51]. In the 1990s, this empirical CDM approach has been firstly extended to predict the high temperature anisotropic creep behaviour of single crystal superalloys by Ghosh and Mclean [52], and Pan et al [53]. The Dyson model is mainly a kinetic creep equation set proposed by Dyson and Osgerby in 1993 [54]. Further improvement has been made by Dyson [55] and Basoalto where appropriate microstructure-based damage equations were coupled to propose a generic microstructure-explicit model of creep in nickel-based superalloys [42].

In the Dyson's model, primary creep is determined by the stress transfer from the matrix to the strengthening particles, represented by the dimensionless state variable H (equal to σ_b/σ where σ_b is the back stress introduced due to stress redistribution).

$$\dot{\epsilon} = \dot{\epsilon}_0 \sinh\left(\sigma(1-H)/\sigma_0\right) \tag{2.13}$$

$$\dot{H} = (h/\sigma)(1 - H/H^*)\dot{\epsilon} \tag{2.14}$$

All the parameters are directly related to a physical constant or measurable microstructure characteristics. These are the dislocation density ρ, jog density C_j, volume diffusivity $D_v = D_0 e^{-Q_{d,j}/RT}$, particle volume fraction ϕ_{p}, the interparticle

spacing λ_{p} and mean Taylor factor M.

$$\dot{\epsilon}_0 = \frac{2\rho_i \phi_{\mathrm{p}}^{1/2}}{\overline{M}}(1-\phi_{\mathrm{p}})\left[(\pi/4)^{1/2} - \phi_{\mathrm{p}}^{1/2}\right] C_j D_v \tag{2.15}$$

$$\sigma_0 = \frac{\overline{M} kT}{b^2 \lambda_{\mathrm{p}}} \tag{2.16}$$

$$h = E\phi_{\mathrm{p}} \tag{2.17}$$

$$H^* = \frac{2\phi_{\mathrm{p}}}{1+\phi_{\mathrm{p}}} \tag{2.18}$$

The equation set above results in a decreasing of creep rate with increasing strain until a steady creep state occurs. Dyson and Mclean have proposed several damage state variables which can contribute to tertiary creep of precipitation strengthening alloys.

(i) Mobile dislocation density multiplication

Dislocation sources will be activated with increasing of creep strain, thus there is an accumulation of dislocation density during creep process. This effect is represented by a damage variable $\dot{D}_d = C\dot{\epsilon}$, where C is a constant and $D_d = \rho/\rho_i - 1$.

(ii) Dispersion particle coarsening

The dislocation climb-glide movement is very sensitive to the interparticle spacing. Coarsening of particles occurs during the service. Assuming Ostwald ripening to occur by volume diffusion with a kinetic rate constant K_p and the evolution is represented by $\dot{D}_p = K_p(1-D_p)^4/3$.

Thus after incorporating all these damages to the model, the full CDM equation set

is:

$$\dot{\epsilon} = \dot{\epsilon}_0(1 + D_d)e^{-Q_{d,j}/RT} \sinh\left\{\frac{\sigma(1-H)}{\sigma_0(1-D_p)}\right\} \tag{2.19}$$

$$\dot{H} = (h/\sigma)(1 - H/H^*)\dot{\epsilon} \tag{2.20}$$

$$\dot{D}_d = C\dot{\epsilon} \tag{2.21}$$

$$\dot{D}_p = \frac{K_p}{3}(1 - D_p)^4 \tag{2.22}$$

The above set of constitutive equations can be applied to predict the constitutive damage of particle strengthened alloys. However, no model has been developed yet to account for the effect of alloy chemistry on creep deformation behaviour, which is needed for the alloy design purposes.

2.3 High Temperature Oxidation

Due to the high service temperature, oxidation resistance is one of the most critical requirements for nickel-based superalloys. Therefore, an understanding of superalloys oxidation and how it is influenced by alloy composition and exposure conditions is essential for the alloy design purpose. The following starts from a brief review of the fundamentals of the oxidation of metals and alloys, and then oxidation behaviour of complex superalloys are discussed.

2.3.1 Fundamental Principles of Oxidation

When pure metals are exposed to an oxidising atmosphere at high temperature, the fundamental theory for chemical reaction is described by

$$\left(\frac{2x}{y}\right)\mathrm{M} + \mathrm{O}_2 \rightarrow \left(\frac{2}{y}\right)\mathrm{M}_x\mathrm{O}_y \tag{2.23}$$

The initial oxide could form very rapidly as a protective layer which decreases the further oxidation rate. The later stage is considered to be ionic diffusion controlling, which involves either the diffusion of cations through the oxide scale towards the gas or the diffusion of gas through the oxide. It is found that the subsequent oxidation rate also depends on the sample geometry such as oxide thickness and surface area [56].

Considering the driving force for oxidation, the total Gibbs free energy for the M_xO_y formation can be described according to the Van't Hoff equation as [57]

$$\Delta G_f = \Delta G_0 + RT \ln K \tag{2.24}$$

where ΔG_0 represents the Gibbs free energy change when all the components are presented in their standard state. R is the gas constant, T is the temperature given by Kelvin and K is the equilibrium constant. For oxidation of pure metals, K is given by the equation

$$K = \frac{a_{M_xO_y}^{2/y}}{a_M^{2x/y} P_{O_2}} \tag{2.25}$$

where a_M and $a_{M_xO_y}$ describe the thermodynamic activities of the metal M and the oxide M_xO_y. In an ideal system, the activities of both the metal and the oxide are taken as unity. Therefore, Equation 2.24 can be simplified to

$$\Delta G_f = \Delta G_0 + RT \ln \left(\frac{1}{P_{O_2}} \right) \tag{2.26}$$

For the special cases of equilibrium ($\Delta G_f = 0$), the standard free energy ΔG_0 is given as

$$\Delta G_0 = RT \ln P_{O_2} \tag{2.27}$$

The dissociation pressure of the oxide can be expressed as

$$P_{\mathrm{O_2}}^{\mathrm{M/M_xO_y}} = \exp\left(\frac{\Delta G_0}{RT}\right) \tag{2.28}$$

One can see that the formation of simple metal oxides is determined by temperature and oxygen partial pressure. The Ellingham diagram, in which the standard free energy of formation (ΔG_0) is plotted versus temperature for the oxides, can be used to compare the relative stabilities of each oxide. The first Ellingham diagram was introduced by Ellingham [58] in 1944, and extended by Richardson and Jeffes [59] in 1948. A typical Ellingham diagram of simple oxides is shown in Figure 2.9. One finds:

- The lower the position of the line on the diagram the more stable is the oxide.
- The values of $P_{\mathrm{O_2}}^{\mathrm{M/M_xO_y}}$ can be obtained directly from the diagram by drawing a straight line from the point marked O on the left side through the free energy line at the temperature of interest and reading the oxygen partial pressure from its intersection with the scale at the right side labelled $P_{\mathrm{O_2}}$.

For typical superalloy systems which contain Ni, Cr and Al, the Ellingham diagram indicates that the Al_2O_3 is thermodynamically more stable and tends to form first. However, in the case of complex alloys, more than one oxidation mechanisms may operate at once, which makes the study of oxidation more complicated. When resolving the oxidation process in terms of thermodynamics, kinetics and microstructure features, it is possible to predict the types of oxidation reactions and the oxidation rate for complex alloy system.

2.3.2 Wagner Theory of Parabolic Oxidation

The high temperature oxidation kinetics is largely determined by the properties of the oxide scale. When the oxide scale grows, the diffusion-controlled growth rate of

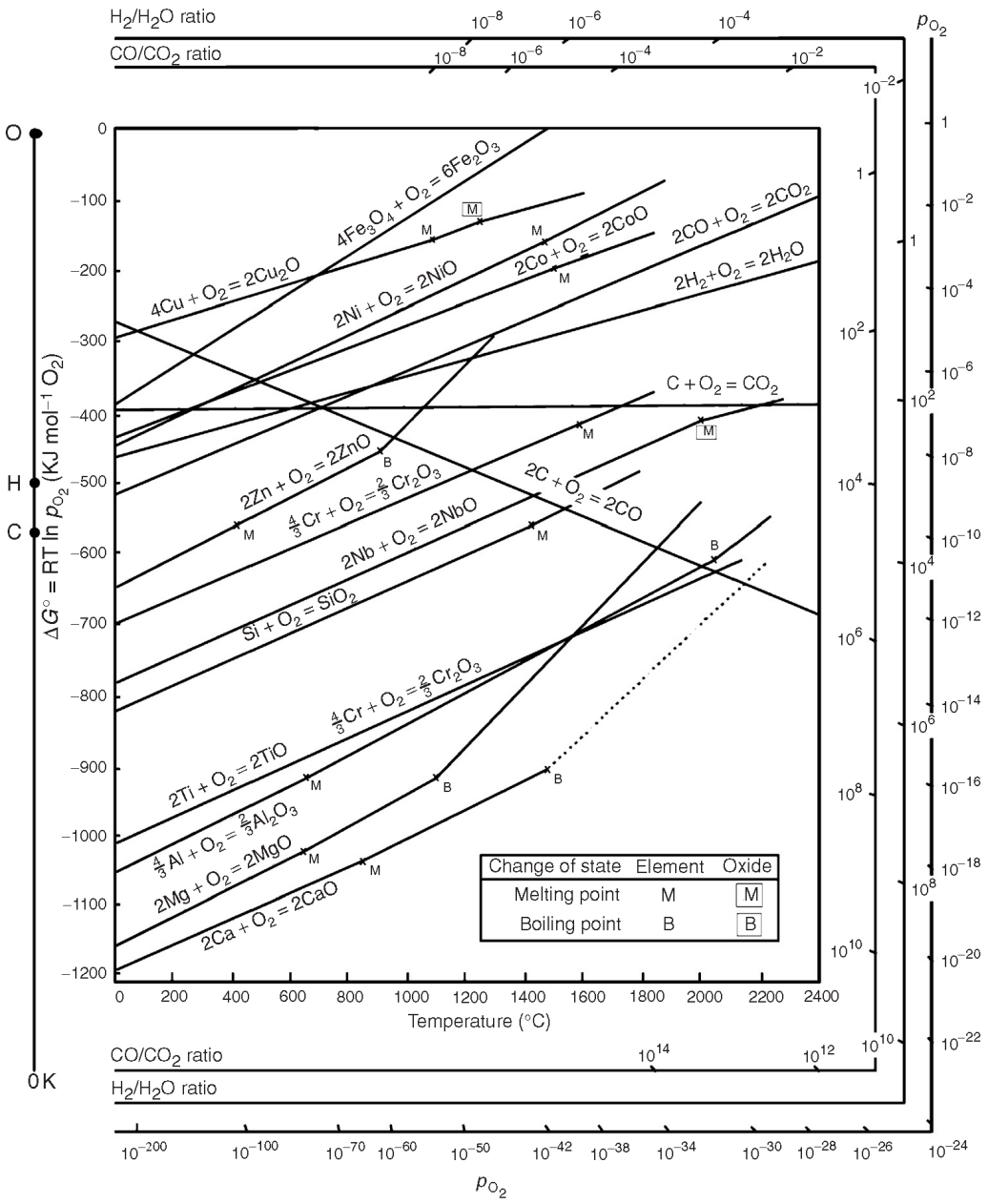

Figure 2.9: Ellingham diagram for the formation of selected oxides [57].

the oxide layer with thickness x is usually given by a parabolic rate law [2]

$$dx/dt = \frac{k'}{x} \tag{2.29}$$

where k' is called the parabolic rate constant. Integrating the equation from $t_0 = 0$, which has

$$x^2 = 2k't \tag{2.30}$$

Wagner [60] provided a theoretical treatment for this rate constant k' based on the concentration of metal and oxygen in the oxide lattice, and the diffusion coefficients of the metal ions and oxygen between the both metal/oxide and oxide/gas interfaces. Two basic assumptions have been made in the Wagner theory: (i) the formed oxide layer is a compact, perfectly adherent scale, and (ii) migration of ions or electrons across the scale is the rate-controlling process. The results of Wagner's derivation of the parabolic rate constant, k', is given by

$$k' = \frac{1}{RT} \int_{\mu_0'}^{\mu_0''} \left(D_{\mathrm{O}} + \frac{Z_{\mathrm{M}} D_{\mathrm{M}}}{2} \right) d\mu_0 \tag{2.31}$$

where D_{M} and D_{O} are the diffusivities of M and O, respectively, in the oxide. Z_{M} is the metal volume and μ_0' and μ_0'' are the chemical potentials of oxygen at the metal/oxide and oxide/gas interfaces. Good agreement can be found between the experimental rate constants and those calculated from Wagner theory for a mumber of metals reacting with oxygen [61]. However, it should be noticed that data derived from the Wagner theory might not be accurate in real systems. This is particularly true when assumption (ii) is not satisfied, in which the rate-controlling process will not follow the simple parabolic relationships as described in Equation 2.30. Nevertheless, the use of parabolic rate constant is still considered as a common practice to compare the oxidation rate for many situations that exhibit approximately parabolic

behaviour.

2.3.3 Oxidation of Ni-Cr-Al Alloy System

Giggins and Pettit have summarised the oxidation morphology and oxidation mechanisms from a series of work on the Ni-Cr-Al ternary alloy system [62, 63]. They observed three different types of oxidation mechanisms occurring, and classified the behaviours into groups based on the morphology of the oxide scale; Group I, Group II and Group III. The description of these groups and the compositions of the alloys which populate them are shown in Figure 2.10.

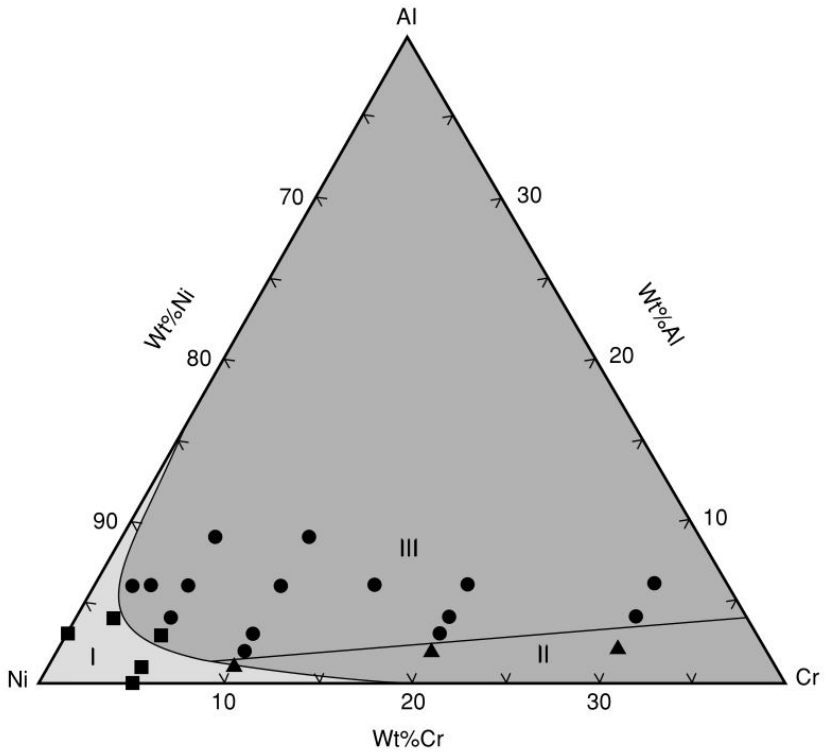

Figure 2.10: Classification of Ni-Cr-Al alloys based on the oxidation mechanism at 1000°C [63].

Group I Figure 2.11(a) represents the microstructure of the Group I oxidation mode, which was observed on Ni-2Cr-4Al alloy after 20 hours at 1000°C. The oxide scales consist of a thick continuous layer of NiO on the top accompanied by a sub-scale below NiO composed of a mixture of Cr_2O_3, Al_2O_3 and/or the spinel

$Ni(Cr, Al)_2O_4$. Oxidation starts with the formation of $Ni(Cr, Al)_2O_4$ and small regions of NiO dispersed in between, as illustrated in Figure 2.12(a). Further growth of the $Ni(Cr, Al)_2O_4$ is overtaken by an external NiO scale due to an insufficient flux of Cr and Al to the reaction interface, as shown in Figure 2.12(b) and (c). The development of the sub-scale oxides beneath the alloy surface is encouraged by the diffusion of oxygen into the bulk material to form discontinuous Cr_2O_3 and Al_2O_3 within the alloy. Since the activity of oxygen required to form Al_2O_3 is much less than that of Cr_2O_3, the precipitation of Al_2O_3 tends to occur to a greater depth. It is also suggested in Figure 2.13 that the oxidation rates of Group I alloys are greater than that for pure nickel because solution of Cr and Al from the alloy increases the cation vacancy concentration in the NiO scale.

Group II The oxidation morphology of Croup II alloys is characterised by an external scale of Cr_2O_3 and an internal precipitation of Al_2O_3. These alloys contain high concentrations of Cr and relative low concentrations of Al. Figure 2.11(b) shows a typical cross-section of the alloy Ni-20Cr-2Al after 21 hours of oxidation at 1100°C. The initial oxidation of Group II alloys is similar to that of Group I alloys, which forms a transient $NiO/Ni(Cr, Al)_2O_4$ mixed external scale and a sub-scale Cr_2O_3/Al_2O_3. However, unlike Group I alloys, there is sufficient Cr to support the formation of a continuous Cr_2O_3 sub-scale, which after time, replaces the $NiO/Ni(Cr, Al)_2O_4$ as the external oxide layer. The formed continuous Cr_2O_3 slows down the diffusion of Ni atoms outwards, which makes the formation of $NiO/Ni(Cr, Al)_2O_4$ very difficult. In the meantime, the reduced activity of oxygen in the alloys is sufficient to oxidise Al internally, but not sufficient to oxidise Cr, resulting in the precipitation only of Al_2O_3 under Cr_2O_3, as illustrated in Figure 2.12(d) and (e).

Group III The oxidation of Group III alloys forms a compact external Al_2O_3 scale without any presence of internal sub-scale precipitation. These alloys possess appreciable concentrations of both Cr and Al. The oxidation morphology is shown

in Figure 2.11(c), for an alloy Ni-20Cr-4Al after 20 hours of oxidation at 1200°C. Group III alloys were found to follow the initial oxidation mechanisms as Group II alloys. At later stage, the relatively high Al concentration of the bulk material results in the continued formation of Al_2O_3 to form a continuous layer. It can be confirmed in Figure 2.13 that Group III alloys exhibit the lowest oxidation rate, which is the case that most of the nickel-based single crystal superalloys are designed to be Al_2O_3-formers.

2.3.4 The Gettering Effect

One of the most important conclusions from Giggins and Pettit's work is that it is possible to form Group III morphologies at Al concentrations as little as 5 wt.%. This is not consistent with what is observed in the Ni-Al binary system, which requires Al concentrations of about 10 wt.% [62]. The ability of Cr to encourage the premature external oxidation of Al has been referred to as a 'gettering effect'. Various theories were proposed to explain the effect of Cr on the formation of Al_2O_3 scale. Wagner's internal oxidation theory [64] indicates that the third element (Cr) acts as a secondary getter for oxygen which decreases the inward flux of oxygen into the alloy. This enables Al to diffuse to the surface from the bulk without any precipitations deep in the substrate. Figure 2.10 shows that with the addition of 5 wt.% Cr, the Al falls to 5 wt.% to form a continuous Al_2O_3 layer. This effect becomes very important for the design of nickel-based superalloys.

2.3.5 Oxidation of Nickel-Based Superalloys

Oxidation of the nickel-based superalloys occurs when the components such as turbine blades and guide vanes are exposed to the hot stream working environment. During the oxidation process, wall thickness and loading bearing capacity are lost, which enhances the likelihood of component failure [10]. Generally, adequate content of alloying additions, e.g. Cr and Al, is required to form a highly protective

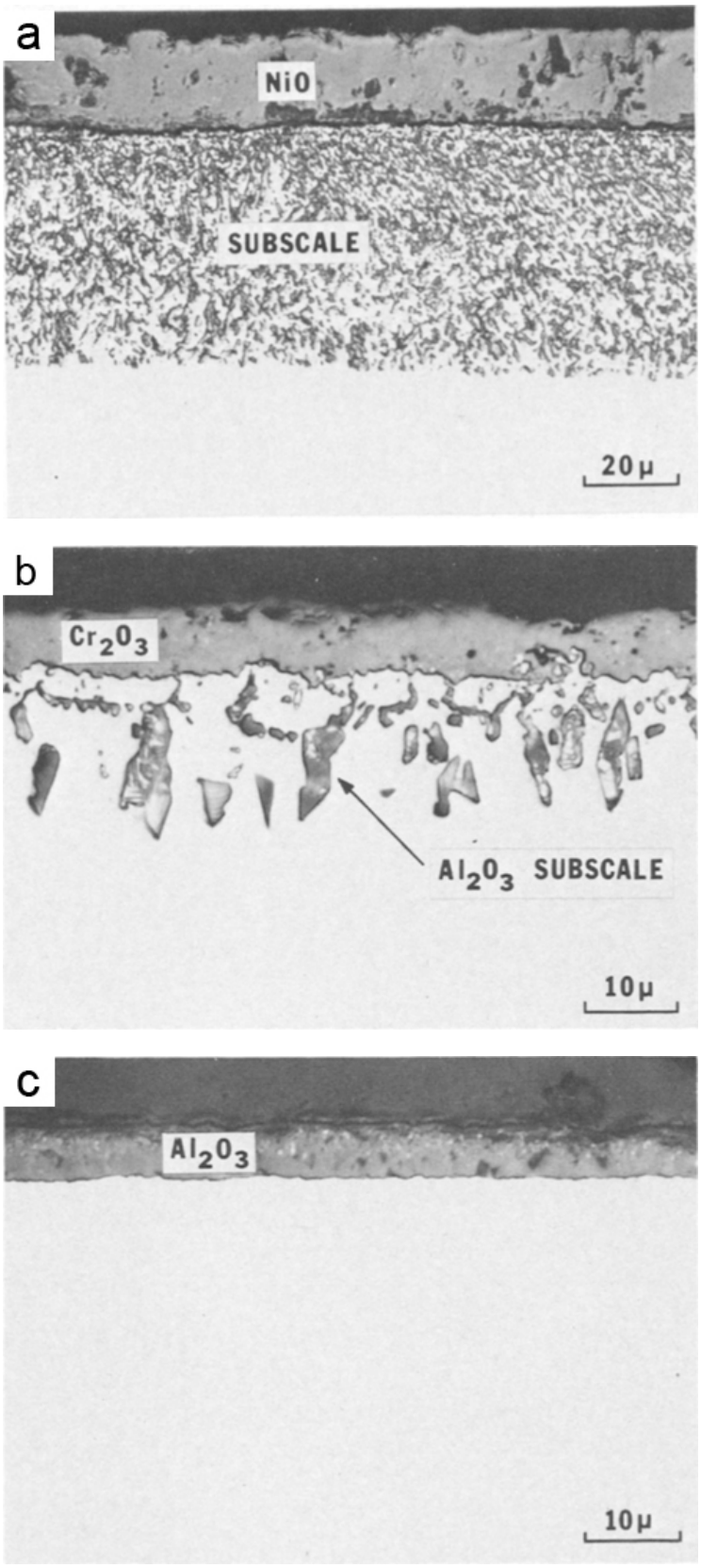

Figure 2.11: Oxide morphology formed on Ni-Al-Cr alloys exposed at temperature between 1000°C to 1200°C. (a) Group I, (b) Group II and (c) Group III [63].

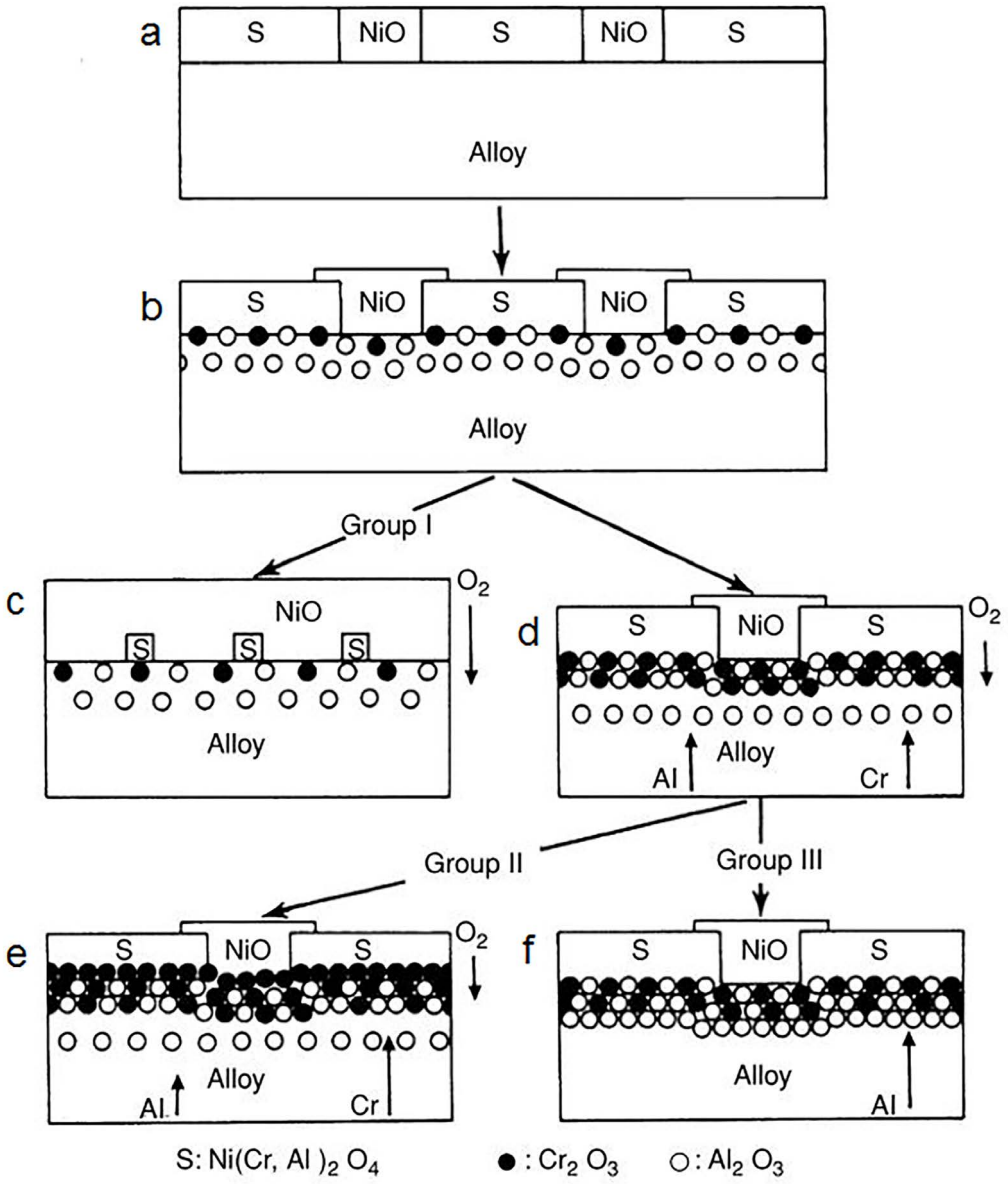

Figure 2.12: Schematic illustration of the oxidation mechanisms occurring in Ni-Cr-Al alloys 1000°C [63].

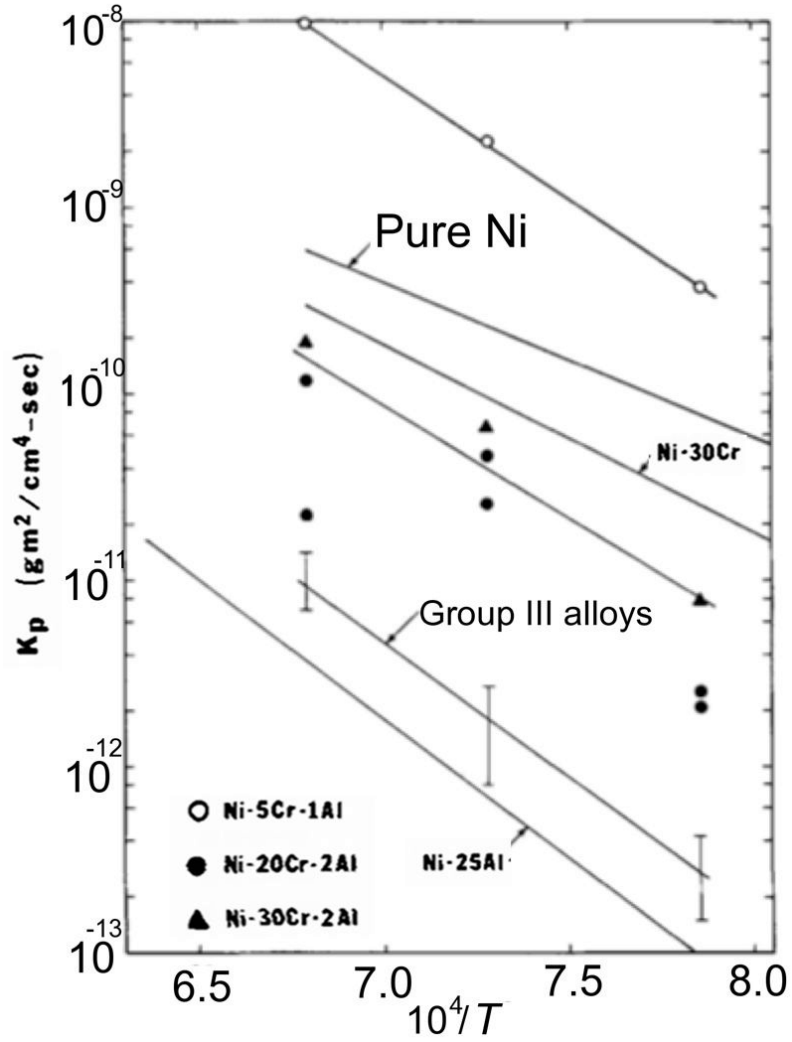

Figure 2.13: Temperature dependence of the parabolic rate constants obtained for the oxidation of a typical Group I alloy (Ni-5Cr-1Al), Group II alloys (Ni-20Cr-2Al, Ni-30Cr-2Al), and Group III alloys. Parabolic rate constants for the growth of NiO on pure nickel, Cr_2O_3 on Ni-30Cr, and Al_2O_3 on Ni-25Al are included for comparison [63].

oxide layer. Therefore, the oxidation rate is decreased and the underlying metal nickel is well prevented from the high temperature oxidation. The oxides formed in nickel-based superalloys fall into several different types, with NiO, Cr_2O_3 and Al_2O_3 the three most common and significant ones. The NiO forms very rapidly, with voids and cracks due to the high concentration of nickel vacancies, which is easily damaged by sustained attack. The Cr_2O_3 layer has a good performance at relatively low temperature (e.g. 900°C); however, the Cr_2O_3 starts to vaporise and the protection breaks down when the temperature rises above 1000°C [65]. In practice, it has been found that the alloys with alumina scales (Al_2O_3) provide the greatest resistance to oxidation. For this reason, the first two generations of single crystal superalloys are commonly alumina formers. The concentration of aluminium required for growth of Al_2O_3 has been developed empirically about 6wt.% [66]. The improvements of oxidation resistance can be demonstrated in the development of the second-generation single-crystal superalloys. The well developed Pratt & Whitney PWA1484 alloy is mainly built on the basis of the first-generation alloy PWA1480 [67]. Figure 2.14 shows the oxidation performance of the two alloys at 1150°C, which indicates that the rate of metal loss due to oxidation is much less for PWA1484, giving an improvement of x1.6 in lifetime. The reasons for this are summarised as follows. Firstly, the concentration of Al was increased from 5.0 to 5.6 wt.%, to ensure the formation of Al_2O_3 scale. Secondly, the removal of Ti is beneficial for the Al_2O_3 formation due to the influence on the ionic mobilities.

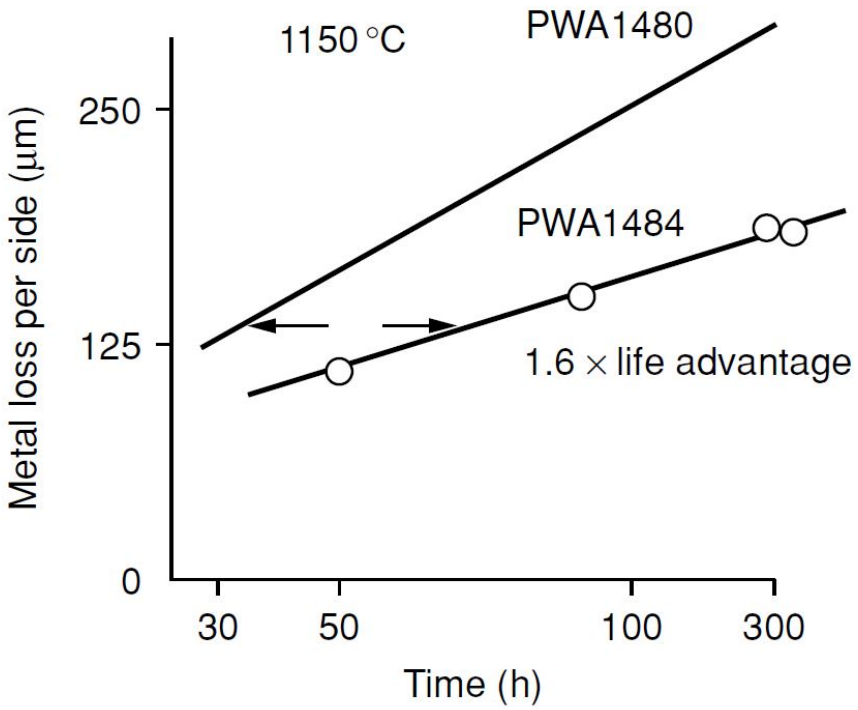

Figure 2.14: Data for the rate of weight loss during oxidation of the PWA1480 and PWA1484 single crystal superalloys, confirming the improved oxidation behaviour of the second-generation alloy [67].

2.3.6 Oxidation Modelling in Nickel-Based Single Crystal Superalloys

In 1981, de Wit [68] rationalised Wagner theory of parabolic oxidation with driving force of oxidation, ΔG_f. One has the parabolic oxidation rate k_t

$$k_t = -\frac{\sigma_t(t_\mathrm{a} + t_\mathrm{c})t_\mathrm{el}}{z_\mathrm{c}^2 z_\mathrm{a}^2 e^2}\Delta G_f \tag{2.32}$$

where σ_t is the conductivity of the $\mathrm{M_xO_y}$ oxide. t_a and t_c represent the transport numbers of metal cations and oxygen anions, and their valences are denoted as z_c and z_a, respectively. t_el is the transport number of electrons. The elementary charge is represented by e.

Consistent with the Van't Hoff isotherm [57], the ΔG_f is given as

$$\Delta G_f = \Delta G_0 + RT \ln\left(\frac{a_{\mathrm{M}_x\mathrm{O}_y}^{2/y}}{a_\mathrm{M}^{2x/y} P_{\mathrm{O}_2}}\right) \tag{2.33}$$

where ΔG_0 is the standard free energy of formation, T is absolute temperature, and R is the gas constant. The activity of the oxide $\mathrm{M}_x\mathrm{O}_y$ is described by $a_{\mathrm{M}_x\mathrm{O}_y}$, commonly substituted by 1, and the activity of the element M in the superalloys is represented by a_M. P_{O_2} is the partial pressure of oxygen.

In practice, the protective $\mathrm{Al_2O_3}$ scale formed in nickel-based superalloys is considered as an n-type oxide rather than a p-type one [69], so that it is an electron conductor with $t_\mathrm{el} \approx 1$. It is also evident that in the case of n-type conductor, one has $t_\mathrm{a} \gg t_\mathrm{c}$. Thus, Equation 2.32 is simplified as

$$k_t = -\frac{\sigma_t t_\mathrm{a}}{z_\mathrm{c}^2 z_\mathrm{a}^2 e^2}\Delta G_f \tag{2.34}$$

When using the NernstEinstein relation, one can write

$$k_t = -\frac{\frac{c_{\mathrm{o}} z_{\mathrm{o}}^2 e^2}{kT} D_{\mathrm{o}}}{z_{\mathrm{c}}^2 z_{\mathrm{a}}^2 e^2} \Delta G_f = -\frac{c_{\mathrm{o}} D_{\mathrm{o}}}{z_{\mathrm{c}}^2 z_{\mathrm{a}}^2 e^2} \Delta G_f \tag{2.35}$$

where c_{o} represents the concentration of oxygen in the oxide, D_{o} represents the diffusion coefficient of oxygen in it, and k is the Boltzmann constant. Recent work by Sato [70] assumed that a doubly charged oxygen vacancy is the dominant defect in Al_2O_3 at high temperatures, one has

$$k_t = -\frac{\frac{c_{\mathrm{o}}}{V_{\ddot{\mathrm{o}}}} D_{V_{\ddot{\mathrm{o}}}}}{z_{\mathrm{c}}^2 z_{\mathrm{a}}^2 e^2} \Delta G_f \tag{2.36}$$

where $D_{V_{\ddot{\mathrm{o}}}}$ represents the diffusion coefficient of a doubly charged oxygen vacancy, and $V_{\ddot{\mathrm{o}}}$ represents its concentration. At a constant temperature, one has

$$k_t \propto V_{\ddot{\mathrm{o}}} \Delta G_f \tag{2.37}$$

Since nickel-based superalloys are multicomponent systems, the presence of other alloying elements will also have a profound influence on Al_2O_3 formation. Considerable amounts of other alloying elements ions (e.g. Ni^{2+} and Ta^{5+}) with different chemical valences compared to Al^{3+} would introduce vacancies to alumina lattice [10]. In Sato's work [70], the total effects of the impurity elements on the oxygen vacancy are summarised by an effective valence of the Al_2O_3, denoted $\mathrm{Val}_t^{\mathrm{eff}}$. One has

$$\mathrm{Val}_t^{\mathrm{eff}} = \sum_{n=i} \left(z_i - z_{\mathrm{Al}}\right) c_i^{\gamma} \tag{2.38}$$

where z_i is the effective valence of element i's ion, and z_{Al} is the valence of Al ion: z_{Al}=3. c_i^{γ} represents the composition of element i in γ phase. Since Al_2O_3 is an n-type conductor, when $\mathrm{Val}_t^{\mathrm{eff}}$ becomes more negative, the concentration of oxygen

anions increases so that the oxidation rate is expected to accelerate.

2.4 Design Of New Single Crystal Superalloys

Over the past 20 years, the chemistry of nickel based single crystal superalloys has been refined to meet the increasing demand of high temperature capability in gas turbine applications. Their compositions are very complex, containing as many as ten different alloying elements, to confer the desired combination of properties. Traditionally, current employed alloys have been designed by empiricism (see e.g. [71, 72, 73]). Thus their chemical compositions have been isolated by carrying out many trial-and-error testings, involving small-scale processing of limited quantities of material and subsequent characterisation of their behaviour. The alloy composition adopted is then the one found to display the best, or desirable, combination of properties. The large number of possible alloying elements indicates that these alloys are not entirely optimised yet, and there are improved alloys in the compositional space which are superior to those current ones. Recent work done by Reed [74] has proposed computer-based modelling procedures, termed Alloys-By-Design methods, for the design of new generations of nickel based single crystal superalloys. The important, overarching strategy is to estimate the compositional dependence of the behaviour and performance (across of alloy space defined by upper and lower bounds of elemental concentrations, to an appropriate resolution). Suitable composition-microstructureproperty relationships must be used when proposing the models for individual important required properties. After this, different search algorithms will be applied to isolate the optimum compositions with good combinations of required properties. The theory-based methods of isolation of optimised alloy compositions give the possibility to propose alloy compositions with specific design purpose. For the best predictive capability, model development section becomes vital and requires better understanding of underlying physical principles governing behaviours.

Chapter 3

A Model for The Creep Deformation Behaviour of Nickel-Based Single Crystal Superalloys

3.1 Summary

A physical model for the creep deformation of single crystal superalloys is presented, which is sensitive to chemical composition and microstructure. The rate-controlling step is assumed to be climb of dislocations at the matrix/particle interfaces and their rate of escape from trapped configurations; a strong dependence on alloy composition then arises. By testing the predictions of the model against the considerable body of published experimental data, the dependence of the kinetics of creep deformation on alloy chemistry is rationalised. The effects of microstructural scale – precipitate size, geometry and spacing – are also studied. The climb processes assumed at the matrix/precipitate interfaces give rise to the vacancy flux required for the mass transport needed for rafting. For creep deformation at higher tempera-

tures, a modification to the basic theory is proposed to account for a rafting-induced strengthening effect. A first order estimate for the rate of creep deformation emerges from the model, which is useful for the purposes of alloy design.

3.2 Introduction

The single crystal superalloys have been developed specifically for applications within the gas turbines used for jet propulsion and electricity generation [10]. Their chemistries are complicated; the list of alloying additions present can often exceed ten in number and usually includes Cr and Co for resistance to environmental degradation, Al, Ti and Ta for precipitation hardening *via* the $Ni_3(Al, Ti, Ta)$ phase and Mo, W, Re and possibly Ru for creep strengthening. At the present time, the existing single crystal superalloys used in service have been designed empirically. Their compositions have been chosen on the basis of testing of trial heats, statistical analysis of experimental data by regression analysis/neural networks, or in some instances metallurgical rules-of-thumb derived from experience. Such approaches are unlikely to derive compositions for these alloys which are entirely optimal, or else well-matched to their intended applications.

Why is this? The overarching reason is that computer-based models which can predict in accurate, quantitative terms the relationship between alloy chemistry and the properties of importance – e.g. creep resistance, oxidation, low cycle fatigue performance – do not exist as yet. In turn, there are related issues. First, it is not clear whether the underlying theory on which to base such computer models – accounting for the complexity of the metallurgical phenomena, the rate-determining steps and their dependence upon the atomic species present on the crystal lattice – is mature enough at present. Second, the predictions of any such theory would in practice depend upon the availability of a number of critical parameters to be placed into the equations employed. Since it is known that the properties of the single

crystal superalloys depend in a sensitive fashion upon the underlying alloy chemistry, the activation energies for the rate-determining steps and associated concentration terms are likely to be of considerable importance. At sufficiently high temperatures, the $Ni_3(Al, Ti, Ta)$ phase evolves to the so-called 'rafted' morphology, the effect of which is contentious.

The work reported in this chapter was carried out with the above in mind. We set out to determine whether the composition dependence of the creep deformation behaviour of the single crystal superalloys could be explained in quantitative terms, with an accuracy useful for the purposes of alloy design. Two factors led us to believe that this might be possible. First, theory for the constitutive behaviour of precipitate-strengthened alloys has matured markedly, so that deformation on the microscale – accounting for the geometry and scale of precipitation for example – can now be related to the macroscopic performance of the component which is clearly of importance for practical applications [41, 75, 76]. Second, recent experimental work has quantified the composition-dependence of rate-controlling steps in thermally-activated processes in these alloys; trends relating activation energies to atomic number have been identified [25, 77]. These factors provided us with an incentive to perform the modelling work reported in this chapter, which contributes to our alloys-by-design efforts [74].

3.3 Background

In this section, the basis for the model is provided, some necessary definitions are given and previous work in this area is acknowledged. The microstructure of a single crystal superalloys consists of a face-centered cubic matrix (denoted γ) in which a large volume fraction ϕ_p of the ordered precipitation strengthening phase (denoted γ') resides. The precipitates are assumed to be cubes of side length d; the matrix channel width separating them is denoted w. For a constant volume fraction of the

γ' phase, it follows that $\phi_\mathrm{p} = d^3/(w+d)^3$ so that

$$w = d\left(1/\phi_\mathrm{p}^{1/3} - 1\right) \tag{3.1}$$

For the purposes of the present work, it is assumed that any matrix/precipitate misfit stresses are negligible. The precipitates are taken to be coherent with the matrix, since the lattice parameters of the two phases are in practice not very different from each other. A uniaxial tensile stress σ is applied externally along the cube normal direction, consistent with the practical application of these materials in turbine applications. We consider particularly the important regime for which the applied stress is lower than 500 MPa and temperature is higher than 850°C, so that the active matrix dislocations of form $a/2\,\langle 1\bar{1}0\rangle\,\{111\}$ – where a is the lattice parameter of the matrix – do not penetrate the γ' particles [78, 79]. Figure 3.1 illustrates the situation. The dislocation density ρ is low; dislocation sources are assumed to be active, e.g. at sub-grain boundaries grown in from the casting process used to fabricate the material. Gliding dislocations are the agents by which creep deformation is accumulated; however since ϕ_p is large, their glide is prevented once the nearest particle is reached. Attention must therefore be placed on the mechanism by which these obstacles are overcome. On account of the high service temperatures employed, climb processes along the particle/matrix interfaces are possible. Consider the dislocation interacting with precipitate 1 in Figure 3.1. A local climb force is necessary. The geometry of the situation dictates the direction of climb which (in this case) requires vacancy absorption – hence the use of the symbol 'a' at particle 1. Notice that coupled climb/glide is needed. If this is sufficient then the dislocation is able to escape (it becomes unpinned) and further glide occurs, until particle 2 is encountered. There, climb processes occur which require in this case vacancy emission – hence the use of the symbol 'e'. One might reasonably expect an equal number of 'e' and 'a' type of climb processes, as suggested in [41]. Moreover,

due to the geometry of the situation, vacancy emission is expected in the horizontal channels and vacancy absorption on the vertical ones, with a concomitant net flux of vacancies set up which flows from the horizontal to vertical channels. Thus on the microscale, atoms migrate from the vertical channels to the horizontal, providing the mass flow needed for the rafting effect. No sense of the lattice misfit (negative or positive) needs to be invoked.

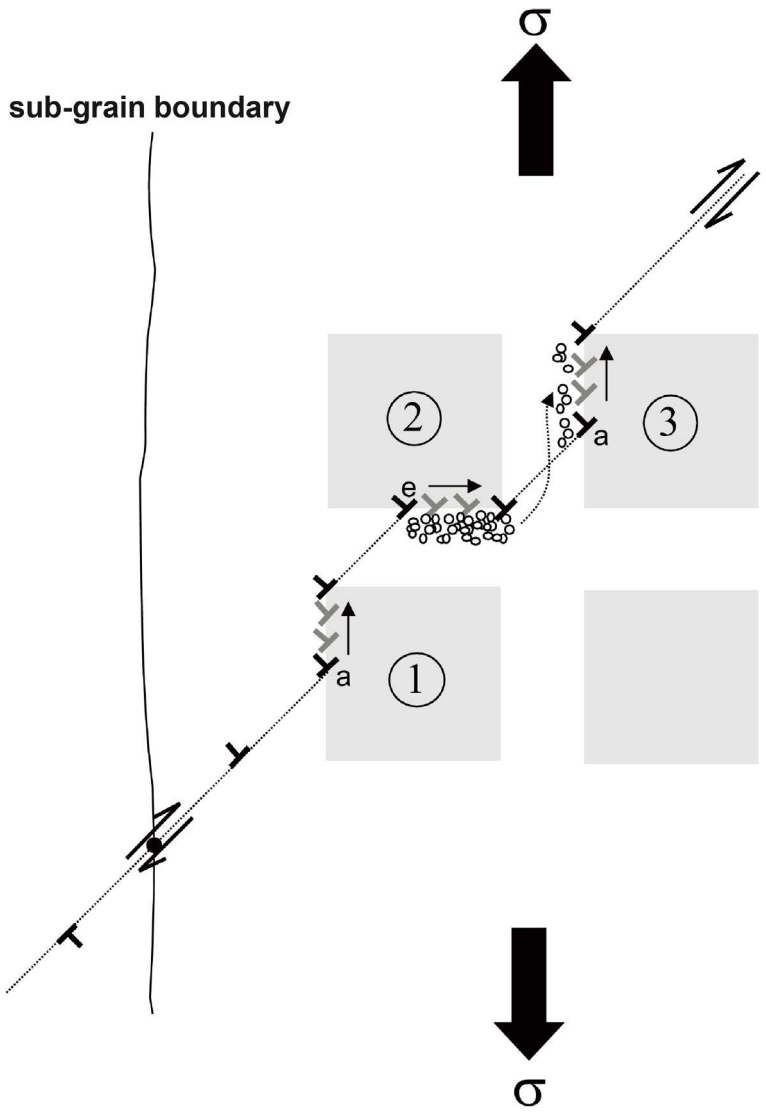

Figure 3.1: Basic geometry of climb/glide events in a nickel-based single crystal superalloy.

The work reported in this chapter builds upon the tradition of continuum damage

mechanics (CDM) modelling of Dyson & McLean [49] which in turn can be traced to the seminal contributions of Kachanov [45], Rabotnov [46], Leckie & Hayhurst [47] and later Williams & Cane [48]. In this spirit, Ashby & Dyson [50] reviewed the microstructural features that affect creep strain evolution and rupture life in different engineering alloys, the principal categories of damage being identified as (i) intrinsic softening of material due to multiplication of dislocations and particle coarsening; (ii) intrinsic softening due to particle cavitation and crack initiation at grain boundaries, and (iii) change of applied stress due to reduction of cross-section under constant load. Ion et al [51] built a first software package which modelled these specific contributions of damage and applied it to demonstrate that creep strain evolution in a wide variety of engineering alloys could be modelled, including directionally solidified superalloys such as IN738LC. At about this time, Pollock & Argon [32] demonstrated unambiguously *via* transmission electron microscopy that the intrinsic softening due to dislocation multiplication – from a very low initial dislocation density – is the principle form of damage in single crystal superalloys in creep; thus the creep strain rate increases monotonically with time over most combinations of stress and temperature to yield creep curves which are tertiary in form. Ghosh & McLean [52] and Pan et al [53] extended the CDM methods to account for the creep anisotropy (orientation dependence) prevalent in these materials. To account for the effects of varying microstructure, kinetic creep equation sets of the type first proposed by Dyson & Osgerby [54] are needed. Basoalto, Dyson & McLean [42] were the first to attempt a true microstructure-explicit modelling of the single crystal superalloys, with the effects of precipitate size and thus microstructural scale being accounted for. A refinement of this model has been presented more recently by Dyson [41]. However as yet no model has been developed which accounts for the effect of alloy chemistry on creep deformation behaviour; it is this which is most pertinent to modelling for alloy design purposes, for which there is considerable current interest.

3.4 The Model

The total content of dislocation segments will consist of (i) those gliding actively through the γ channels, and (ii) those trapped at the γ/γ' interfaces which move non-conservatively to overcome the precipitates. A postulate can then made, on which the proposed model relies. At any instant, it is assumed that the majority of the dislocations are trapped; it is their rate of release – and the necessary climb processes implied – which is the origin of the differing macroscopic creep rates of the various grades of single crystal superalloy. On the other hand, it is the active glide of the recently released dislocations – before the next trapping event – which contributes most to the creep strain accumulation. Thus the mean free path through which the dislocation can travel becomes vital; this depends upon the scale of the microstructure but is independent of the alloy chemistry, once the latter's influence on the microstructural architecture is accounted for. The situation is further illustrated in Figure 3.2, where the configuration denoted 'A' represents the instant at which the dislocation encounters the particle and becomes held up. In general, a non-zero climb force will be available due to the externally-applied stress field. Thus a non-equilibrium vacancy concentration near the vicinity of the dislocation is set up which induces a chemical potential difference causing migration of vacancies. The absorption/emission of vacancies from dislocations results in the formation of jogs which propagate along the dislocation lines leading to climb of the dislocation along the surface of the particle, configuration 'B'. Eventually, the dislocation approaches a configuration such that thermal activation of a single jog is enough to release it from its trapped configuration. This is situation 'C' in Figure 3.2 and corresponds to the critical escape event. Clearly, any accurate model will require an estimate of the frequency of these escape events.

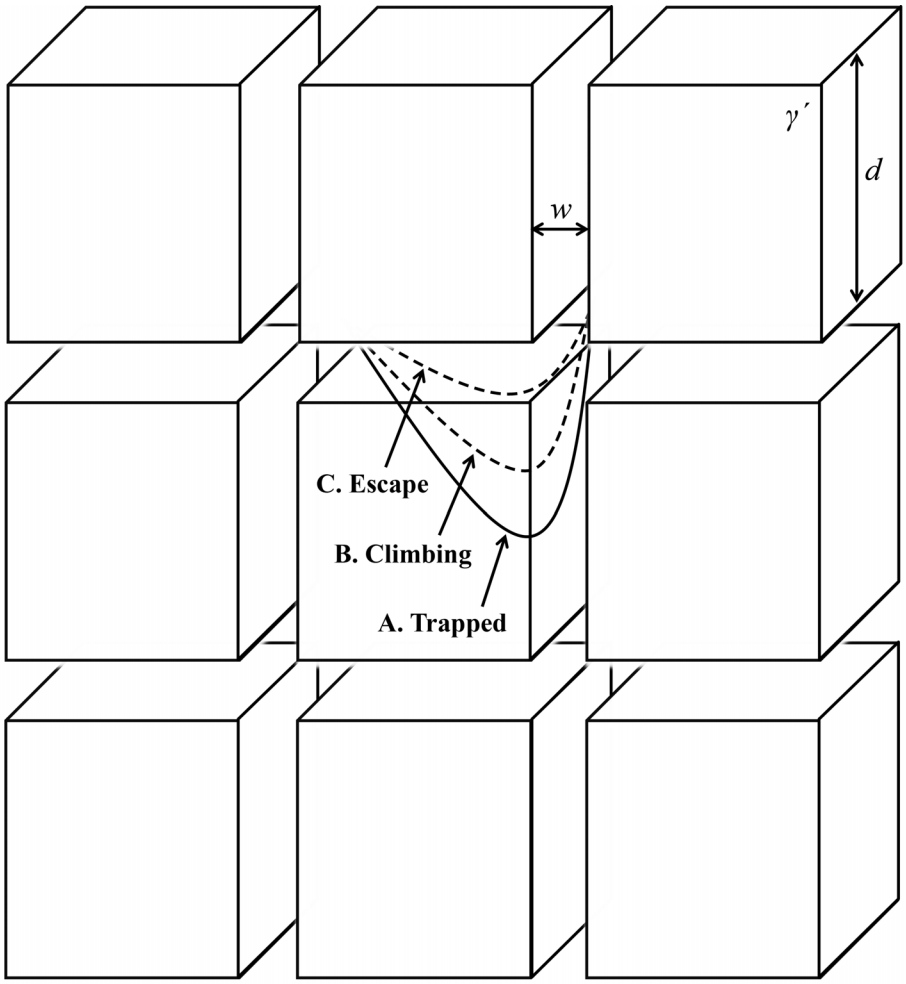

Figure 3.2: Dislocation configurations during dislocation creep in a nickel-based single crystal superalloy.

3.4.1 Estimation of Shear Strain Rate

One focuses attention on the microscopic creep shear strain rate $\dot{\gamma}$. This can be related to the mobile gliding dislocation density ρ_{g} *via* the Orowan equation $\dot{\gamma} = b\rho_{\mathrm{g}}v_{\mathrm{g}}$ where b is the Burgers vector and v_{g} the average glide velocity. For precipitate-strengthened alloys of the type considered here, only the matrix will be sheared whilst the particles deform merely elastically. A simple correction is thus introduced to acknowledge that deformation is limited to the matrix channels, so that

$$\dot{\gamma} = (1 - \phi_{\mathrm{p}})b\rho_{\mathrm{g}}v_{\mathrm{g}} \tag{3.2}$$

The total mobile dislocation density ρ_{m} is partitioned into that climbing at the interfaces ρ_{c} – thus held up by the γ' particles – and that gliding within the γ channels ρ_{g}. Thus

$$\rho_{\mathrm{m}} = \rho_{\mathrm{g}} + \rho_{\mathrm{c}} \tag{3.3}$$

so that the net rate of change of gliding dislocations is the sum of the rates of release and arrest of gliding dislocations. The release rate can be related to the fraction of the total trapped dislocations in Configuration 'C', which are released at a frequency Γ_{e}, to be determined. The probability that a dislocation in this position will escape is dependent on the probability that the dislocation will encounter a particle. This is approximately equal to ϕ_{p}, and a geometrical factor taken to be $b/(d/2)$, which accounts for the dislocation being in the correct configuration for this to happen. Similarly, the rate at which a gliding dislocation becomes trapped depends on the time for the dislocation to move from one particle and then to be trapped again by the next particle. The rate is approximated by the glide velocity v_{g} divided by the inter-particle spacing w. From these considerations the net rate of gliding

dislocations is given by

$$\dot{\rho}_{\mathrm{g}} = \rho_{\mathrm{c}}\phi_{\mathrm{p}}\frac{2b}{d}\Gamma_{\mathrm{e}} - \rho_{\mathrm{g}}\frac{v_{\mathrm{g}}}{w} \tag{3.4}$$

Substituting for ρ_{c} from Equation 3.3 and factorising for the gliding dislocation density ρ_{g}, one arrives at

$$\dot{\rho}_{\mathrm{g}} + \rho_{\mathrm{g}}\left(\phi_{\mathrm{p}}\frac{2b}{d}\Gamma_{\mathrm{e}} + \frac{v_{\mathrm{g}}}{w}\right) = \rho_{\mathrm{m}}\phi_{\mathrm{p}}\frac{2b}{d}\Gamma_{\mathrm{e}} \tag{3.5}$$

In the present model one can assume that $t_{\mathrm{c}} \gg t_{\mathrm{g}}$, where t_{g} is the time for a dislocation to glide from on particle to the next, and t_{c} is the time for a trapped dislocation to escape ($\Gamma_{\mathrm{e}} = 1/t_{\mathrm{c}}$). Recalling that the glide velocity is given by $v_{\mathrm{g}} = w/t_{\mathrm{g}}$, it follows that $v_{\mathrm{g}}/w \gg \Gamma_{\mathrm{e}}$. Thus Equation 3.5 becomes

$$\dot{\rho}_{\mathrm{g}} + \rho_{\mathrm{g}}\frac{v_{\mathrm{g}}}{w} = \rho_{\mathrm{m}}\phi_{\mathrm{p}}\frac{2b}{d}\Gamma_{\mathrm{e}} \tag{3.6}$$

Integrating of Equation 3.6 and application of the lower limit $\rho_{\mathrm{g}} = 0$ at $t = 0$, one has

$$\rho_{\mathrm{g}} = \rho_{\mathrm{m}}\phi_{\mathrm{p}}\frac{2b}{d}\Gamma_{\mathrm{e}}\frac{w}{v_{\mathrm{g}}}\left[1 - \exp\left\{-\frac{v_{\mathrm{g}}}{w}t\right\}\right] \tag{3.7}$$

Since one seeks an expression for the creep rate over a duration which is long compared to the escape time, one can assume $\left[1 - \exp\left\{-\frac{v_{\mathrm{g}}}{w}t\right\}\right] \approx 1$. Thus

$$\rho_{\mathrm{g}}v_{\mathrm{g}} = \rho_{\mathrm{m}}\phi_{\mathrm{p}}b\frac{2w}{d}\Gamma_{\mathrm{e}} \tag{3.8}$$

Recalling Equation 3.2 and substituting for w from Equation 3.1, the shear strain rate is then

$$\dot{\gamma} = 2\rho_{\mathrm{m}}b^2\phi_{\mathrm{p}}\left(1 - \phi_{\mathrm{p}}\right)\left(1/\phi_{\mathrm{p}}^{1/3} - 1\right)\Gamma_{\mathrm{e}} \tag{3.9}$$

As expected, much depends on the escape frequency Γ_e. From [80], the frequency Γ_e at which a jogged dislocation segment is expected to escape by a vacancy emitting process is given by

$$\Gamma_e = n\nu \exp\left\{-\frac{\Delta E - \Delta W}{kT}\right\} \tag{3.10}$$

where n is the density of locations which can either emit or absorb vacancies and ν is the Debye frequency. The term ΔE is the activation energy for the process and ΔW the work done by the dislocation moving from the pinned configuration to the released (gliding) state. During the release process the escape of climbing dislocation will allow localised glide in the matrix. The slipped area is bw here with the shear stress τ acting on the dislocation line, so that

$$\Delta W = \tau b^2 w \tag{3.11}$$

Combining Equation 3.10 and 3.11, the escape frequency can be written as

$$\Gamma_e = n\nu \exp\left\{-\frac{\Delta E}{kT}\right\} \exp\left\{\frac{\tau b^2 w}{kT}\right\} \tag{3.12}$$

Since the necessary mass transport will be effected by vacancy flow [80], the effective diffusivity for the necessary climb has the form

$$D_{\text{eff}} = n\nu b^2 \exp\left\{-\frac{\Delta E}{kT}\right\} \tag{3.13}$$

Therefore, combining Equation 3.12 and 3.13, the escape frequency of a vacancy emitting jogged segment on the horizontal channel (see Figure 3.1) is

$$\Gamma_{e,e} = \frac{D_{\text{eff}}}{b^2} \exp\left\{\frac{\tau b^2 w}{kT}\right\} \tag{3.14}$$

where the second subscript 'e' refers to the vacancy *emission* occurring. Similarly, for a vacancy absorbing jogged segment on the vertical channel, the escape frequency is given by

$$\Gamma_{\mathrm{e,a}} = \frac{D_{\mathrm{eff}}}{b^2} \exp\left\{-\frac{\tau b^2 w}{kT}\right\} \tag{3.15}$$

The number of vacancy emitting and absorbing jogs is expected to be approximately equal so that the overall escape frequency is given by the mean of Equations 3.14 and 3.15. Thus

$$\Gamma_{\mathrm{e}} = \frac{D_{\mathrm{eff}}}{b^2} \sinh\left\{\frac{\tau b^2 w}{kT}\right\} \tag{3.16}$$

The expression for the shear strain rate on the active slip system is arrived at by combining Equations 3.9 and 3.16 to give

$$\dot{\gamma} = 2\rho_{\mathrm{m}}\phi_{\mathrm{p}} D_{\mathrm{eff}} \left(1-\phi_{\mathrm{p}}\right)\left(1/\phi_{\mathrm{p}}^{1/3} - 1\right) \sinh\left\{\frac{\tau b^2 w}{kT}\right\} \tag{3.17}$$

Notice that the microstructural parameters ϕ_{p}, w and the implied d appear in Equation 3.17 in a way which make their contribution to $\dot{\gamma}$ unclear at first sight. Further analysis is needed; this is presented in Section 3.5.2.

3.4.2 Constitutive Equations for Relating Microscopic and Macroscopic Behaviour

For practical applications one is interested in uniaxial deformation along the $\langle 001 \rangle$ axis, and thus the contribution of the shear strain rate $\dot{\gamma}$ of Equation 3.17 to the macroscopic creep strain rate $\dot{\epsilon}_{\langle 001 \rangle}$. This can be estimated from the contributions from the active $a/2\,\langle 1\bar{1}0 \rangle\,\{111\}$ slip systems. For the symmetrical loading considered here, there are eight octahedral slip system with non-zero resolved shear stress and

equal Schmid factors [52]. Thus one has

$$\dot{\epsilon}_{\langle 001\rangle} = \frac{8}{\sqrt{6}}\dot{\gamma} \tag{3.18}$$

Consistent with the modelling approach reported in [42], one then has the coupled equation set

$$\dot{\epsilon}_{\langle 001\rangle} = \frac{16}{\sqrt{6}}\rho_{\mathrm{m}}\phi_{\mathrm{p}}D_{\mathrm{eff}}\left(1-\phi_{\mathrm{p}}\right)\left(1/\phi_{\mathrm{p}}^{1/3}-1\right)\sinh\left\{\frac{\sigma b^2 w}{\sqrt{6}K_{\mathrm{CF}}kT}\right\} \tag{3.19}$$

$$\dot{\rho}_{\mathrm{m}} = C\dot{\epsilon}_{\langle 001\rangle} \tag{3.20}$$

which can be integrated from time zero using standard finite difference methods. Note that in the case of Equation 3.20 one needs an estimate of the dislocation multiplication parameter C and the initial dislocation density $\rho_{\mathrm{m},0}$. The term $K_{\mathrm{CF}} = 1 + 2\phi_{\mathrm{p}}^{1/3}/3\sqrt{3\pi}(1-\phi_{\mathrm{p}}^{1/3})$ is a constraint factor [42], which accounts for the close proximity of the cuboidal particles in these alloys, as first identified in [81].

3.4.3 Estimation of Effective Diffusivity of Multicomponent Alloys

A net flux of vacancies from horizontal to vertical channels is required with an associated effective diffusivity D_{eff}; this needs to be estimated. For multicomponent alloys this is not a trivial task. The necessary expression is expected to have the Arrhenius form

$$D_{\mathrm{eff}} = D_0^{\mathrm{eff}}\exp\left\{-\frac{Q_{\mathrm{eff}}}{RT}\right\} \tag{3.21}$$

where D_0^{eff} and Q_{eff} are the pre-exponential coefficient and activation energy respectively, associated with this process. Here, the effective activation energy is calculated

by assuming that the effect of solute elements on the solvent alters Q_{eff} from that of pure nickel by an amount equal to the weighted average of contributions from the different solutes. Thus

$$Q_{\text{eff}} = Q_{\text{Ni}} + \sum_m x_m Q_{m,\text{Ni}} \tag{3.22}$$

where Q_{Ni} is the activation energy for self-diffusion of nickel and $Q_{m,\text{Ni}}$ is the activation energy for interdiffusion of solute m with nickel, and x_m is the atomic concentration of element m. Note that the approach taken is similar to that of the CALPHAD method which uses the Redlich-Kister polynomial with no cross-terms to determine the activation energy relevant to a multi-component system [82]. In the absence of proof to the contrary, no interaction coefficients (cross-terms) are included for now.

For calculation of the effective pre-exponential factor, absolute reaction rate theory suggests two possible choices: either an arithmetic or a harmonic mean, $D_{0,\text{A}}$ or $D_{0,\text{H}}$, respectively. These are defined according to

$$D_{0,\text{A}}^{\text{eff}} = \sum_m x_m D_0^{m,\text{Ni}} \tag{3.23}$$

and

$$D_{0,\text{H}}^{\text{eff}} = \frac{1}{\sum_m \frac{x_m}{D_0^{m,\text{Ni}}}} \tag{3.24}$$

In both cases, $D_0^{m,\text{Ni}}$ is the pre-exponential factor of solute m in nickel. Whether Equation 3.23 or 3.24 is the more appropriate for the present calculations is considered in the following Section 3.5.1.

3.5 Results and Discussion

In what follows, we consider first the appropriate form for the effective diffusivity controlling the climb processes at the particle/matrix interfaces. Then, preliminary calculations are carried out to test the behaviour of the equations developed, particularly Equation 3.17. Next, predictions are made for the creep deformation of the alloy CMSX-4, one of the most widely employed single crystal superalloys, for which a significant amount of creep data is available in the literature. Following that, the equations are used to test whether the composition dependence of the creep deformation behaviour is predicted accurately. Finally, some limitations of the modelling are identified, and modifications suggested.

3.5.1 On The Effective Diffusivity For Climb-Assisted Creep Deformation

Single crystal superalloys have undergone technological development, which has enabled new classes of alloy to emerge with improved resistance to creep deformation. Early first generation alloys had the grain boundary strengthening elements C and B removed. Second and third generation alloys are characterised by additions of Re at levels of 3wt% and 5-6wt% respectively. The latest fourth generation alloys contain significant amounts of Ru. Any model which aims to account for the dependence of creep deformation on alloy chemistry must account for the improved performance which these successive generations of alloy display. In this chapter, the alloys SRR99, CMSX-4, TMS-75 and PWA1497 are taken as representative alloys for the four successive generations. Their nominal compositions are given in Table 3.1.

For the calculations, the pre-exponential factors and activation energies for the solute elements have been taken from the considerable body of experimental work on diffusion couples by Karunaratne et al. [26, 77, 83, 84]. The data employed are

Table 3.1: Nominal chemical compositions (wt.%) of different generations of nickel-based single crystal superalloys.

Generation	Alloy	Cr	Co	Mo	Re	Ru	W	Al	Ti	Ta	Ni
First	SRR99	8	5	-	-	-	10	5.5	2.2	3	Bal
Second	CMSX-4	6.5	9	0.6	3	-	6	5.6	1	6.5	Bal
Third	TMS-75	3	12	2	5	-	6	6	-	6	Bal
Fourth	PW1497	2	16.5	2	5.95	3	6	5.55	-	8.25	Bal

listed in Table 3.2. Using Equations 3.21-3.24 the effective D_0^{eff} and Q_{eff} can be calculated for the four different generations of superalloys; the results are summarised in Table 3.3. A decrease in effective pre-exponential factor and an increase in effective activation energy are found, such that at any given temperature the effective diffusivities will decrease in going from the first to the fourth generation alloys. This is in at least qualitative agreement with observations; quantitative comparison and agreement remains to be demonstrated in Section 3.5.3.

Considering the two methods proposed for the determination of the effective pre-exponential factor, the value calculated using the arithmetic mean is five times larger than when the harmonic mean pre-exponential factor is employed; it is also very close to the value for elemental nickel at 1.9×10^{-4}. On the other hand, use of the harmonic mean leads to a value which is much more sensitive to the presence of a small fraction of critical elements such as Re, W or Ru, which have a strong influence on retarding diffusion-driven phenomena due their low diffusivities can be traced to the higher solute/vacancy exchange energies [26]. Therefore, the pre-exponential factor $D_{0,\text{H}}^{\text{eff}}$ calculated by the harmonic mean method is the more appropriate for the modelling employed in this work. It is used without exception in the calculations which follow, although it should be noted that the results of the calculations are not too sensitive to the method used to determine the pre-exponential factor.

Table 3.2: Pre-exponential factors and activation energies for solutal diffusion in nickel [26, 77, 83, 84].

Element	$D_0\,[\mathrm{m^2 s^{-1}}]$	$Q_{m,\mathrm{Ni}}\,[\mathrm{kJmol^{-1}}]$
Cr	3×10^{-6}	170.7
Co	7.5×10^{-5}	285.1
Mo	1.15×10^{-4}	281.3
Re	8.2×10^{-7}	255
Ru	2.48×10^{-4}	304.4
W	8.0×10^{-6}	264
Ni	1.9×10^{-4}	284

Table 3.3: Calculated effective pre-exponential factors and effective activation energies for different generations of superalloys.

Alloy	$D_{0,\mathrm{A}}^{\mathrm{eff}}\,[\mathrm{m^2 s^{-1}}]$	$D_{0,\mathrm{H}}^{\mathrm{eff}}\,[\mathrm{m^2 s^{-1}}]$	$Q_{\mathrm{eff}}\,[\mathrm{kJmol^{-1}}]$
SRR99	1.31×10^{-4}	2.59×10^{-5}	322.3
CMSX-4	1.29×10^{-4}	2.26×10^{-5}	332.1
TMS-75	1.32×10^{-4}	2.52×10^{-5}	339.1
PW1497	1.26×10^{-4}	2.40×10^{-5}	360.2

Table 3.4: Initial microstructural model parameters and physical constant used for CMSX-4.

Initial dislocation density $\rho_{\mathrm{m},0}$	$10^{10}\mathrm{m}^{-2}$
Dislocation multiplication parameter C	$100\mathrm{m}^{-2}$
Burgers vector b	$2.54 \times 10^{-10}\mathrm{m}$
γ' particle size d	400nm
Volume fraction of γ' phase ϕ_{p}	0.68

3.5.2 On The Creep Deformation Behaviour of the CMSX-4 Superalloy

To illustrate the capability of our model, the predicted strain-time evolution for the single crystal superalloy CMSX-4 is compared with the experimental data published in [28, 85]. For illustrative purposes, calculations are first carried out at a temperature of 900°C for various applied uniaxial stresses. The parameters needed for the model are summarised in Table 3.4. There are four of these; two define the microstructural architecture of the problem: the fraction of the precipitate phase ϕ_{p} and its size d. The remaining two are the initial dislocation density $\rho_{\mathrm{m},0}$ and its rate of multiplication C. The C of Equation 3.20 – the rate of multiplication of $\rho_{\mathrm{m},0}$ with accumulated strain – relates to its dynamics. Estimates of the last two parameters have been taken from [42]. The sensitivity of the predictions to variations in the four parameters are considered later in this section.

Before examining the predictions, consider first the implications of the expression for the creep strain rate given Equation 3.19 and in particular the predicted variation with the precipitate fraction ϕ_{p} and microstructure scale implied by differing ratios of w/d. Figure 3.3 illustrates how the initial creep strain rate varies as a function of ϕ_{p} in this case for a temperature of 900°C and various values of w – note that this then implies different values of d. The applied normal stress σ is taken to be 400 MPa; other initial parameters are given in Table 3.4. It is found that $\dot{\epsilon}$ tends asymptotically to $+\infty$ and 0 as the particle fraction varies from zero to unity

respectively, with a very sensitivity to the channel width w. For the technologically important range in which ϕ_{p} varies from 0.50 to 0.75, the initial creep strain rate is predicted to decrease by an order of magnitude or more as the channel width decreases by 10 nm. Therefore, a very strong dependence upon microstructural scale arises from the equations.

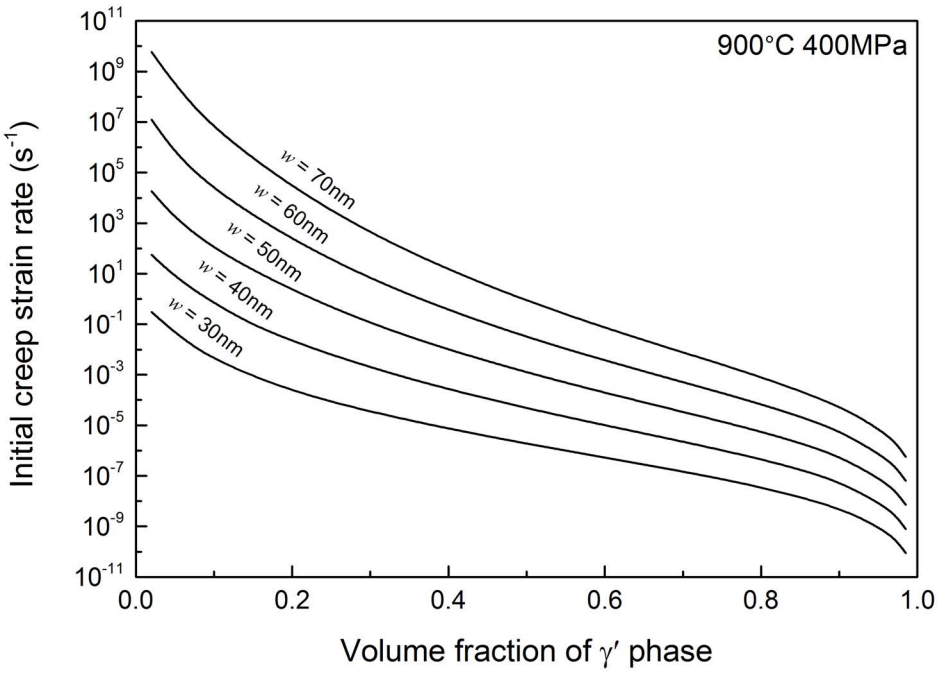

Figure 3.3: Variation of the dependence of creep strain rate on volume fraction of γ' and matrix channel width.

The predicted creep curves for CMSX-4 at 900°C are plotted in Figure 3.4. Also shown are experimental data taken from [28, 85]. One can see that there is a good agreement between the predicted creep curves and the experimental data for almost all the stress levels. The creep strain rate increases monotonically with creep strain, consistent with all known single crystal superalloys in the so-called tertiary regime [10]. A more stringent test involves examination of the predicted temperature dependence of the creep deformation behaviour. Predictions of 1% strain life and rupture life have also been carried out for CMSX-4 within the temperature range $850 - 1100$°C, see Figure 3.5(a) and 3.5(b). At each temperature the calculated 1%

strain life curves pass close to most of experimental data. Note that ϕ_p is actually a function of temperature, see Figure 3.6, and this temperature dependence has been included in the modelling by making use calculations using the the Thermocalc software. The predictions for the rupture life are close, which is encouraging when one acknowledges the very few parameters needed. At the very highest temperatures considered and particularly for the lowest applied stresses, the modelling does however underpredict the creep strength observed. We believe this to be due to the rafting effect; this is considered further in Section 3.5.4.

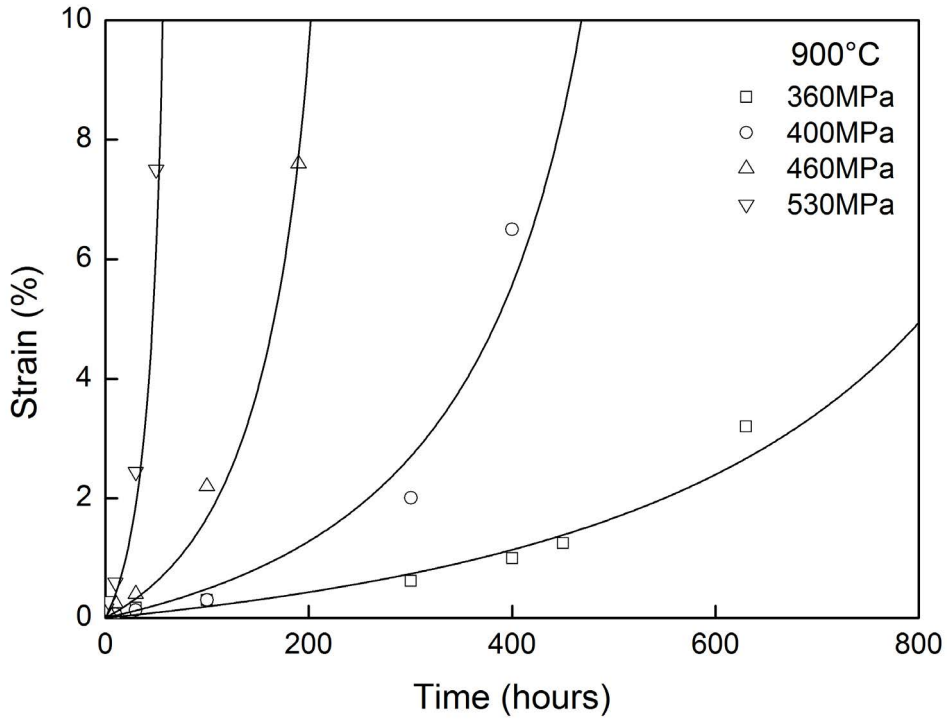

Figure 3.4: Comparisons of simulated creep curves with experimental data for CMSX-4 at 900°C.

It is of interest to determine the sensitivity of the calculations to changes in the values of the four parameters needed. Calculations are again carried out for CMSX-4, at 900°C and 400 MPa. Results from calculations with varying γ' volume fraction ϕ_p, γ' particle size d, initial dislocation density $\rho_{m,0}$ and dislocation multiplication parameter C are given in Figures 3.7(a)-3.7(d). In Figure 3.7(a), the fraction of γ'

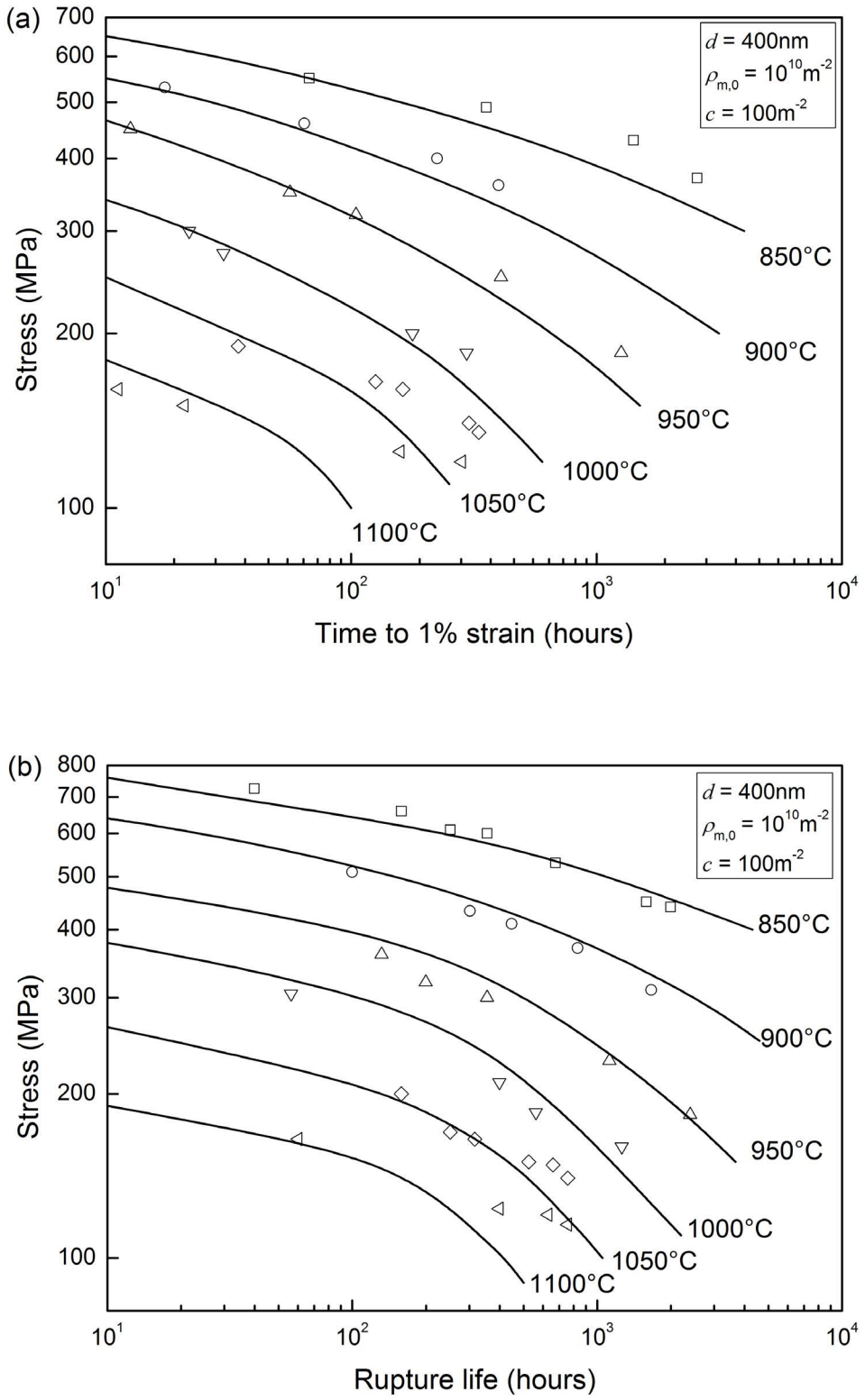

Figure 3.5: Comparisons of simulated creep 1% strain life and rupture life with experimental data for CMSX-4.

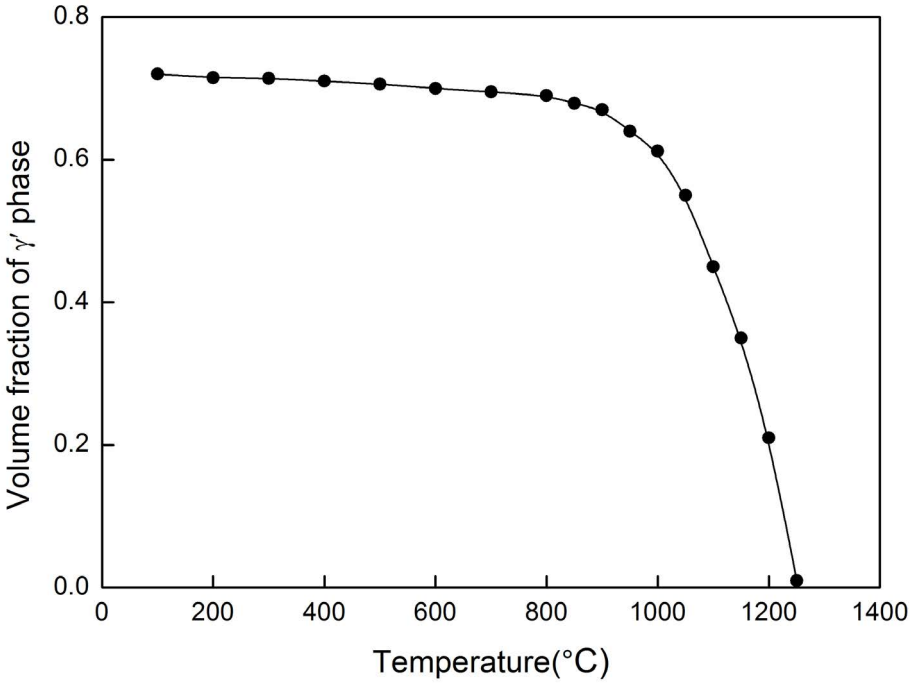

Figure 3.6: Temperature dependence of the γ' volume fraction for the CMSX-4 single crystal superalloy.

varies from 67% to 69% with constant γ' particle size, initial dislocation density and dislocation multiplication parameter C. The predicted creep performance is very sensitive to the volume fraction of the reinforcing phase, with a larger ϕ_{p} increasing the strength significantly. These predictions are in qualitative agreement with the data reported in Murakumo's work [9]. In Figure 3.7(b), a γ' particle size is varied from 440nm to 360nm; an improvement in creep rupture life by a factor of two is predicted with a decrease of 40nm in particle size. This can be explained on the basis that finer γ' particle sizes will result in smaller γ matrix channel widths and reduced creep strain rates, consistent with the data in Figure 3.3. In Figure 3.7(c), the initial dislocation density is varied by $\pm 5 \times 10^{9}\mathrm{m}^{-2}$; as expected, the creep performance is improved strongly when the initial dislocation density is reduced. The dislocation multiplication parameter C also affects the predicted life strongly, see Figure 3.7(d), with the rupture life being increased as C is reduced. The predictions made in this last part of this section are worthy of experimental testing to examine their validity;

the necessary experimental data are presently lacking.

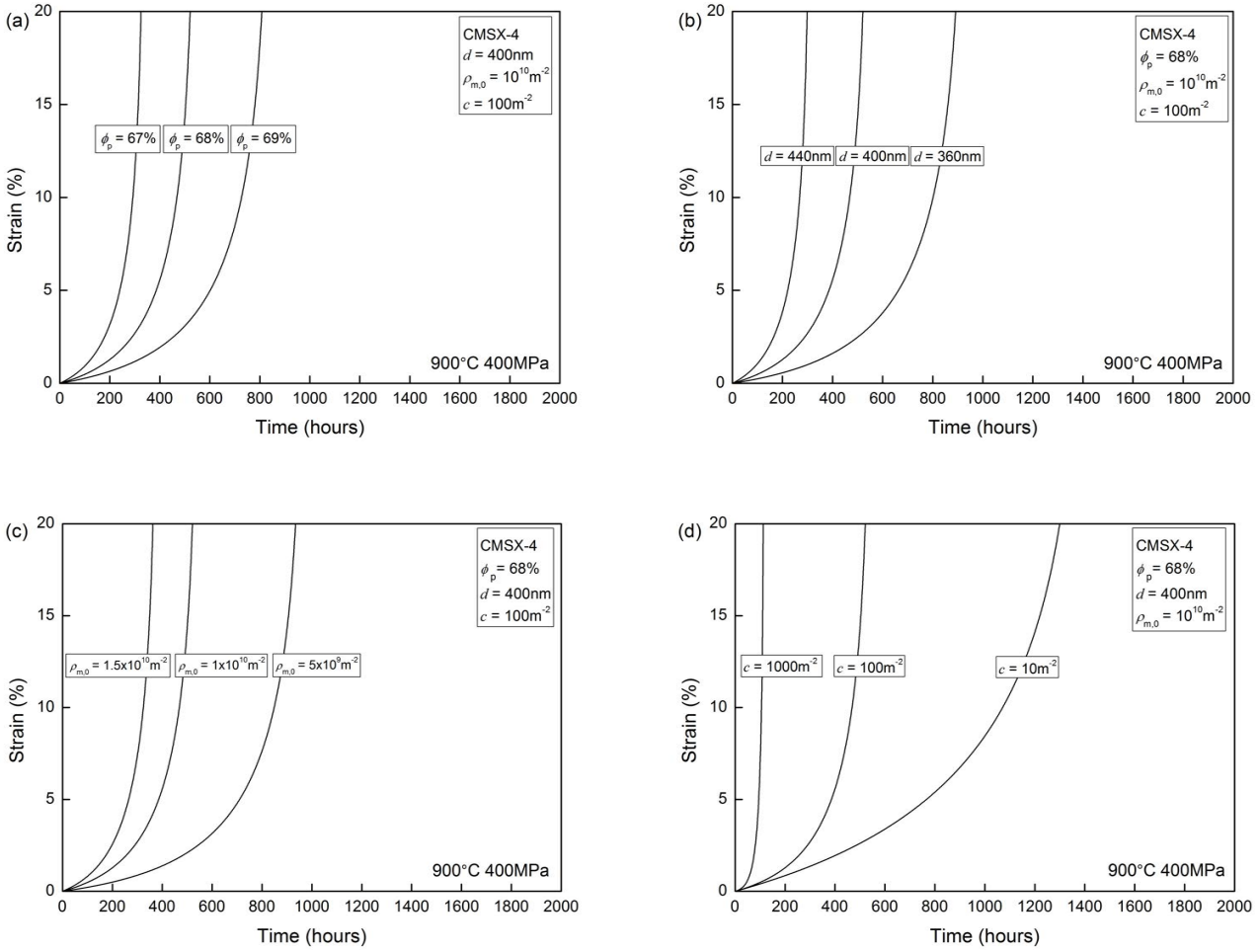

Figure 3.7: Simulated creep curves for CMSX4 at 900°C/400MPa with various assumed values of microstructural parameters: (a) volume fraction of γ', (b) γ' particle size, (c) initial dislocation densities, (d) dislocation multiplication parameter.

3.5.3 On The Dependence of Creep Deformation on Alloy Composition

We now proceed to illustrate that the dependence of creep deformation on chemical composition is rationalised by this model. For the purposes of component lifetime estimation, it is the Larson-Miller plots for life to 1% strain and stress rupture which are of the most significant practical importance. These are given in Figures 3.8(a)-3.8(d) for the four successive generations of single crystal superalloys identified in Section 4.1, for 1% strain and rupture respectively. The symbols represent the experimental data and the solid lines the results of the calculations. One can see that the improvement in creep deformation resistance is very well captured by the modelling. For the determination of the graphs in Figure 3.8, the concentration terms x_m of Equations 3.22 and 3.24 have been taken to be the mean compositions of the alloys concerned; this should be considered to be consistent with determining the effective diffusivities associated with mass transport at the γ/γ' interfaces. When one evaluates the concentration terms x_m consistent with compositions determined for the matrix phase after elemental partitioning is accounted for, the results are as given in Figures 3.8(c)-3.8(d) – a further strengthening of about 0.5 Larson-Miller parameters is found, with a somewhat too great a dependence on alloy composition displayed. This effect can be traced to the very strong partitioning of Re to the matrix phase, where it can retard climb kinetics. On balance, we believe that the mean alloy compositions are the most appropriate for the calculations, consistent with the mass transport needed at the interfaces. Then, for the important design point of 900°C/400MPa, see Figure 3.9, the approximate 10-fold improvement in time to 1% creep strain creep life displayed by the fourth generation compared to the first generation alloy is correctly recovered.

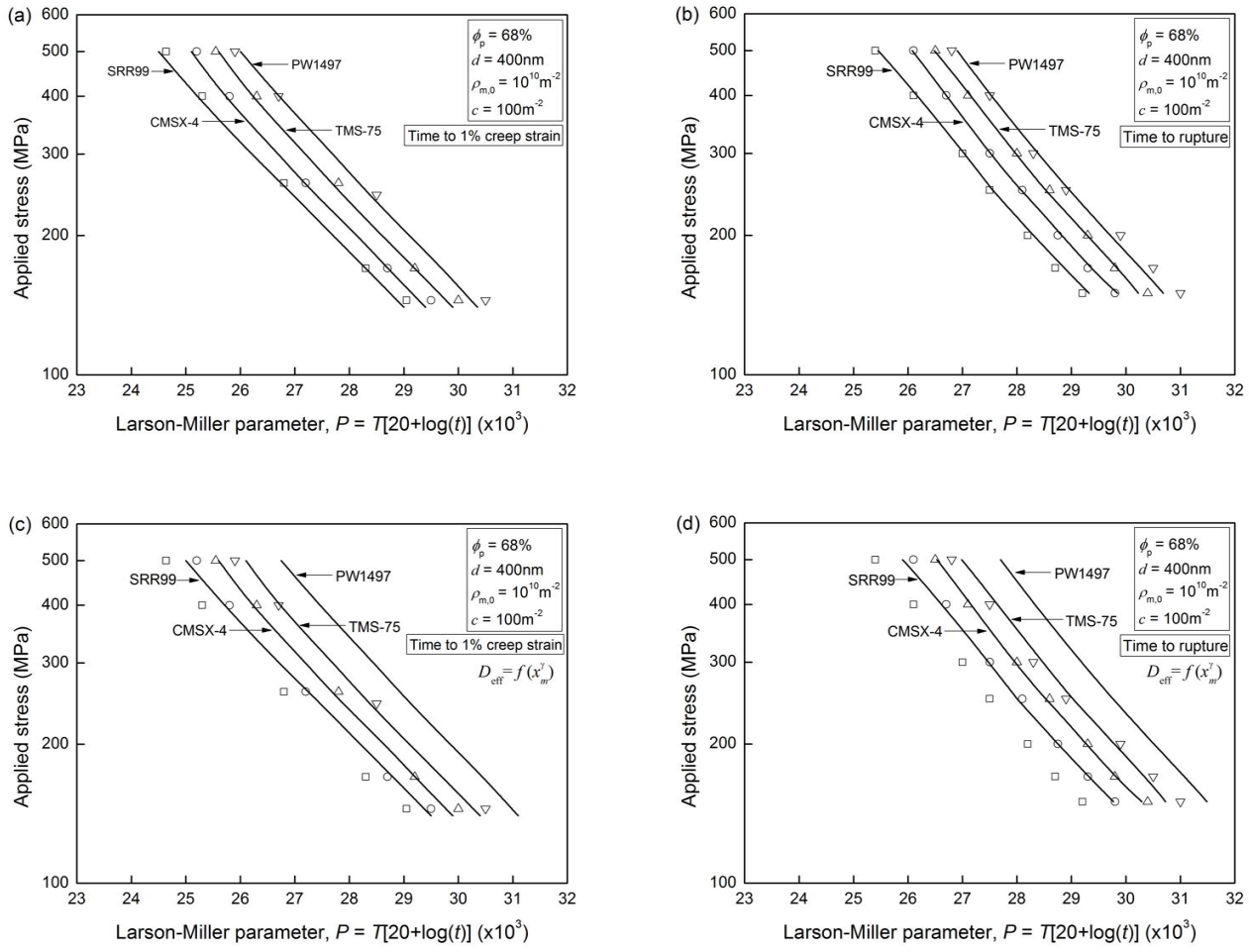

Figure 3.8: Comparisons of simulated Larson-Miller plots with experimental data. (a) and (b): Calculations by using mean concentrations; (c) and (d): Calculations by using concentrations in gamma phase. The data are derived from LM plots in [10].

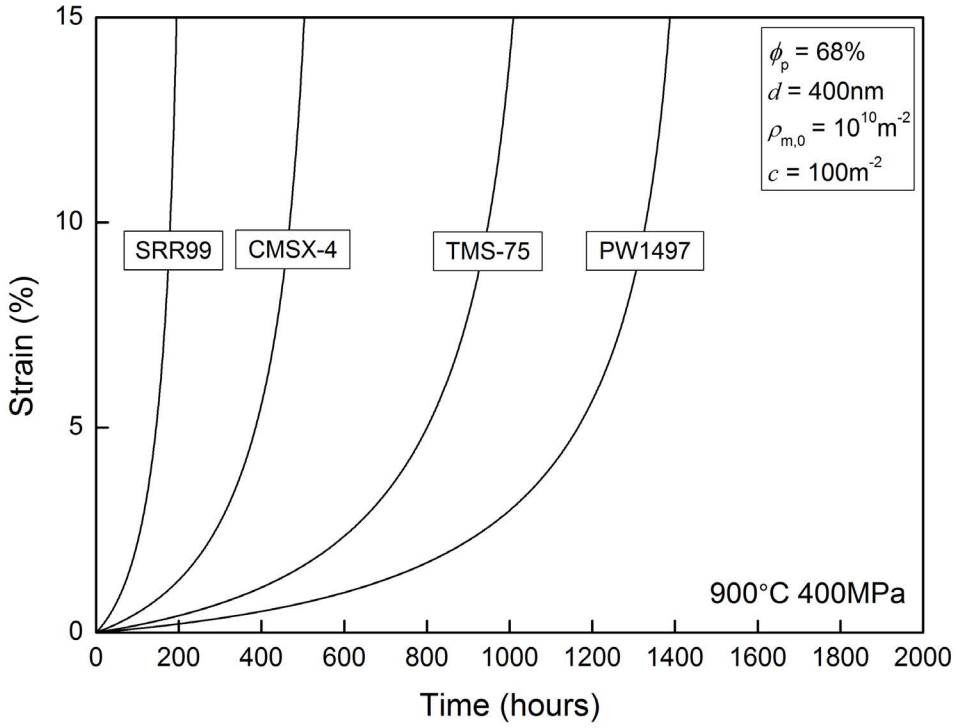

Figure 3.9: Simulated creep curves for different generations of single crystal nickel based superalloy at 900°C/400MPa.

A further point relates to the origin of the dependence of creep deformation on alloy composition. Can a first order effect be identified? For the alloy design approach reported in [74], many different superalloy compositions were ranked in order of their increasing creep resistance. For this purpose, a full integration of the underlying equations reported for each composition is unnecessary, for the following reason. A consideration of Equation 3.19 indicates that the microstructural architecture of the trial alloys are not appreciably different, e.g. ϕ_p is always approximately 70% and γ' particle size is 0.5 μm. Therefore, any significant differences in creep resistance arise from differences in the effective diffusivity D_{eff}. In particular, the time to 1% creep strain – a period over which the creep strain rate might be assumed to be constant – is predicted to be inversely proportional to D_{eff}, so that $t_{1\%} \propto 1/D_{\text{eff}}$. Figure 3.10 confirms that for test condition at 900°C/400MPa, $1/D_{\text{eff}}$ does indeed have a favourable linear relationship with the available exper-

imental data, from [86, 87]. This finding supports further the assumptions made in our model, and suggests that the origin of the composition dependence of creep deformation is rationalised by it.

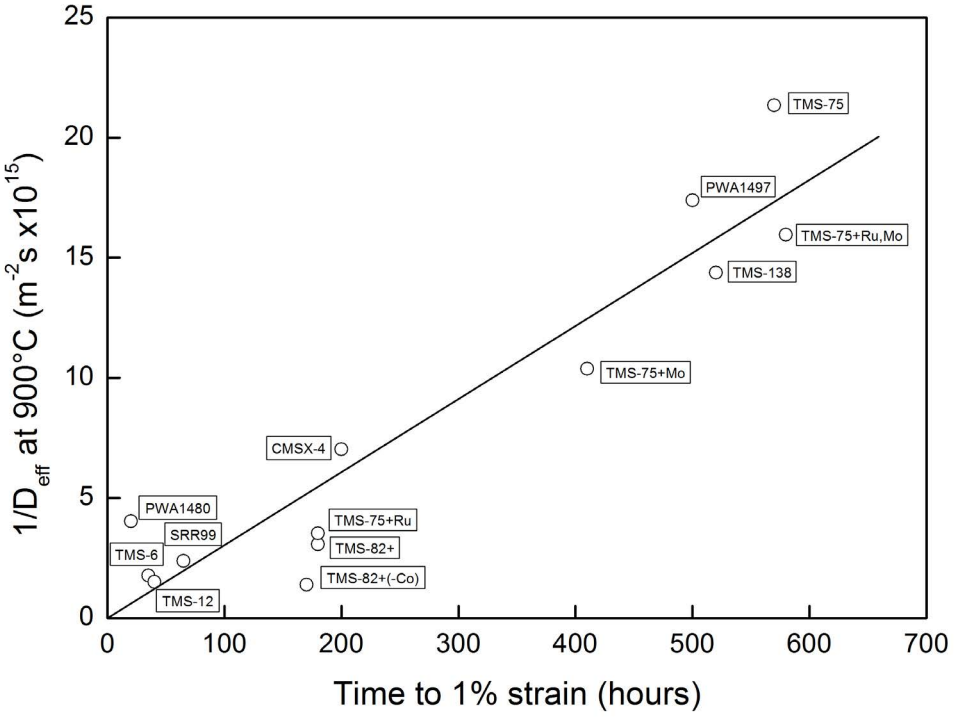

Figure 3.10: Comparison of predicted $1/D_{\text{eff}}$ with experimentally measured time to 1% strain for various nickel-based single crystal superalloys.

3.5.4 Adaptation To Account For Effect of Rafting

The underestimation of the creep resistance in the high temperature/low stress regime – as implied by the data in Figure 3.5 – can be rationalised by accounting for the so-called rafting effect. When rafting occurs, one invalidates the assumption that the γ' precipitate size and spacing remains invariant during deformation. Further complexity needs to be introduced into the modelling.

It is necessary first to consider the mechanism by which the rafting effect occurs, so that the correct physics is introduced. Traditionally, the mechanism of rafting has been controversial [88], however it is now accepted that the phenomenon is

not merely elastic in origin, but instead involves dislocation flow and differential microplasticity on the scale of the γ/γ' microstructure. The vacancy flow envisaged in the present model is consistent with this picture. Nevertheless, the exact details of the necessary diffusional flow remain unclear, as pointed out by Pollock [81]. A first, potentially plausible, situation requires simple flow of material from the vertical γ channels into the horizontal ones, see Figure 3.11; the γ' precipitates are forged together, with their centroids separating consistent with an increase in the horizontal channel width Δw_{h} such that

$$\Delta w_{\mathrm{h}} = w + \frac{w^2}{d} \tag{3.25}$$

so that a net unaxial strain ϵ_{h} is developed according to

$$\epsilon_{\mathrm{h}} = \frac{\Delta w_{\mathrm{h}}}{d + w} \tag{3.26}$$

For the CMSX-4 microstructure assumed earlier in this work, one has $d = 400$nm and $\phi_{\mathrm{p}} = 0.68$ so that $w = 54.9$nm. In this first situation, the mass flow associated with a fully rafted structure is then consistent with $\Delta w_{\mathrm{h}} = 62.4$nm and $\epsilon_{\mathrm{h}} = 10.4\%$. The latter value in particular is substantially greater than the few tenths of a percent which can be all that is necessary for rafting to be completed [85]. On this basis, a second situation is probably more realistic, see Figure 3.12, which invokes two counter-related fluxes: (i) flow of γ stabilising elements (Co, Cr and Re etc) from vertical to horizontal channels coupled with (ii) flow of γ' forming elements (Al, Ti, Ta) into the vertical channels [89]. Note that one cannot rule out the possibility of the necessary mass transport occurring close to, and perhaps within, the γ/γ' interfaces. In this second situation, the centroids of the γ' particles do not separate,

and instead one has

$$\Delta w_{\mathrm{h}} = \frac{\Delta w_{\mathrm{v}}}{1 + \Delta w_{\mathrm{v}}/d} \tag{3.27}$$

so that $\Delta w_{\mathrm{h}} = 48.3\mathrm{nm}$, a value very similar to that for the first scenario. However, in this second case, the precipitates contract in the direction of the applied stress, so that no net strain is accumulated. The stereological data supports the second mechanism, see [28]. Notice that is the geometry of the situation, rather than any sign of the lattice or modulus misfit, which causes rafts to lengthen in the transverse direction.

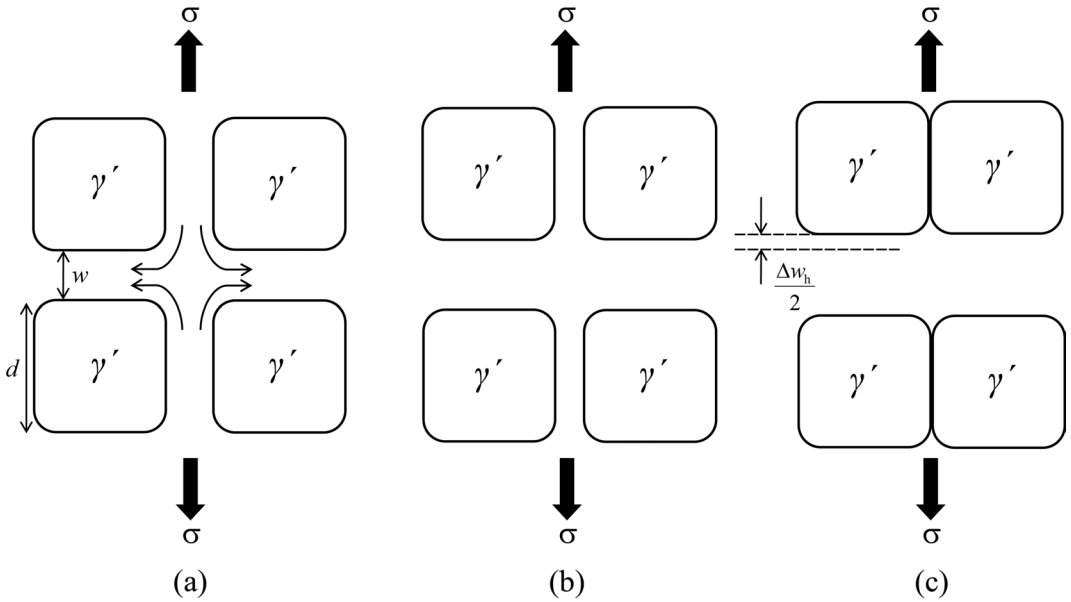

Figure 3.11: Schematic illustration of the changes in microstructural dimensions during rafting by a simple flow of matrix material from the vertical channels to the horizontal channels. From (a) to (c) the γ' precipitates are assumed to retain their cuboidal shape and will coalese along their vertical interfaces.

It follows from the above argument that the overarching influence of the rafting effect will be to cause a net decrease in the overall escape frequency Γ_e of Equation 3.16, which will diminish to a vanishingly small value as w – more specifically the vertical channel width w_{v} – as rafting continues to completion. The rate of thinning $\dot{w}_{\mathrm{v}}$ is expected to be proportional to the product ρv_{climb} on account of its

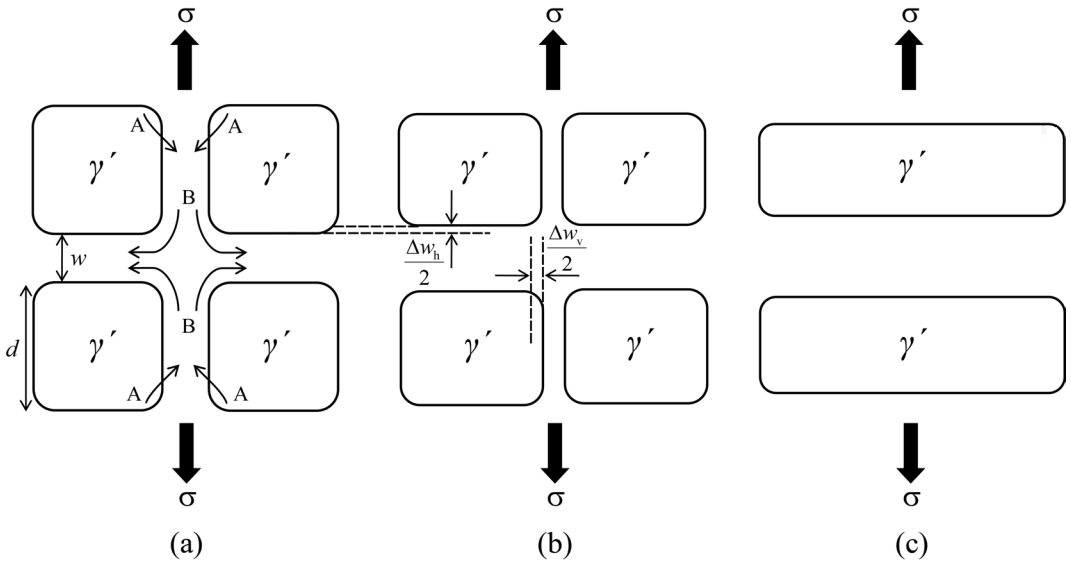

Figure 3.12: Schematic illustration of the changes in microstructural dimensions during rafting by a more complex preferential flow of γ and γ' forming elements within the matrix channels: (a) initial state; (b) microstructure in a rafted state, no coalescence of γ' particles; (c) fully rafted structure. 'A' indicates the flux of γ' forming elements; 'B' indicates the flux of γ stabilising elements.

anticipated dependence on the rate of vacancy absorption at the γ/γ' interfaces. It follows that

$$\dot{w}_{\mathrm{v}} = A\rho d^2 v_{\mathrm{climb}} = A\rho d^2 \frac{D_{\mathrm{eff}}}{b} \sinh\left\{\frac{\tau b^2 w_{\mathrm{v}}}{kT}\right\} \tag{3.28}$$

where A is a parameter which is dimensionless on account of the introduction of the term d^2. Examination of the data in the literature, specifically the data for CMSX-4 in [90], suggests $A = 2.36 \times 10^{-2}$, which gives the optimum fit to the experimental data (see Figure 3.13). The width of vertical channels w_{v} is then a state variable which needs to be updated as the simulation of creep deformation proceeds, according to

$$w_{\mathrm{v}} = w - \Delta w_{\mathrm{v}} \tag{3.29}$$

so that one employs in place of Equation 3.19

$$\dot{\epsilon} = \frac{16}{\sqrt{6}} \rho_{\mathrm{m}} \phi_{\mathrm{p}} D_{\mathrm{eff}} \left(1 - \phi_{\mathrm{p}}\right) \left(1/\phi_{\mathrm{p}}^{1/3} - 1\right) \sinh \left\{ \frac{\sigma b^2 w_{\mathrm{v}}}{\sqrt{6} K_{\mathrm{CF}} k T} \right\} \tag{3.30}$$

Figure 3.14 shows the predictions of time to 1% strain for the same conditions plotted in Figure 3.5(a), with rafting taken into account using Equations 3.27 to 3.30. The effect of rafting is accounted for in the dash curves, but not in the solid curves which remain as before. The influence of rafting is most prevalent at temperatures greater than 1000°C, and lower stress levels which enable sufficient time to rafting to proceed. At lower temperatures the original predictions of the model are sufficient. Our analysis indicates that rafting contributes to creep strengthening in single crystal superalloys in a potent way as the temperature is increased beyond 950°C.

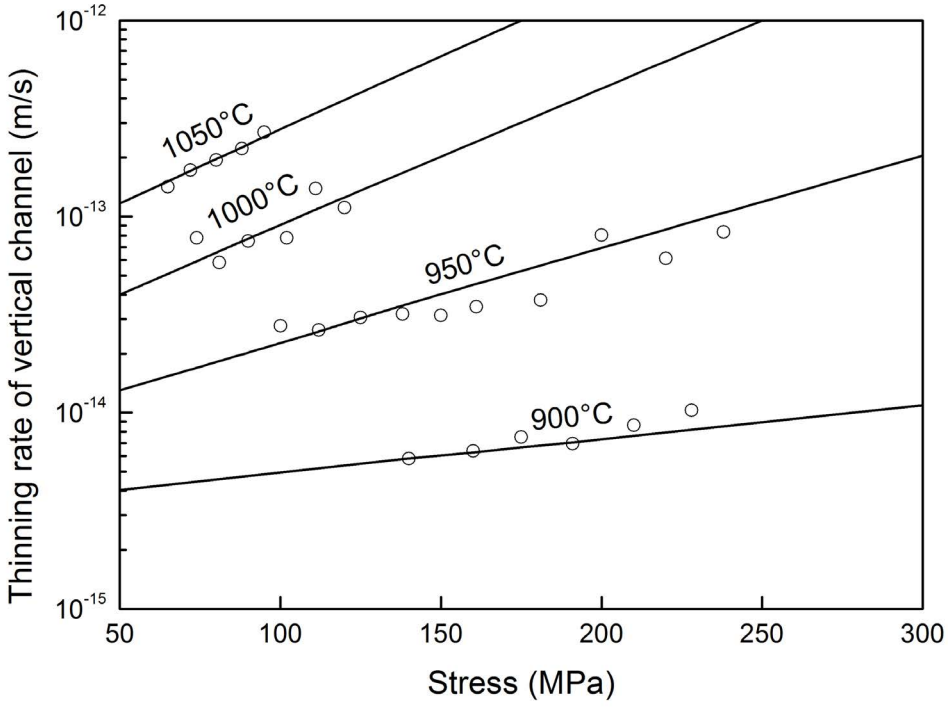

Figure 3.13: Comparisons of simulated thinning rate of γ matrix vertical channel with experimental data for CMSX-4.

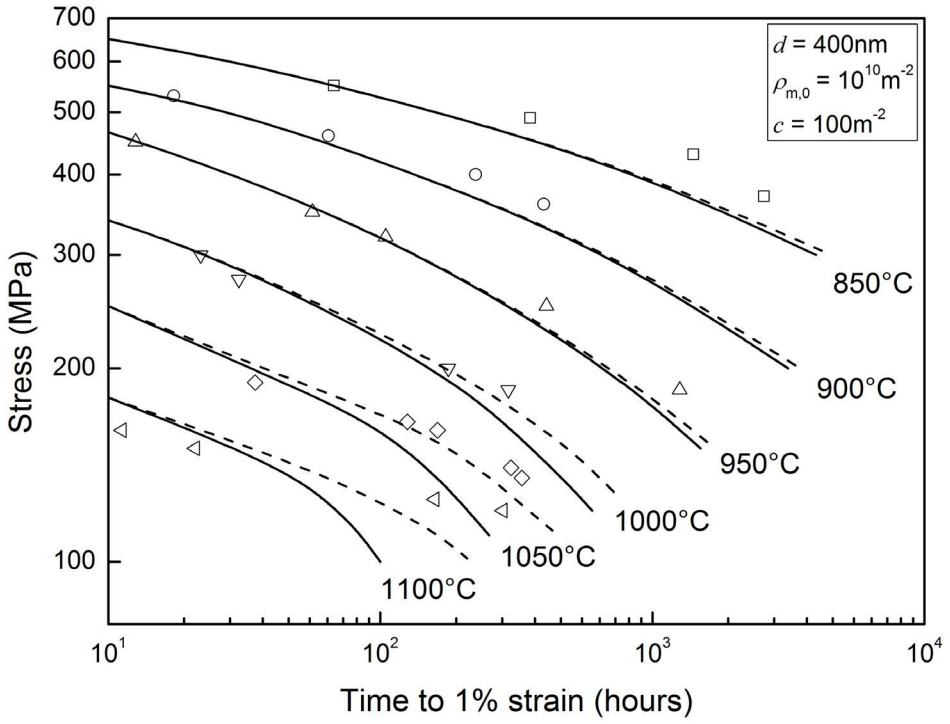

Figure 3.14: Comparisons of simulated time to 1% strain with experimental data for CMSX-4, dashed curves demonstrate the predictions with rafting.

3.6 Summary and Conclusions

The following conclusions can be drawn from this work:

1. A model for the creep deformation behaviour of nickel-based single crystal superalloys is proposed, which couples a physics-based constitutive description of time-dependent plastic flow to the alloy chemistry.

2. The strengthening γ' particles are assumed to be impenetrable. Dislocations are assumed to be either (i) free to glide in the γ matrix, or (ii) trapped at the γ/γ' interfaces. Trapped dislocations climb at a rate controlled by vacancy emission and absorption; it is the rate of unpinning which give rise to the dependence of creep deformation on alloy chemistry.

3. The model is physically-based with no empirical parameters needed. Sensitivity studies have been carried out to determine the relative effects of parameters – such as the γ' volume fraction – on the macroscopic strain rate.

4. The model has been used to rationalise in quantitative terms the relative creep strengths of different generations of single crystal superalloy. The important role of Re and W in imparting creep strength is rationalised, on the basis of their influence in retarding the diffusional flow of vacancies needed for climb to occur at the γ/γ' interfaces.

5. A simple extension of the model is proposed to account for strengthening due to the rafting effect, which relates the kinetics of γ channel thinning/thickening to the migration of vacancy absorption/emission fluxes at the γ/γ' interfaces.

6. The calculations are sensitive to the values assumed for the initial dislocation density and the rate at which this accumulates with increasing creep strain. Further experimental work is needed to define these values more precisely; this will be a valuable test of the veracity of the model.

Chapter 4

Isolation and Testing of New Single Crystal Superalloys Using Alloys-By-Design Method

4.1 Summary

Three new single crystal superalloys are isolated using theory-based computational modelling approaches, termed alloys-by-design methods. They are (i) an oxidation-resistant low Re-containing alloy with balanced properties, intended for general-purpose gas turbine applications; (ii) an alloy containing 5.6 wt.% Re and 2.6 wt.% Ru suitable for high performance jet engine applications, when creep resistance needs to be maximised without oxidation performance being excessively compromised and (iii) a cheap, corrosion-resistant alloy for power generation applications designed with ease-of-processing in mind. The new alloys have been manufactured using investment casting techniques, and their creep and oxidation behaviour evaluated. The robustness of the so-called alloys-by-design methods is demonstrated, although the predictions for microstructural stability need to be improved.

4.2 Introduction

Over the past half century, there is a long history showing that most of the nickel-based superalloys have been designed empirically [71, 72, 73]. Their chemical compositions have been isolated by carrying out many make/test iterations, involving small-scale processing of limited quantities of material and subsequent characterisation of their behaviour. The alloy composition adopted is then the one found to display the best, or desirable combination of properties. However, the work of developing a composition-dependent creep model in Chapter 3 has shed light on the potential to build theory-based computational methods for the design of new nickel based single crystal superalloys. For doing this, more quantitative composition-microstructure-property relationships regarding to oxidation resistance, cost, density and microstructural stability need to be discovered.

In this chapter, modelling procedures are proposed, termed alloys-by-design methods [74], for isolation of new single crystal nickel-based superalloys used in both jet propulsion and power generation turbine sections. For best predictive capability, any improved alloy design procedures should ideally be based on accurate, theory-based models. The methods of isolation of optimised alloy compositions – given wide possibilities of alloying elements – are also of considerable interest. And finally, because computer-based modelling methods are only of use if their application leads to new alloys which exhibit useful properties, experimental validation is important. The research reported in this chapter was carried out with these factors in mind.

4.3 Description of Alloy-By-Design Method for Single Crystal Superalloys

A modelling-based approach for the isolation of new grades of single crystal superalloys is now described in this section. Some necessary terminology is first introduced. It will also be argued that this class of material is particularly amenable to the computer-modelling approach proposed.

The single crystal nickel-based superalloys contain as many as ten different alloying elements, to confer the desired combination of properties [10]. Thus, Cr and Si are added to impart resistance to oxidation and Co for sulphidisation. For creep resistance, Mo, W, Re and sometimes Ru are introduced, since these retard the thermally-activated processes such as dislocation climb which determine the rate of creep deformation. To promote the precipitation hardening needed for static and cyclic strength, Al, Ta and Ti are introduced since these are needed for the precipitation of the γ' reinforcing phase. This is embedded within the face-centered cubic (FCC) matrix phase which is referred to as γ. Figure 4.1 illustrates the typical γ/γ' 'brick and mortar' microstructure displayed by these materials. It is found that the best mechanical properties are displayed when the γ' phase is the majority phase; experiments have demonstrated that for creep deformation the optimum γ' fraction is in the range 0.60 to 0.70, so that initial dislocation activity is confined to the thin matrix channels between precipitates [9]. Provided that the lattice parameters of the γ and γ' phases are not too dissimilar, the γ' phase is embedded coherently in the γ matrix with a cube-cube orientation relationship displayed [11]. The interfaces are parallel to the $\{100\}$ planes of matrix and precipitate. The size of the γ' precipitates is found to be not too sensitive to the alloy composition – being more dependent upon the cooling rate from the solutioning heat treatment temperature.

The large number of possible alloying elements and their considerable solubility

in nickel mean that the extent of the possible alloy design space – and thus the number of possible alloys which can be contemplated – is very considerable. Moreover, the contributions made by each element to the microstructure and properties are not independent of each other, so that alloying alters the balance of properties in a subtle way which is difficult – maybe impossible – to judge by rules-of-thumb. This situation has contributed to the present state-of-the-art in which existing alloy compositions have been chosen empirically, for example using statistical analysis of experimental data. Thus considerable use has been made of trial-and-error based testing, and ranking of alloy performance on the basis of measured rather than predicted behaviour. But this rich chemical complexity – together with the added simplification offered by the absence of grain boundaries the necessarity to strengthen them – make the single crystal superalloys amenable to numerical modelling. The target problem is made tractable by the fact that the optimum microstructural architecture, see Figure 4.1, is well understood with the chemical composition not seeming to influence its scale too strongly.

4.3.1 Description of Alloy Isolation Procedure

The algorithm used is illustrated schematically in Figure 4.2. It relies upon a series of procedural steps represented by the boxes linked by arrows. The important, overarching strategy is to estimate the composition-dependence of the mechanical behaviour and environment performance. In this sense it relies upon brute, computational-force. Required in practice – at minimum – are many tens of thousands of calculations. Consider the compositions of some common, existing single crystal superalloys, see Table 4.1. Commonly Cr, Co, Al, Ta, Ti, Mo, W and Re are present; sometimes Ru and Si also. Compositional specifications are usually made to an accuracy of 0.1 wt% for each element added; assuming that these need to be chosen between upper and lower limits which differ by perhaps 5 wt.%, then 50^8 or

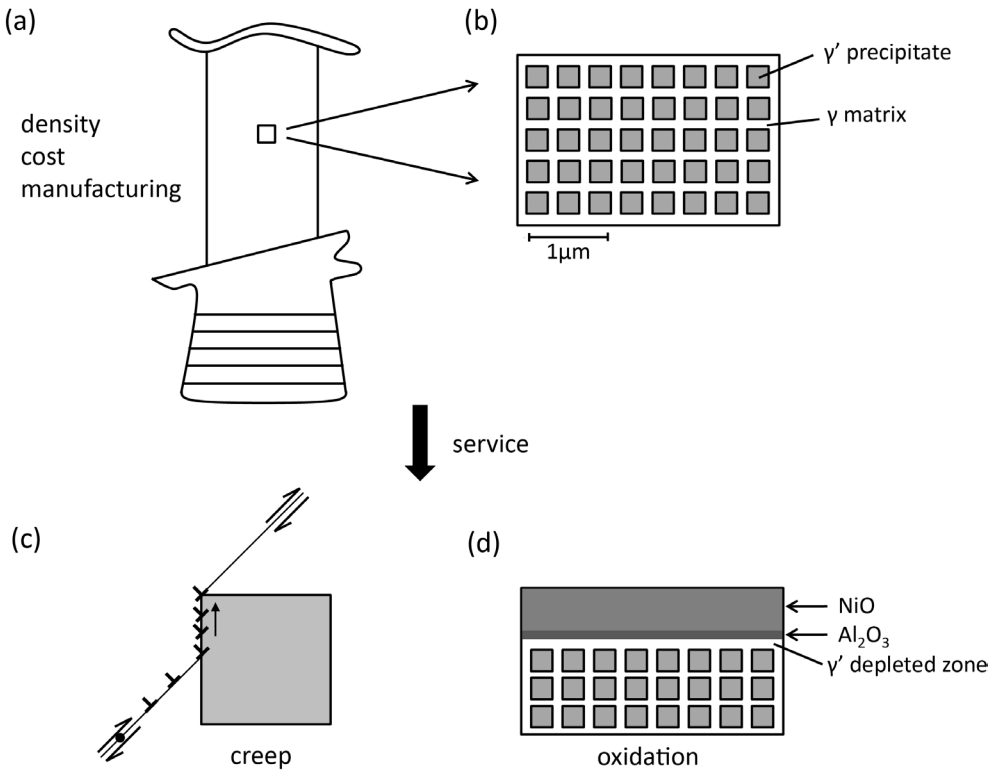

Figure 4.1: Illustrations of microstructure-property relationships in nickel-based single crystal superalloys..

4×10^{13} calculations are needed. This is a large number – significantly greater than the 3 billion bases of genetic information in human cells which have been sequenced by the Human Genome project for example – and in our experience, beyond the capacity of existing computational resources. Alternatively, if an accuracy of 1.0 wt% is accepted, then 5^8 or 4×10^5 calculations are needed. This becomes tractable.

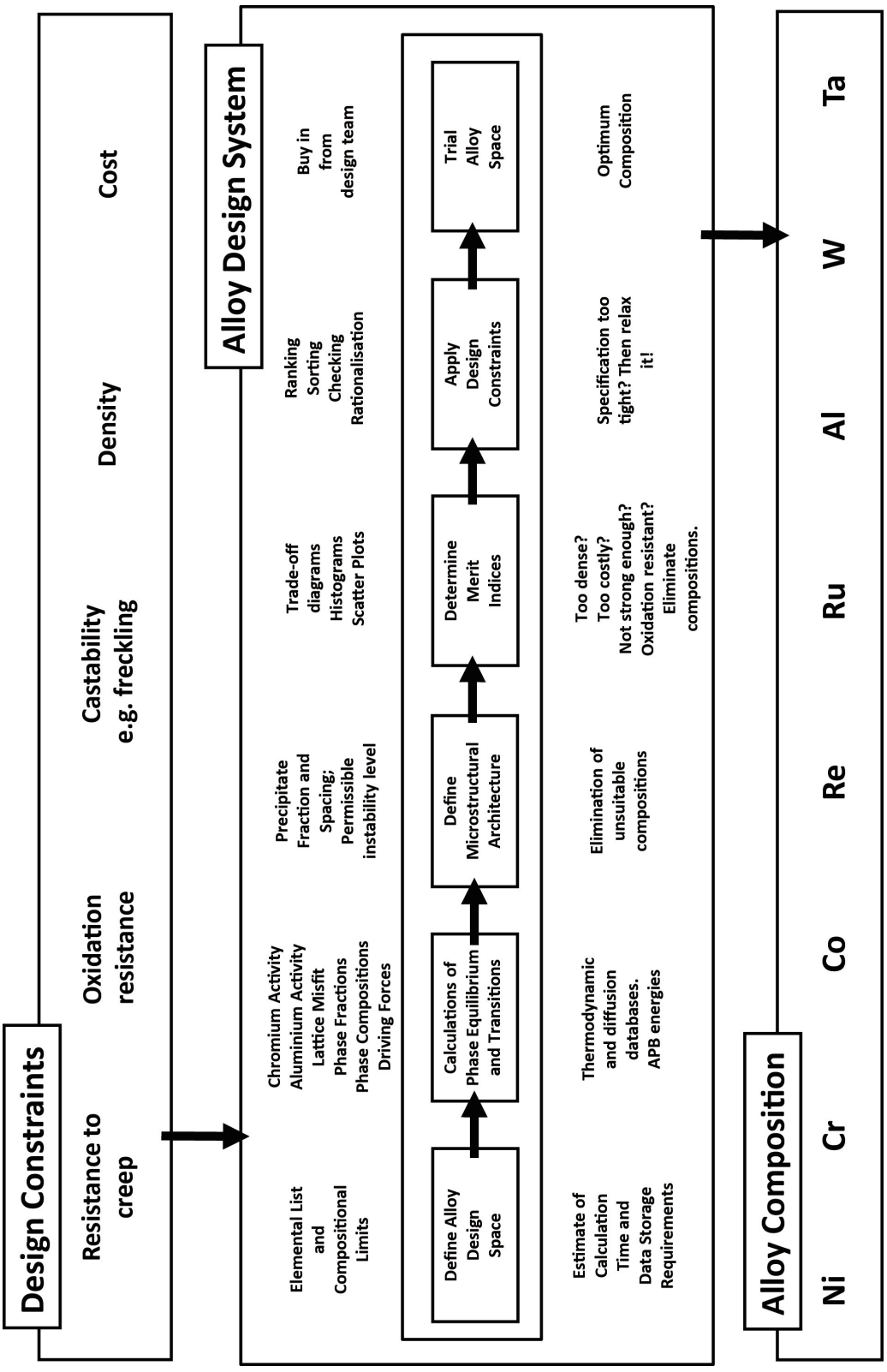

Figure 4.2: Typical procedures of an alloy design system.

Table 4.1: Nominal chemical compositions (wt.%) of some common superalloys.

Alloy	Cr	Co	Mo	Re	Ru	W	Al	Ti	Ta	Ni	Density(g/cm^3)
SRR99	8	5	-	-	-	10	5.5	2.2	3	Bal	8.56
CMSX-4	6.5	9	0.6	3	-	6	5.6	1	6.5	Bal	8.70
CMSX-10	2	3	0.4	6	-	5	5.7	0.2	8	Bal	9.05
TMS-75	3	12	2	5	-	6	6	-	6	Bal	8.89
TMS-138A	3.2	5.8	2.8	5.8	3.6	5.6	5.7	-	5.6	Bal	9.05
PWA1483	12.2	9.2	1.9	-	-	3.8	3.6	4.2	5	Bal	8.45
PWA1484	5	10	2	3	-	6	5.6	-	8.7	Bal	8.95

The first step therefore – see Figure 4.2 – is the definition of an elemental list and associated upper and lower compositional limits for each one. Estimates of storage time and data storage requirements are sensible at this point, to avoid excessive computational loads. The second step makes use of thermodynamic calculations made using the CALPHAD method, specifically using the Thermocalc software package and an associated database of thermodynamic parameters. For each trial composition, an estimate is made of the fraction and composition of the strengthening γ' phase at equilibrium, and the associated composition of the matrix phase. Other thermodynamic quantities such as chemical potentials – which are needed for estimation of the susceptibility to oxidation – are determined and stored at this point. It is also convenient to estimate kinetic parameters such as diffusional mobilities at this stage, which are needed for the creep calculation. Driving forces describing phase instability – for example to the topologically close-packed (TCP) phases – are also made here.

A third stage involves the definition of the microstructural architecture which is needed, and the elimination of trial compositions which do not conform to this estimate. For single crystal superalloys, the creep rupture life is maximised when the γ' fraction lies between 60%-70% [9], the performance being impaired at larger and smaller values; this estimate is made at a suitable service temperature, e.g. 900°C. The γ/γ' lattice misfit should also conform to a small value, either positive or

negative, since coherency is otherwise lost; thus limits are placed on its magnitude. The lattice misfit δ is defined as the mismatch between γ and γ' phases, and is determined according to

$$\delta = \frac{2\left(a_{\gamma'} - a_{\gamma}\right)}{a_{\gamma'} + a_{\gamma}} \tag{4.1}$$

where a_{γ} and $a_{\gamma'}$ are the lattice parameters of γ and γ' phases. They are given by equations

$$a_{\gamma} = 3.559257 + 0.0000198T + \sum_{i} \Gamma_i^{\gamma} x_i^{\gamma} \tag{4.2}$$

$$a_{\gamma'} = 3.552743 + 0.0000552T + \sum_{i} \Gamma_i^{\gamma'} x_i^{\gamma'} \tag{4.3}$$

where x_i^{γ} and $x_i^{\gamma'}$ represent the mole fractions of element i in γ and γ' phases and the temperature T is given in kelvin. The terms Γ_i^{γ} and $\Gamma_i^{\gamma'}$ are Vegard coefficients and their values are reported in [74]. Rejection on the basis of unsuitable microstructural architecture is also made on the basis of susceptibility to TCP susceptibility. In the first part of this work, use is made of the d-orbital energy levels of the alloying elements (referred as Md) to determine the total effective $\overline{\mathrm{Md}}$ level according to

$$\overline{\mathrm{Md}} = \sum_{i} x_i \mathrm{Md}_i \tag{4.4}$$

where the x_i represents the mole fraction of i in the alloy. Values of the Md_i parameters for each element are taken from [91]. Higher values of $\overline{\mathrm{Md}}$ are indicative of higher probability of TCP formation. In the later part of the chapter, see Section 4.7.1, an improved method for the prediction of alloy stability is introduced.

In the fourth stage, merit indices are estimated for the remaining alloys in the dataset. The estimated cost – or density – are examples of physical properties which can be used as merit indices. Alternatively, merit indices can be defined on

the basis of predicted creep or oxidation performance; these are considered below in further detail below. Experience has shown that it is helpful to determine critical values of the merit indices which correspond to the well-known alloys for which the performance is well-characterised experimentally; this provides a series of targets to which newly designed alloys can be compared.

In the fifth stage, the computed merit indices are compared with limits of behaviour or properties which are unacceptable, on the basis of design constraints which should be considered to be boundary conditions to the problem. At this stage, the trial datatest will have been reduced in size quite markedly; should the specification be too tight or unrealistic, it will be very small and it may be necessary to re-visit the design specification and associated merit indices to relax them.

The final, sixth stage involves analysing the dataset of compositions which remains. Our experience has shown that this can be done in various ways. One can sort through the database for alloys which exhibit maximal values of the merit indices – the lightest, the most creep resistant, the most oxidation resistant, the cheapest for example. Or alternatively, one can use the database to determine the relative trade-off in performance which arises from different combination of properties.

Notice in Figure 4.2 that in the left upper and right lower portions of Figure 4.2 are represented the design constraints and the chemical composition respectively. The alloy design system which is proposed describes a viable method for progressing from the former to the latter. Examples are given in Section 3 in greater detail, including the details of the various limits (lattice misfit, γ' Md values etc) which are needed. The alloy design system solves the inverse of the usual empirical route for alloy design which proceeds from the bottom right to the top left.

4.3.2 Model for Creep Resistance

The overarching observation is that time-dependent deformation of single crystal superalloy occurs by dislocation creep with the initial activity being restricted to the γ phase. Thus, since the fraction of the γ' phase is large, dislocations segments rapidly become pinned at the γ/γ' interfaces. The rate-controlling step is then the escape of trapped configurations from γ/γ' interfaces, and it is the dependence of this on local chemistry which gives rise to a significant influence of alloy composition on creep properties; this effect needs to be accounted for here. No attempt is made to model the possibility of γ' shearing by complex shear bands which might include stacking faults and anti-phase boundaries, a process which occurs only if the temperature range is 750-850°C and stress is 500 MPa or greater, when primary creep is initiated [78].

Under these assumptions, a physically-based microstructure model [92] can be invoked for the rate of accumulation of creep strain $\dot{\epsilon}$ when loading is uniaxial and along the $\langle 001 \rangle$ crystallographic direction. The equation set is

$$\dot{\epsilon}_{\langle 001 \rangle} = \frac{16}{\sqrt{6}} \rho_{\mathrm{m}} \phi_{\mathrm{p}} D_{\mathrm{eff}} \left(1 - \phi_{\mathrm{p}}\right) \left(1/\phi_{\mathrm{p}}^{1/3} - 1\right) \sinh \left\{ \frac{\sigma b^2 w}{\sqrt{6} K_{\mathrm{CF}} k T} \right\} \tag{4.5}$$

$$\dot{\rho}_{\mathrm{m}} = C \dot{\epsilon}_{\langle 001 \rangle} \tag{4.6}$$

where ρ_{m} is the mobile dislocation density, ϕ_{p} is the volume fraction of the γ' phase ϕ_{p}, and w is width of the matrix channels. The terms σ and T are the applied stress and temperature respectively. The terms b and k are the Burgers vector and Boltzmann constant respectively. The term $K_{\mathrm{CF}} = 1 + 2\phi_{\mathrm{p}}^{1/3}/3\sqrt{3\pi}(1 - \phi_{\mathrm{p}}^{1/3})$ is a constraint factor [42], which accounts for the close proximity of the cuboidal particles in these alloys, as first identified in [81]. Equation 4.6 describes the dislocation multiplication process which needs an estimate of the multiplication parameter C and the initial dislocation density $\rho_{\mathrm{m},0}$. The term D_{v} is the effective diffusivity

controlling the climb processes at the particle/matrix interfaces. A method for the evaluation of D_{v} in the case of multicomponent alloys – and the associated values needed for contributions from each element i – is given in [92]. Note that in the above, the composition dependence arises from the two terms ϕ_{p} and D_{eff}.

Note that in the above, the composition dependence arises from the two terms ϕ_{p} and D_{eff}. Thus, provided that the microstructural architecture is assumed constant so that ϕ is fixed, any dependence upon chemical composition arises through D_{eff}. Even so, at least for the purposes of the alloy design modelling here, it turns out to be unnecessary to implement a full integration of Equations 4.5 and 4.6 for each prototype alloy composition; in any case this would be prohibitively expensive. Instead, a first order merit index M_{creep} is employed which needs to be maximised, which is given by

$$M_{\mathrm{creep}} = \sum_i x_i / \widetilde{D}_i \tag{4.7}$$

where x_i is the atomic fraction of solute i in the alloy and $\widetilde{D}_i$ is the appropriate interdiffusion coefficient taken from [83, 77]. The definition of D_{eff} implied by the above equation is consistent with absolute reaction rate theory [74].

4.3.3 Model for Oxidation Resistance

Oxide scales forming on multicomponent nickel-based superalloys are generally complex, consisting of layers of different phases which appear in an order consistent with their relative equilibrium partial pressures of oxygen. The phases NiO, Cr_2O_3 and Al_2O_3 are the three most common and important ones. Experience indicates that alloys promoting alumina scales (Al_2O_3) provide the greatest resistance to oxidation. For this reason, single crystal superalloys are commonly designed to be alumina formers, with the empirical rule being that the concentration of aluminium required

for growth of Al_2O_3 and thus adequate oxidation resistances is around 6 wt.% [66]. But in practice, prediction of scale formation remains a significant and unresolved challenge; simplified approaches are needed in the present context.

Here, the approach described in [70] is implemented. The parabolic thickening constant k_t for alumina on single crystal superalloys is considered critical and is modelled consistent with the Wagner approach according to

$$k_t \propto \mathrm{Val}_t^{\mathrm{eff}} \cdot \Delta G_f \tag{4.8}$$

where ΔG_f is the Gibbs free energy required during the oxide formation and effective valence $\mathrm{Val}_t^{\mathrm{eff}}$ term is introduced to explain the impurity effects on the formation of Al_2O_3 in nickel-based superalloy multi-component system. Their equations are written as below

$$\Delta G_f = \Delta G_0 + RT \ln \left\{ \frac{1}{a_{\mathrm{Al}}^{4/3} \cdot P_{\mathrm{O_2}}} \right\} \tag{4.9}$$

$$\mathrm{Val}_t^{\mathrm{eff}} = \sum_{n=i} \left(z_i - z_{\mathrm{Al}} \right) c_i^{\gamma} \tag{4.10}$$

where in Equation 4.9 ΔG_0 represents the standard Gibbs free energy of formation and a_{Al} represents the activity of aluminium in the superalloy which is subject to oxidation. The partial pressure $P_{\mathrm{O_2}}$ is 0.23 atm in one atmosphere air. In Equation 4.10 z_i is the effective valence of element i's ion, and z_{Al} is the valence of Al ion: z_{Al}=3. c_i^{γ} represents the composition of element i in γ phase.

To further justify this approach, consider the diagram of Figure 4.3 which consists of a plot of $\mathrm{Val}_t^{\mathrm{eff}}$ versus ΔG_f, for oxidation at 900°C. Alloys exhibiting Al_2O_3 layer formation are expected to lie towards the bottom left of the diagram (large negative ΔG_f and $\mathrm{Val}_t^{\mathrm{eff}}$) for both thermodynamic and kinetic reasons, whilst those towards the top right (small negative ΔG_f and $\mathrm{Val}_t^{\mathrm{eff}}$) are unlikely to form an effective Al_2O_3 barrier. A dashed line is marked to define a threshold for Al_2O_3 layer

formation. Data for some well-known superalloys have been plotted on this diagram, whose oxidation characteristics are known [70]. One can see that CMSX-4, Rene N5 and PWA1484 lie below the critical contour, consistent with these alloys forming an Al_2O_3 layer at 900°C, and in agreement with the literature [10, 93, 94]. Some controversy is found on the oxidation performance of CMSX-10. Although it is widely used in current turbine engines, Akhtar's work in [95] confirmed that oxidation of CMSX-10 at temperatures below 1000°C does not produce continuous Al_2O_3 layer, which is commonly observed in the internal oxidation zone of the earlier generations of superalloys, e.g. CMSX-4. However, there is indication that beyond 1000°C, the formation of the δ phase (Ni_2Al_3) slows the oxidation rate, thus providing comparative performance as CMSX-4.

Based upon this approach, an oxidation merit index $M_{\text{oxidation}}$ is introduced which is taken to be proportional to the distance from the plotted point (corresponding to the alloy composition) and the dashed threshold line. It combines two predicted factors for Al_2O_3 formation (ΔG_f and $\text{Val}_t^{\text{eff}}$) to a single criterion, which makes it flexible for further quantitative trade-offs with other parameters, e.g. creep resistance. A positive value for the index indicates a point above the dashed line and the positive value indicates the point below the dashed line. A positive and maximised $M_{\text{oxidation}}$ is required for an alloy to optimal adequate oxidation resistance.

4.3.4 Models for Density

The density of pure nickel under ambient conditions is $8907\,\text{kg/m}^3$ [74], but alloying leads to densities of single crystal superalloys which are appreciably different from this value. A first estimate of the density of a new single crystal superalloy can be made from the values of the pure elements, provided that a rule of mixtures is assumed. This procedure underestimates the true density by a factor of about 5%, due to the differing bonding characteristics which then prevail. Once this correction

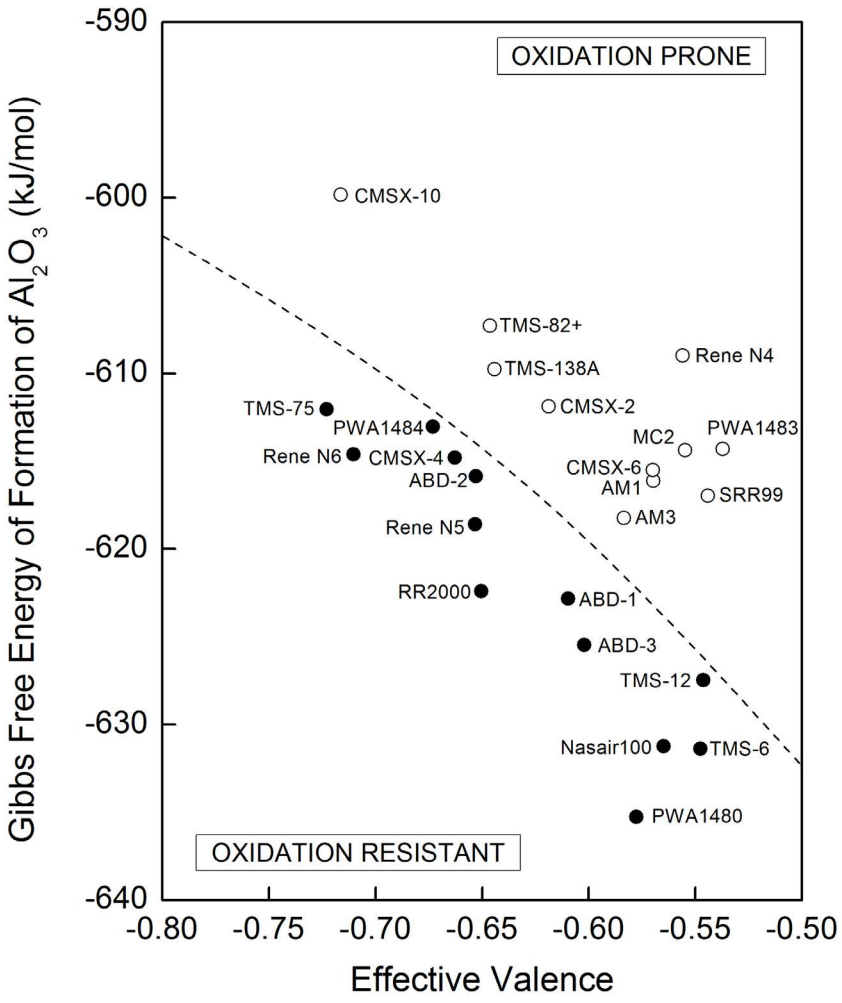

Figure 4.3: Oxidation diagram for well-known nickel-based single crystal superalloys, in which the predicted Gibbs free energy of Al_2O_3 formation is plotted against the total effective valence in Al_2O_3 scale. Below the dashed line indicates that the Al_2O_3 layer becomes continuous.

factor is accounted for, the density can be estimated accurately, to within 1%.

4.3.5 Models for Cost

The cost of a prototype single crystal superalloy is determined provided that estimates are available for the costs of the raw elements employed. These are subject to the movements of metal markets. The values used in our calculations are taken from our precious work [74] to maintain consistency. Our estimates assume that processing costs are identical for all alloys, i.e. that the product yield is not affected by composition.

4.4 Isolation of Three New Single Crystal Superalloys

Three new single crystal superalloys are now isolated. In doing this, different design scenarios are contemplated to reflect different service environments. Table 4.2 represents an overview of the design targets and criteria for the three new alloys. The first, christened ABD-1, is aimed at general gas turbine applications; we aim in particular to (i) strike a compromise between the creep resistance and susceptibility to oxidation, and (ii) to reduce the required alloying by Re relative to commonly used alloys such as CMSX-4 and PWA1484 for which 3 wt% is added – due to the substantial cost of this element and concerns about the environmental impact of its use. The second, termed ABD-2, is aimed at high performance applications where the very best creep resistance is needed but cost is of secondary importance. Some alloys are available for this application which contain significant concentrations of Re and Ru, but these are prone to excessive oxidation which has restricted their implementation in practice. The challenge here is to find alloys which display sufficient oxidation resistance for practical applications. Finally, for industrial gas

turbine applications – of the type used for electricity generation – the inclusion of expensive elements such as Re and Ru cannot be justified; resistance to hot corrosion and/or oxidation is of paramount importance as is the ease of processing. An alloy designated ABD-3 has been designed for these applications. Nominal chemical compositions for the three ABD alloys are given in Table 4.1. In what follows, the methods used to identify these are described.

Table 4.2: Design target and design criteria of three ABD alloys.

Alloy	ABD-1	ABD-2	ABD-3
Design target	Jet propulsion	Jet propulsion	Industrial gas turbines
Design system	Ni-Cr-Co-Re-W-Al-Ta	Ni-Cr-Co-Re-Ru-W-Al-Ta	Ni-Cr-Co-W-Al-Ta
Creep resistance	$\approx$ CMSX-4	$\approx$ TMS-138A	$\approx$ PWA1483
Oxidation resistance	$>$ CMSX-4	$>$ TMS-138A	$>$ PWA1483
γ' volume fraction	60%-70%	60%-70%	50%
Lattice misfit	Slightly negative	Slightly negative	Slightly negative
Phase stability	$\overline{\text{Md}} < 0.99$eV	$\overline{\text{Md}} < 0.99$eV	$\overline{\text{Md}} < 0.975$eV
Density	$< 9.0\text{g/cm}^3$	$< 9.0\text{g/cm}^3$	$< 9.0\text{g/cm}^3$
Cost	$<$ CMSX-4	$<$ TMS-138A	$\approx$ PWA1483

4.4.1 Design of alloys for jet propulsion – comparable to current second-generation superalloys

For ABD-1, the Ni-Cr-Co-Re-W-Al-Ta multicomponent system is considered and upper/lower compositional limits are chosen. The Cr concentration is taken to vary from 4 to 12 wt.%, the Co concentration from 0 to 10 wt.%, the Re concentration from 0 to 5 wt.%, the W concentration from 0 to 8 wt.%, the Al concentration from 4 to 7 wt.% and the Ta concentration from 4 to 8 wt.%. Calculations are carried out at a resolution of 1 wt.%. Thus calculations need to be carried out for 106920 alloys.

Applying the constraint that an optimised creep rupture life requires the predicted γ' fraction to lie in the range 60%-70% at 900°C [9] reduces the dataset to ∼16700 compositions. All these have predicted density less than 9.0g/cm^3. Further reduction of the size of the dataset is achieved by appropriate choice of the lattice misfit δ. The alloy CMSX-4 has a predicted value of δ of 8×10^{-4} at 900°C. Therefore, one can choose an alloy which has a value of δ within the range $\pm 2.5 \times 10^{-4}$ of this, so that $\delta = 8 \pm 2.5 \times 10^{-4}$. Alternatively, a misfit close to zero or a small negative misfit also might be useful for the alloy design, i.e. $\delta = 0 \pm 2.5 \times 10^{-4}$ or $\delta = -8 \pm 2.5 \times 10^{-4}$, respectively. Application to these criteria reduces the size of dataset to 838, 2306 and 2611 alloys for the positive, zero and negative misfit ranges identified.

It is of interest to analyse the alloys in these much smaller datasets more carefully. Since the resistances to oxidation, corrosion and sulphidisation will be improved at higher Cr content, it is useful to plot the alloys with the best M_{creep} in the positive, zero and negative misfit ranges as function of Cr concentration, Figure 4.4. One sees that negatively misfitting alloys are predicted to be best for creep resistance, particularly when Cr content is higher than 7 wt.%. Alloy stability can be taken

into account by plotting the Md value as function of Cr concentration. Figure 4.5 indicates that the 8 wt.% Cr concentration is likely to be an upper limit before TCP precipitation becomes excessive.

Further refinement design has been carried out for the dataset of 2611 (negatively misfitting) alloys by increasing the calculation resolution to 0.1 wt.% for the elements Al, W, Ta and Re. This requires an additional 11^4 calculations for each of the alloys in the remaining dataset of 2611. From the results of this refinement in alloy design, one can isolate the alloy composition of lowest Re content which is predicted to match the creep resistance of CMSX-4. The composition is Ni-8Cr-10Co-1.6Re-8.5W-5.8Al-8.5Ta (wt.%). It has a relative density of 8.84g/cm^3 and a creep merit index of 7.2×10^{15}m^{-2}s, which is a bit higher than the creep merit index of CMSX-4, 7.0×10^{15}m^{-2}s. This alloy is referred to as Alloy ABD-1 in what follows.

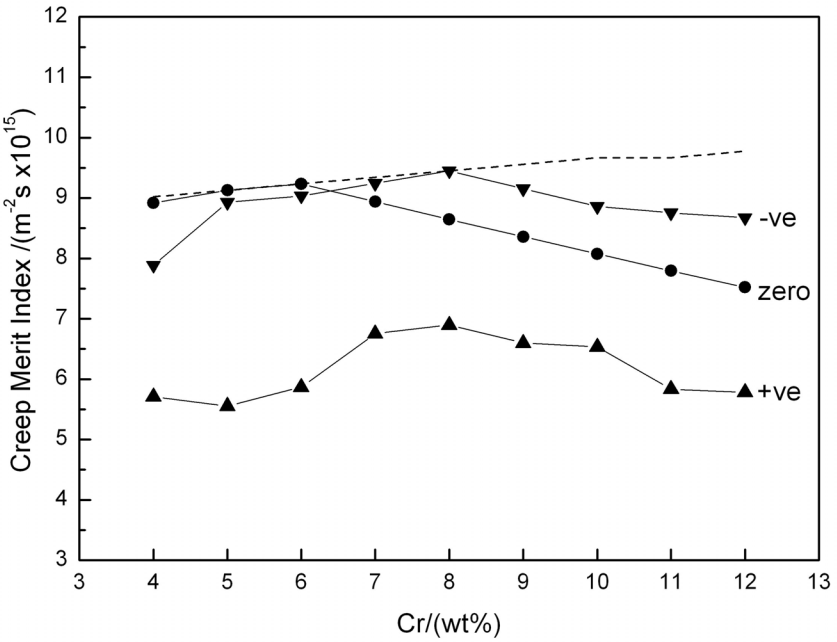

Figure 4.4: Variation of the maximum predicted Creep Merit Index as a function of Cr content, for different misfit ranges. Also plotted is a dotted line corresponding to the best creep merit index in the original dataset.

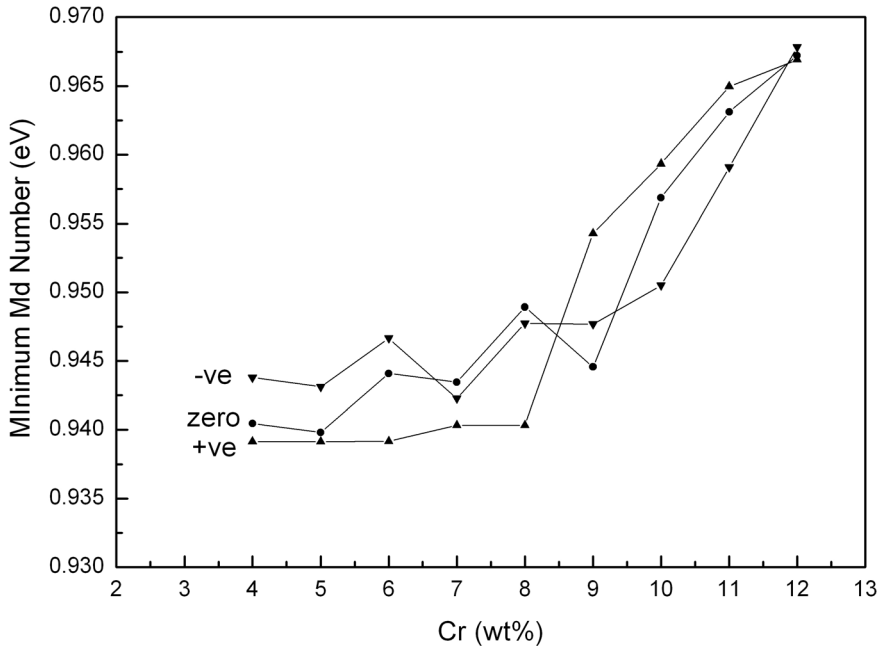

Figure 4.5: Variation of the stability number Md of the alloys predicted to be the most stable as a function of Cr content, for different misfit ranges.

4.4.2 Design of alloys for high performance jet engine – comparable to current fourth-generation superalloys

The Ni-Cr-Co-Re-Ru-W-Al-Ta system is considered. The aim is to design a very high performance alloy of superior creep resistance without excessive susceptibility to oxidation, with cost being of lesser importance. The Cr concentration is taken to vary from 2 to 8 wt.%, the Co concentration from 4 to 9 wt.%, the Re concentration from 3 to 7 wt.%, the Ru concentration from 2 to 5 wt.%, the W concentration from 1 to 8 wt.%, the Al concentration from 5 to 7 wt.% and the Ta concentration from 4 to 11 wt.%. Calculations are carried out at a resolution of 1 wt.%. The first dataset consists of a total of 161280 alloys.

A scatter diagram for predicted creep merit index against oxidation merit index is plotted for the 161280 alloys in Figure 4.6. Obviously, a preliminary choice of alloys

with a good combination of creep resistance and oxidation resistance is needed to take forward into the next design stage; these lie to the top right of this diagram. Elimination of alloys with negative oxidation index reduces the size of the dataset to 35902 alloys. A constraint placed on the γ' phase fraction within the range 60%-70% results in a further reduction to 8508 alloys.

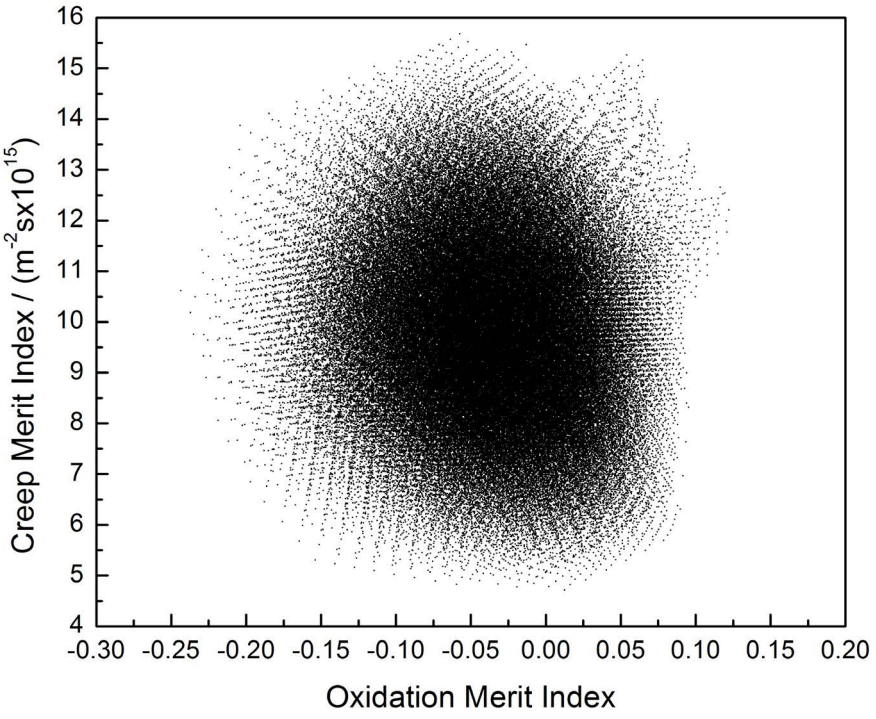

Figure 4.6: Scatter diagram (Creep Merit Index vs. Oxidation Merit Index) for original 161280 alloys dataset.

Lattice misfit is considered next, for the purposes of ensuring good resistance to γ' coarsening. The histograms in Figure 4.7 indicate that values of γ/γ' lattice misfit become generally more negative for ABD-2 when compared to the equivalent stage for ABD-1. This is due to the additional Ru content and increase of Re content; these partition preferentially into the γ phase thus increasing the γ lattice parameter. According to the statistical spread shown in the histogram of Figure 4.8, lattice misfit can be divided into three different ranges: (a) zero $-1.5 \times 10^{-3} \sim -0.5 \times 10^{-3}$; (b)

negative $-4 \times 10^{-3} \sim -3 \times 10^{-3}$; (c) very negative $-7 \times 10^{-3} \sim -5 \times 10^{-3}$. With these criteria, the remaining dataset is separated into zero lattice misfit with 1103 alloys, negative lattice misfit with 2113 alloys and very negative lattice misfit with 1528 alloys. Since the values of lattice misfit are likely to contain errors, it is helpful to compare with predictions for comparable known alloys. The predicted γ/γ' lattice misfit for TMS-138A is -3.77×10^{-3}; it is also known from experience that a slightly negative misfit is preferable. Hence the constraint of lattice misfit is applied in the range $\delta_{\mathrm{TMS-138A}} \rightarrow 0$. Application of this criterion reduces the size of dataset to just 4635 alloys.

For the purpose of avoiding an alloy which is excessively dense, a limit of 9.0g/cm^3 is placed. The remaining dataset is thus split into three based on the density criteria: (i) less than 9.0g/cm^3, (ii) less than 8.8g/cm^3 and (iii) less than 8.6g/cm^3, see Figure 4.9. One can see that good creep resistance is compromised when the constraint on density becomes more restrictive. The reason is that the creep-strengthening elements, e.g. Ru and Re, are much heavier compared to the other alloying elements. A total of 180 alloys were then selected from each density range by taking only those which were predicted to have the best creep resistance. The alloys were taken across a range of Cr contents, from 2 to 8 wt.%.

A refinement design was then carried out with the 180 alloys to improve the resolution of the element concentration. For each composition, the concentrations of elements Re, Ru, W, Al and Ta were refined to within a resolution of 0.2 wt.%. The concentrations of elements Cr and Co were not refined, since one can argue that these might not need to be known to greater precision. Thus calculations are needed for a further 187500 alloys. Once again, the density criteria of less than 9.0, 8.8, 8.6g/cm^3), the constraints on γ' phase fraction and γ/γ' lattice misfit were applied as above. Alloys with the best creep performance are plotted in Figure 4.10 as a function of Cr content. Also plotted are their corresponding stability number Md. Furthermore, the values of creep merit index/(density×cost) are plotted in

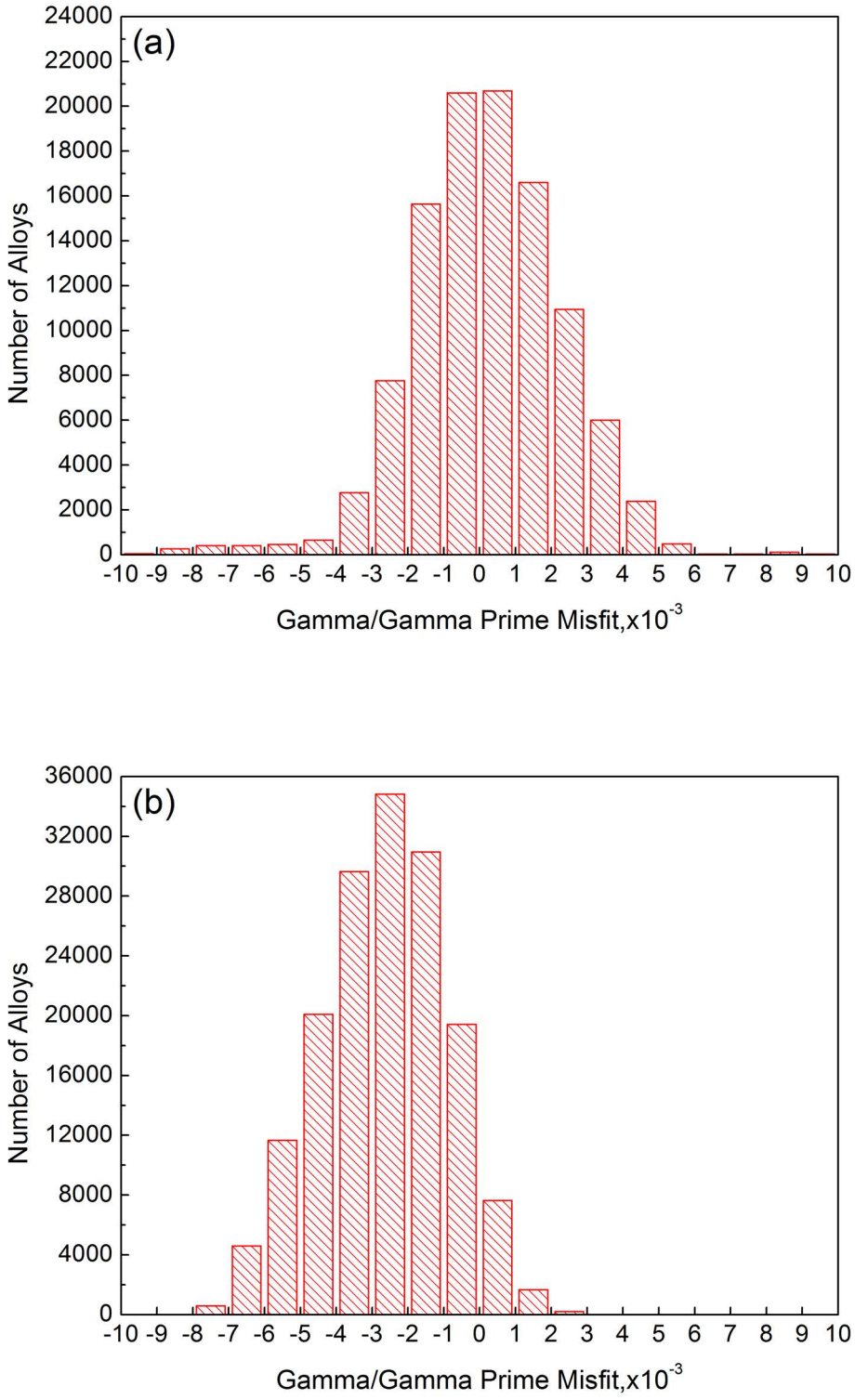

Figure 4.7: Comparison of histograms for predicted lattice misfit in different design systems: (a) Previous design in Ni-Cr-Co-Re-W-Al-Ta system; (b) Present design in Ni-Cr-Co-Re-Ru-W-Al-Ta system.

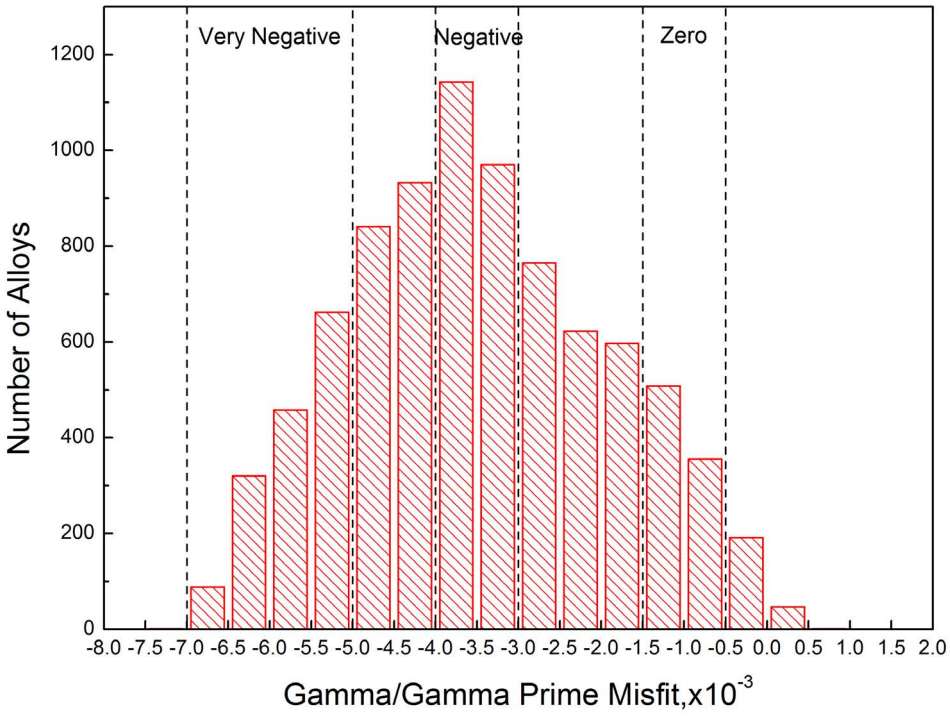

Figure 4.8: Definition of different lattice misfit range: zero, negative and very negative.

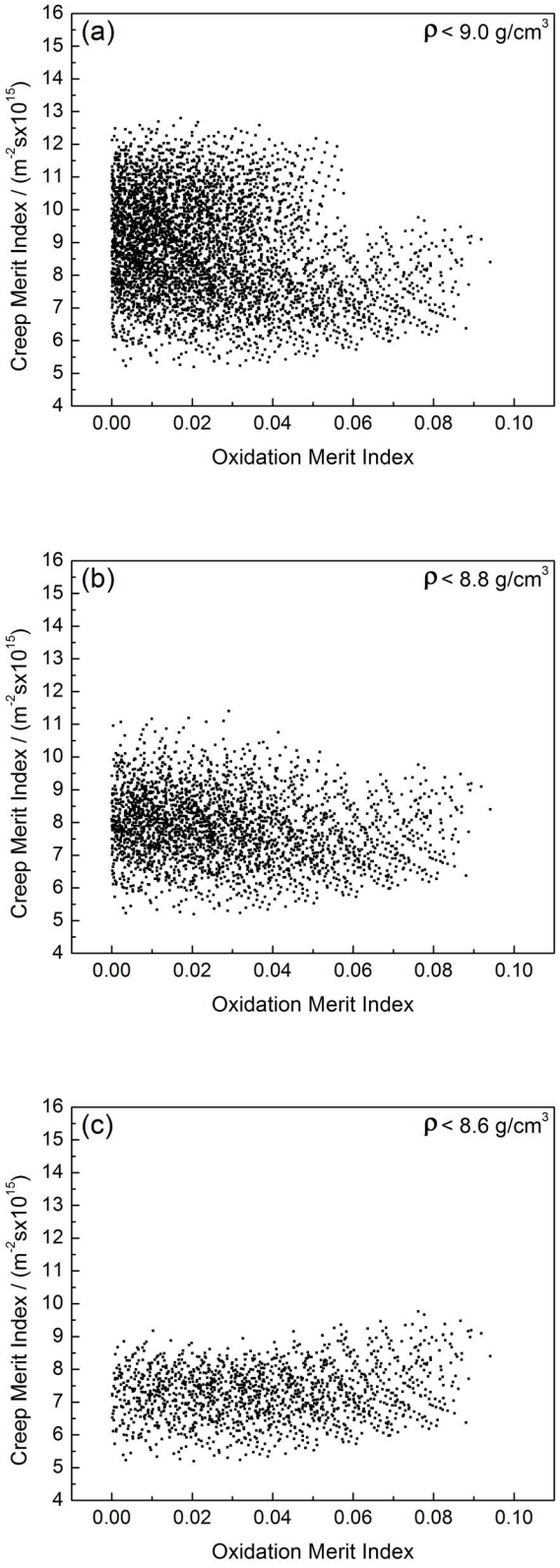

Figure 4.9: Scatter diagrams (Creep Merit Index vs. Oxidation Index) for different density ranges: (a) density less than 9.0g/cm^3; (b) density less than 8.8g/cm^3; (c) density less than 8.6g/cm^3.

Figure 4.11. Estimates for TMS-138A and CMSX-4 are also given. One can see from Figure 4.10 that some alloys are available which exhibit predicted higher creep resistance than TMS-138A but their densities are also relatively high. But when density and cost of the alloys are taken into account, see Figure 4.11, almost all the down-selected alloys exhibit better predicted performance than that of TMS-138A. This is because the cost of Re and particularly Ru is prohibitive.

From all the analysis above, the composition of ABD-2 is chosen as Ni-4Cr-9Co-5.6Re-2.6Ru-7.4W-6.4Al-5.6Ta. Our predictions indicate that it should have adequate creep resistance, acceptable microstructure stability, good oxidation resistance, lower density and cost, especially when compared to an alloy such as TMS-138A.

4.4.3 Design of alloys for industrial gas turbines – appreciable creep strength and adequate corrosion resistance

For industrial gas turbines (IGTs), greater corrosion resistance is required since the fuels used are aggressive. Furthermore, the blades are considerably larger than aeroengine ones, so that the cost of raw elements such as Re becomes a substantial issue. Castability also should be maximized because defect levels such as freckles are enhanced as the casting size increases. There has been a tendency to migrate alloys proven on aeroengines to IGTs, but these have proven largely inappropriate probably because the necessary design intent is then not respected.

The following criteria have been applied for the design of a new grade of single crystal superalloy for IGT applications: (i) Re was removed to improve the castability and reduce the cost; (ii) the Cr content should be considerable high to meet the requirement of better corrosion resistance, normally in the range 12-20wt.%; (iii) the volume fraction of γ' phase was kept close to $\sim$50%, a little lower than that of aeroengine alloys, to maintain a good combination of creep, fatigue performance

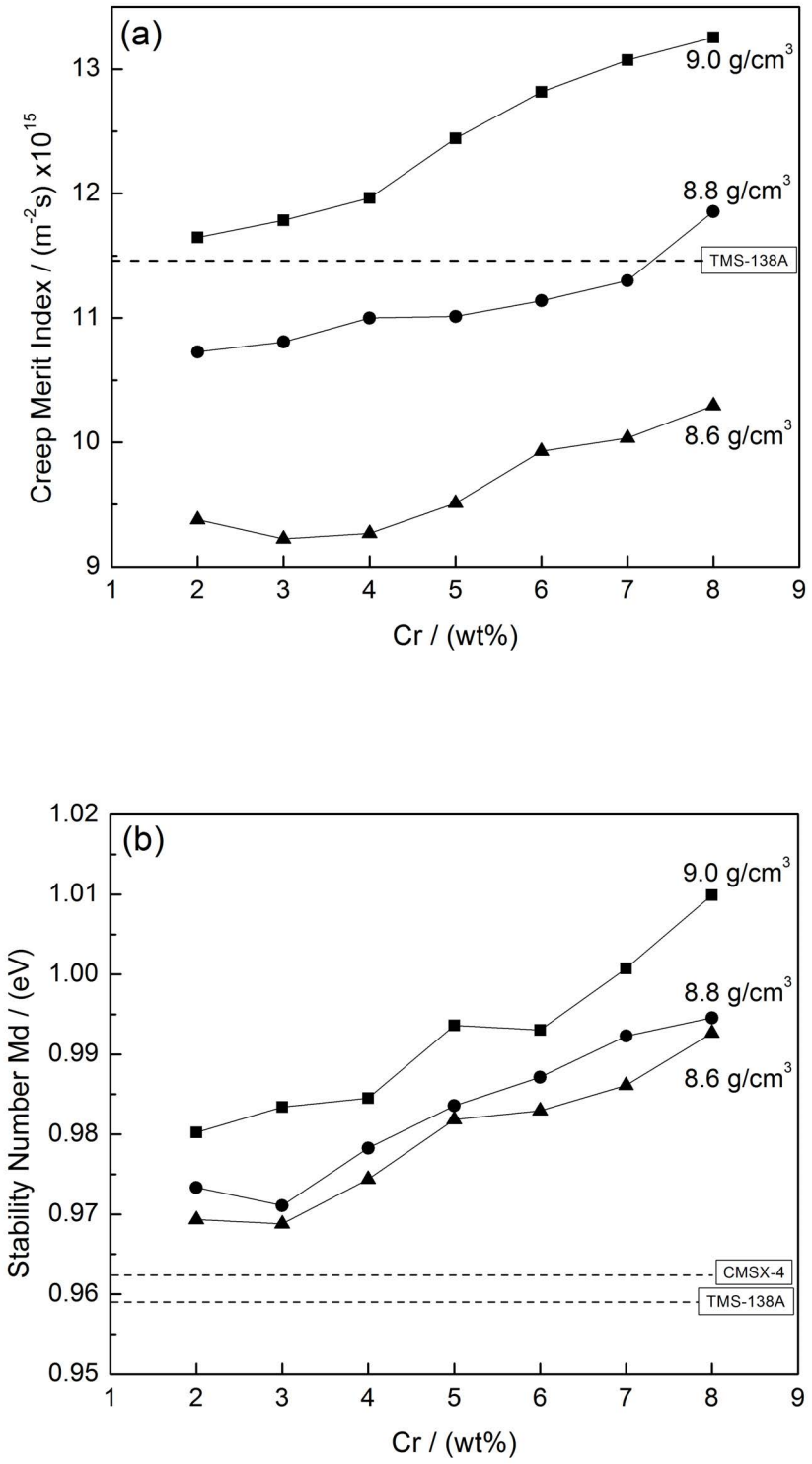

Figure 4.10: (a) Variation of maximum predicted Creep Merit Index as a function of Cr content for different density ranges; (b) Corresponding Stability Number Md values of these alloys.

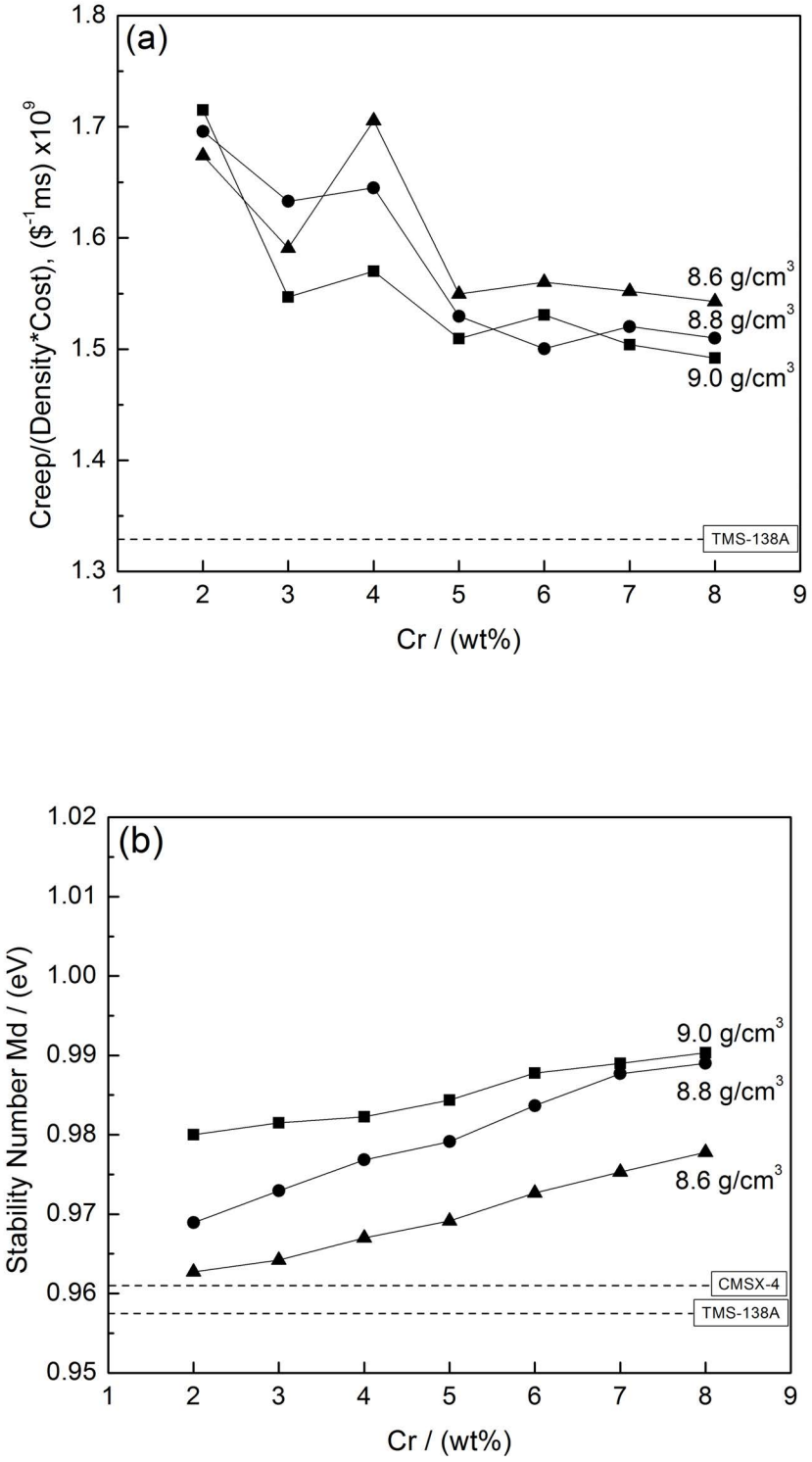

Figure 4.11: (a) Variation of maximum predicted ratio of Creep Merit Index/(Density×Cost) as a function of Cr content for different density ranges; (b) Corresponding Stability Number Md of these alloys.

and microstructural stability; (iv) the lattice misfit was chosen within the range $\delta = -8 \pm 2.5 \times 10^{-4}$.

Based on these constraints, calculations were carried out within the Ni-Cr-Co-W-Al-Ta system. In Figure 4.12 the best creep resistant alloys are plotted as a function of Cr content and Md value; these compositions are listed in Table 4.3. It is predicted that creep resistance decreases as Cr content increases. With a suitable constraint applied to the Md value, Alloys 70-81 were selected for detailed consideration; these are plotted on a scatter diagram of creep merit index vs. oxidation merit index, see Figure 4.13. Studies carried out by Mrowec et al. [96] suggest that 13 wt.% Cr content is required to maintain the resistance to sulphidisation. In Figure 4.13, boundary conditions of creep resistance and oxidation resistance are determined to approach to the predicted properties of the existing alloys PWA1483 and CMSX-4. On this basis, Alloy 73 was selected for the final composition of ABD-3. It has composition Ni-13Cr-10Co-5W-5.4Al-7Ta (wt.%).

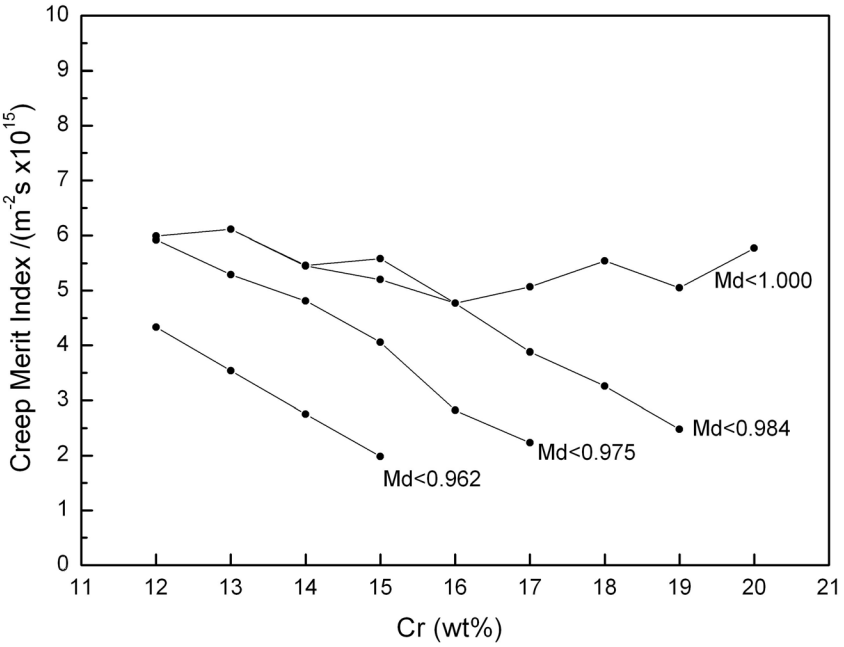

Figure 4.12: Variation of maximum predicted creep merit index as a function of Cr content, for alloys with various values of the stability index.

Table 4.3: The compositions of IGT alloys designed in this study.

Alloy	Cr	Co	W	Al	Ta	Ni	Density(g/cm^3)
Md < 1.000							
Alloy 55	12	10	7	5.2	8.0	Bal	8.71
Alloy 56	13	10	7	5.0	8.0	Bal	8.73
Alloy 57	14	10	5	5.4	8.0	Bal	8.55
Alloy 58	15	10	5	5.2	8.0	Bal	8.57
Alloy 59	16	9	3	5.4	8.0	Bal	8.43
Alloy 60	17	10	3	5.4	8.0	Bal	8.41
Alloy 61	18	10	4	5.2	8.0	Bal	8.47
Alloy 62	19	7	4	5.2	8.0	Bal	8.45
Alloy 63	20	10	4	5.0	8.0	Bal	8.47
Md < 0.985							
Alloy 64	12	10	7	5.2	8.0	Bal	8.71
Alloy 65	13	10	7	5.0	8.0	Bal	8.73
Alloy 66	14	10	5	5.4	7.8	Bal	8.54
Alloy 67	15	10	4	5.4	7.8	Bal	8.57
Alloy 68	16	9	3	5.4	8.0	Bal	8.43
Alloy 69	17	4	3	5.4	7.8	Bal	8.25
Alloy 70	18	4	1	5.8	7.2	Bal	8.30
Alloy 71	19	1	0	5.8	7.4	Bal	8.27
Md < 0.975							
Alloy 72	12	10	7	5.2	7.0	Bal	8.67
Alloy 73	13	10	5	5.4	7.0	Bal	8.53
Alloy 74	14	9	4	5.6	6.6	Bal	8.42
Alloy 75	15	10	1	6.0	6.6	Bal	8.22
Alloy 76	16	3	1	6.0	6.6	Bal	8.20
Alloy 77	17	1	0	6.0	6.8	Bal	8.15
Md < 0.962							
Alloy 78	12	10	3	6.0	5.0	Bal	8.29
Alloy 79	13	7	2	6.0	5.4	Bal	8.25
Alloy 80	14	4	1	6.0	5.4	Bal	8.19
Alloy 81	15	1	0	6.0	5.8	Bal	8.15

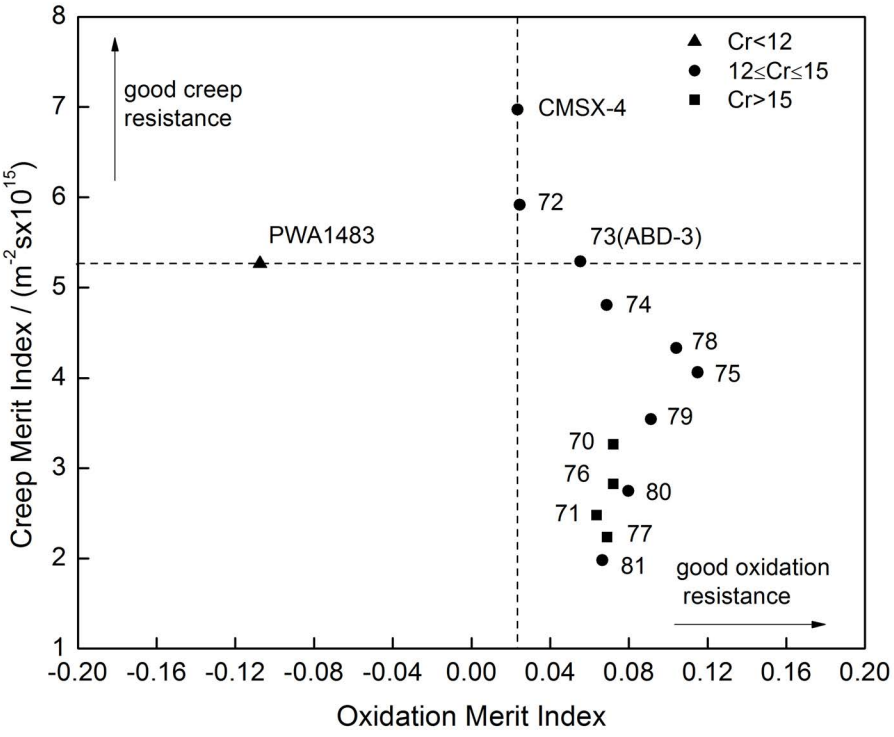

Figure 4.13: Scatter diagram (Creep Merit Index vs. Oxidation Merit Index) for selected compositions of IGT Alloy 70-81.

4.5 Experimental Methods

4.5.1 Investment Casting

Single crystal castings of alloys ABD-1, ABD-2 and ABD-3 were prepared using an industrial scale investment casting facility at the University of Birmingham, in the form of cylindrical bars of 10 mm diameter and length 160 mm (see Figure 4.14). Typically, three bars were cast in each run with a withdrawal speed of 229 mm/hour and a mould temperature of 1540°C. Casting was carried out under the vacuum of better than 10^{-4} Pa. The casting stock for the new alloys were prepared by Ross & Catherall in Sheffield, UK to industry-consistent standards. Impurity levels in barstock for C, S, O and N are listed in Table 4.4, and were deemed acceptable. The single crystal bars were carefully removed from the mould, and then sand blasted. To check for the absence of grain boundaries, bars were macro-etched using a solution of

HCl+5-10 vol.% H_2O_2; castings with grain boundaries were rejected. The nominal compositions, barstock compositions and casting compositions of these three alloys are summarised in Table 4.5, which shows that the target compositions have been successfully achieved.

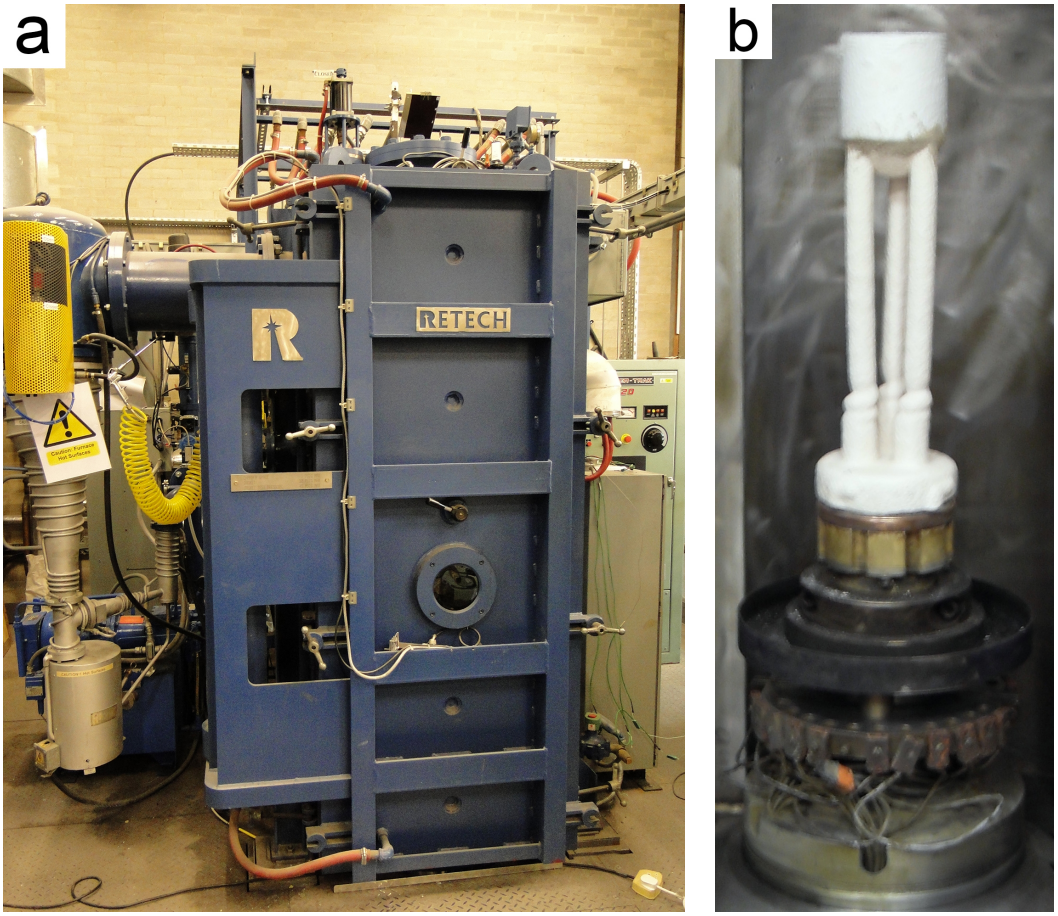

Figure 4.14: (a) Casting furnace in University of Birmingham; (b) Typical mould used for single crystal bars in this study.

4.5.2 Heat Treatment

To remove microsegregation introduced from casting and to develop appropriate precipitate morphologies, suitable heat treatments were designed. Firstly, optimal conditions of solution heat treatment were decided from Differential Thermal Analysis (DTA). Specimens of size 3 mm diameter and 1.5 mm thickness were cut from the fully heat treated bars, and then inserted into a NETZSCH DSC404C machine

Table 4.4: Impurity levels (unit: ppm) in bar stocks of each alloy.

Alloy	ABD-1	ABD-2	ABD-3
Carbon(C)	<10	30	<10
Nitrogen(N)	4	5	14
Oxygen(O)	3	5	7
Sulphur(S)	8	3	2

Table 4.5: Nominal compositions, barstock compositions and casting compositions for ABD alloys (wt.%).

Composition	Cr	Co	Re	Ru	W	Al	Ta	Ni
ABD-1								
Nonimal	8	10	1.6	-	8.5	5.8	8.5	Bal
Barstock	8.17	10.07	1.61	-	8.36	5.79	8.47	Bal
Casting	8.07	9.79	1.60	-	8.32	5.64	8.44	Bal
ABD-2								
Nonimal	4	9	5.6	2.6	7.4	6.4	5.6	Bal
Barstock	4.13	8.96	5.58	2.58	7.38	6.38	5.59	Bal
Casting	4.10	8.95	5.55	2.53	7.35	6.32	5.53	Bal
ABD-3								
Nonimal	13	10	-	-	5	5.4	7	Bal
Barstock	13.20	10.20	-	-	5.10	5.50	7.15	Bal
Casting	12.82	9.95	-	-	4.98	5.43	7.04	Bal

in pure alumina crucibles and analysed between 800°C to 1400°C. The heating and cooling rates used were 5°C/min and 10°C/min, respectively. Solution heat treatment temperature is then decided based on the results of DTA curves, to dissolve all the eutectic γ' and also avoid the incipient melting. Therefore, the solution heat treatments chosen were 1305°C/6 hours for ABD-1, 1325°C/6 hours for ABD-2 and 1300°C/4 hours for ABD-3, respectively.

In order to reprecipitate the γ' phase after solution treatment, appropriate ageing treatments have been designed. Several trial treatments were carried out between 1120 to 1140°C for a temperature increment of 5°C, with holding time of 2, 3 and 4 hours. Their microstructures have been examined by Scanning Electron Microscopy (SEM) to check the γ' particles size and distribution. Then the first ageing treatment was selected on the basis of these trial treatments, giving 1120°C/3 hours for ABD-1, 1120°C/2 hours for ABD-2 and 1125°C/1 hour for ABD-3. A secondary ageing of 870°C/16 hours was used in all cases according to the common industrial standard.

4.5.3 Creep Testing

Specimens of 20mm gauge length and 4mm diameter were machined from fully heat-treated single crystal bars (Figure 4.15). The orientations of specimens were shown to be within 10° from the $\langle 001 \rangle$ direction, using Laue analysis. Considerable care was taken to ensure that the surface finish was better than 1.6 μm along the gauge length, so that premature failure of the specimens would be avoided. Test temperatures range from 800 to 1100°C, planned to represent the three deformation modes in single crystal superalloys: cutting of γ', climb/glide around cubic γ', and climb/glide around rafted γ'. The experimental conditions used for the testing of the new alloys are summarised in Table 4.6.

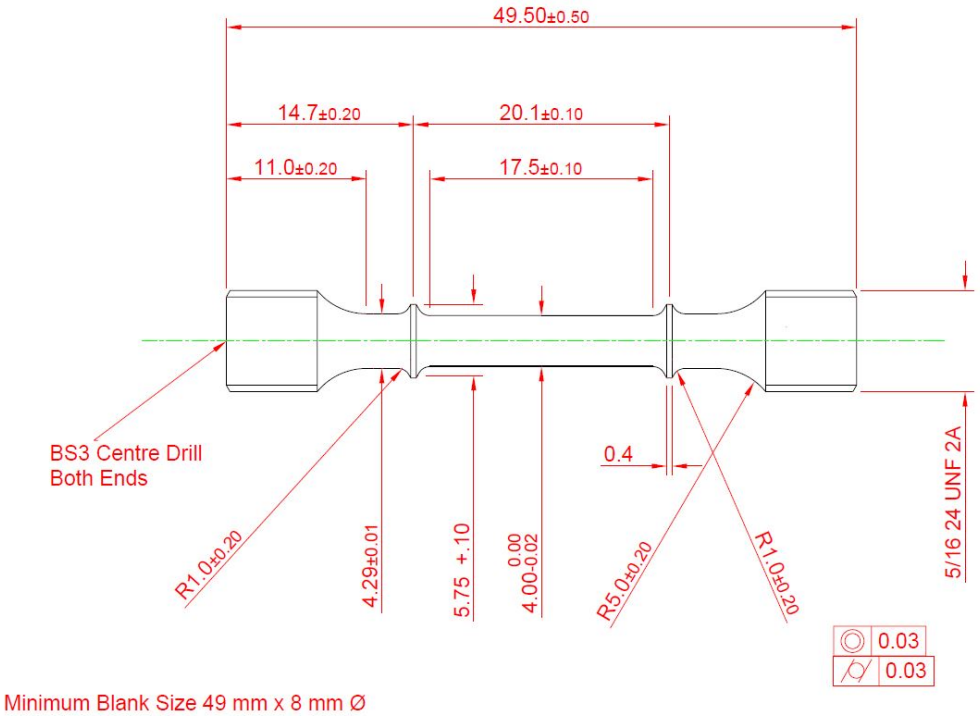

Figure 4.15: Schematic illustration of specimen geometry for creep testing.

Table 4.6: Creep test conditions of ABD alloys.

Alloy	Creep test conditions
ABD-1	800°C/680MPa
	800°C/750MPa
	900°C/350MPa
	900°C/450MPa
	1050°C/135MPa
	1050°C/150MPa
ABD-2	900°C/460MPa
	900°C/550MPa
	1000°C/230MPa
	1000°C/325MPa
	1100°C/110MPa
	1100°C/200MPa
ABD-3	760°C/655MPa
	871°C/345MPa
	982°C/172MPa

Table 4.7: Measured densities of ABD alloys.

Alloy	Predicted density(g/cm^3)	Measured density(g/cm^3)
ABD-1	8.840	8.831
ABD-2	8.894	8.901
ABD-3	8.537	8.512

4.5.4 Cyclic Oxidation Testing

Specimens for cyclic oxidation testing were prepared from fully heat-treated single crystal bars with rectilinear geometry of dimensions 20mm × 10mm × 1mm. Prior to testing, the surfaces were finished with 1200 grade grit paper, polished and then cleaned in acetone in an ultrasonic bath. To assess the oxidation resistance, cyclic oxidation tests were carried out at 1000°C and 1100°C (2 hours per cycle) up to 50 hours; the weight change of the specimens was measured at the end of each cycle using a standard balance.

4.5.5 Determination of Density

Density measurement of designed ABD alloys was carried out by using an electronic densimeter ED-120T. Method is simply based on the Archimedes' principle that only need to measure the sample mass in the air and the mass while immersed in water. Every sample has been measured by three times and their average densities are summarised in Table 4.7.

4.5.6 Hot Mounting Sample Preparation

Samples were cut using 0.5 mm thickness SiC disc on Struers Acutom 5 cutting machine. The feed rate was 0.015mm/sec with rotation speed of 3000 rpm. No oscillation was used. Hot mounting was carried out with conductive bakelite by

ATM Opa1400 mounting machine at less than 200°C for 15 minutes. Samples were ground and polished in the order 240 grade sandpaper, MD-Largo, MD-Dac and MD-Nap polishing discs, with the required suspension, which are water, 9μm, 3μm and 1μm diamond liquid, respectively. Samples are finally cleaned thoroughly in an ultrasonic bath with acetone.

4.5.7 Cold Mounting Sample Preparation

In order to avoid cracks at the oxide/metal interface, oxidised samples were prepared by cold mounting with epoxy resin (Struers Specifix20), and then ground and polished to the same standard as hot mounted ones. Samples were cleaned thoroughly in an ultrasonic bath with acetone. Finally, specimens were carbon coated for subsequent SEM analysis.

4.5.8 Scanning Electron Microscopy (SEM)

In this study, tungsten filament SEM, JEOL6060LV, and Field Emission Gun SEM, JEOL7000F, were used. Both were equipped with an Oxford Instruments INCA system for energy dispersive spectroscopy (EDX). Electrolytic etching was performed to obtain clear observation of γ and γ' structure. Samples were etched by using solution Kalling's No.2 Etchant (5g $CuCl_2$, 100ml HCl and 100ml ethanol).

4.5.9 Electron Probe Microanalysis (EPMA)

Microprobe analysis was carried out on mounted and polished cross-sections of oxidised superalloys using a JEOL JXA 8800 Superprobe with four spectrometers for parallel detection of four elements. Concentration maps of Cr, Ta, Al, Ni, O, Re, W and Ru were obtained in the following way. Measurements were made over a 512 by 512 point square at a spacing of 0.07μm. The wavelength dispersive spectrometers

(WDS) which were employed were equipped with crystals of TAP (used for Al and W), PET (used for Cr, Re and Ru), LIF (used for Ni and Ta) and LDE (used for O). X-ray counts were recorded simultaneously for Kα (Al, Cr, Ni, O), Lα (Ta, Ru) and Mα (Re, W). These were converted to concentration values using standard correction procedures and signals from pure-element standards. The acceleration voltage and beam current for the analyses were 25kV and 32nA respectively and the dwell time for each point was 100ms.

4.6 Results

The ABD-1, ABD-2 and ABD-3 alloys were first observed by scanning electron microscopy, to check whether the microstructural design and processing had been accomplished successfully, see Figure 4.16. One can see that appropriate microstructures have indeed been developed. For ABD-1 and ABD-2, a cuboidal γ' morphology is found. For ABD-3, the morphology is more spheroidal, indicative of a larger lattice misfit. Image analysis indicated that the volume fractions of γ' phase in ABD-1 to 3 alloys are 68.5%, 62.9% and 65.3%, with the average particles sizes of 350.8nm, 243.8nm and 252.2nm, respectively.

4.6.1 Cyclic Oxidation

Cyclic oxidation data are given in Figure 4.17 for each of the ABD alloys. Data for CMSX-4, TMS-138A and PWA1483 which were measured here are also given for comparative purposes with ABD-1, ABD-2 and ABD-3 respectively.

At 1000°C, the ABD alloys exhibit better oxidation resistance than the ones with which they are to be compared. ABD-1 exhibits very little weight gain and there is evidence that it starts to stabilise after 6 hours exposure. The weight gain of ABD-2 is significantly less than that of TMS-138A and a stable regime also arises

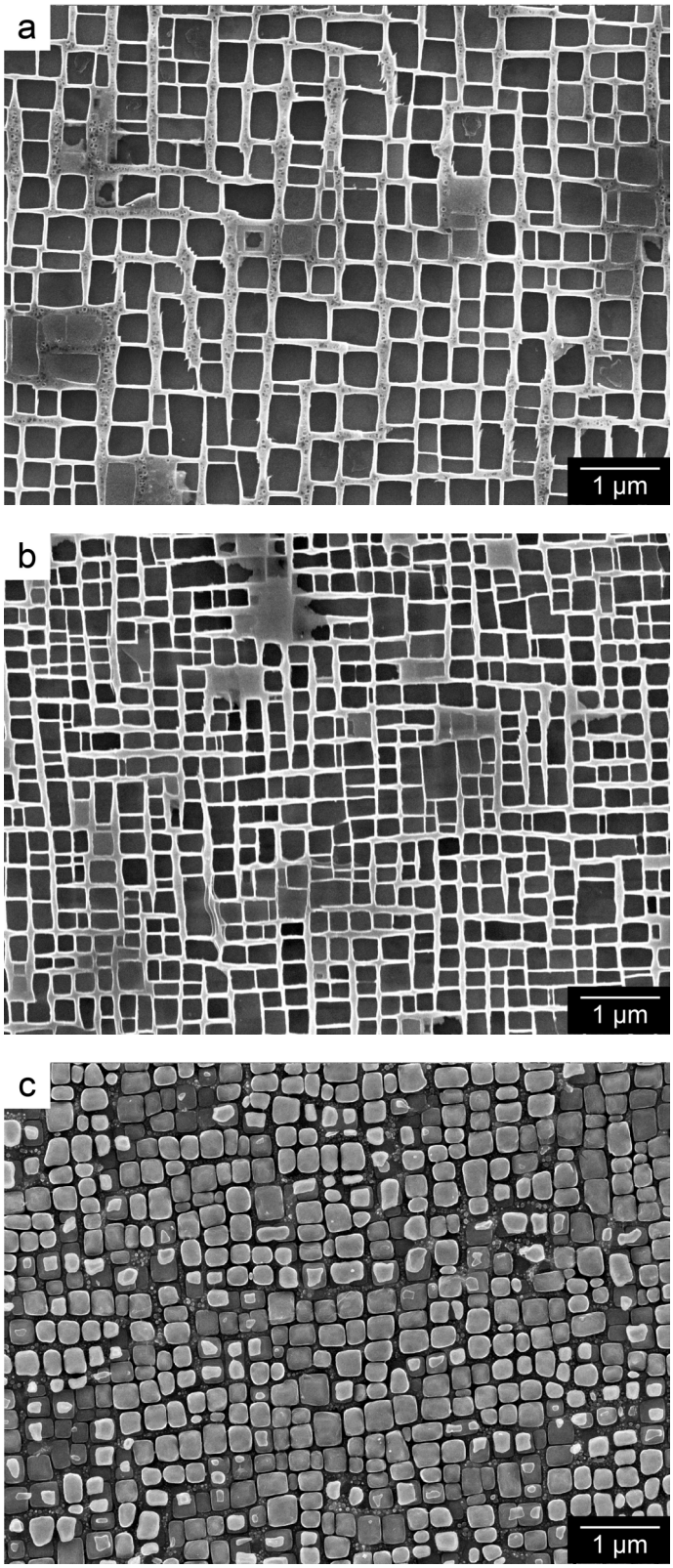

Figure 4.16: The heat treated microstructures of ABD alloys, with cuboidal γ' particles and γ matrix,(a) ABD-1, (b) ABD-2, (c) ABD-3.

after around 6 hours exposure. It is also confirmed that ABD-3 performs better than PWA1483. The data for 1100°C are given in Figure 4.17(b). After 50 hours exposure at this higher temperature, ABD-1 remained relatively stable, again indicative of excellent oxidation performance. Both ABD-2 and TMS-138A started to show weight loss, suggesting spallation. Note however that the weight loss of ABD-2 becomes slower after about 20 hours, perhaps due to the formation of Al_2O_3 under the NiO and Cr_2O_3 so that the scale is partially protective. ABD-3 shows very similar weight change kinetics to ABD-2 and performs better than PWA1483; however the data are consistent with spallation. It is possible to determine instantaneous values of the parabolic thickening constant k_p from the experimental data, see Figure 4.18. Figure 4.17(a) indicates that the parabolic oxidation rate drops to a rate expected for Al_2O_3 region only after about 2 hours exposure. Figure 4.17(b) indicates that ABD-2 requires longer time to fall into Al_2O_3 region, about 10 hours exposure. For ABD-3, the time is about 4 hours.

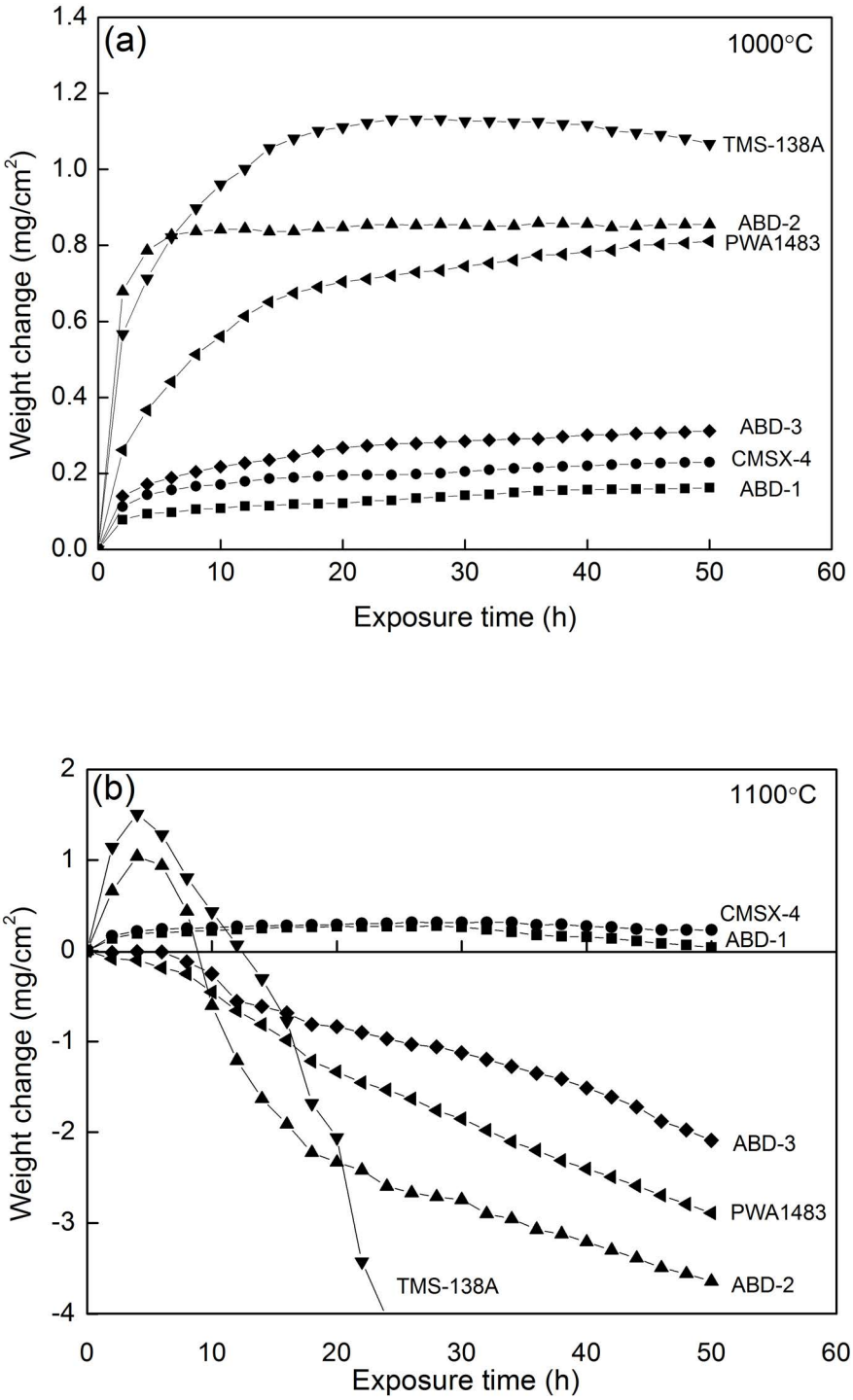

Figure 4.17: Weight change of ABD alloys at different temperatures (a)1000°C and (b)1100°C. Also shown are tests of current employed alloys CMSX-4 and TMS-138A.

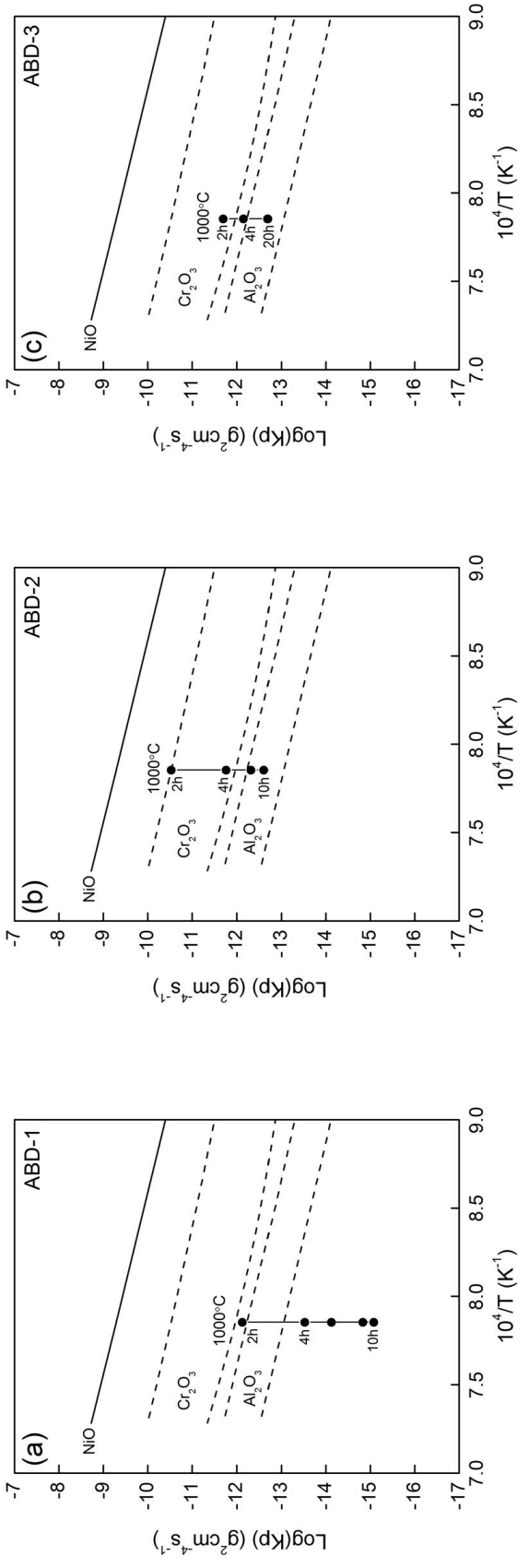

Figure 4.18: Parabolic oxidation constants k_p of ABD alloys at 1000°C. Also shown kp of pure oxides from literatures [97].

Further confirmation is carried out by microstructural analysis of cross-sections of the oxidised samples, see Figure 4.19. Consistent with the weight gain curves, the analysis is carried out after 10 hours exposure time is selected to confirm whether ABD alloys form continuous Al_2O_3 layers; the temperature of 1000°C is considered. For each of the ABD alloys, it is confirmed that a continuous layer of Al_2O_3 is formed in contact with the underlying metallic substrate; it grows inwards and appears dark in the backscattered images shown. Its location is consistent with its very low equilibrium partial pressure of oxygen, and Ellingham diagram considerations.

Detailed arrangement of oxide scales formed in each alloy can be deduced from the results of EPMA analysis in Figure 4.20. In ABD-1, NiO is formed on the very top surface; there is evidence that it is friable and discontinuous. The Cr_2O_3 layer sits underneath the NiO layer. The Ta_2O_3 layer beneath this is the brightest part in the image due to the heavy Ta enrichment. Below all these oxide scales, a continuous Al_2O_3 layer was present to provide the good oxidation resistance. Oxide scales are more complex in ABD-2 due to the higher concentration of refractory elements, e.g. Ta, W and Re. A very thick NiO layer is found on top of the scale. Then the other oxides form in the order of WO_3, Cr_2O_3, Ta_2O_3, spinel ($NiCr_2O_4$, $NiAl_2O_4$) and Al_2O_3. For the IGT alloy ABD-3, a thick Cr_2O_3 film forms due to the high concentration of Cr. The Al_2O_3 oxides initially form as fingers protruding into the metal substrate, and become continuous after longer exposure.

The experimental results and analysis demonstrate that the ABD alloys form protective Al_2O_3 films at 1000°C within a very short time. It is likely that this effect contributes to the superior oxidation resistance displayed.

4.6.2 Creep Behaviour

The creep data are displayed as Larson-Miller diagrams in Figure 4.21 for ABD-1 and ABD-2 and also in Figure 4.22 for ABD-3. Also shown are data for CMSX-4, TMS-

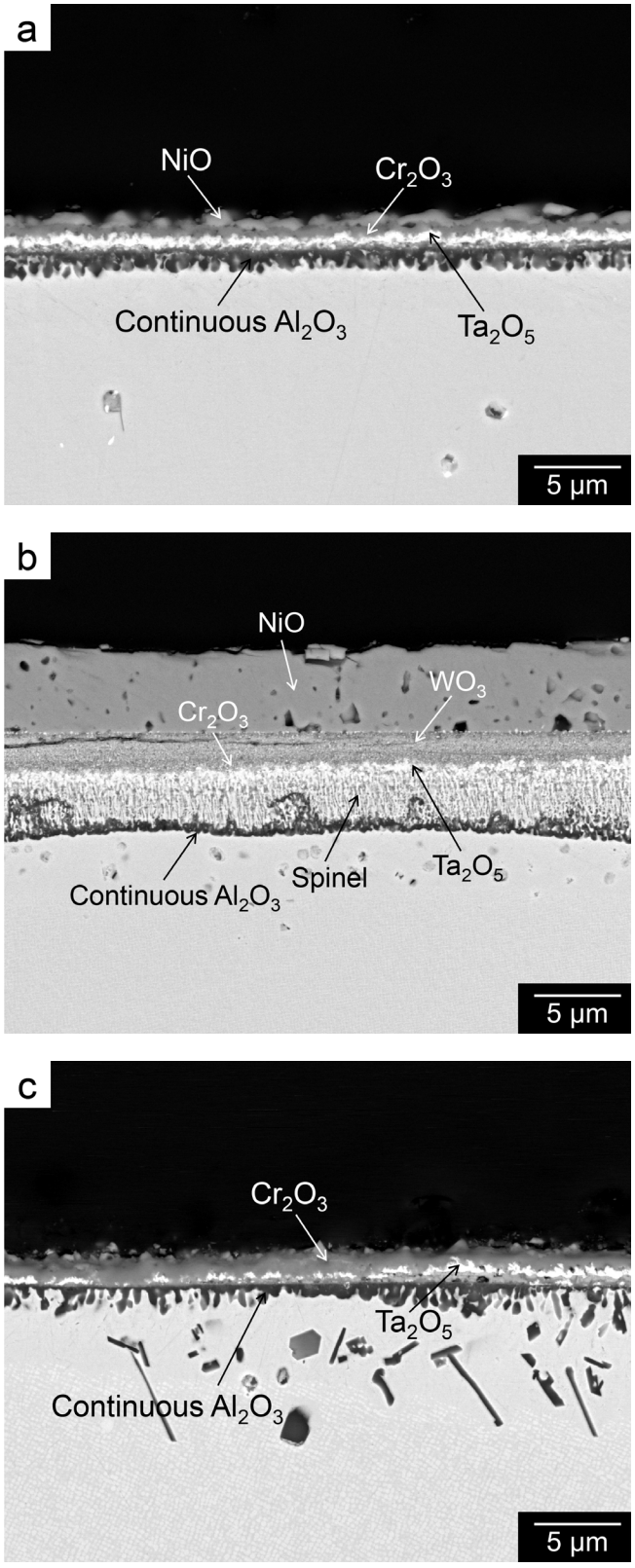

Figure 4.19: Microstructures of cross-sections of oxidized superalloys after 10 hours exposure at 1000°C, (a) ABD-1, (b) ABD-2, (c) ABD-3.

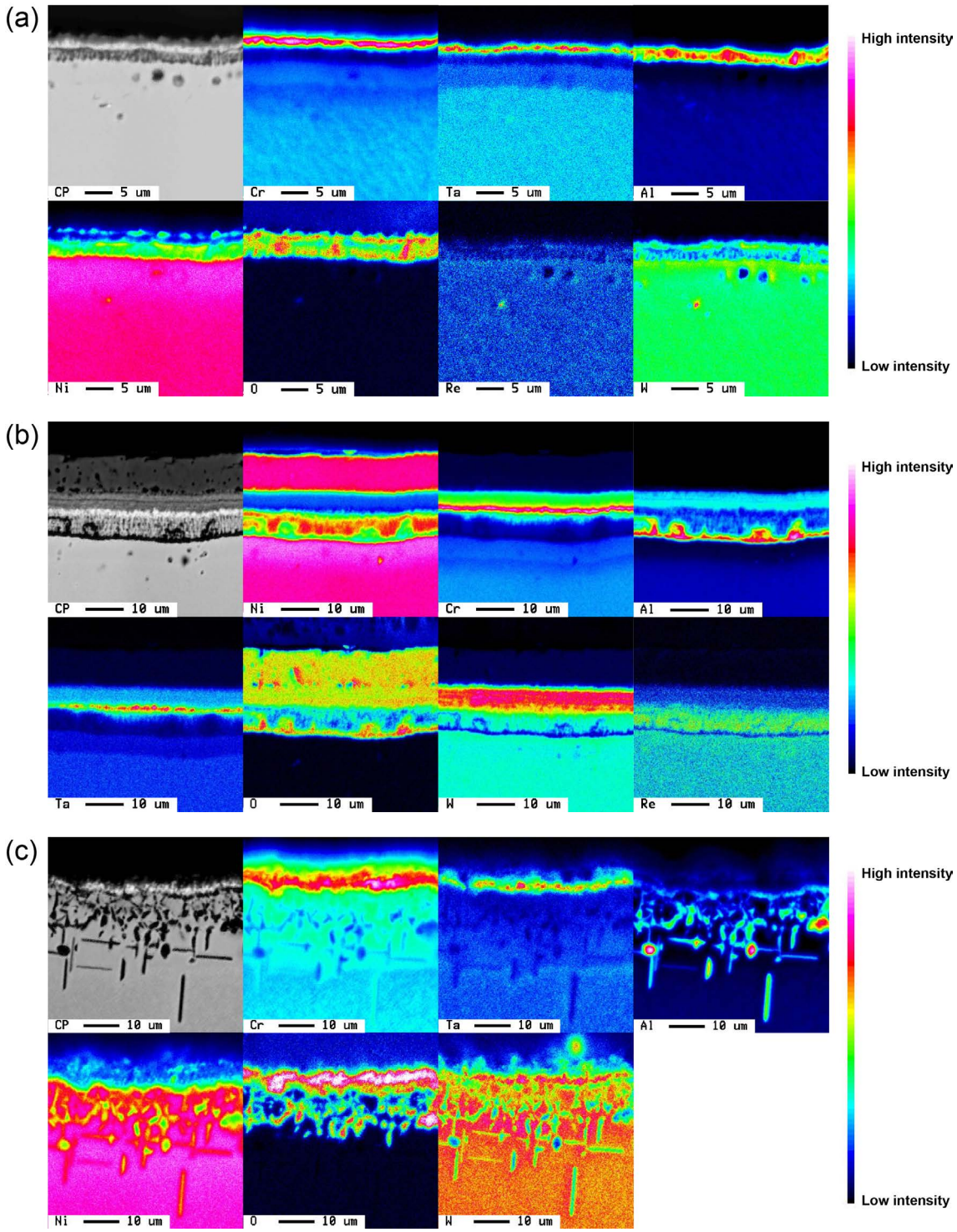

Figure 4.20: EPMA chemical mapping of oxidized superalloys after 10 hours exposure at 1000°C, (a) ABD-1, (b) ABD-2, (c) ABD-3.

138A and STAL-15/PWA1484, which are taken from various sources [98, 29, 99, 100].

The creep performance of ABD-1 is found to be comparable to CMSX-4 for the stress range beyond 400 MPa but is somewhat inferior at the lower stress range when testing times are generally longer. One explanation is that the alloy is still somewhat metallurgically unstable, despite being designed to be otherwise. To test this hypothesis, further interrupted creep tests were carried out at 900°C/400MPa and 1050°C/135MPa for 300 hours, and the structures examined for TCP phase formation. SEM images are shown in Figure 4.23. At 900°C, ABD-1 has an almost fully rafted structure with a few long needle-shape bright particles, consistent with the morphology observed in [11], see Figure 4.23(a). When examining the 1050°C test, a large number of small TCP particles were found, see Figure 4.23(b), and some parts of the rafted structure had already broken up, further contributing to the short rupture life.

ABD-2 exhibits better creep resistance than alloy TMS-138A within the higher stress range. However, TCP phases formation again becomes important in the low stress/high temperature regime where ABD-2 is somewhat inferior to it. The situation is thus somewhat similar to that for ABD-1. The findings for both ABD-1 and ABD-2, taken together, suggest that TCP phases formation should be controlled very carefully for any pursuit of high level of creep resistance. Tighter tolerances and/or more accurate models are needed and their application is likely to lead to improved creep properties. This is discussed further in Section 4.7.1.

Concerning the IGT alloy ABD-3, it is located on the right of the newly designed STAL-15 alloy; its creep properties are therefore somewhat superior to it although not quite as good as PWA1483 which of course does not display such good environmental resistance. It shows considerable promise for IGT applications.

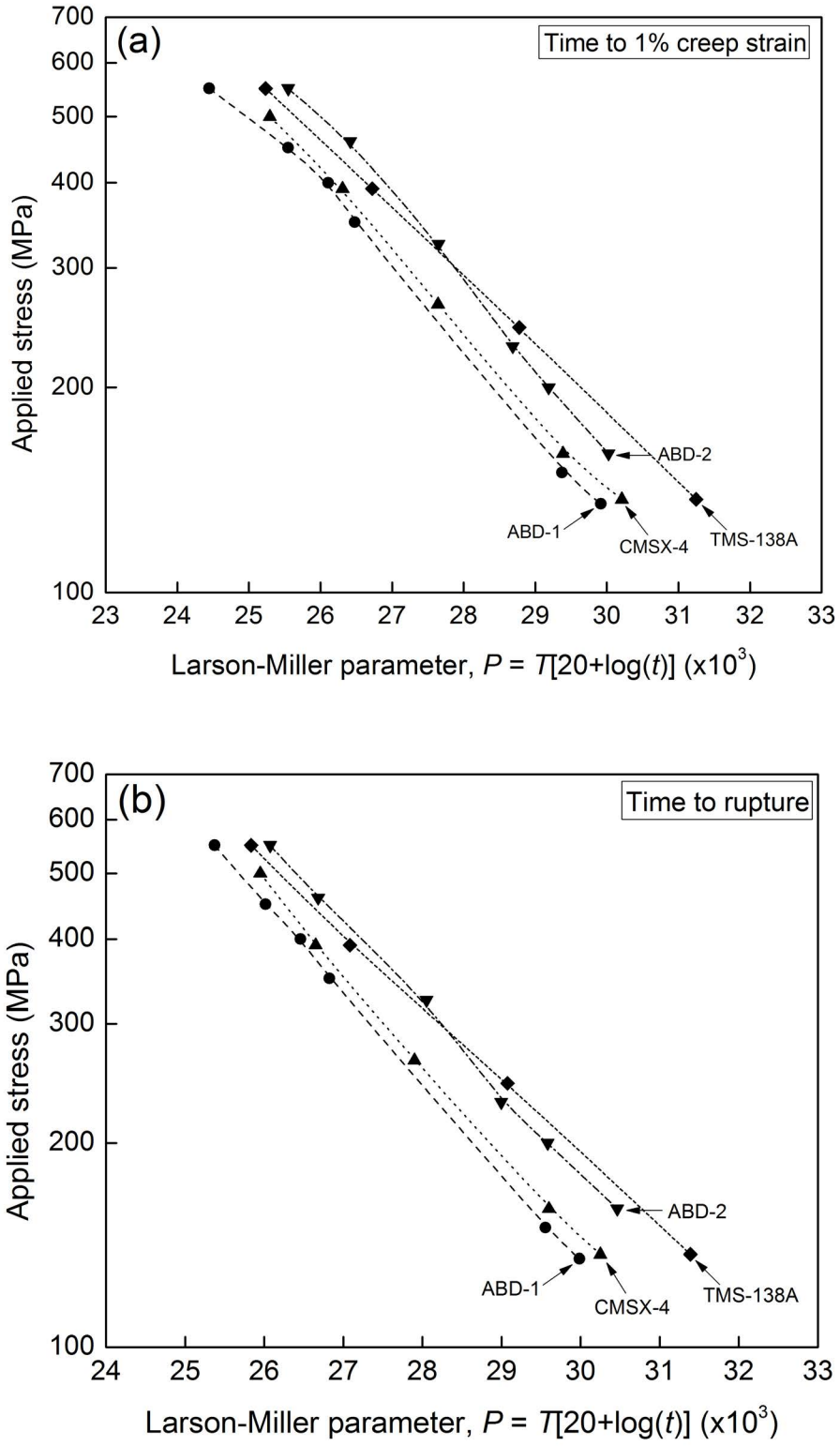

Figure 4.21: Larson-Miller curves of ABD-1 and 2 for time to 1% strain and rupture life.

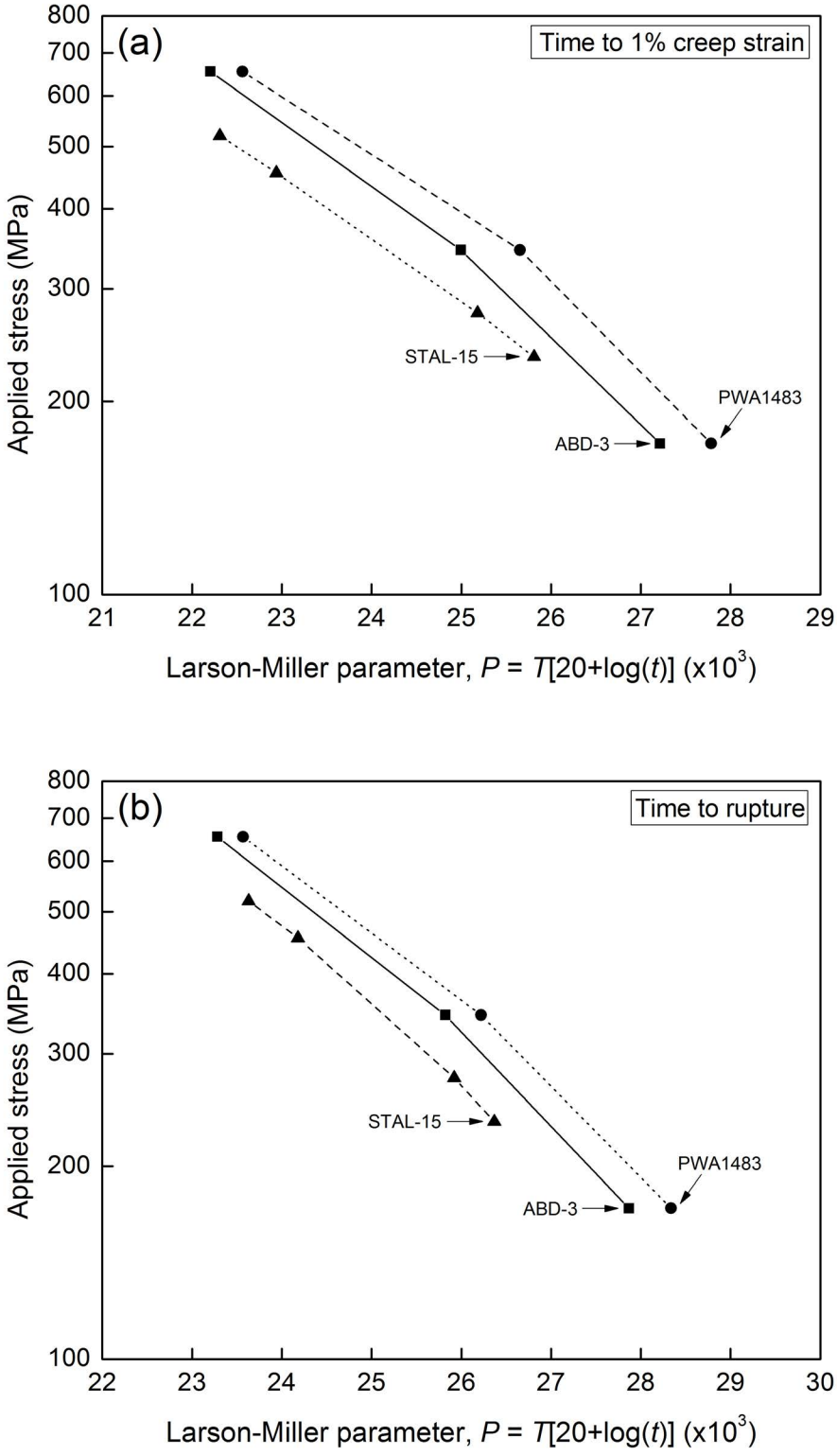

Figure 4.22: Larson-Miller curves of ABD-3 for time to 1% strain and rupture life.

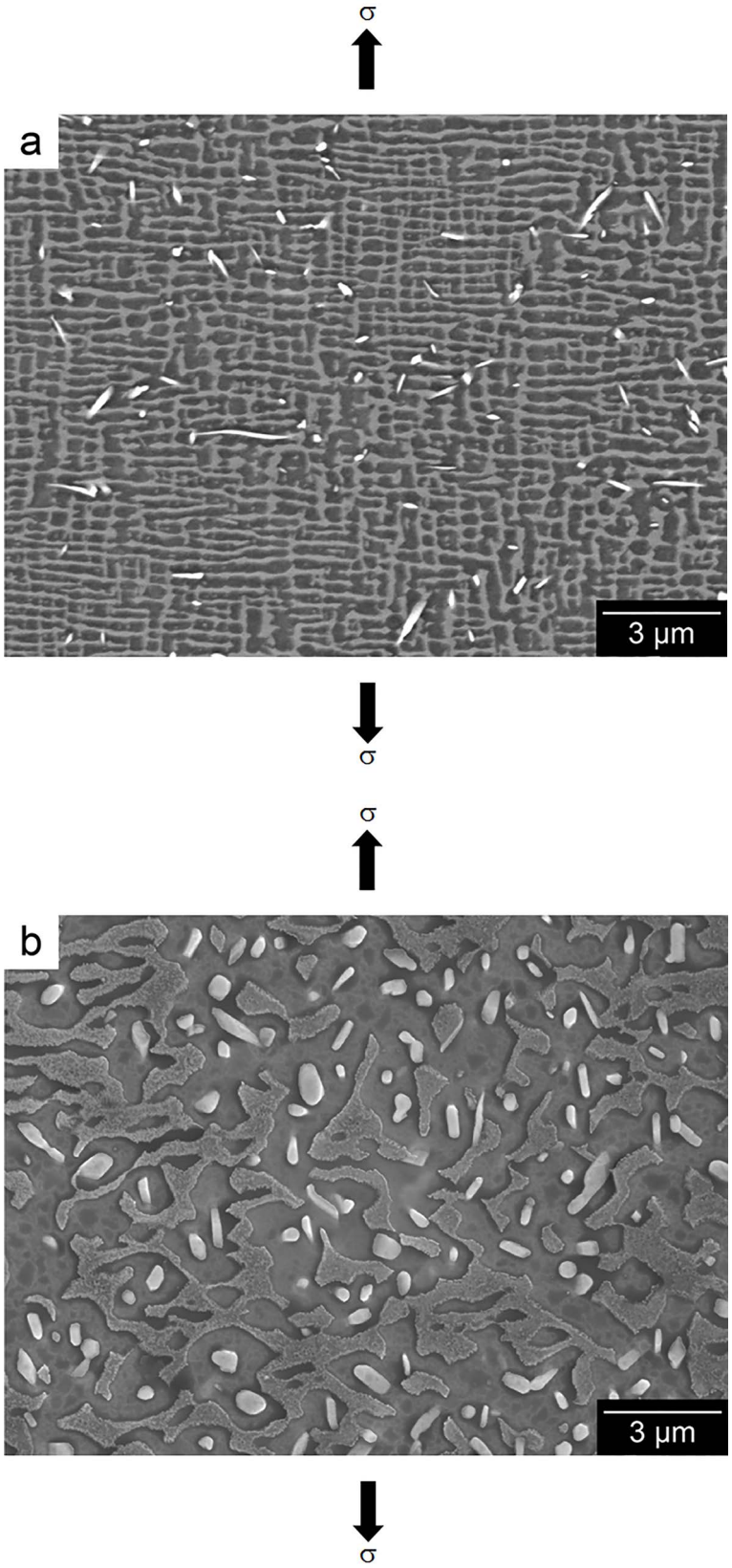

Figure 4.23: Microstructures of interrupted creep tests of ABD-1, (a) 900°C/400MPa, (b) 1050°C/135MPa.

4.7 Discussion: Future Direction for Alloy Design

Lessons can be learned from the results presented above. Moreover, design requirements for gas turbine engines continue to evolve as operating conditions get ever more demanding. Some comments are now made in this regard.

4.7.1 Design of alloys for better microstructural stability

In the design methods used above, the tendency of TCP phases formation is evaluated by the average energy level of the d-orbital, which has been termed the new PHACOMP method [101]. Using this approach, a limit is placed on the Md value which can be tolerated before the alloy is deemed unstable. In the present work, one must state that either (i) the limiting value of Md employed was not strict enough, or alternatively (ii) the theory is unacceptably crude, so that it is not accurate enough. This situation warrants further consideration.

Recently, Seiser [102] has proposed a novel two-dimensional structure map which takes account of both the valence d-band electron concentration (as for new PHACOMP) but also size-factor effects. Detailed considerations using electron theory indicated that further electronegativity effects were unlikely to be important [103]. In Seiser's approach, the equations for the two coordinates are given as

$$\overline{N} = \sum_i c_i N_i \tag{4.11}$$

$$\overline{\Delta V/V} = \sum_{i,j} |V_i - V_j| \,/\, [(V_i + V_j)\,/2] \tag{4.12}$$

where N_i is the average electron vacancy number of element i, c_i is the concentration of element i and V_i is the atomic volume of element i. It seems likely that the structure map approach might be useful when TCP phase precipitation is to be

avoided.

Here we follow Seiser but use the Md number on the abscissa rather than the PHACOMP number N; as before the average volume difference $\overline{\Delta V/V}$ is used on the ordinate. Calculations are carried out on the 106920 alloy Ni-Cr-Co-Re-W-Al-Ta ABD-1 database of Section 4.4.1, for illustrative purposes. Calculations are also carried out using the CALPHAD database, to predict the susceptibility to TCP phase formation and thus TCP-prone and TCP-free regions. Consider Figure 4.24(a), which is a histogram illustrating the statistical distribution of alloys on the basis of computed Md number. The two smaller distributions are sub-sets of the larger one, divided on the basis of whether the CALPHAD predictions indicate TCP instability or not. Only below a limiting Md value of about 0.90 are the Md and CALPHAD calculations totally consistent. Above this value, alloys of identical Md value can be found to be predicted by CALPHAD to be either stable or unstable, implying that a cut-off value for Md for instability is over-simplistic. Figure 4.24(b) shows the corresponding two-dimensional structure map ($\overline{\mathrm{Md}}$, $\overline{\Delta V/V}$) which takes into account the size effect. It can be seen that both of the figures display a very large overlapping region where the possibility of TCP phase formation cannot be clearly confirmed either way. Interestingly, Figure 4.24(a) and Figure 4.24(b) show a high degree of correlation: Md correlates with $\overline{\Delta V/V}$ but not completely. Figure 4.24(b) indicates that resistance to TCP instability is greatest when $\overline{\Delta V/V}$ is lowest.

The following illustrates how the two-dimensional structure map may be utilised. Consider the 106920 alloy Ni-Cr-Co-Re-W-Al-Ta ABD-1 database of Section 4.4.1 once again. Applying the constraints of γ' phase volume fraction, density, lattice misfit and oxidation resistance once again, the database is reduced to a size of 2611 alloys. Thereafter, only alloys predicted by CALPHAD to be TCP-free are kept and further elimination is carried out to remove those alloys with lower M_{creep} than CMSX-4 (6.97×10^{15} m^{-2}s). The totality of these conditions results in 38 alloys remaining in the dataset; their compositions are summarized in Table 4.8.

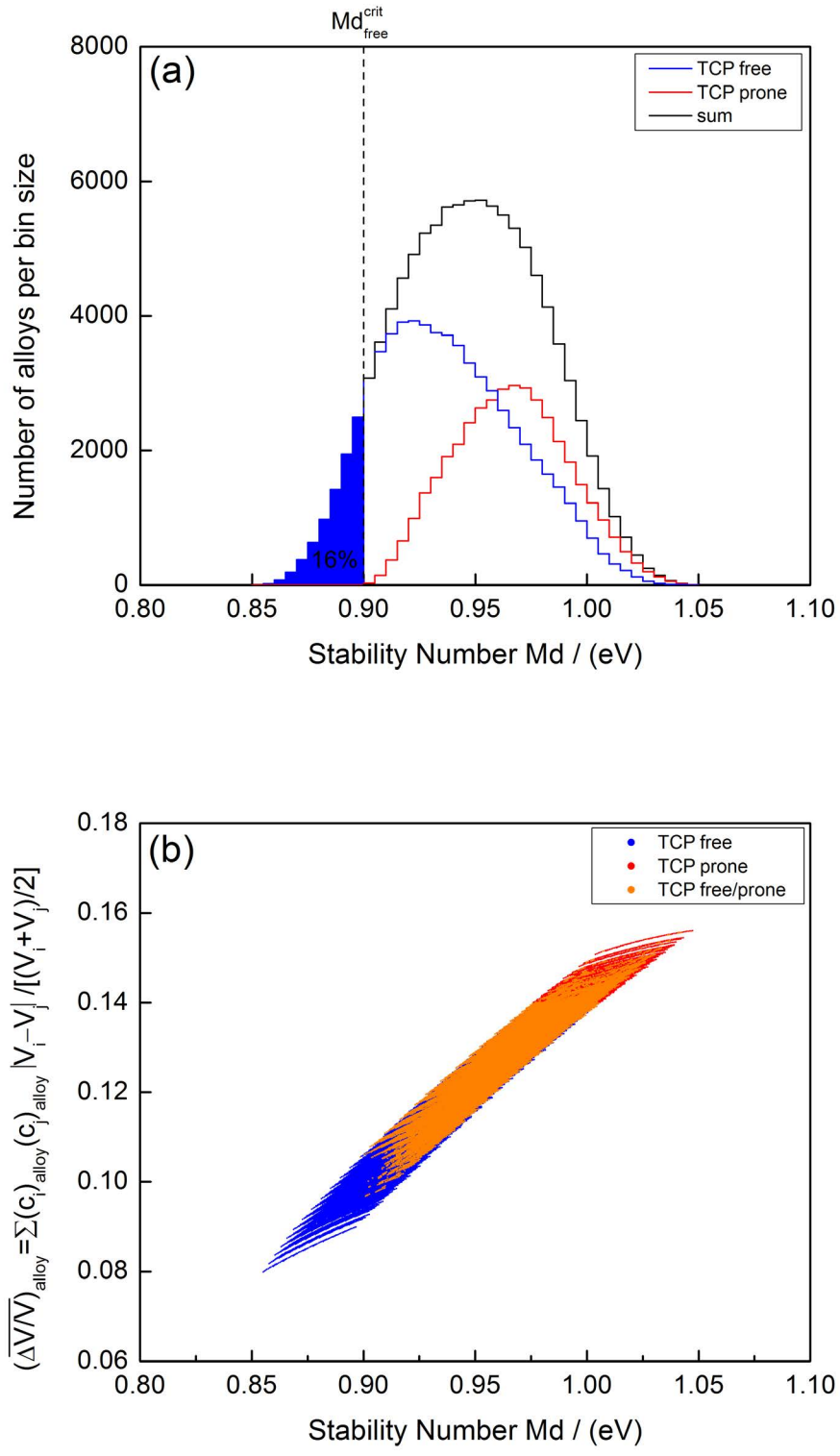

Figure 4.24: (a) Histogram of 106920 alloys in Ni-Cr-Co-Re-W-Al-Ta system showing statistic spread of alloys that are TCP-prone or TCP-free as a function of their corresponding Md values. (b) Structure map ($\overline{\text{Md}}$, $\overline{\Delta V/V}$) of 106920 alloys in Ni-Cr-Co-Re-W-Al-Ta system.

Table 4.8: The 38 compositions selected in ABD-1 design system for improvement design of TCP susceptibility.

No.	Alloy Number	Cr	Co	W	Al	Ta	Re	Ni	Density(g/cm^3)
0.990 < Md < 1.000									
1	46404	7	9	8	6	7	5	Bal	8.90
2	47484	7	10	8	6	7	5	Bal	8.90
3	58168	8	9	7	6	8	3	Bal	8.78
4	58283	8	9	8	6	7	4	Bal	8.84
5	59248	8	10	7	6	8	3	Bal	8.78
6	69928	9	9	6	6	8	3	Bal	8.72
7	70048	9	9	7	6	8	3	Bal	8.76
8	71008	9	10	6	6	8	3	Bal	8.72
9	81684	10	9	5	6	7	5	Bal	8.71
10	81808	10	9	6	6	8	3	Bal	8.70
11	82888	10	10	6	6	8	3	Bal	8.70
12	90324	11	6	5	6	7	5	Bal	8.69
13	91404	11	7	5	6	7	5	Bal	8.69
14	92484	11	8	5	6	7	5	Bal	8.69
15	93564	11	9	5	6	7	5	Bal	8.69
0.980 < Md < 0.990									
1	46397	7	9	8	6	6	4	Bal	8.82
2	47358	7	10	7	6	6	5	Bal	8.82
3	47478	7	10	8	6	6	5	Bal	8.87
4	57082	8	8	7	6	7	3	Bal	8.74
5	59118	8	10	6	6	6	5	Bal	8.76
6	59122	8	10	6	6	7	3	Bal	8.70
7	59238	8	10	7	6	6	5	Bal	8.80
8	59242	8	10	7	6	7	3	Bal	8.74
9	59243	8	10	7	6	7	4	Bal	8.79
10	64518	9	4	6	6	6	5	Bal	8.74
11	65598	9	5	6	6	6	5	Bal	8.74
12	69922	9	9	6	6	7	3	Bal	8.68
13	71002	9	10	6	6	7	3	Bal	8.68
14	78438	10	6	5	6	6	5	Bal	8.68
15	93443	11	9	4	6	7	4	Bal	8.60
Md < 0.980									
1	32238	6	7	7	6	6	5	Bal	8.84
2	32358	6	7	8	6	6	5	Bal	8.89
3	33318	6	8	7	6	6	5	Bal	8.84
4	46277	7	9	7	6	6	4	Bal	8.77
5	47238	7	10	6	6	6	5	Bal	8.78
6	47357	7	10	7	6	6	4	Bal	8.77
7	56838	8	8	5	6	6	5	Bal	8.71
8	65478	9	5	5	6	6	5	Bal	8.69

Now the two dimensional structure map Figure 4.25 can be constructed to examine these 38 alloys. Two dashed lines are also plotted to give the threshold values of $\overline{\Delta V/V}$ and Md relevant to the CMSX-4 alloy. A total of 14 alloys are located in the quadrant corresponding to values of both Md and $\overline{\Delta V/V}$ smaller than the values for CMSX-4. For illustrative purposes, we set the threshold of $\overline{\Delta V/V}$ and Md to be 0.14 and 0.99eV, which give rise to 23 alloys remaining. Like the previous refinement calculations, the concentrations of elements Re, Ru, W, Al and Ta are refined within a resolution of 0.2 wt.%, resulting in calculations for a further 14375 alloys. In order to select a good creep resistant alloy, the criterion for the creep merit index is set to be 7.5×10^{15} $m^{-2}s$, which is beyond the CMSX-4 level (6.97×10^{15} $m^{-2}s$). After all these design constraints are applied, 14 alloys remain in the dataset, see Table 4.9. Their creep merit index and Md values are plotted in Figure 4.26. The dashed line indicates that only four alloys are located below the the Md level of CMSX-4. The one which shows the highest creep merit index is the best choice, Alloy 7; its composition is Ni-8Cr-10Co-3Re-7.2W-5.8Al-7Ta. Alloys isolated in this way – with the aid of the two-dimensional structure map and with additional input from CALPHAD – are worthy of further experimental study.

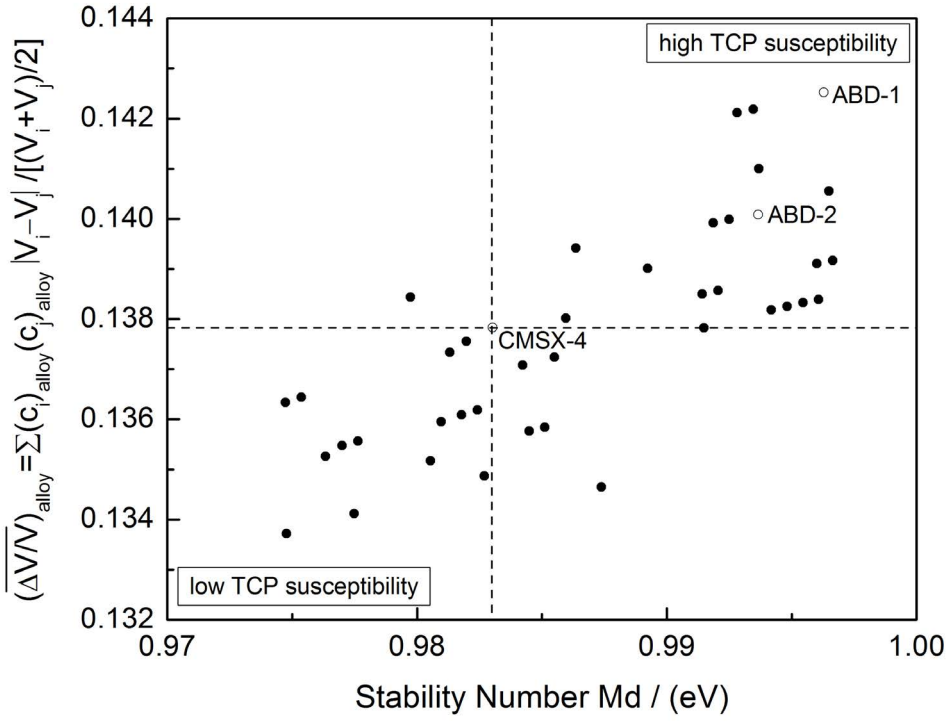

Figure 4.25: Structure map ($\overline{\mathrm{Md}}$, $\overline{\Delta V/V}$) of final selection 38 alloys for refinement design.

Table 4.9: The 14 compositions selected form refinement results.

No.	Alloy Number	Cr	Co	W	Al	Ta	Re	Ni	Density(g/cm^3)
1	4658	8	10	7	5.8	6.8	3	Bal	8.77
2	4663	8	10	7	5.8	7	3	Bal	8.78
3	4688	8	10	7	6	7	3	Bal	8.74
4	4693	8	10	7	6	7.2	3	Bal	8.75
5	4698	8	10	7	6	7.4	3	Bal	8.76
6	4783	8	10	7.2	5.8	6.8	3	Bal	8.78
7	4788	8	10	7.2	5.8	7	3	Bal	8.79
8	4793	8	10	7.2	5.8	7.2	3	Bal	8.80
9	4803	8	10	7.2	6	6.6	3	Bal	8.74
10	4808	8	10	7.2	6	6.8	3	Bal	8.75
11	4813	8	10	7.2	6	7	3	Bal	8.75
12	4818	8	10	7.2	6	7.2	3	Bal	8.76
13	4823	8	10	7.2	6	7.4	3	Bal	8.77
14	4933	8	10	7.4	6	6.8	3	Bal	8.75

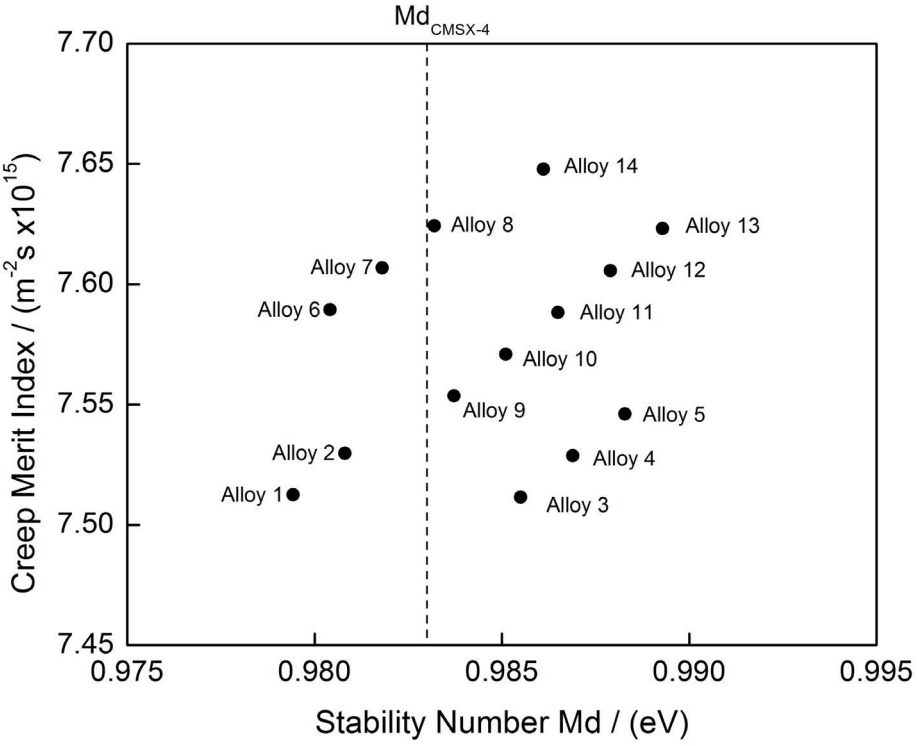

Figure 4.26: Scatter diagrams (Creep Merit Index vs. Md values) for final selected 14 alloys.

4.7.2 Design of alloys for low density

The creep strength of the nickel-based single crystal superalloys has improved markedly over recent years; this has been achieved by increasing the content of refractory alloying elements, particularly of Re, W and Ta, whose contributions to high temperature strengthening are now very much better understood. However, such alloying has caused the relatively density of the alloys to increase markedly towards 9.0 and beyond; excessive loads are then placed on the rims of turbine discs. This explains the recent interest in lower-density alloys, see for example [104]. One can argue that the relative balance of creep and density needed is shifting such that lower density alloys without the very best creep resistance might be more appropriate for these applications.

One might therefore reconsider the design considerations above to reflect this. Consider the ABD-1 alloy designed in Section 4.4.1. Calculations for the sensitivity of the creep merit index and density can be made to changes in the alloying content, by ± 1 wt.%. The results are summarised in Figure 4.27, with vectors identified to confirm the influence of altering the concentration of each alloying element. One can see that Al and Re are found to exert the strongest influence on the creep performance/density ratio. Re additions are significantly beneficial for creep performance but it also brings about a significant increase in density. Al addition confers a dramatic decrease of density; this might provide the best strategy for lowering the density, provided that higher γ' contents can be tolerated.

The compositional factors that influence the properties of creep and density can be studied further within the dataset for ABD-1. Consider Figure 4.28, a scatter diagram plotted for alloys with 60-70% γ' volume fraction, consistent with the original compositional design space. The data fall into two distinct sub-groups owing to the resolution of 1 wt% used for the calculations; consistent with the above, it is the Al concentration which confers this effect. Thus higher content of Al tends

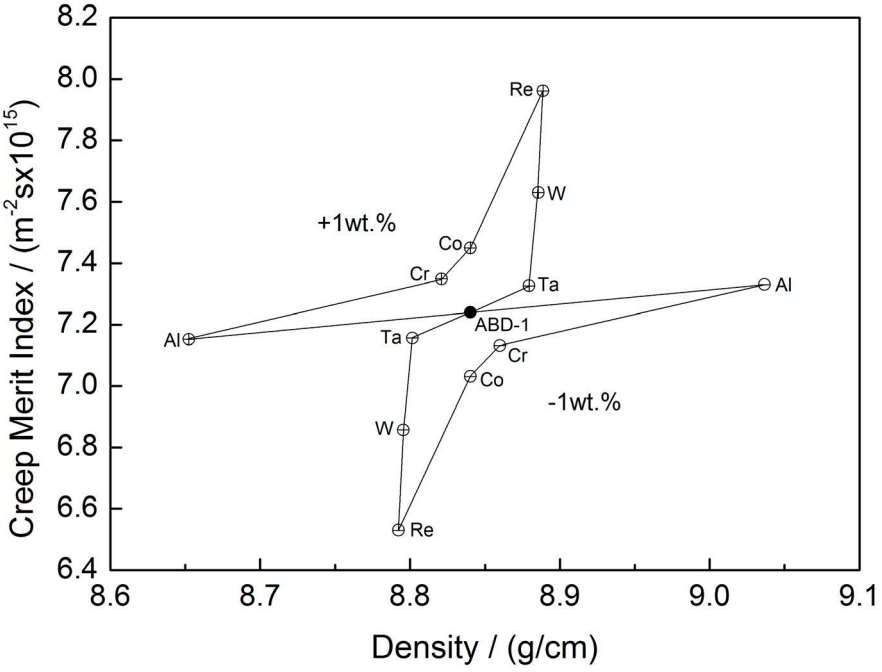

Figure 4.27: The effect of altering alloying element concentration on properties of creep and density.

to give lower density alloys. It is also confirmed that Re content increases from the bottom left to top right, which provides the alloy more creep strength.

To illustrate what might be done to isolate a low density alloy and moreover to illustrate the very lowest density alloy possible, isolation procedures were carried out with constraints of density lower than 8.4 g/cm^3 and predicted creep resistance similar to CMSX-4 level. This provides 41 alloys in total, whose position are marked on Figure 4.28. Further calculations were applied to the 41 alloys, by improving the resolution of the calculations to 0.2 wt.% for Re, Ru, W, Al and Ta, resulting in a further 25625 new compositions for calculation. A final composition can be isolated from this refined dataset. Design constraints on microstructural and density as before reduce the total number of alloys to 8919. Different levels of Md value (less than 1, 0.99 and 0.98eV) lessen the dataset further to 5386, 2602 and 931 alloys respectively. To ensure the stability of the designed alloy, its final composition is

selected from the lowest Md value dataset, at minimum density. This procedure gives an alloy of composition Ni-8Cr-10Co-5.4Re-3.4W-7Al-3.6Ta. It is predicted to have density 8.39g/cm^3 and creep merit index 7.44×10^{15} m^{-2}s, superior to CMSX-4. Future work should test the properties of this alloy which we believe to be optimal.

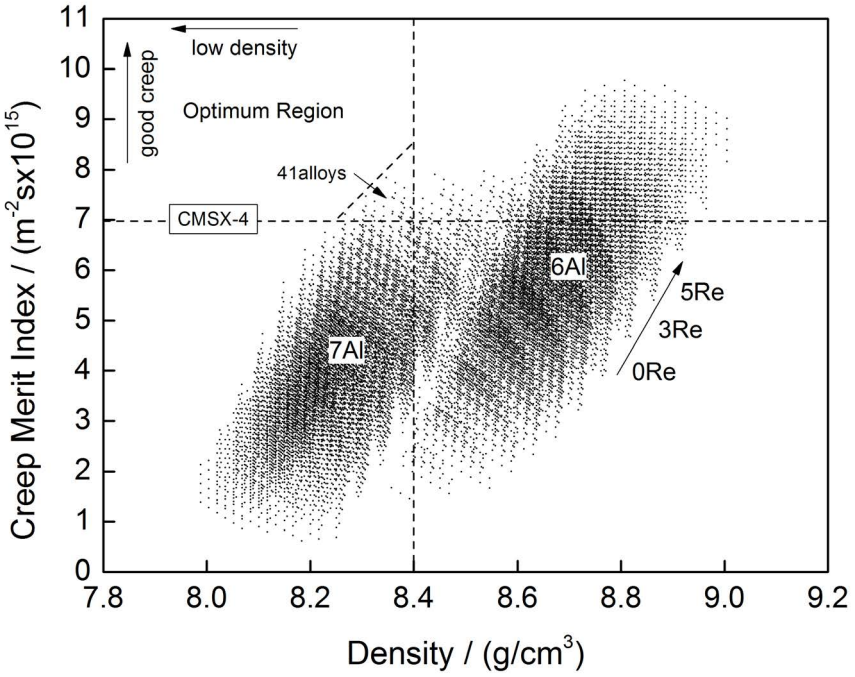

Figure 4.28: Mapping of creep merit index vs. density for alloys with 60-70% γ' volume fraction.

4.8 Summary and Conclusions

The following conclusions can be drawn from this work:

1. A theory-based modelling method has been described which allows the compositions of new grades of single crystal superalloy to be isolated. There is no recourse needed to empirical methods or statistical analysis of experimental information such as creep curves or oxidation weight gain data.

2. The isolation of optimal chemical compositions is carried out by eliminating –

from initial, trial compositional spaces – alloys which have unacceptable microstructural characteristics. Unsuitable microstructural architectures (γ' precipitate fraction, γ/γ' misfit) and insufficient stability with respect to the precipitation of topologically close-packed (TCP) phases are considered grounds for rejection from the initial composition space.

3. Next, compositions are ranked on the basis of their anticipated performance in creep and oxidation; estimation of their density and cost are also made at this point. Due to the computational cost, simplified merit indices are used for this purpose. Once again, unacceptable alloys are discounted on the basis of their mechanical behaviour, environmental performance and physical properties.

4. Remaining compositions represent acceptable compositions – they pass the design constraints – and are ranked/sorted on the basis of their properties. Optimal compositions can then be chosen on the basis of best properties and/or combinations of these.

5. To prove the effectiveness of this new approach, the compositions of three new single crystal superalloys have been isolated. The alloys have been prepared by investment casting methods. An acceptable balance of creep and oxidation behaviour is found to be displayed at minimal density and cost; the performance of existing grades of superalloy are approached, matched or exceeded in some important respects.

6. The work emphasises that there is no one alloy composition which is optimal for all applications; trade-offs exist between the important properties: creep versus density, creep versus oxidation, creep versus cost for example. Thus, for any given application, compromises need to be made and accounted for at the design stage. This is one further advantage of the modelling approach proposed: these trade-offs can be studied on a quantitive basis.

7. It seems likely that the methods used for the prediction of TCP precipitation can be improved; procedures by which this can be accomplished are suggested. In this way, new TCP-resistant compositions have been proposed for future experimental testing.

Chapter 5

Mapping of Alloy Design Space for Single Crystal Superalloys

5.1 Summary

The multicomponent composition space pertinent to the single crystal nickel-based superalloys is mapped and searched, using computational modelling. A resolution of 0.1 wt.% for the alloying elements is assumed, consistent with manufacturing practice. Databases are constructed of alloy compositions which are predicted to be of promising microstructural architecture: e.g. equal fractions of the γ and γ' phases. These may be regarded as maps – one might term them genomes – of this class of structural alloy. By combining the databases with additional composition-dependent property models, it is demonstrated that compositions can be identified which – subject to the accuracy and limitations of the sub-models – are likely to prove optimal, e.g. on the basis of their creep resistance, density and cost. The methods circumvent the need for the traditional empirically-driven approaches to alloy design.

5.2 Introduction

The alloy design procedures proposed in Chapter 4 have demonstrated rich possibilities for manipulating microstructure of nickel-based single crystal superalloy by altering their compositions. A typical compositional space considered in Chapter 4 has elements such as Cr, Co, Al, Ta, Re, W, and well as Ni (balance) present. With defined upper and lower bounds for each alloying element, one can expect $\sim 10^6$ compositions in total at a resolution of 1 wt.%. However, to match the industrial manufacturing standard, it becomes necessary to improve the calculation accuracy to a resolution of 0.1 wt.%, in which case current compositional spaces would be expanded dramatically. A number of $\sim 10^{12}$ alloys in total can be generated, which is obviously beyond the current computational limit for thermodynamic calculations in Thermo-Calc software.

Therefore, a numerical algorithm is proposed in this chapter, to identify all possible alloys within this class which possess the necessary microstructural architecture. By using this, the thermodynamic calculations in total can be reduced to a reasonable range. Then from this list, alloys are selected which are predicted to have an optimum property or optimised set of properties. A unique feature of this work is then the mapping of the necessary alloy design space – for the first time – to identify a list of alloys from which optimised ones can be chosen. Such an approach represents a new paradigm in the search for superalloys with the very best properties.

5.3 Computational Modelling: The Challenge and Approach Taken

The single crystal superalloys display at least two characteristics which need to be taken into account. First, they display a well-known 'brick and mortar' microstruc-

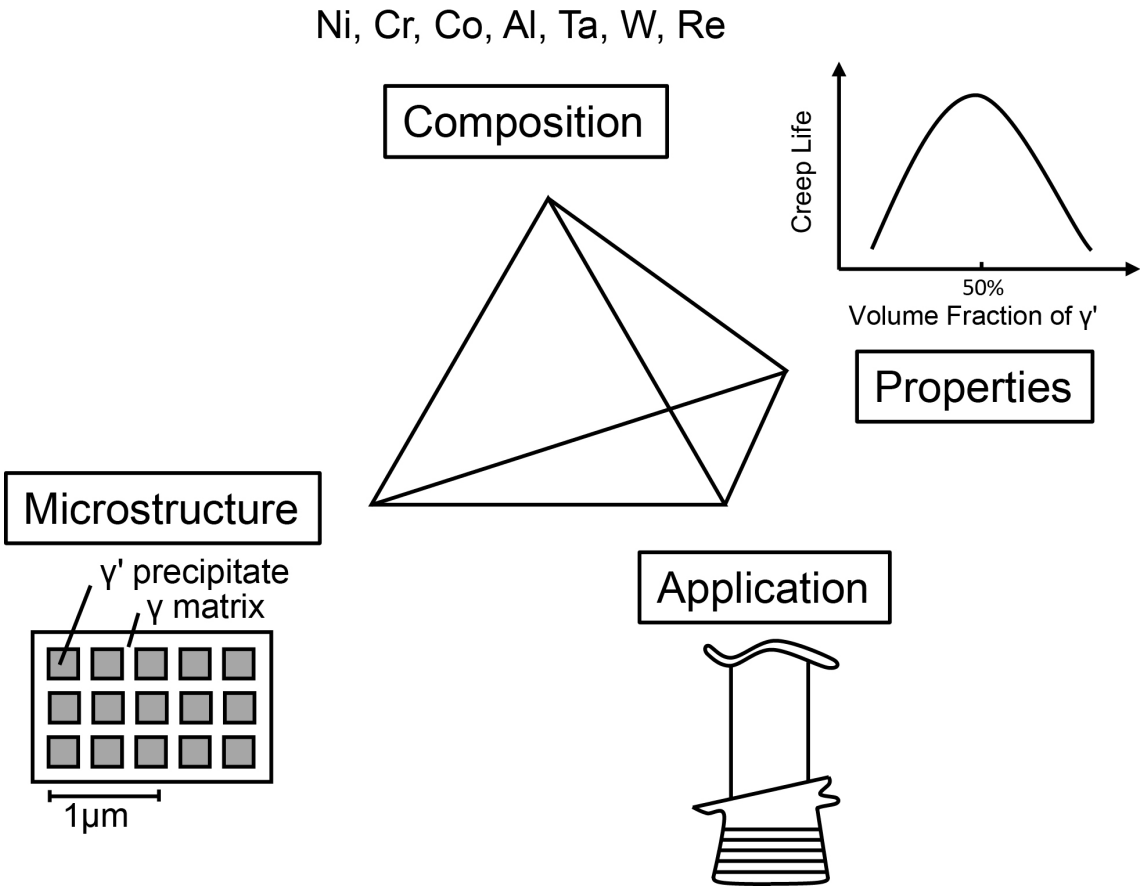

Figure 5.1: Illustrations of composition-microstructure-property relationships in nickel-based single crystal superalloys.

ture consisting of cuboidal precipitates of the $L1_2$ phase – known as γ' – embedded within a face centred cubic (FCC) matrix [10]. The arrangement of precipitate and matrix are often remarkably regular. Properties – for example in creep and fatigue – are found to be well balanced when the proportion of the γ' phase is approximately 50% [9, 105], so that an equi-molar mixture of the two phases is present. Second, a considerable degree of alloying complexity is possible, due to the possible addition of elements such as Al, Ta, Cr, Co, W and Re. Figure 5.1 provides a schematic illustration of the composition-microstructure-property relationships in single crystal superalloys.

The above allows a grand challenge to be posed. For this metallurgical system, can the entire alloy space be mapped so that compositions likely to prove promising

are identified? Consistent with the above, one could identify all compositions for instance which are predicted to display an equi-molar mixture of the γ and γ' phases. A database of all compositions estimated to have optimal microstructure might be thought of as the genome of this metallurgical system [106, 107]. Clearly, it is of interest to construct it. But at what resolution? Since components made of the single crystal superalloys are usually fabricated using investment casting, it seems sensible to appeal to the accuracy of compositional control which is considered practical for this manufacturing method: of order 0.1 wt% for each of the alloying elements. The challenge posed therefore is to find all compositions conferring the requisite microstructure, to this resolution.

In what follows, all calculations have been carried out using in-house FORTRAN computer codes coupled the software Thermo-Calc version 3.1 via the TQ-interface version 8.0 [108]. The associated thermodynamic database used is TCNI6 [109]. Calculations are carried out at 900°C, which is close to the service temperature for these materials. The hardware used is a Intel(R) Xeon(R) CPU E5-2687W 3.10GHz processor. The calculations reported in Section 5.3 for ternary and quaternary systems are carried out on a desktop machine. In Section 5.4, dataset was separated into several segments and calculated over a high performance cluster of 32 cores.

5.3.1 Example of Ternary System: Ni-Al-Cr

To illustrate the approach taken, consider the calculated ternary Ni-Al-Cr phase diagram at 900°C [108, 109], see Figure 5.2(a); one notes however our approach is quite general and can be readily extended to other systems. The portion shown contains γ (Ni-based solid solution), γ' (Ni_3Al), β (NiAl) and α (Cr-based solid solution). The compositions which confer a 50%-50% mixture of the γ and γ' phases reside in the γ+γ' two phase region. An enlarged view of the γ+γ' region is given in Figure 5.2(b); the tie-lines are also shown which intersect the two single phase

Table 5.1: Numbers of possible combinations for given alloying elements and resolutions, which indicate the numbers of compositions in their corresponding alloy systems.

	Number of alloying elements				
Resolution (wt.%)	2	3	4	5	6
1	$\sim 10^3$	$\sim 10^5$	$\sim 10^6$	$\sim 10^7$	$\sim 10^9$
0.1	$\sim 10^5$	$\sim 10^8$	$\sim 10^{10}$	$\sim 10^{12}$	$\sim 10^{15}$
0.01	$\sim 10^7$	$\sim 10^{11}$	$\sim 10^{14}$	$\sim 10^{17}$	$\sim 10^{21}$
0.001	$\sim 10^9$	$\sim 10^{14}$	$\sim 10^{18}$	$\sim 10^{22}$	$\sim 10^{27}$

fields of γ and γ'. Consistent with the laws of metallurgical thermodynamics, all alloys on a single tie-line have the same compositions of the two phases (γ and γ') but exhibit different proportions of them.

A first step involves the definition of an initial alloy design space at a given resolution. For an alloy system containing k alloying elements, the number of compositions in the alloy design space can be estimated by the combination equation

$$ {}^{n}C_k = \frac{n!}{(n-k)!k!} \tag{5.1} $$

where n represents the possible concentrations of each element. For example, one has n=99 if one assumes a resolution of 1 wt.% (a range of 1 to 99 wt.%). The numbers of calculations needed for this kind of approach are summarised in Table 5.1. One finds that as the number of alloying elements gets larger and the resolution finer, the computational effort needed becomes excessive. For instance, at a resolution of 0.1 wt.% a multicomponent alloy with six alloying elements contains $\sim 10^{15}$ compositions to be estimated. We have found that this already exceeds the loads of current computational capacity. However, carrying out calculations at coarser resolution, e.g. 1 wt.%, followed by more localised calculations at finer resolution makes the challenge tractable. This is the approach we have taken.

The second step is to determine whether appropriate equilibrium phases are

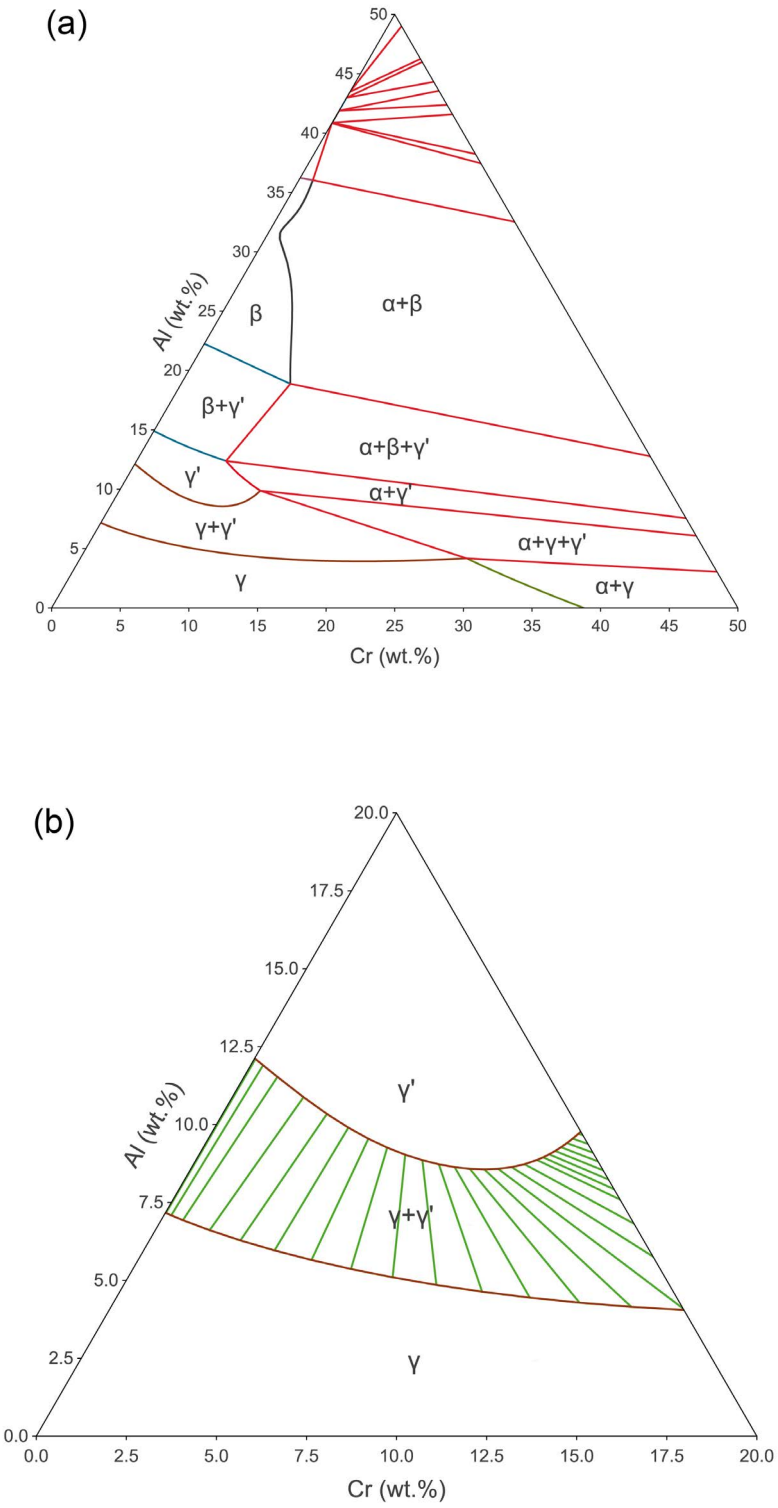

Figure 5.2: (a) Ni-Al-Cr ternary phase diagram at 900°C (generated by the Thermo-Calc software [108, 109]); (b) enlarged view of $\gamma+\gamma'$ region on which tie-lines are superimposed.

present for each composition, e.g. γ and γ'. Figure 5.3 provides a schematic illustration of all compositions in the Ni-Al-Cr ternary system, at the coarse 1 wt.% resolution. Compositions located in the γ and γ' two-phase region on the basis of the computed phases found are marked as black points in the figure; the white points fail this test. Thus the identification of compositions with both two phases presented is achieved by making a phase equilibrium calculation for each composition in the initial alloy design space, which gives the fractions of γ and γ', and their associated phase compositions. Unsatisfied compositions are eliminated so that remaining ones have mixture of γ and γ', denoted as the trial compositions x_i^{trial} in the following steps.

The third step involves adjusting the trial compositions along the tie-lines for the correct fractions of phases, e.g. 50% γ'. Detailed procedures in the Ni-Al-Cr ternary system are illustrated schematically in Figure 5.4. For each trial composition, the phase equilibrium calculation carried out previously has provided the compositions of the γ and γ' phases, so one can determine the atomic concentrations of elements Cr and Al in both phases, x_{Cr}^{γ}, x_{Al}^{γ}, $x_{\text{Cr}}^{\gamma'}$ and $x_{\text{Al}}^{\gamma'}$, respectively. These two coordinates (x_{Cr}^{γ},x_{Al}^{γ}) and ($x_{\text{Cr}}^{\gamma'}$,$x_{\text{Al}}^{\gamma'}$) then define the tie-line (shown as the dashed line) for this trial composition. Therefore, the adjusted compositions which have 50% γ', denoted as x_i^{correct}, are given by

$$x_{\text{Cr}}^{\text{correct}} = x_{\text{Cr}}^{\gamma}(1-\phi_{\gamma'}) + x_{\text{Cr}}^{\gamma'}\phi_{\gamma'} \tag{5.2}$$

$$x_{\text{Al}}^{\text{correct}} = x_{\text{Al}}^{\gamma}(1-\phi_{\gamma'}) + x_{\text{Al}}^{\gamma'}\phi_{\gamma'} \tag{5.3}$$

where $\phi_{\gamma'}$ is the mole fraction of γ' phase and in this case $\phi_{\gamma'}$=0.5. These considerations confirm that the spacing between the compositions x_i^{correct} depends on (i) the width of the two phase region (the number of two phase compositions lying within it), and (ii) the topology of the $\gamma/(\gamma+\gamma')$ and $\gamma'/(\gamma+\gamma')$ phase boundaries.

In the fourth step, a further algorithm has been introduced to map out the

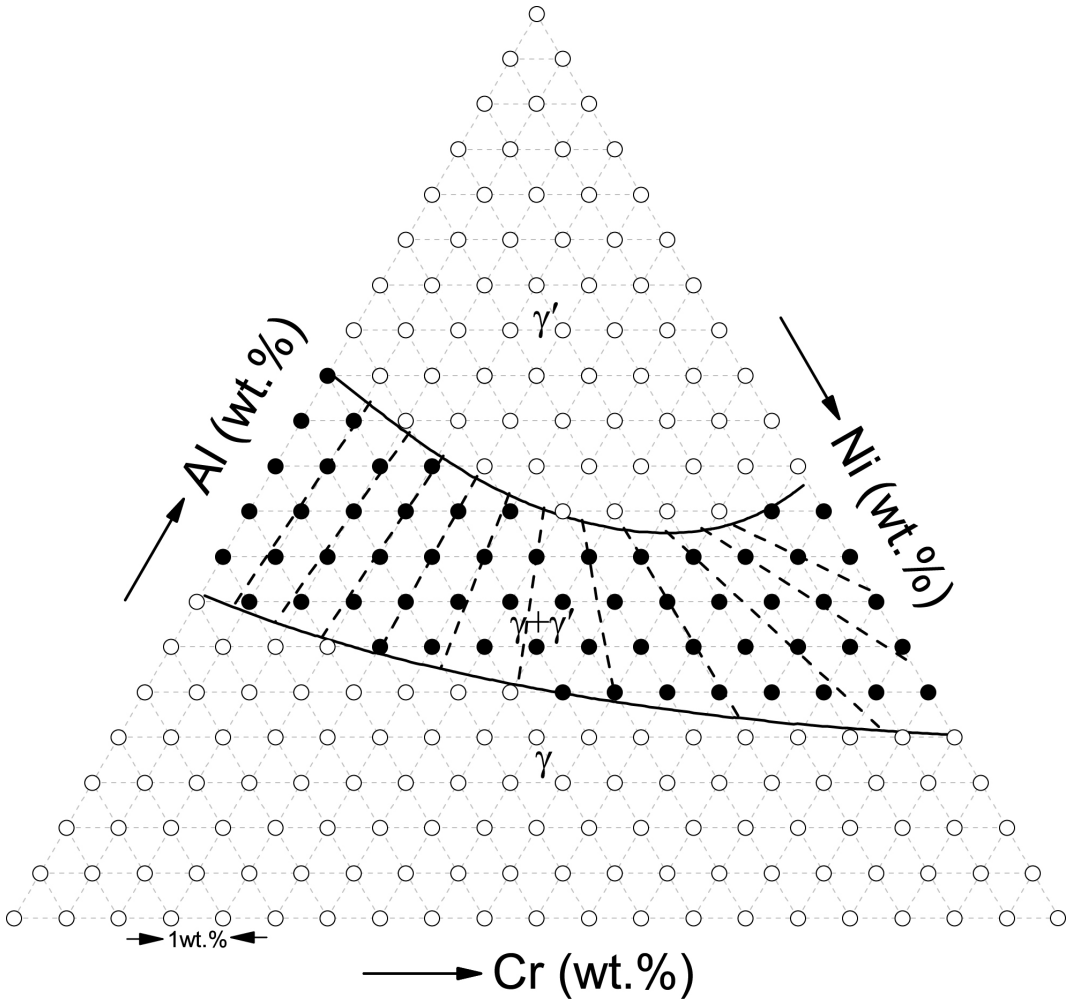

Figure 5.3: Schematic illustration of all compositions in the Ni-Al-Cr ternary system, at a resolution of 1 wt.%. Trial compositions x_i^{trial} located in the γ and γ' two-phase region can be identified, shown as the black points. White points represent all the other compositions located in the single phase region, either γ or γ'. Also plotted are the corresponding tie-lines of some trial compositions.

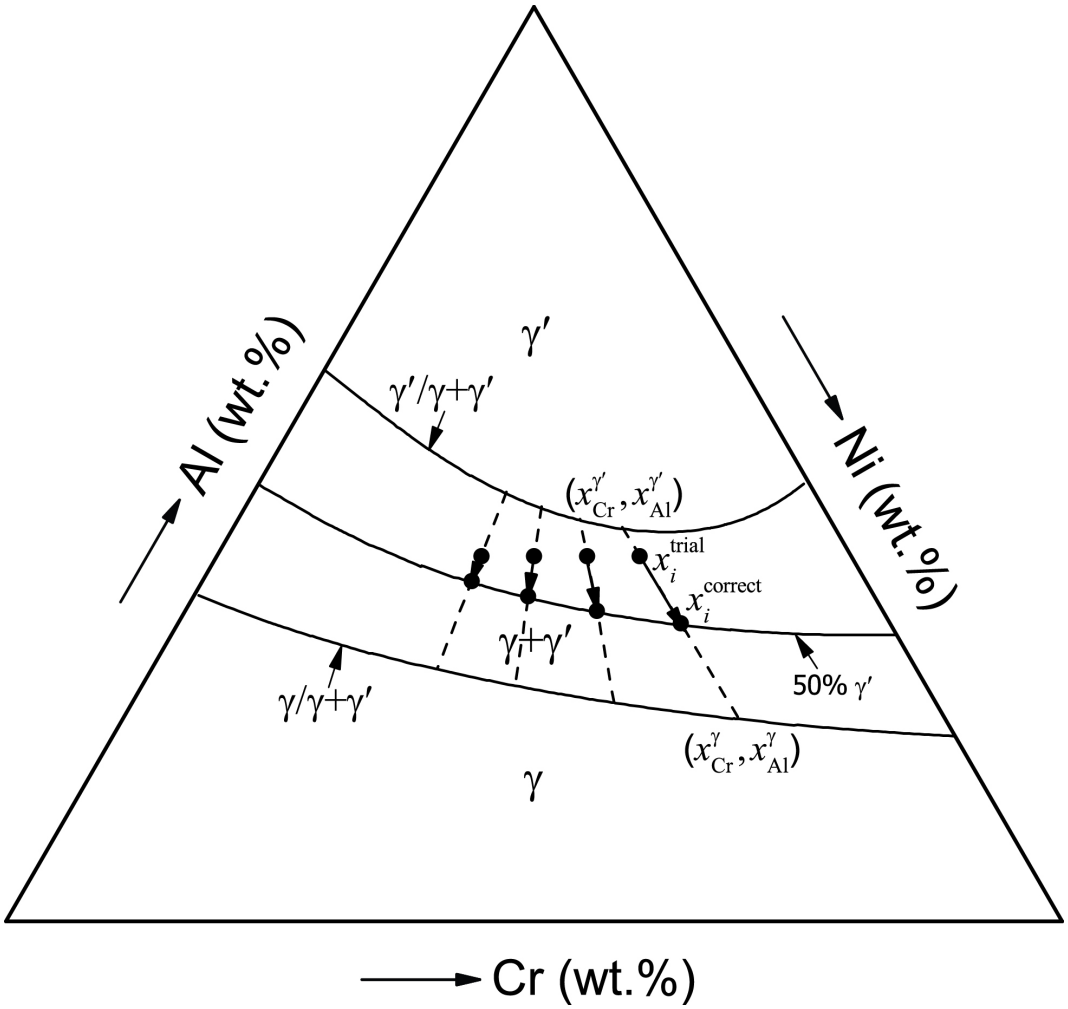

Figure 5.4: Schematic illustration of method to adjust the trial compositions along the γ/γ' tie-lines in the Ni-Al-Cr ternary system, for compositions with correct fractions of phases, x_i^{correct}.

compositions around each x_i^{correct}, to a finer resolution, e.g. 0.1 wt.%. One first defines the number of compositions needed to be mapped out between x_i^{correct} and x_{i+1}^{correct}, consistent with

$$N_i = \left\lceil \frac{x_{i+1}^{\text{correct}} - x_i^{\text{correct}}}{\Delta x_i} \right\rceil \tag{5.4}$$

The ceiling function $\lceil x \rceil$ takes the smallest integer not less than the calculated result. The term Δx_i represents the increment of mapping process. In the case of Ni-Al-Cr ternary system, the nature of the compositions x_i^{correct}, which are arranged on a single line in the phase diagram, indicates that there is only one direction each time when doing the mapping process, either Cr or Al. Therefore, to map the compositions that satisfy the criterion of a fixed phase fraction of γ', i.e. 50%, one appeals to the equation

$$df^{\gamma'} = \frac{\partial f^{\gamma'}}{\partial x_{\text{Cr}}} dx_{\text{Cr}} + \frac{\partial f^{\gamma'}}{\partial x_{\text{Al}}} dx_{\text{Al}} = 0 \tag{5.5}$$

where $\partial f^{\gamma'}/\partial x_{\text{Cr}}$ and $\partial f^{\gamma'}/\partial x_{\text{Al}}$ are partial derivatives with respect to Cr and Al. To use Equation 5.5, one should first estimate the derivatives numerically using finite differences, according to

$$\frac{\partial f^{\gamma'}}{\partial x_{\text{Cr}}} \approx \frac{\Delta f^{\gamma'}}{\Delta x_{\text{Cr}}} \tag{5.6}$$

$$\frac{\partial f^{\gamma'}}{\partial x_{\text{Al}}} \approx \frac{\Delta f^{\gamma'}}{\Delta x_{\text{Al}}} \tag{5.7}$$

Mapping can be first performed along the Cr direction, as illustrated schematically in Figure 5.5. For a given dx_{Cr}, one can calculate the unknown Al change, dx_{Al}, by

the equation

$$dx_{\mathrm{Al}} = \frac{-\dfrac{\partial f^{\gamma'}}{\partial x_{\mathrm{Cr}}}}{\dfrac{\partial f^{\gamma'}}{\partial x_{\mathrm{Al}}}} dx_{\mathrm{Cr}} \tag{5.8}$$

It is shown in Figure 5.5 that when the Cr concentration of the mapped composition is larger than that of the next correct composition $x_{i+1}^{\mathrm{correct}}$, the mapping process can be repeated by using $x_{i+1}^{\mathrm{correct}}$. This algorithm ensures that every single composition x_i^{correct} will be scanned, so that the complete alloy design space required can be mapped without missing any compositions. Alternatively, the Al direction can be used for mapping; the unknown Cr change, dx_{Cr}, can be calculated by equation

$$dx_{\mathrm{Cr}} = \frac{-\dfrac{\partial f^{\gamma'}}{\partial x_{\mathrm{Al}}}}{\dfrac{\partial f^{\gamma'}}{\partial x_{\mathrm{Cr}}}} dx_{\mathrm{Al}} \tag{5.9}$$

One should notice that the derivatives used for mapping will not be accurate when the mapped compositions are far away from the one started, as shown in Figure 5.5; thus the mapped compositions gradually deviate from the line of 50% γ'. Therefore, extra equilibrium calculations can be introduced after mapping over a certain number of compositions, in order to calibrate the compositions to have precisely 50% γ'. But this is at the expense of further computational cost.

5.3.2 Extension to Quaternary and Multicomponent Systems

The method can be extended to quaternary systems, for example Ni-Al-Cr-Ta. Figure 5.6 provides a schematic illustration of the quaternary phase diagram including the γ and γ' single phase regions. In the three dimensional space needed, the phase boundaries defining the limits of the single phase regions are two curved surfaces,

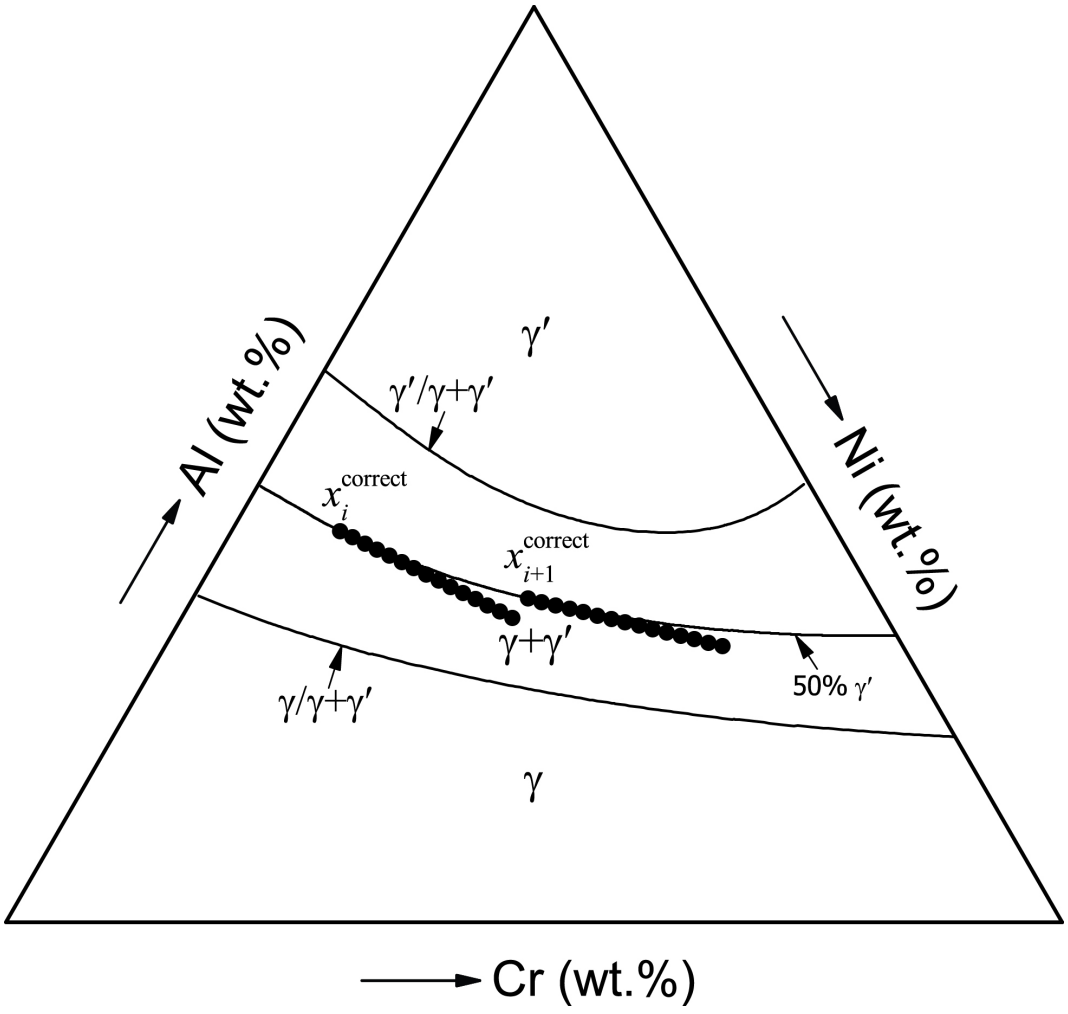

Figure 5.5: Schematic illustration of mapping compositions between x_i^{correct} and x_{i+1}^{correct} in the Ni-Al-Cr ternary system.

and the compositions corresponding to 50% γ' lie on a further surface between the two. The first two steps for mapping the required alloy design space in the Ni-Al-Cr-Ta system are carried out as before: the initial alloy design space is defined and the trial compositions identified. The third step adjusts the trial compositions along the tie-lines for 50% γ'. As illustrated in Figure 5.6, the two coordinators which define the tie-line for each composition in the Ni-Al-Cr-Ta system are given as (x^{γ}_{Cr},x^{γ}_{Al},x^{γ}_{Ta}) and ($x^{\gamma'}_{\mathrm{Cr}}$,$x^{\gamma'}_{\mathrm{Al}}$,$x^{\gamma'}_{\mathrm{Ta}}$). They can be calculated by

$$x^{\mathrm{correct}}_{\mathrm{Cr}} = x^{\gamma}_{\mathrm{Cr}}(1-\phi_{\gamma'}) + x^{\gamma'}_{\mathrm{Cr}}\phi_{\gamma'} \tag{5.10}$$

$$x^{\mathrm{correct}}_{\mathrm{Al}} = x^{\gamma}_{\mathrm{Al}}(1-\phi_{\gamma'}) + x^{\gamma'}_{\mathrm{Al}}\phi_{\gamma'} \tag{5.11}$$

$$x^{\mathrm{correct}}_{\mathrm{Ta}} = x^{\gamma}_{\mathrm{Ta}}(1-\phi_{\gamma'}) + x^{\gamma'}_{\mathrm{Ta}}\phi_{\gamma'} \tag{5.12}$$

In the fourth step, more considerations are needed due to the extra complexity of the quaternary systems. The compositions expected to be mapped out around each correct composition x_i^{correct} will form a part of the surface corresponding to 50% γ'. Therefore, in order to map this surface, one needs two mapping directions each time. The details of the mapping process in the Ni-Al-Cr-Ta quaternary system are illustrated schematically in Figure 5.7. For each x_i^{correct}, the two directions could be, for example, Cr and Ta. The number of compositions needed to be mapped out between x_i^{correct} and $x_{i+1}^{\mathrm{correct}}$ can be calculated by the equation

$$N_i = N_{i,\mathrm{Cr}} \times N_{i,\mathrm{Ta}} = \left\lceil \frac{x^{\mathrm{correct}}_{i+1,\mathrm{Cr}} - x^{\mathrm{correct}}_{i,\mathrm{Cr}}}{\Delta x_{i,\mathrm{Cr}}} \right\rceil \times \left\lceil \frac{x^{\mathrm{correct}}_{i+1,\mathrm{Ta}} - x^{\mathrm{correct}}_{i,\mathrm{Ta}}}{\Delta x_{i,\mathrm{Ta}}} \right\rceil \tag{5.13}$$

Consistent with what has been used for the ternary systems, one has an equation for the mapped compositions with fixed phase fractions of γ' given by

$$df^{\gamma'} = \frac{\partial f^{\gamma'}}{\partial x_{\mathrm{Cr}}} dx_{\mathrm{Cr}} + \frac{\partial f^{\gamma'}}{\partial x_{\mathrm{Al}}} dx_{\mathrm{Al}} + \frac{\partial f^{\gamma'}}{\partial x_{\mathrm{Ta}}} dx_{\mathrm{Ta}} = 0 \tag{5.14}$$

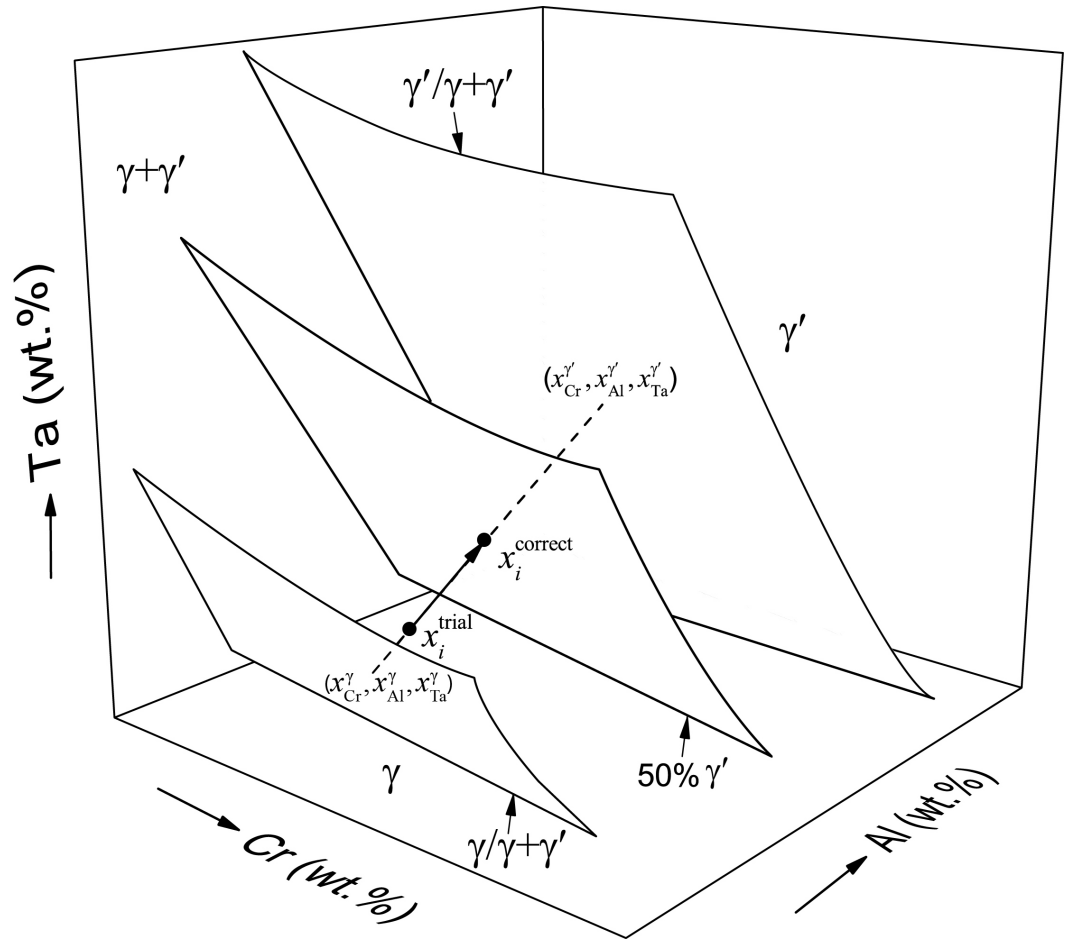

Figure 5.6: Schematic illustration of method to adjust the trial compositions along the γ/γ' tie-lines in the Ni-Al-Cr-Ta quaternary system.

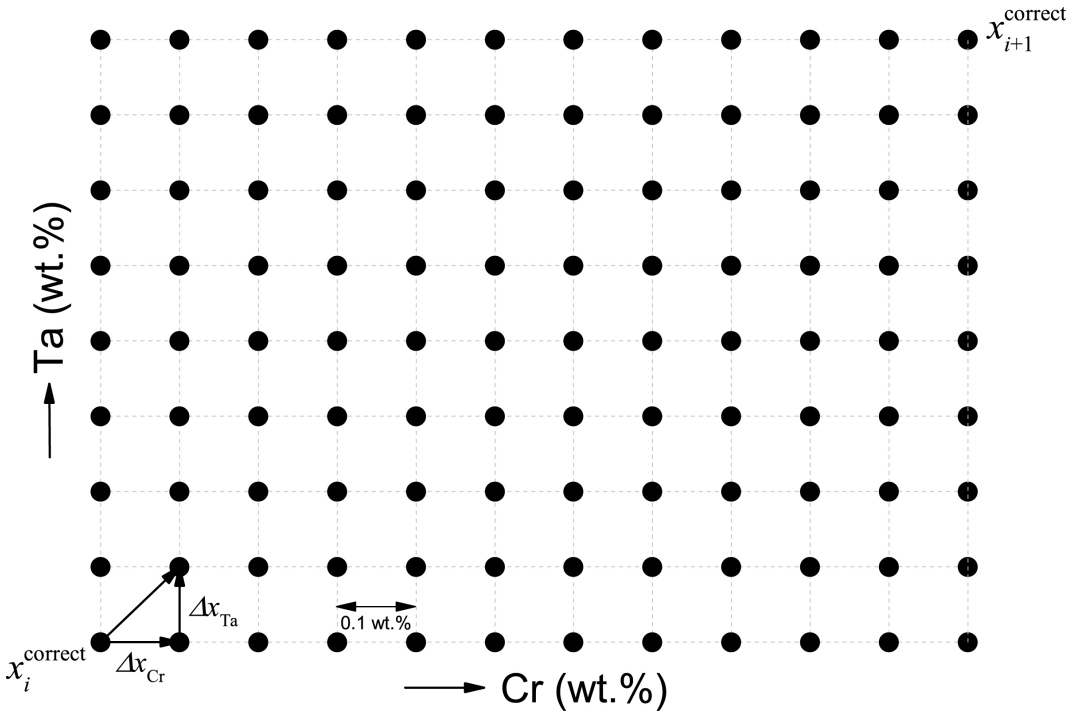

Figure 5.7: Schematic illustration of mapping compositions in the Ni-Al-Cr-Ta quaternary system. Two directions should be considered each time during mapping process.

The partial derivatives are now

$$\frac{\partial f^{\gamma'}}{\partial x_{\text{Cr}}} \approx \frac{\Delta f^{\gamma'}}{\Delta x_{\text{Cr}}} \tag{5.15}$$

$$\frac{\partial f^{\gamma'}}{\partial x_{\text{Al}}} \approx \frac{\Delta f^{\gamma'}}{\Delta x_{\text{Al}}} \tag{5.16}$$

$$\frac{\partial f^{\gamma'}}{\partial x_{\text{Ta}}} \approx \frac{\Delta f^{\gamma'}}{\Delta x_{\text{Ta}}} \tag{5.17}$$

Assuming the mapping directions from Cr and Ta, the unknown Al change can be calculated by the equation

$$dx_{\text{Al}} = \frac{-\left(\dfrac{\partial f^{\gamma'}}{\partial x_{\text{Cr}}} dx_{\text{Cr}} + \dfrac{\partial f^{\gamma'}}{\partial x_{\text{Ta}}} dx_{\text{Ta}}\right)}{\dfrac{\partial f^{\gamma'}}{\partial x_{\text{Al}}}} \tag{5.18}$$

For the quaternary system mentioned here, it is also possible to map compositions by using the directions Cr–Al or Al–Ta.

When the method is generalised to multicomponent systems, the equation set needed is summarised as

$$N_i = \prod_j \left\lceil \frac{x_{i+1,j}^{\text{correct}} - x_{i,j}^{\text{correct}}}{\Delta x_{i,j}} \right\rceil \tag{5.19}$$

$$x_{i,j}^{\text{correct}} = x_{i,j}^{\gamma}(1 - \phi_{\gamma'}) + x_{i,j}^{\gamma'}\phi_{\gamma'} \tag{5.20}$$

$$df^{\gamma'} = \sum_j \frac{\partial f^{\gamma'}}{\partial x_j} dx_j = 0 \tag{5.21}$$

$$\frac{\partial f^{\gamma'}}{\partial x_j} \approx \frac{\Delta f^{\gamma'}}{\Delta x_j} \tag{5.22}$$

where j represents the alloying element in multicomponent systems, which can be Al, Cr, Ta, et al. Several considerations can arise from the mapping process in multicomponent systems. In the first step, the number of compositions in the initial design space can potentially exceed the current computational limit. Assuming a multicomponent system which contains six alloying elements, the number of possible compositions in total at a resolution of 1 wt.% is ${}^{99}C_6 \approx 10^9$. This is far beyond the range for a feasible calculation that can be performed. Therefore, upper and lower concentration limits for each alloying element should be given in this stage. In the fourth step, the number of possible mapping directions and their corresponding combinations make it more complex for mapping process. For a system containing k alloying elements, the alloy design space required is now displayed in the form of a k-1 dimensional hypervolume. Therefore, one should perform k-1 mapping directions each time, in addition of k possible combinations.

Figure 5.8 summarises the algorithm which is proposed, and illustrates it schematically. It represents a viable method to map the alloy design space. When coupled with composition-dependent models, the databases so-produced can be searched for compositions predicted to exhibit the best properties or combinations of them. Examples are given in Section 5.3 and Section 5.4, in what follows.

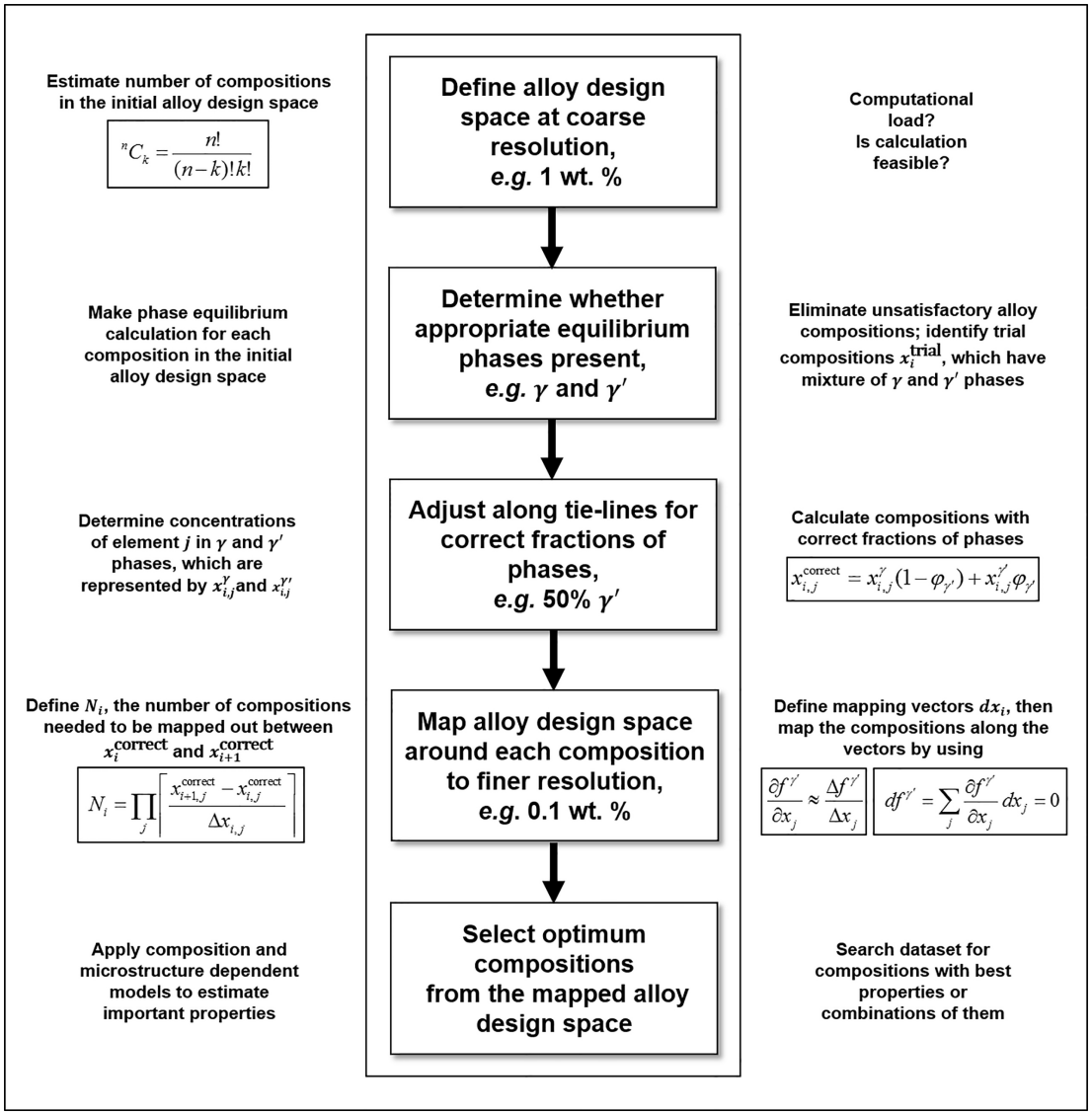

Figure 5.8: Procedures of mapping of an alloy design space.

5.4 Results

5.4.1 Ternary Systems Ni-Al-X: Identification of Alloys of Optimum Architecture

Quantitative results are given for the Ni-Al-Cr ternary system first. Calculations are carried out at a coarse resolution of 1 wt.%. The number of compositions in the initial alloy design space is ${}^{99}C_2 = \dfrac{99!}{(99-2)!2!} = 4851$. Applying the constraint to identify compositions which have mixture of γ and γ' two phases, the number of compositions in total is reduced to 93, see Figure 5.9. From here, further changes can be made by adjusting these trial compositions along the tie-lines, to obtain a group of correct compositions which have 50% γ', see Figure 5.10. It is of interest to calculate the spacings between these corrected compositions. The results are summarised in Figure 5.11. One can see that most of the compositions have spacings around 0.1 wt.%, but between some of them the spacings are not fine enough to match the ultimate resolution which is being aimed for. Therefore, the next step is to map the alloy design space to the final required resolution of 0.1 wt.%. In the Ni-Al-Cr ternary system, compositions can be mapped by using Cr direction and Al direction, respectively. Applications of these two directions result in a final mapped alloy design space containing 244 compositions, see Figure 5.12. One can examine the spacings between these final mapped compositions. Figure 5.13 confirms that the spacing between any two nearest compositions is no greater than $\sqrt{0.1^2 + 0.1^2} = 0.141$ wt.%, which proves that the complete alloy design space has been mapped as envisaged. It is also of interest to map compositions which correspond to different fractions of γ' phase, e.g. 60% and 70% in Figure 5.14. These compositions are represented by a series of lines in the γ+γ' region from the bottom up.

In Figure 5.15, results are given for a number of ternary systems, including Ni-Al-

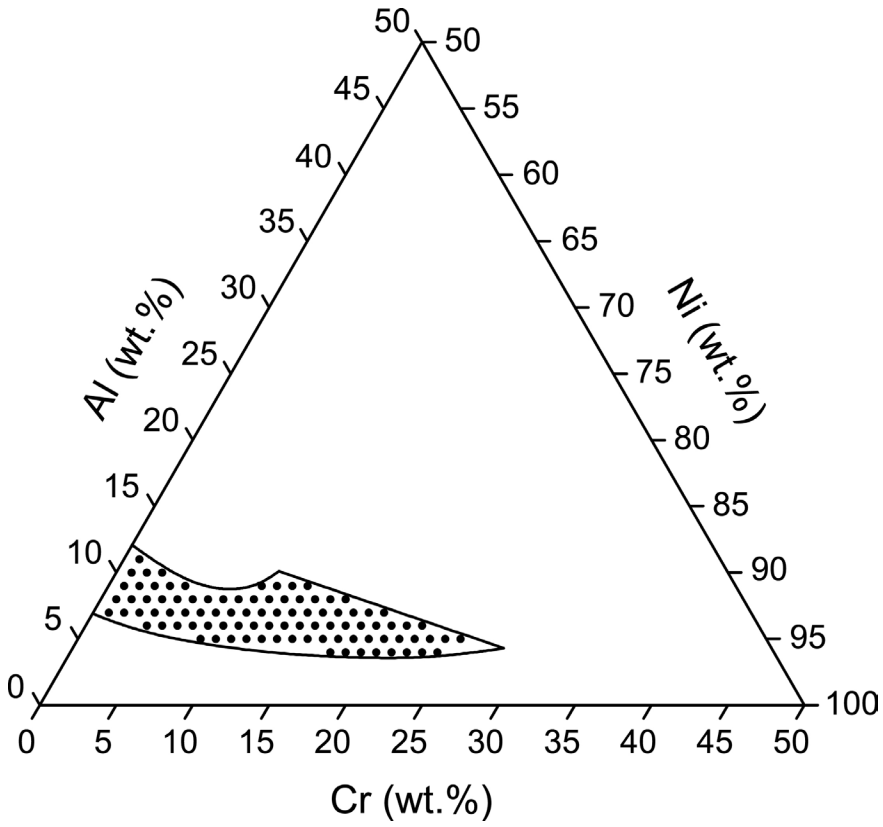

Figure 5.9: Trial compositions which have mixture of γ and γ' two phases in the Ni-Al-Cr ternary system.

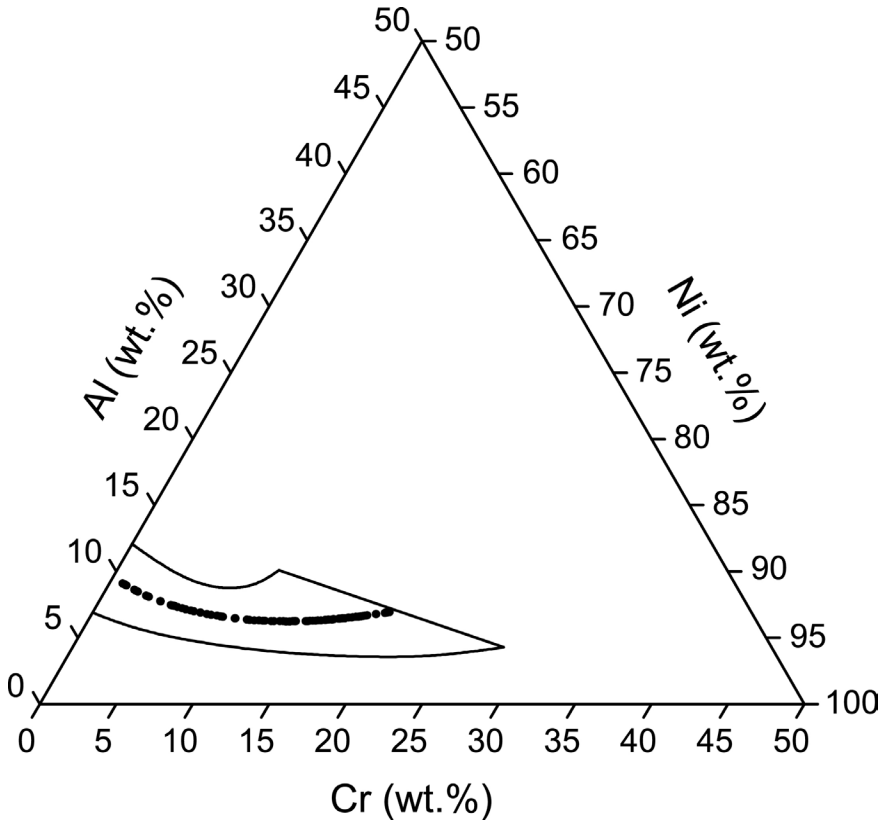

Figure 5.10: Correct compositions which have 50% γ' phase in the Ni-Al-Cr ternary system.

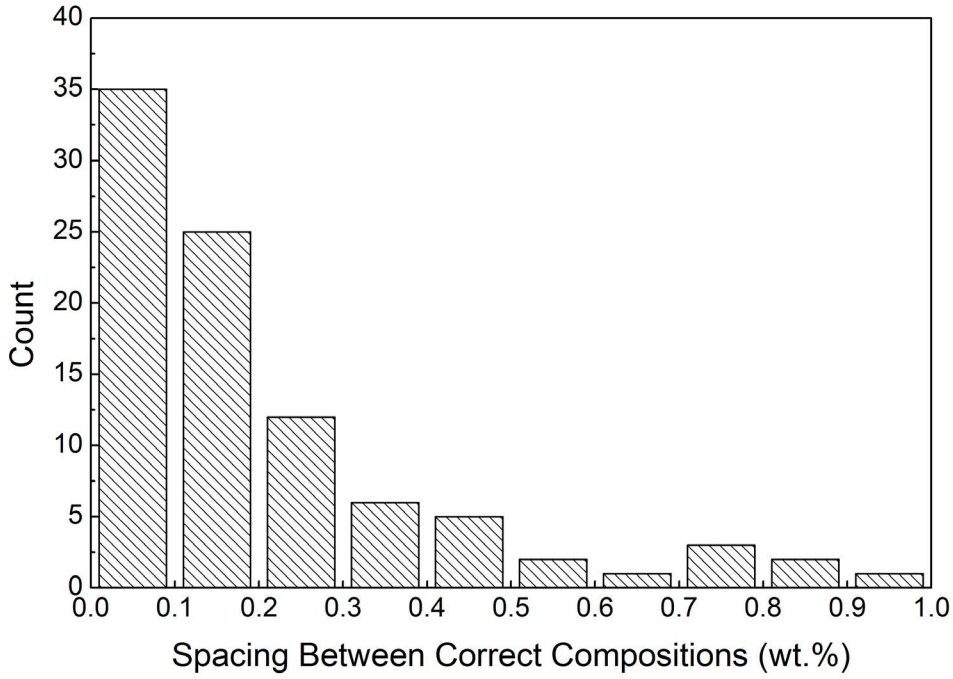

Figure 5.11: Spacing between correct compositions in the Ni-Al-Cr ternary system.

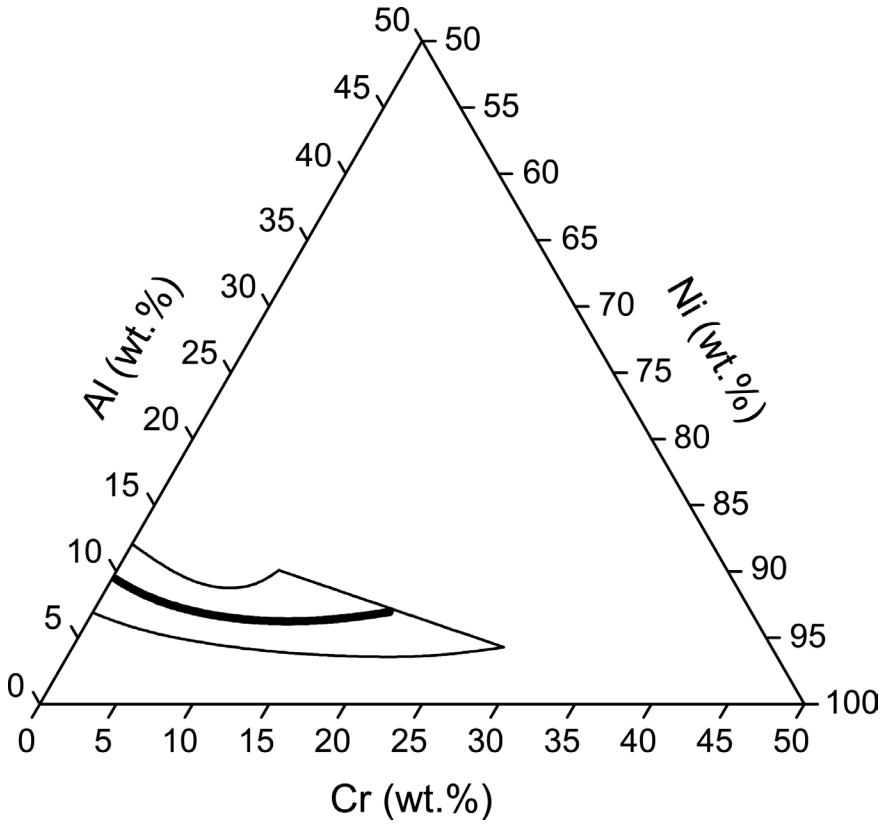

Figure 5.12: Mapped compositions which correspond to 50% γ' phase in the Ni-Al-Cr ternary system.

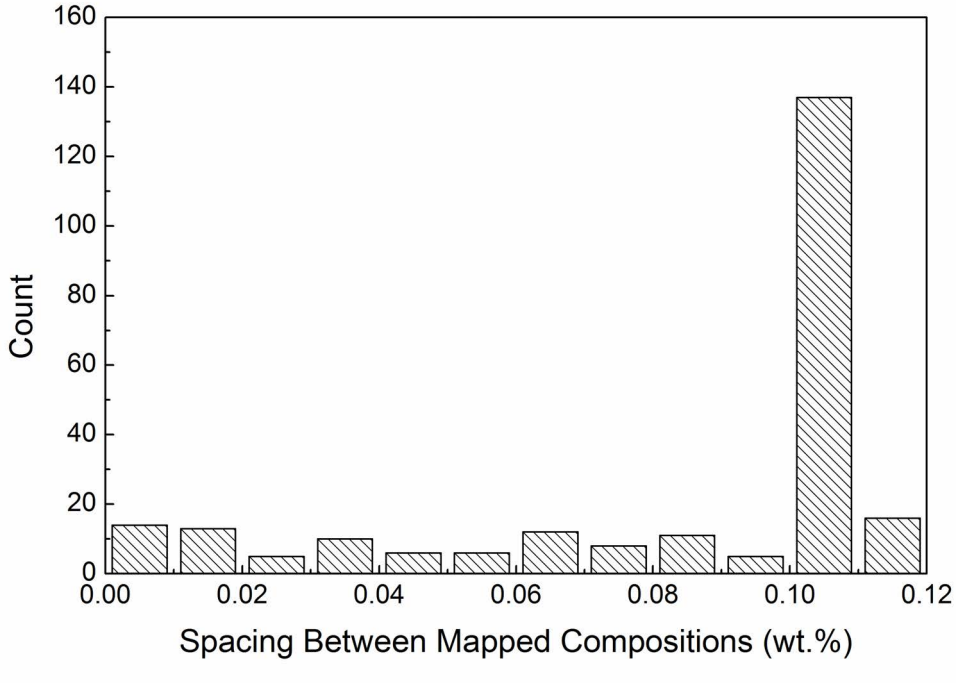

Figure 5.13: Spacing between mapped compositions in the Ni-Al-Cr ternary system.

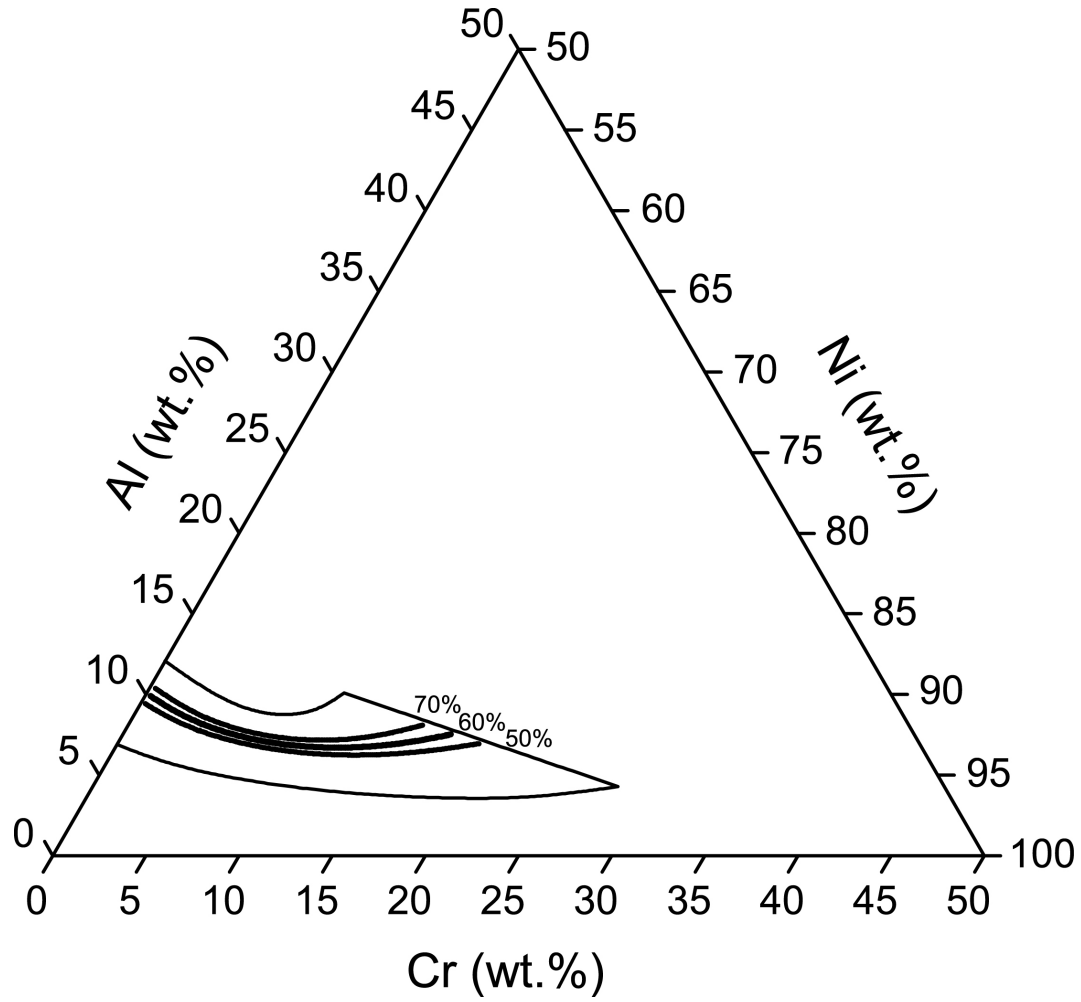

Figure 5.14: Mapped compositions which corresponds to different fractions of γ' phase, 50%–70%, in the Ni-Al-Cr ternary system.

Table 5.2: Numbers of correct compositions and their average spacings in all possible Ni-Al-X ternary systems.

Alloy system	Number of correct compositions	Average spacing (wt.%)
Ni-Al-Co	253	0.217
Ni-Al-Re	24	0.223
Ni-Al-Ta	97	0.165
Ni-Al-W	99	0.266

Co, Ni-Al-Re, Ni-Al-Ta and Ni-Al-W. Table 5.2 summarises the numbers of correct compositions and their average spacings when arranged on the line of 50% γ'. It is evident that the number of the correct compositions depends on the size of the γ and γ' two-phase region; thus the Ni-Al-Co system has the most corrected compositions. The spacing of the correction compositions is determined by the topology of the γ and γ' two-phase region. Since the Ni-Al-Ta system has a relatively short but wide two-phase region, the average spacing is found to be the smallest among all the Ni-Al-X ternary systems. The number of mapped compositions in each ternary system is summarised as a column plot in Figure 5.16. The average computational time for mapping a ternary system is 40 minutes on a single processor.

5.4.2 Extension to Quaternary Systems: Ni-Al-X-Y

The method can be applied readily to quaternary systems. Consider the Ni-Al-Cr-Ta system as an example. For a resolution of 1 wt%, the number of calculations in total is ${}^{99}C_3 = \dfrac{99!}{(99-3)!3!} = 156849$. Examining the dataset to isolate the trial compositions which have a mixture of γ and γ' two phases, the number decreases dramatically to 1409. Then the trial compositions are adjusted along the tie-lines for 50% γ' proportion of the phase. The 1409 correct compositions are plotted in Figure 5.17; this is thus a preliminary structure of the surface corresponding to 50% γ'. It is of interest to calculate the spacings between these correct compositions. Results in Figure 5.18 show that the correct compositions on the surface have an average

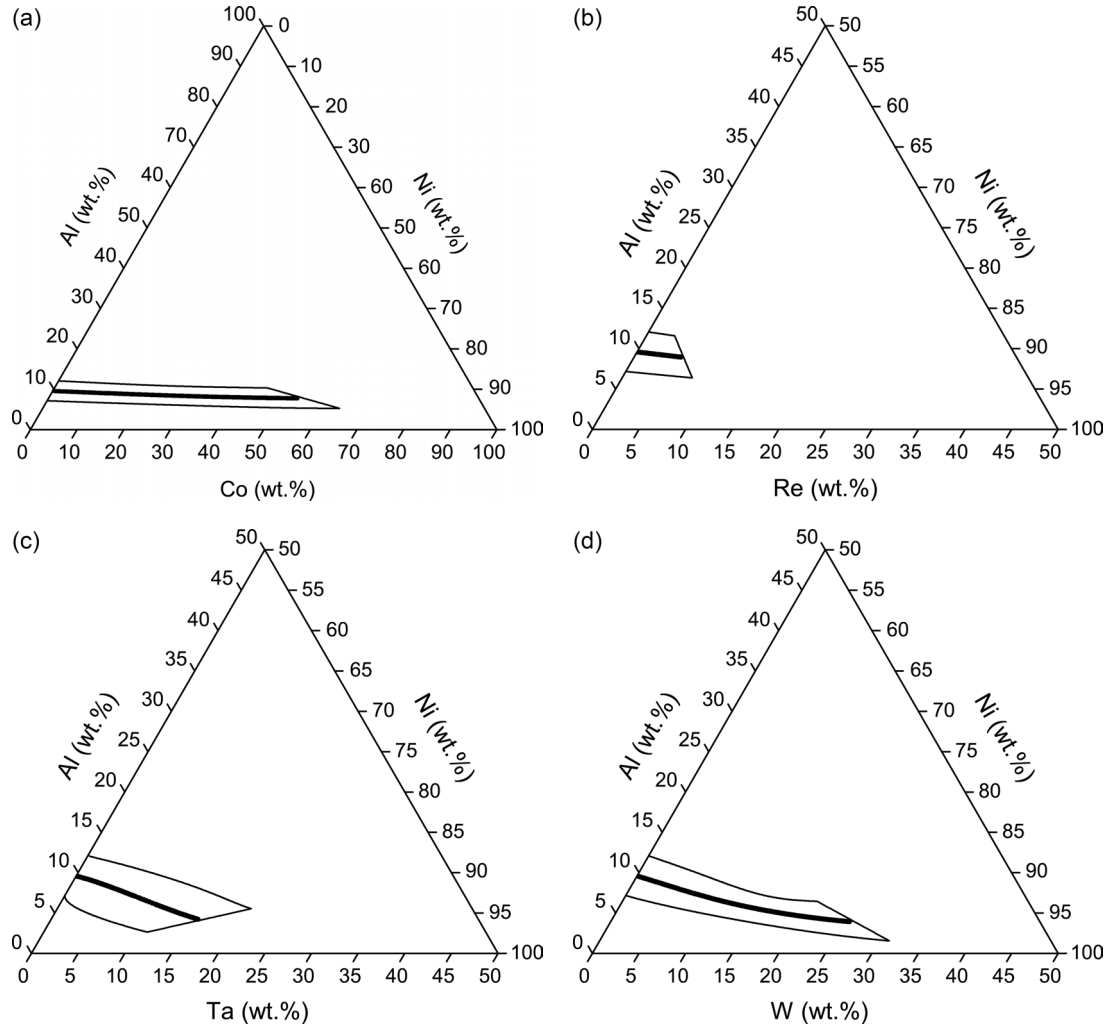

Figure 5.15: Mapped compositions which correspond to 50% γ' phase in the possible Ni-Al-X ternary system: (a) Ni-Al-Co; (b) Ni-Al-Re; (c) Ni-Al-Ta; (d) Ni-Al-W.

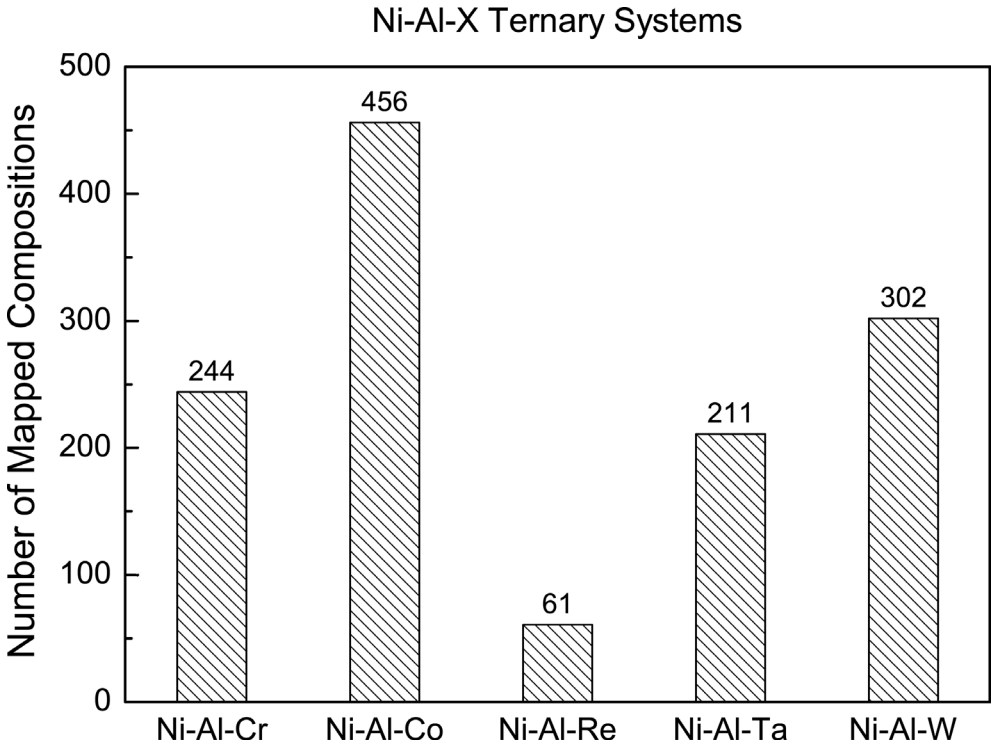

Figure 5.16: Number of mapped compositions in each Ni-Al-X ternary system.

spacing of ∼0.25 wt.%, together with a maximum spacing of ∼0.5 wt.%. As discussed in Section 5.3.2, mapping of a surface in the quaternary system requires two directions each time. In the Ni-Al-Cr-Ta system, mapping has been carried out by using combinations of directions, Cr–Ta, Cr–Al and Al–Ta. The three combinations give rise to a final alloy design space containing 46769 compositions. In Figure 5.19, they are constructed as a surface. The spacings between these mapped compositions are also examined. The histogram in Figure 5.20 demonstrates that every two nearest compositions on the surface have a spacing less than $\sqrt{0.1^2 + 0.1^2 + 0.1^2} = 0.173$ wt.%.

In Figure 5.21, results from the different Ni-Al-X-Y quaternary systems are given, and the number of mapped compositions in each system summarised. One can see that most of the quaternary systems contain $\sim 10^4$ compositions, but some of them have numbers that are close to $\sim 10^5$. The effectiveness of the algorithm is proven. The average computational time for mapping a quaternary system is 3 hours as

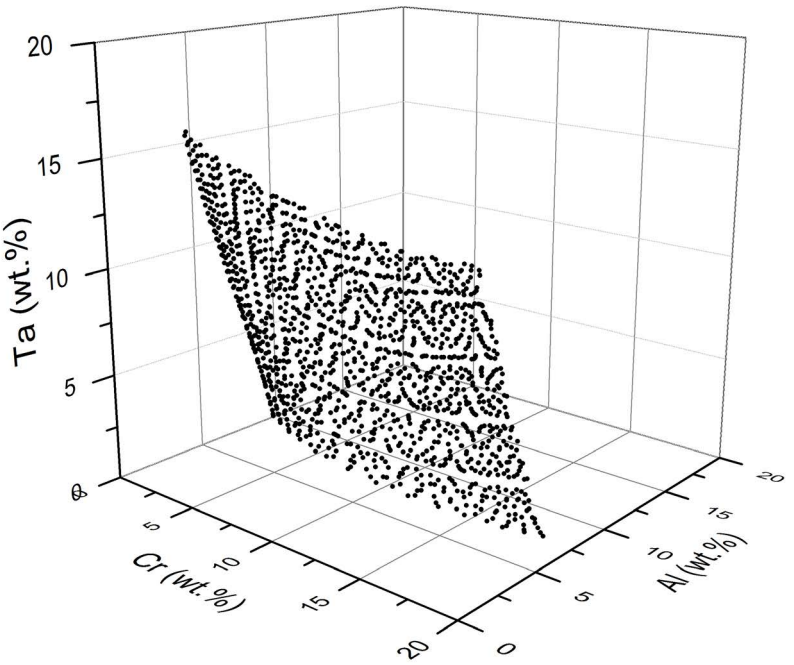

Figure 5.17: Correct compositions which have 50% γ' phase in the Ni-Al-Cr-Ta quaternary system.

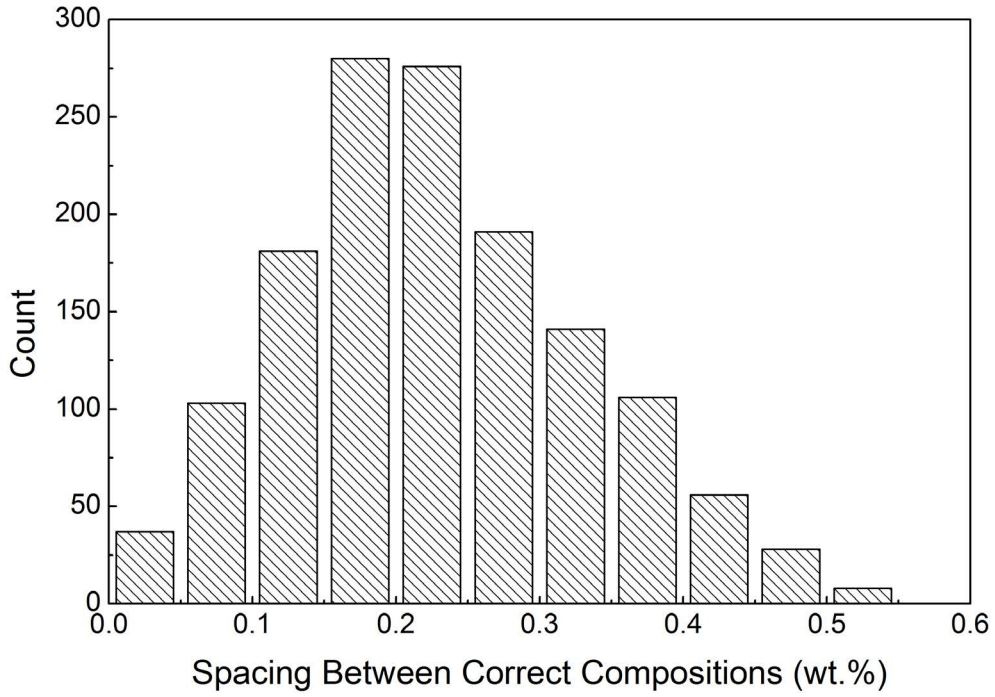

Figure 5.18: Spacing between correct compositions in the Ni-Al-Cr-Ta quaternary system.

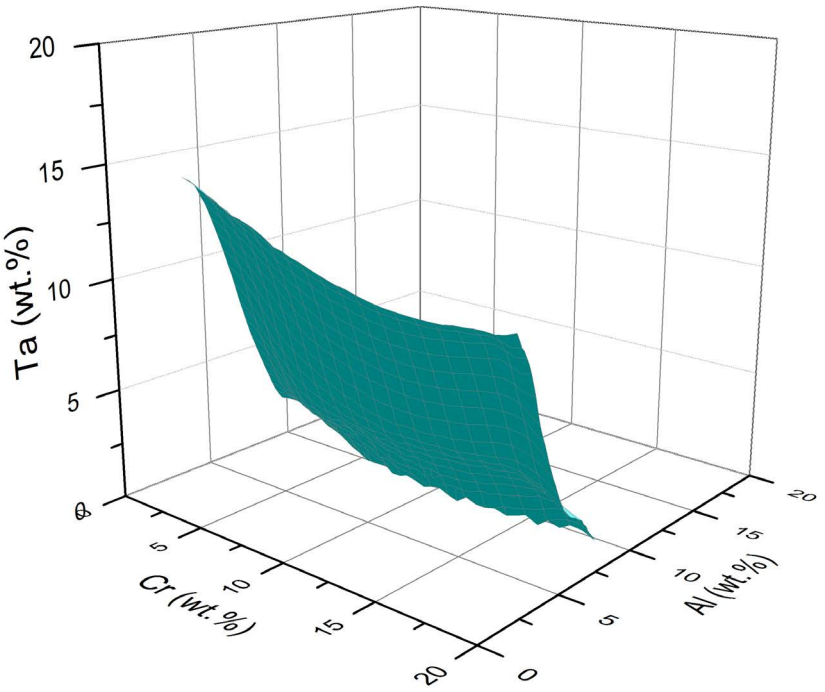

Figure 5.19: Mapped compositions which have 50% γ' phase in the Ni-Al-Cr-Ta quaternary system.

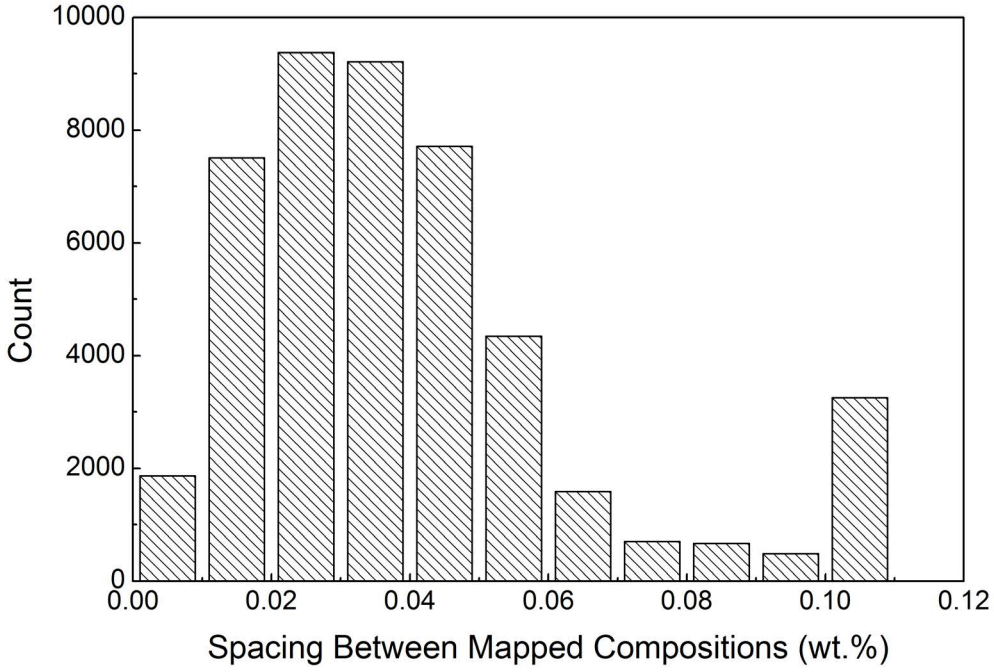

Figure 5.20: Spacing between mapped compositions in the Ni-Al-Cr-Ta quaternary system.

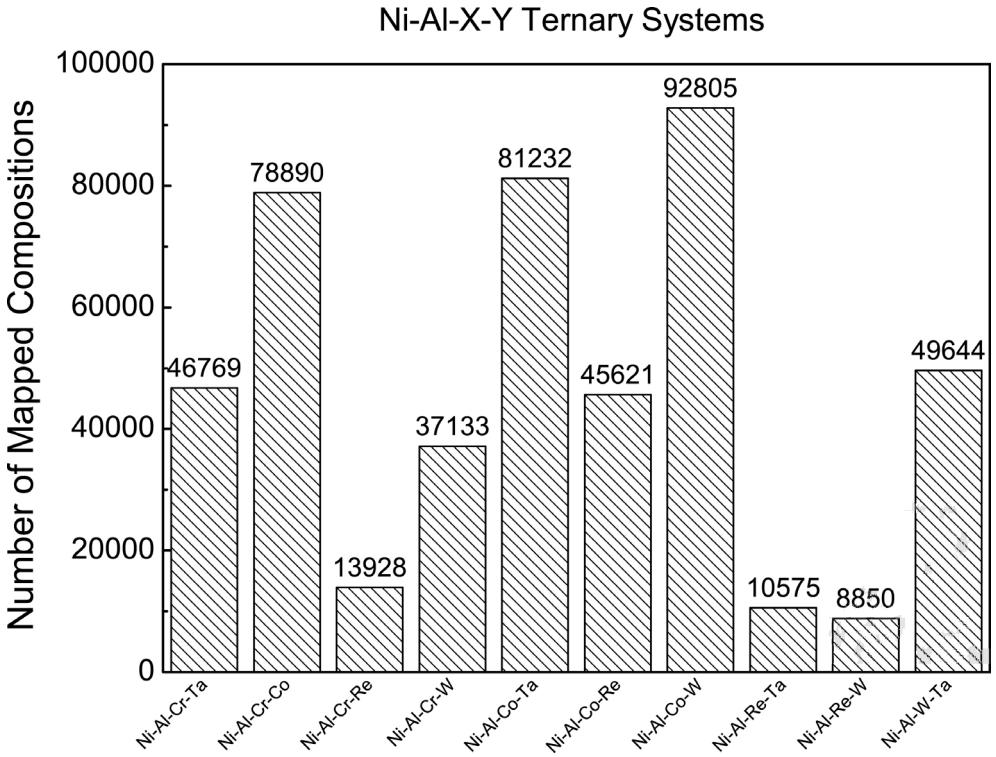

Figure 5.21: Number of mapped compositions in each Ni-Al-X-Y quaternary system.

recorded.

5.4.3 Multicomponent Systems

Finally, the method is generalised to a multicomponent system. It is reasonable to start with an alloy system used for turbine blade applications; for illustrative purposes a six component system is considered including Cr, Co, Re, W, Al and Ta. The initial alloy design space is defined such that the Cr concentration varies from 4 to 12 wt.%, the Co concentration from 0 to 10 wt.%, the Re concentration from 0 to 5 wt.%, the W concentration from 0 to 8 wt.%, the Al concentration from 4 to 7 wt.% and the Ta concentration from 4 to 8 wt.%. Thus some use is made of prior experience so that unnecessary calculations are avoided. Thus for a coarse resolution of 1 wt.%, calculations need to be carried out for 106920 alloys. One first identifies trial compositions which have mixture of γ and γ' two phases. Application of this constraint reduces the size of dataset to 22371 alloys. The

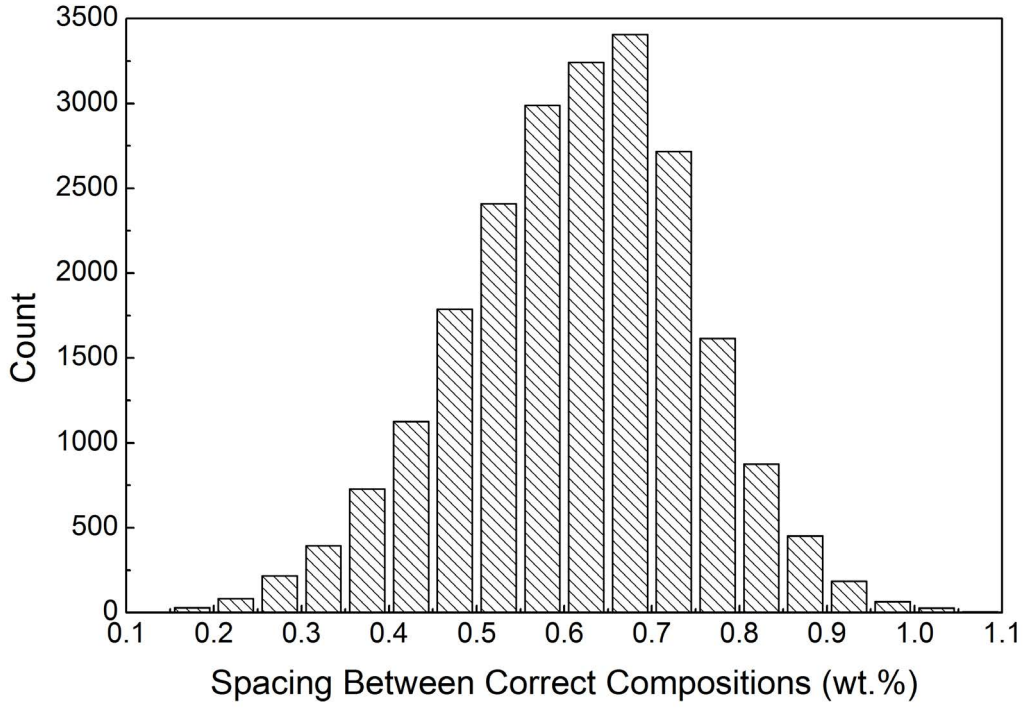

Figure 5.22: Spacing between correct compositions in the Ni-Cr-Co-Re-W-Al-Ta system.

next step involves adjusting the compositions along the tie-lines for 50% γ' phase. The spacings between these correct compositions are summarised in Figure 5.22. The initial spacing has an average value of ∼0.6 wt.%. As stated in Section 5.3.2, mapping of a multicomponent system that has k alloying elements requires k-1 directions each time. Therefore, in the Ni-Cr-Co-Re-W-Al-Ta system, mapping can be carried out by using any five of them, for example Cr, Co, Re, W and Ta, so that the unknown Al change can be calculated. The number of possible combinations in this system is ${}^6C_5$=6. With all the combinations being considered and the mapping completed, the final dataset contains 357636 alloys. One can walk along the compositional space – the hyper volume – to calculate the spacing between every two nearest compositions. The results in Figure 5.23 confirm that all the spacings are no greater than $\sqrt{6 \times 0.1^2} = 0.2449$ wt%. The computational time used for this calculation is 45 hours.

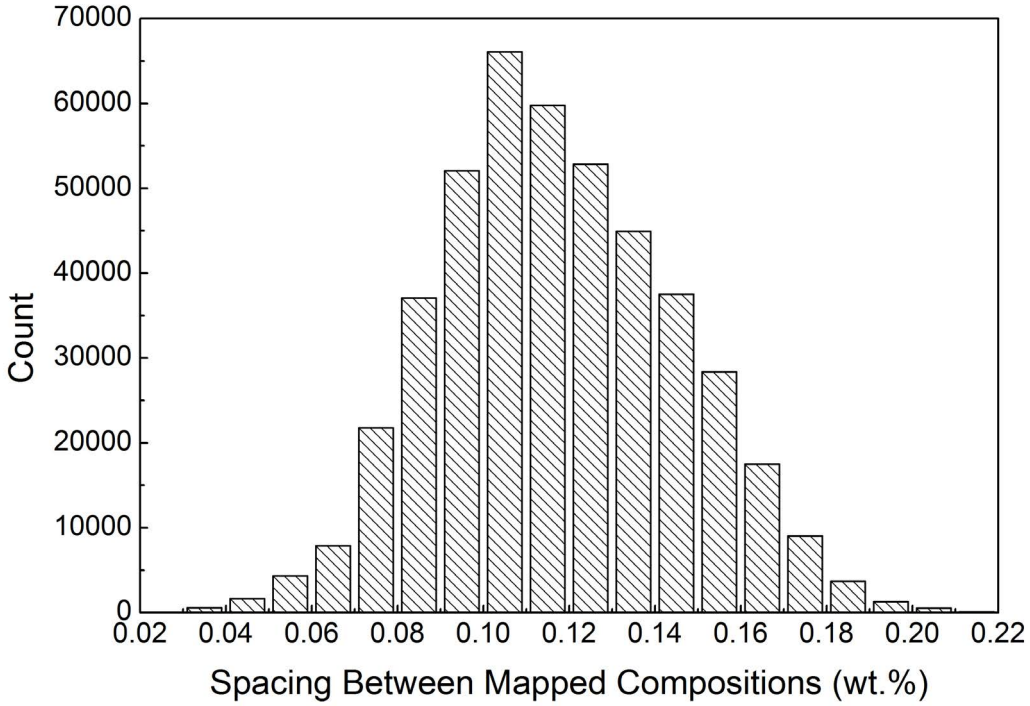

Figure 5.23: Spacing calculated from random migrations in the Ni-Cr-Co-Re-W-Al-Ta system.

5.5 Application: Isolation of Optimal Alloys

The databases constructed above contain all alloy compositions which are predicted to display microstructural characteristics conferring optimal behaviour. But we believe that the approach becomes even more powerful when the databases are coupled with composition-dependent models for the important properties of interest, for example creep resistance, density and cost. Examples of such models are given in [74]. In what follows, use is made of the database constructed for the Ni-Cr-Co-Re-W-Al-Ta system in Section 5.4.3 above; the estimates of creep resistance, density and cost follow [74]. The combined approach can be used to isolate compositions of new optimised alloys and to study the various trade-offs between the different properties implied by changes in chemical composition.

Table 5.3: Optimal compositions (wt.%) with the best creep resistance for different density limits.

Density limit (g/cm^3)	Cr	Co	Re	W	Al	Ta	Ni
8.4	11.9	9.1	3.0	2.4	5.9	4.4	Bal
8.6	9.8	9.6	4.9	2.5	5.6	5.0	Bal
8.8	7.6	9.4	4.5	5.8	5.4	4.6	Bal
9.0	5.9	9.8	4.8	6.0	5.1	6.4	Bal

5.5.1 Design of Creep Resistant Alloys with Density Limit

Consider the design of alloys for high performance jet engine applications, when creep resistance needs to be maximised in combination with an appropriate density limit to avoid excessive centrifugal loads. Scatter diagrams for predicted creep merit index against density are plotted in Figure 5.24; each alloy composition is plotted as a point so that a total of 357636 are present. For any given density, alloys predicted to have the greatest creep resistance exhibit the largest creep merit index. Therefore, the plot reveals straight away that alloys with greater creep resistance tend to be denser. The region of optimal alloy compositions is marked in Figure 5.24. The best creep resistant alloys for different density ranges from 8.4 to 9.0 g/cm^3 then can be identified within this region. Their compositions are summarised in Table 5.3. Generally, the alloy density is increased by more of the heavy elements, e.g. Re, W and Ta, and less of the light elements, e.g. Al and Cr. The compositional effects on creep and density need to be explored in more detail.

When examining the dataset carefully one finds that Al has a very strong effect on alloy density, see Figure 5.25. The scatter diagrams show the distributions of alloys at Al concentrations from 4 to 6 wt.%. One can see that there is a distinct trend for alloys progressing from right to left as the Al concentration increases. From this, a contour plot is summarised in Figure 5.26(a) to illustrate the effect of Al. The contours delimit the least dense alloys which can be achieved at the quoted level

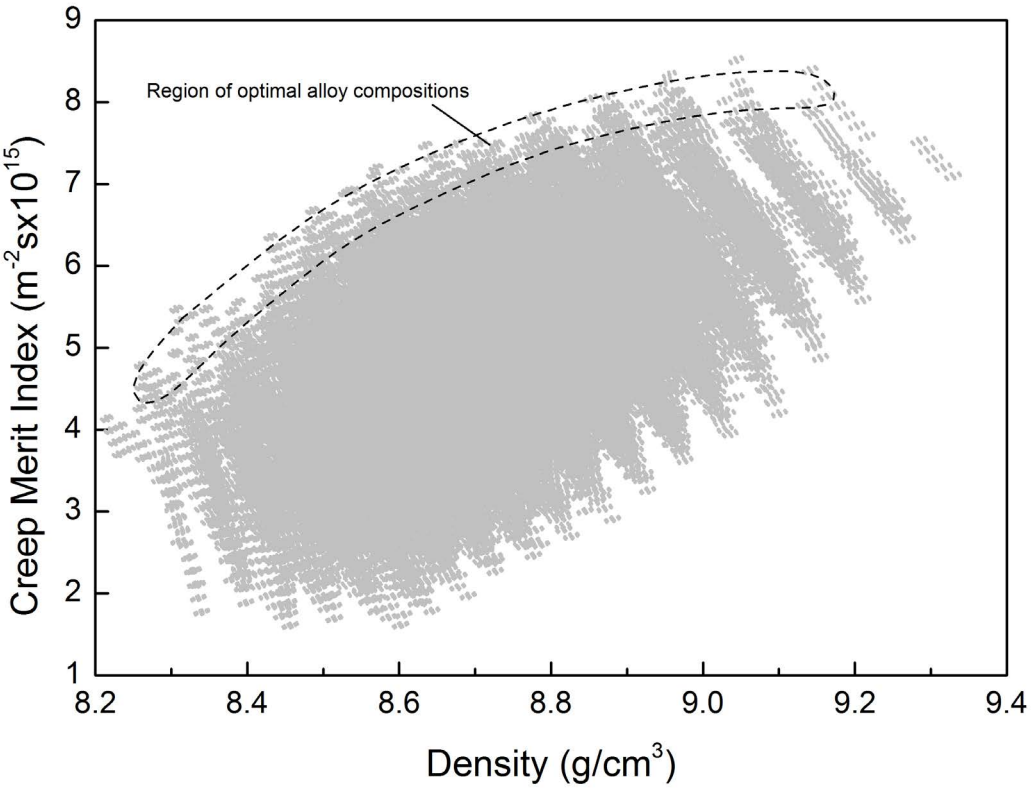

Figure 5.24: Scatter diagram (Creep Merit Index vs. Density) for the mapped 357636 alloys in the Ni-Cr-Co-Re-W-Al-Ta system.

of Al. Clearly, the alloy density can be reduced by increasing the concentration of Al. Figure 5.26(b) demonstrates that another important alloying element Re confers greater creep resistance at a higher concentration, but this is at the expense of elevated density. The contours define the alloys with the best creep resistance at each Re concentration, from 1 to 5 wt.%. Figure 5.26(c) shows that W exhibits a similar effect as Re, which has the effect of pushing alloy compositions to the top right. However, one finds that higher concentrations of W induce a more significant increase of density compared to Re additions. In Figure 5.26(d), Co demonstrates a strong strengthening effect at higher concentration; the creep resistance is improved as the concentration of Co increases from 2 to 8 wt.%.

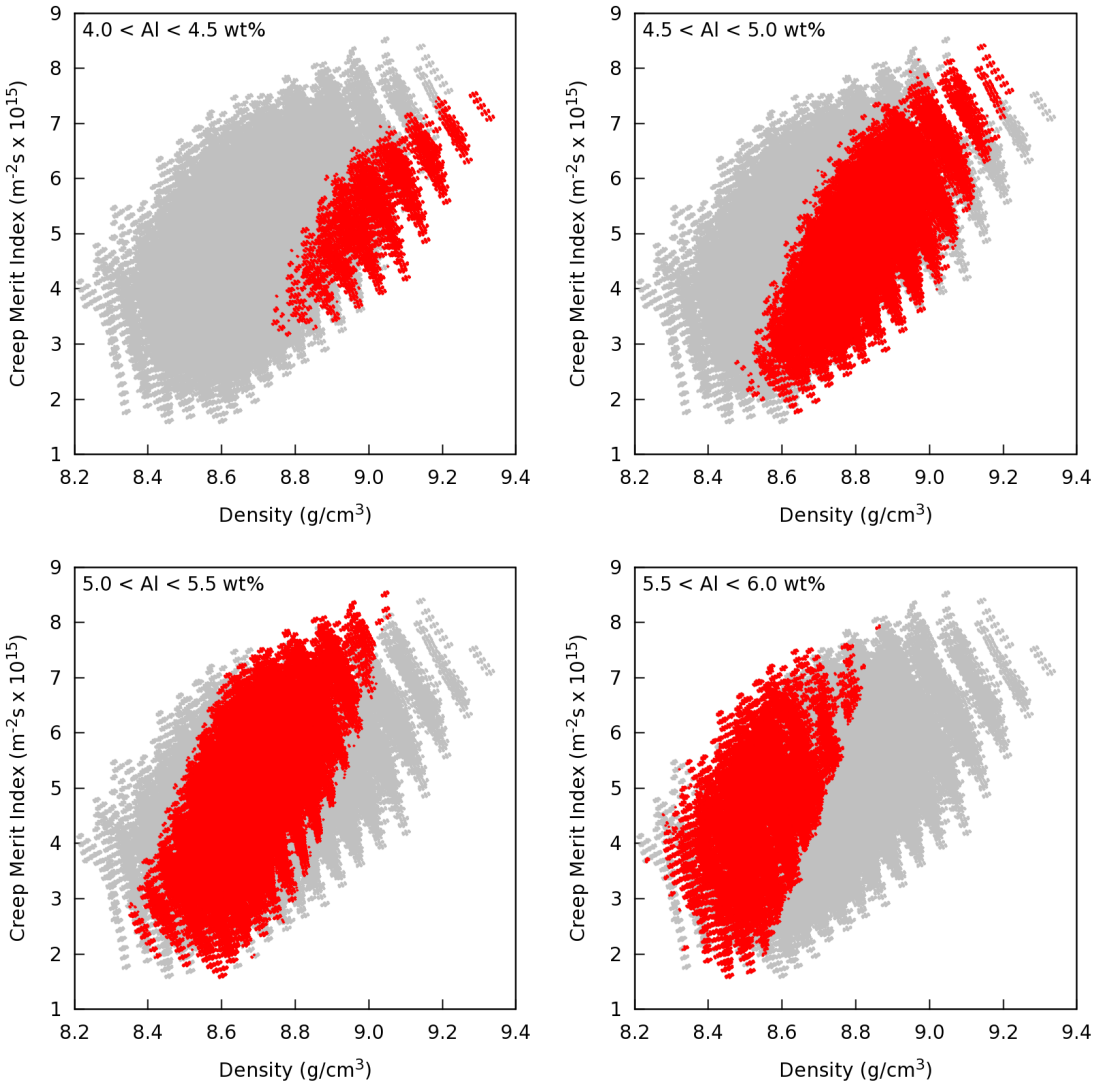

Figure 5.25: Scatter diagrams (Creep Merit Index vs. Density) for the mapped alloys corresponding to different Al concentrations: (a) 4.0∼4.5 wt.%; (b) 4.5∼5.0 wt.%; (c) 5.0∼5.5 wt.%; (d) 5.5∼6.0 wt.%;

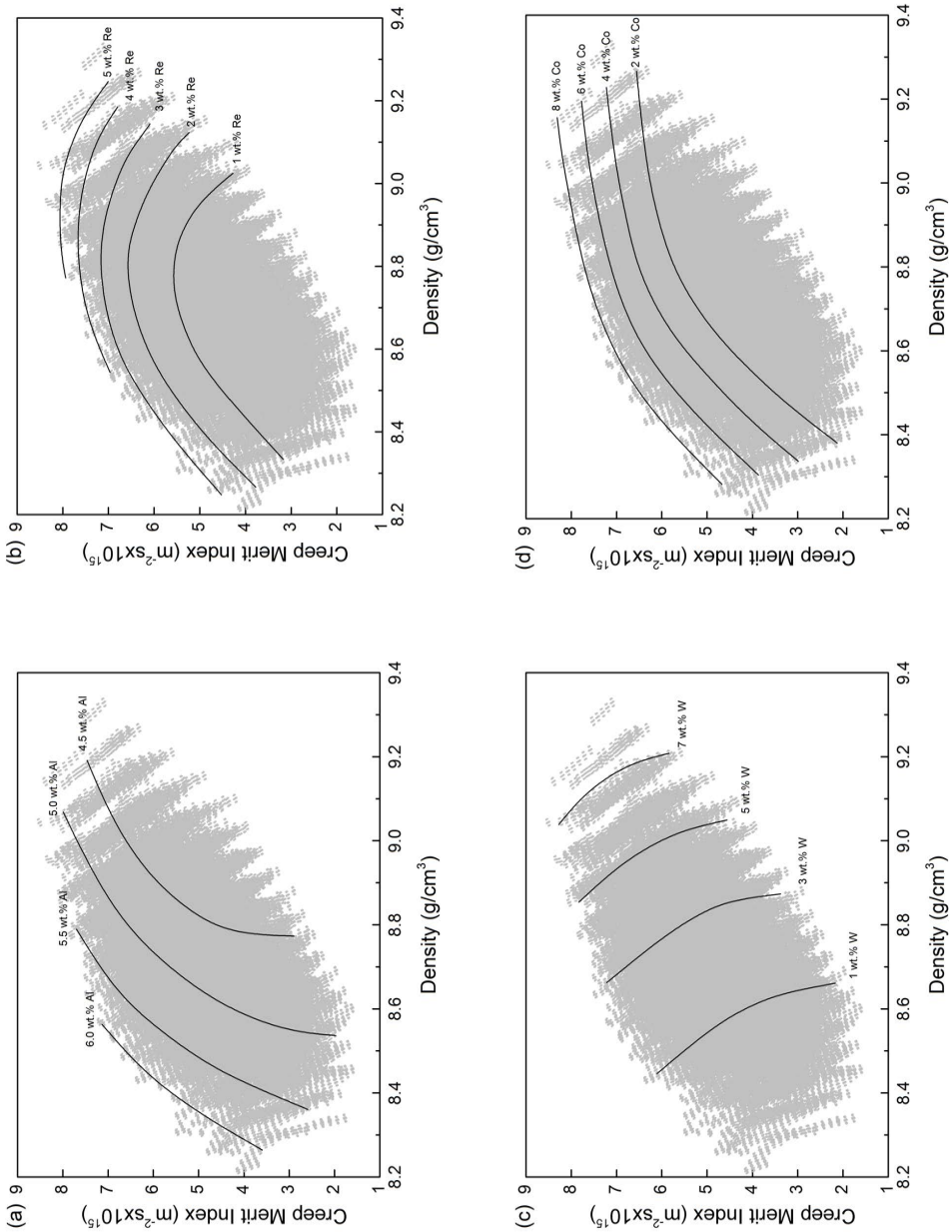

Figure 5.26: Scatter diagrams (Creep Merit Index vs. Density) which illustrate the compositional effects on creep and density. (a) different Al concentrations; (b) different Re concentrations; (c) different W concentrations; (d) different Ta concentrations.

5.5.2 Design of Creep Resistant Alloys with Microstructure Stability and Cost Limit

It is also necessary to consider aspects of alloy stability, since excessive alloying by W and particularly Re promotes precipitation of topologically close-packed phases. This can be accounted for by making an estimate of the Md number for each alloy, following [74]. Consider Figure 5.27; one can see that Md value increases from the bottom up to the high creep resistance region, implying increasing alloy instability. For a given density limit, the best creep resistant alloys can be identified on the lines representing different Md values. As shown in Figure 5.27, different density limits from 8.4 to 9.0 g/cm^3 have been set, and the optimal alloys are identified at each Md limit. Compositions of these alloys are summarised in Table 5.4. It is clear that a decrease in the Cr concentration is needed to make the alloys more stable. Ta is also found to be less than 5 wt.% for the best alloy stability.

For many high temperature applications particularly involving industrial gas turbines for power generation, the cost of the alloy is also a major consideration. In Figure 5.28, different cost limits from 200 to 400 $/kg are plotted on the scatter diagram for creep merit index against density. One sees that the cost of the alloy increases from the left corner to the top right, consistent with the direction of best creep resistance. It is of interest to list the compositions with the best creep resistance for different cost limits, see Table 5.5. One can see that the most obvious change between these compositions is the concentration of Re. It is known that Re gives a significant improvement in high temperature creep performance, but will bring a substantial increase in the cost. The table indicates that as the Re concentration increases from 1 to 5 wt.%, the cost of the raw materials for the alloy is approximately doubled. The calculations quantify the performance/cost trade-off implied by Re alloying.

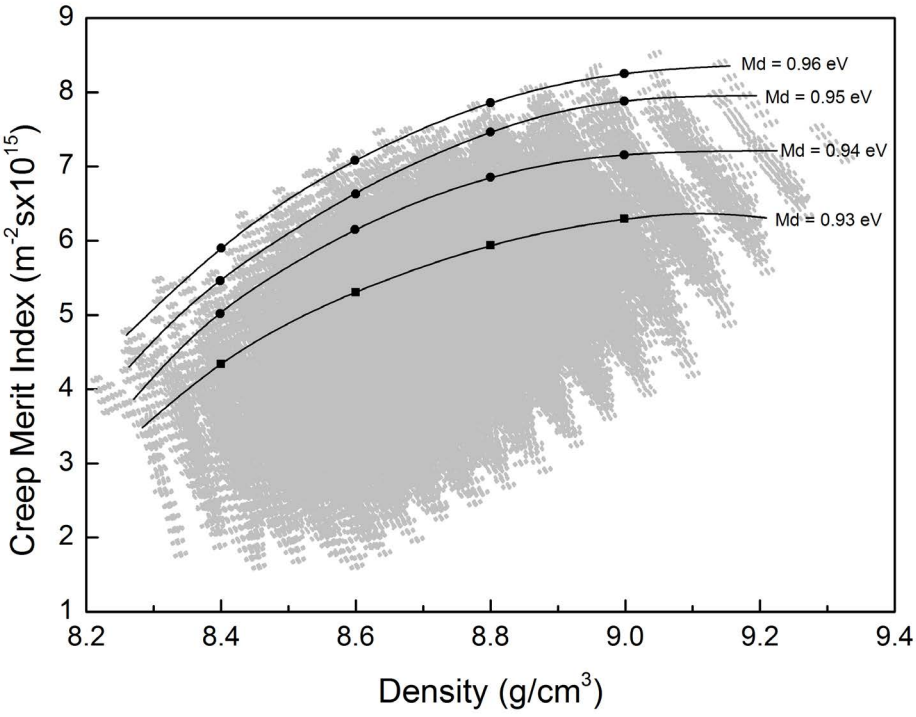

Figure 5.27: Scatter diagram (Creep Merit Index vs. Density) for the mapped alloys in the Ni-Cr-Co-Re-W-Al-Ta system. Also plotted are the limits of different Md values.

Table 5.4: Optimal compositions (wt.%) with the best creep resistance for different density limits, with stability number Md being considered.

Density limit (g/cm^3)	Cr	Co	Re	W	Al	Ta	Ni
Md<0.96 eV							
8.4	11.9	9.1	3.0	2.4	5.9	4.4	Bal
8.6	9.8	9.6	4.9	2.5	5.6	5.0	Bal
8.8	7.6	9.4	4.5	5.8	5.4	4.6	Bal
9.0	5.9	9.8	4.8	6.0	5.1	6.4	Bal
Md<0.95 eV							
8.4	10.3	9.3	3.1	1.1	5.9	4.8	Bal
8.6	8.7	9.8	3.4	4.3	5.6	4.6	Bal
8.8	8.6	7.8	4.7	4.9	5.2	5.4	Bal
9.0	5.0	7.0	4.8	7.1	5.1	5.3	Bal
Md<0.94 eV							
8.4	6.8	8.7	2.8	1.1	6.2	4.4	Bal
8.6	6.5	6.8	4.9	2.5	5.7	4.1	Bal
8.8	4.4	8.9	3.4	6.5	5.5	4.5	Bal
9.0	5.0	5.3	4.3	7.2	5.0	5.3	Bal
Md<0.93 eV							
8.4	4.8	7.5	2.7	1.0	6.3	4.6	Bal
8.6	6.5	4.4	4.6	2.1	5.6	4.4	Bal
8.8	4.8	3.8	4.5	4.7	5.4	4.7	Bal
9.0	5.2	1.1	4.2	7.3	4.8	4.7	Bal

Table 5.5: Optimal compositions (wt.%) with the best creep resistance for different cost limits.

Cost limit ($/kg)	Cr	Co	Re	W	Al	Ta	Ni
200	10.2	9.3	0.9	7.6	5.4	4.7	Bal
250	10.2	9.8	1.8	7.7	5.4	4.1	Bal
300	8.6	9.6	2.8	7.8	5.3	4.5	Bal
350	6.8	9.6	3.7	7.8	5.3	4.4	Bal
400	4.8	9.6	4.6	7.9	5.3	4.5	Bal

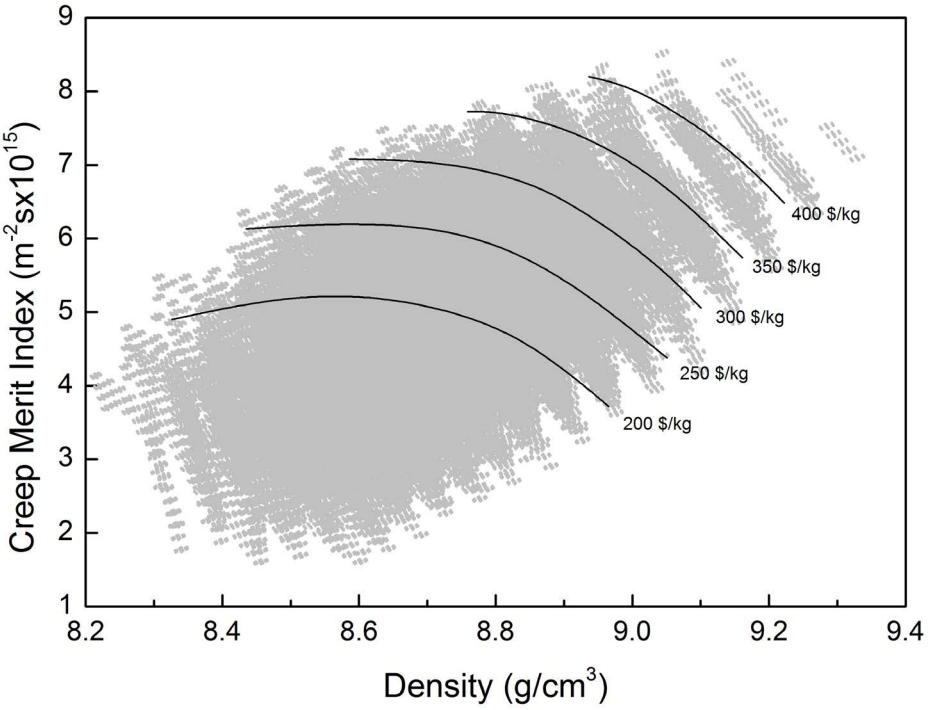

Figure 5.28: Scatter diagram (Creep Merit Index vs. Density) for the mapped alloys in the Ni-Cr-Co-Re-W-Al-Ta system. Also plotted are the limits of different cost.

5.5.3 Design of Creep Resistant Alloys with Oxidation Resistance Combined

As temperature requirements become more stringent, there is an urgent demand for improvements in the high temperature oxidation performance. The requirement then is to design a creep resistant alloy which also displays sufficient oxidation resistance for practical applications. A scatter diagram for creep merit index against oxidation merit index [70] is plotted in Figure 5.29. One sees that the best alloys with a good combination of creep and oxidation resistances lie towards the top right of this diagram. For current nickel-based single crystal superalloys, an adequate content of Al is needed to form a highly protective oxide layer, Al_2O_3. The effect of Al on oxidation property is demonstrated in Figure 5.30. The oxidation ranking of some typical second generation superalloys, CMSX-4, PWA1484 and TMS-82+, is

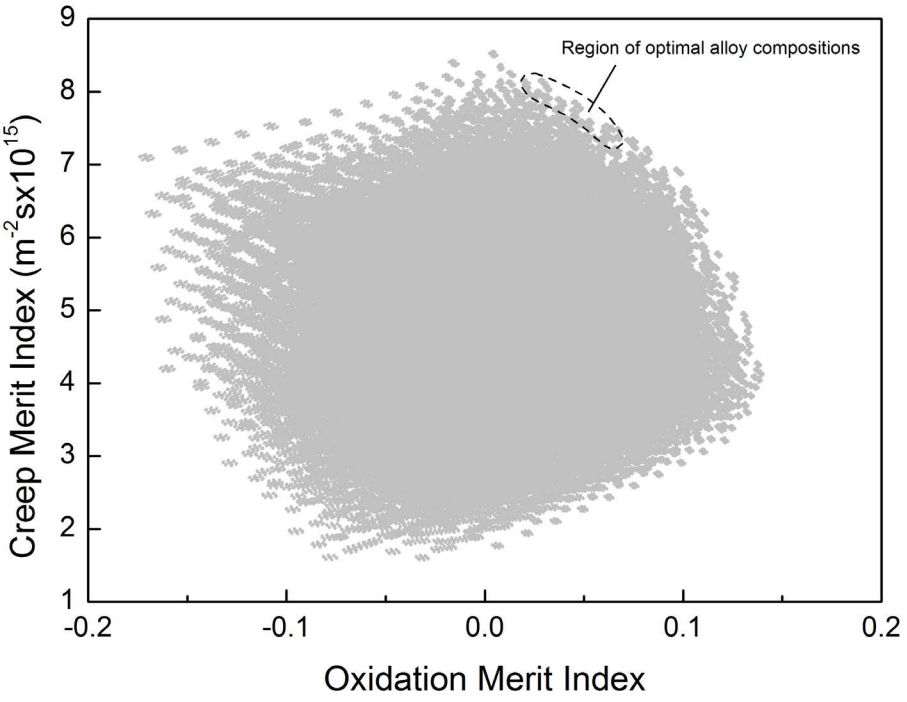

Figure 5.29: Scatter diagram (Creep Merit Index vs. Oxidation Merit Index) for the mapped alloys in the Ni-Cr-Co-Re-W-Al-Ta system.

also plotted. It is evident that oxidation resistance is improved as the concentration of Al increases from 4.5 to 6.0 wt.%. Since a positive value of oxidation merit index is needed to ensure the formation of Al_2O_3 [70], one finds ∼5wt.% Al is necessary. It is of interest to identify some representative alloys which display best combinations of creep and oxidation resistances. The minimum oxidation merit index is given from 0.2 to 1.0; the compositions of the best creep resistant alloys under these limits are summarised in Table 5.6. The concentration of Al increases gradually as the oxidation limit becomes more restricted. The concentration of Cr is also increased consistent with the observation that additions of Cr will encourage the formation of Al_2O_3.

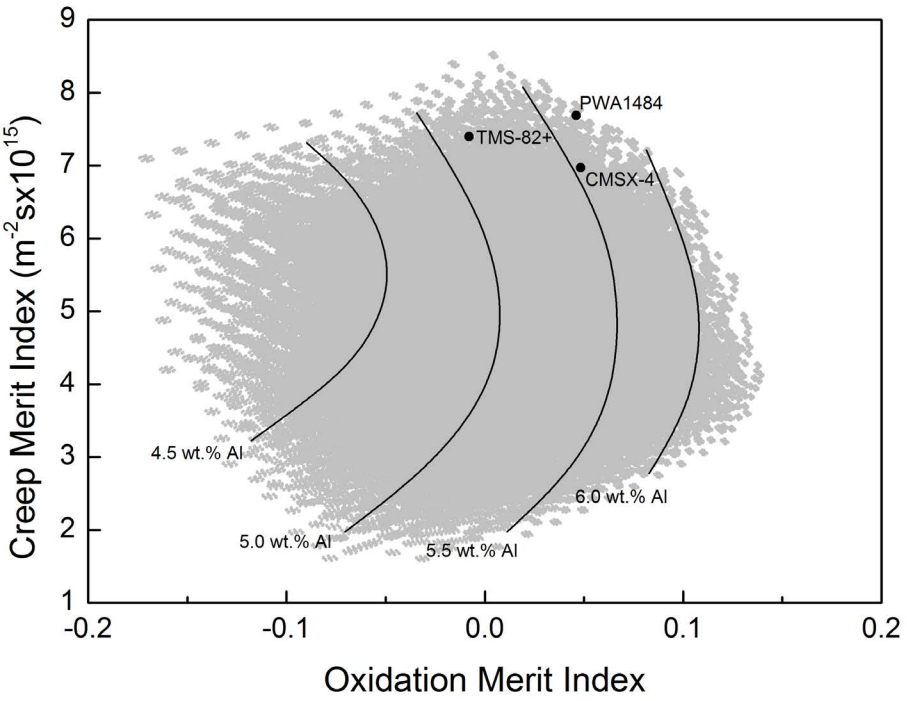

Figure 5.30: Scatter diagram (Creep Merit Index vs. Oxidation Merit Index) which illustrates the effect of Al on creep and oxidation.

Table 5.6: Optimal compositions (wt.%) with the best combinations of creep and oxidation resistances.

Oxidation limit	Cr	Co	Re	W	Al	Ta	Ni
0.2	6.7	8.6	4.7	5.8	5.2	5.5	Bal
0.4	4.6	9.3	4.9	4.5	5.4	5.9	Bal
0.6	9.7	9.7	4.8	3.0	5.5	7.5	Bal
0.8	10.8	9.0	4.3	2.7	5.6	5.0	Bal
1.0	9.6	9.6	4.8	1.4	5.7	5.1	Bal

5.6 Summary and Conclusions

The following conclusions can be drawn from this work:

1. For the important ternary, quaternary and multicomponent systems relevant to the single crystal nickel-based superalloys, the compositions of alloys conferring the microstructures needed for optimal properties have been identified.

2. To do this, new numerical algorithms have been developed; their use has allowed compositions consistent with fixed (for example equi-molar) proportions of the matrix and precipitate phases to be identified at a resolution of $\sim$0.1 wt.%, i.e. close to the limit of compositional control needed for investment casting practice.

3. In doing so, databases have been constructed which contain estimates of all possible chemical compositions available in these systems, which are predicted to display appropriate microstructure. It can therefore be claimed that the available alloy design space has been mapped at the resolution appropriate for technological application of these materials.

4. When coupled with composition- and microstructure-dependent property models, the databases can be searched to identify new alloys predicted to exhibit the very best properties or combinations of them. Thus, provided that the property models are accurate and in particular due to the completeness of the mapping across the alloy design space, alloys chosen in this way are likely to be close to those which are optimal.

5. The accuracy of the approach relies heavily upon the underlying thermodynamic databases and the accuracy of the property models; nevertheless, the approach proposed represents a new paradigm for the design of new alloys, which eliminates the need for the traditional empirical approaches based upon statistical design.

Chapter 6

Conclusions and Future Work

6.1 Summary and Conclusions

The work presented here represents an investigation into the properties of nickel-based single crystal superalloys. Underlying quantitative relationships between alloy chemistry and the important properties have been proposed. To design new grade of single crystal superalloys, computational modelling methods have been designed which build on the composition-microstructure-property relationships.

In Chapter 1 the background and objectives of the research are presented. The increasing demand for improvements in engine efficiency has provided the big momentum for the research and development of new single crystal superalloys. A literature survey relevant to the scope of this research is presented in Chapter 2, to provide the knowledge on metallurgy of nickel-based superalloys, high temperature creep and oxidation behaviour of nickel-based superalloys, and current modelling approaches of these important properties.

In Chapter 3, a physical model for the creep deformation of single crystal superalloys is proposed, which makes a first attempt to couple a physics-based constitutive description of time-dependent plastic flow to the alloy chemistry. It is found

that the creep deformation of single crystal superalloys is sensitive to both chemical composition and microstructure. The rate-controlling step is assumed to be climb of dislocations at the matrix/particle interfaces and their rate of escape from trapped configurations, which gives rise to a strong dependence on alloy composition. The model has been used to rationalise in quantitative terms the relative creep strengths of different generations of single crystal superalloy, showing good agreement with available experimental data. For creep deformation at higher temperatures, a simple extension of the model is proposed to account for a rafting-induced strengthening effect. A first order estimate for the rate of creep deformation emerges from the model, which is useful for the purposes of alloy design.

Chapter 4 provides a detailed description of an alloy design method for nickel-based single crystal superalloys. The isolation of optimal chemical compositions is carried out by eliminating - from initial, trial compositional spaces - alloys which have unacceptable microstructural characteristics. Unsuitable microstructural architectures (γ' fraction, γ/γ' misfit) and insufficient stability are considered for rejection from the initial composition space. Next, compositions are ranked on the basis of their anticipated performance in creep and oxidation; estimation of their density and cost are also made at this point. Once again, unacceptable alloys are discounted on the basis of their mechanical behaviour, environmental performance and physical properties. Remaining compositions represent acceptable compositions, which has passed the design constraints. Optimal compositions can then be chosen on the basis of best properties and/or combinations of these. The compositions of three new single crystal superalloys are isolated for different design purposes, which are (i) an oxidation-resistant low Re-containing alloy with balanced properties, intended for general-purpose gas turbine applications; (ii) an alloy containing 5.6 wt.% Re and 2.6 wt.% Ru suitable for high performance jet engine applications, when creep resistance needs to be maximised without oxidation performance being excessively compromised and (iii) a cheap, corrosion-resistant alloy for power generation ap-

plications designed with ease-of-processing in mind. To test the accuracy of the approach, the new alloys have been prepared using investment casting techniques, and their creep and oxidation behaviour evaluated. Future direction for alloy design is also discussed, in order to achieve alloys with better microstructural stability and lower density.

In Chapter 5, the multicomponent composition space pertinent to the single crystal nickel-based superalloys is mapped and searched, using computational modelling. New numerical algorithms have been developed, which allowed compositions of alloys conferring the microstructures needed for optimal properties to be identified. A resolution of 0.1 wt.% for the alloying elements is assumed, consistent with manufacturing practice. Databases have been constructed which contain estimates of all possible chemical compositions available in these systems, which are predicted to display promising microstructure. It can therefore be claimed that the available alloy design space has been mapped at the resolution appropriate for technological application of these materials. When coupled with composition- and microstructure -dependent property models, the databases can be searched to identify new alloys predicted to exhibit the very best properties or combinations of them. Alloys chosen in this way are likely to be close to those which are optimal, due to the completeness of the mapping across the alloy design space.

6.2 Suggestions for Future Work

The study performed in Chapter 3 has provided the first attempt to couple the chemical dependence to a physical model for the creep deformation of single crystal superalloys. The model is physically-based with no empirical parameters needed. Some initial microstructural parameters, e.g. initial dislocation density $\rho_{\mathrm{m},0}$, γ' particle size d and γ' volume fraction ϕ_{p}, are assumed based upon estimates published in the literature. However, it is possible to characterise the initial dislocation den-

sity by using TEM on the creep test specimens of author's work in Chapter 5. In unstrained creep specimens, the original solidification dendrites display areas with very small misorientations, which are accommodated by densely spaced dislocations. These dislocations are considered to be the nucleation sites for creep dislocations. It is also of interest to introduce the size and volume fraction distributions of γ' particles, instead of using the mean values of these two parameters. These can be built on the basis of SEM measurements in Chapter 4.

In Chapter 4, oxidation testings were carried out cyclically, for a time period of 50 hours at different temperatures. However, long term oxidation testing would be beneficial to simulate the practical service environment of turbine engines. Testing conditions then can be extended to 1000 hours at 900°C, 500 hours at 1000°C and 250 hours at 1100°C. Moreover, the mechanism of topologically close-packed (TCP) phases formation in the new alloys is still unclear. More testing conditions need to be considered for the characterisation on the fractions of TCP phases that form under given temperatures. For creep testing, ruptured creep samples could also be examined in more detail under SEM conditions, to analyse the microstructure evolution during creep.

References

[1] Rolls-Royce plc. *The Jet Engine*. Derby, UK: The Technical Publications Department, Rolls-Royce plc., 1996.

[2] C. T. Sims, N. S. Stoloff, and W. C. Hagel. *Superalloys II: High Temperature Materials for Aerospace and Industrial Power*. New York: John Wiley and Sons, 1987.

[3] M. Durand-Charre. *The Microstructure of Superalloys*. Amsterdam: Gordon & Breach Science Publishers, 1997.

[4] W. Hume-Rothery and G. V. Raynor. *The Structure of Metals and Alloys*. The Institute of Metals, London, 4th edition, 1967.

[5] A. K. Jena and M. C. Chaturvedi. The role of alloying elements in the design of nickel-base superalloys. *Journal of Materials Science*, 19(10):3121–3139, 1984.

[6] P. C. J. Gallagher. The influence of alloying, temperature, and related effects on the stacking fault energy. *Metallurgical Transactions*, 1:2429–2461, 1970.

[7] R. M. N. Pelloux and N. J. Grant. *Transactions of the Metallurgical Society of AIME*, 218:232, 1960.

[8] B. E. P. Beeston and L. K. France. *Journal of the Institute of Metals*, 96:105, 1969.

[9] T. Murakumo, T. Kobayashi, Y. Koizumi, and H. Harada. Creep behaviour of Ni-base single-crystal superalloys with various γ' volume fraction. *Acta Materialia*, 52(12):3737–3744, 2004.

[10] R. C. Reed. *The Superalloys: Fundamentals and Applications*. Cambridge University Press, 2006.

[11] P. Caron. High γ' solvus new generation nickel-based superalloys for single crystal turbine blade applications. In T.M. Pollock, R.D. Kissinger, R.R. Bowman, K.A. Green, M. McLean, S.L. Olson, and J.J. Schirra, editors, *Superalloys 2000*, pages 737–746, Warrendale, PA, USA, 2000. Minerals, Metals & Materials Soc.

[12] M. H. Yoo. On the theory of anomalous yield behavior of Ni_3Al - effect of elastic-anisotropy. *Scripta Metallurgica*, 20(6):915–920, June 1986.

[13] B. H. Kear and G. F. Wilsdorf. Dislocation configurations in plastically deformed polycrystalline Cu_3Au alloys. *Transactions of the Metallurgical Society of AIME*, 224:382–386, 1962.

[14] A. E. Staton-Beavan and R. D. Rawlings. Deformation behavior of single-crystal $Ni_3(Al, Ti)$. *Physica Status Solidi A-Applied Research*, 29(2):613–622, 1975.

[15] W. Betteridge and S. W. K. Shaw. Development of superalloys. *Materials Science and Technology*, 3(9):682–694, September 1987.

[16] P. Beardmore, R. G. Davies, and T. L. Johnston. On temperature dependence of flow stress of nickel-base alloys. *Transactions of the Metallurgical Society of AIME*, 245(7):1537–1545, 1969.

[17] M. R. Winstone. Microstructure and Alloy Developments in Nickel-based Superalloys. In A. Strang, J. Cawley, G. W. Greenwood, and England) Insti-

tute of Materials (London, editors, *Microstructural stability of creep resistant alloys for high temperature plant applications*, Book (Institute of Materials (London, England)) ;. IOM Communications, London, 1998.

[18] D. N. Duhl and C. P. Sullivan. Some Effects of Hafnium Additions On Mechanical Properties of A Columnar-grained Nickel-base Superalloy. *Journal of Metals*, 23(7):38, 1971.

[19] J.E. Doherty, A.F. Giamei, and B.H. Kear. The importance of grain boundary morphology and cohesion on intergranular strength. *Canadian Metallurgical Quarterly*, 13(1):229–236, January 1974.

[20] C. Lund. Effects of Refractory Additions on the Structure and Mechanical Properties of a Hf Containing Nickel Base Superalloy. In J. Tien, S. Wlodek, H. Morrow, M. Gell, and G. Maurer, editors, *Superalloys 1980*, pages 85–98, Pennsylvania, 1980. Minerals, Metals and Materials Society.

[21] J. M. Dahl, W. F. Danesi, and R. G. Dunn. Partitioning of refractory metal elements in hafnium-modified cast nickel-base superalloys. *Metallurgical Transactions*, 4(4):1087–1096, 1973.

[22] F. L. VerSnyder and R. Guard. Directional grain sructures for high temperature strength. *Transactions of the Metallurgical Society of AIME*, 52:485, 1960.

[23] D. Blavette, P. Caron, and T. Khan. An atom probe investigation of the role of rhenium additions in improving creep resistance of Ni-base superalloys. *Scripta Metallurgica*, 20(10):1395–1400, 1986.

[24] A. Mottura, M. K. Miller, and R. C. Reed. Atom probe tomography analysis of possible rhenium clustering in nickel-based superalloys. In R. C. Reed, K. A. Green, P Caron, T. P. Gabb, M. G. Fahrmann, and E. S. Huron, edi-

tors, *Superalloys 2008*, pages 891–900, Warrendale, PA, USA, 2008. Minerals, Metals & Materials Soc.

[25] A. Janotti, M. Krcmar, C. L. Fu, and R. C. Reed. Solute diffusion in metals: Larger atoms can move faster. *Physical Review Letters*, 92(8):4, 2004.

[26] C. L. Fu, R. Reed, A. Janotti, and M. Krcmar. On the diffusion of alloying elements in the nickel-base superalloys. In K. A. Green, T. M. Pollock, H. Harada, T. E. Howson, R. C. Reed, J. J. Schirra, and S. Walston, editors, *Superalloys 2004*, pages 867–876, Warrendale, PA, USA, 2004. Minerals, Metals & Materials Soc.

[27] G. A. Whittaker. Precision casting of aero gas-turbine components. *Materials Science and Technology*, 2(5):436–441, May 1986.

[28] N. Matan, D. C. Cox, P. Carter, M. A. Rist, C. M. F. Rae, and R. C. Reed. Creep of CMSX-4 superalloy single crystals: Effects of misorientation and temperature. *Acta Materialia*, 47(5):1549–1563, 1999.

[29] N. Matan. *Rationalisation of the creep performance of the CMSX-4 single crystal superalloy.* PhD thesis, University of Cambridge, 1999.

[30] G. R. Leverant, B. H. Kear, and J. M. Oblak. Creep of precipitation-hardened nickel-base alloy single-crystals at high-temperatures. *Metallurgical Transactions*, 4(1):355–362, 1973.

[31] G. L. Drew, R. C. Reed, K. Kakehi, and C. M. F. Rae. Single crystal superalloys: The transition from primary to secondary creep. In K. A. Green, T. M. Pollock, H. Harada, T. E. Howson, R. C. Reed, J. J. Schirra, and S. Walston, editors, *Superalloys 2004*, pages 127–136, Warrendale, PA, USA, 2004. Minerals, Metals & Materials Soc.

[32] T. M. Pollock and A. S. Argon. Creep resistance of CMSX-3 nickel-base superalloy single-crystal. *Acta Metallurgica Et Materialia*, 40(1):1–30, 1992.

[33] V. Sass, U. Glatzel, and M. Feller-Kniepmeier. Creep anisotropy in the monocrystalline nickel-base superalloy CMSX-4. In R. D. Kissinger, D. J. Deye, and D. L. Anto, editors, *Superalloys 1996*, pages 283–290, Warrendale, PA, USA, 1996. Minerals, Metals & Materials Soc.

[34] F. R. N. Nabarro and H. L. de Villiers. *The Physics of Creep*. London: Taylor and Francis, 1995.

[35] T.M. Pollock and R.D. Field. Dislocations and high-temperature plastic deformation of superalloy single crystals. In F.R.N. Nabarro and M.S. Duesbery, editors, *Dislocations in Solids*, volume Volume 11, pages 547–618. Elsevier, 2002.

[36] J. J. Gilman. *Micromechanics of Flow in Solids*. McGraw-Hill, New York, 1969.

[37] T. P. Gabb, S. L. Draper, D. R. Hull, R. A. Mackay, and M. V. Nathal. The role of interfacial dislocation networks in high-temperature creep of superalloys. *Materials Science and Engineering A*, 118:59–69, October 1989.

[38] R. C. Reed, N. Matan, D. C. Cox, M. A. Rist, and C. M. F. Rae. Creep of CMSX-4 superalloy single crystals: Effects of rafting at high temperature. *Acta Materialia*, 47(12):3367–3381, 1999.

[39] O. D. Sherby and P. M. Burke. Mechanical behavior of crystalline solids at elevated temperature. *Progress In Materials Science*, 13(7):323, 1967.

[40] G. S. Ansell and J. Weertman. Creep of a dispersion-hardened aluminium alloy. *Transactions of the Metallurgical Society of AIME*, 215(5):838–843, 1959.

[41] B. F. Dyson. Microstructure based creep constitutive model for precipitation strengthened alloys: theory and application. *Materials Science and Technology*, 25(2):213–220, 2009.

[42] H. Basoalto, S. K. Sondhi, B. F. Dyson, and M. McLean. A generic microstructure-explicit model of creep in nickel-base superalloys. In K. A. Green, T. M. Pollock, H. Harada, T. E. Howson, R. C. Reed, J. J. Schirra, and S. Walston, editors, *Superalloys 2004*, pages 897–906, Warrendale, PA, USA, 2004. Minerals, Metals & Materials Soc.

[43] B. F. Dyson. Use of CDM in materials modeling and component creep life prediction. *Journal of Pressure Vessel Technology*, 122(3):281–296, 2000.

[44] F. R. Larson and J. Miller. Time-temperature relationship for rupture and creep stresses. *Transactions ASME*, 74:765, 1952.

[45] L.M. Kachanov. On creep rupture time. *Izv. Akad. Nauk SSSR*, 8:26–31, 1958.

[46] Y.N. Rabotnov. Creep problems in structural members. In *Proc. XII IUTAM Congress*, page 137. Springer, Stanford, 1969.

[47] F. A. Leckie and D. R. Hayhurst. Constitutive equations for creep-rupture. *Acta Metallurgica*, 25(9):1059–1070, 1977.

[48] K. R. Williams and B. J. Cane. Creep-behavior of 1/2Cr1/2Mo1/4V steel at engineering stresses. *Materials Science and Engineering A*, 38(3):199–210, 1979.

[49] B. F. Dyson and M. McLean. Particle-coarsening, σ_0 and tertiary creep. *Acta Metallurgica*, 31(1):17–27, 1983.

[50] M.F. Ashby and B. F. Dyson. Creep damage mechanics and micromechanism. In S.R. Valluri, editor, *Advances in Fracture Research*, volume 1, pages 3–30. Pergamon Press, 1984.

[51] J.C. Ion, A. Barbosa, M.F. Ashby, B. F. Dyson, and M. McLean. The modelling of creep for engineering design. Technical report, Teddington, UK, 1986.

[52] R. N. Ghosh, R. V. Curtis, and M. McLean. Creep deformation of single-crystal superalloys modelling the crystallographic anisotropy. *Acta Metallurgica Et Materialia*, 38(10):1977–1992, 1990.

[53] L.-M. Pan, I. Scheibli, M.B. Henderson, B.A. Shollock, and M. McLean. Asymmetric creep deformation of a single crystal superalloy. *Acta Metallurgica et Materialia*, 43(4):1375–1384, April 1995.

[54] B. F. Dyson and S. Osgerby. Modelling and analysis of creep deformation and fracture in a 1Cr1/2Mo ferritic steel. Technical report, Teddington, UK, 1993.

[55] B. F. Dyson. Creep mechanism transition in precipitation strengthened alloys: Theory and validation. Creep Behavior of Advanced Materials for the 21st Century, pages 3–12, Warrendale, 1999. Minerals, Metals & Materials Soc.

[56] P. Kofstad. *High-Temperature Oxidation of Metals*. John Wiley & Sons, 1966.

[57] N. Birks, G. H. Meier, and F. S. Pettit. *Introduction to the high-temperature oxidation of metals*. Cambridge University Press, 2006.

[58] H. J. T. Ellingham. Reducibility of oxides and sulfides in metallurgical processes. *Journal of the Society of Chemical Industry*, 63:125–133, 1944.

[59] F. D. Richardson and J. H. E Jeffes. The thermodynamics of substances of interest in iron and steel making from 0°C to 2400°C. *Journal of the Iron and Steel Institute*, 160(3):261, 1948.

[60] C. Wagner. The theory of the warm-up process. *Zeitschrift Fur Physikalische Chemie-Abteilung B-Chemie Der Elementarprozesse Aufbau Der Materie*, B21:25–41, 1933.

[61] R. A. Rapp. The high-temperature oxidation of metals forming cation-diffusing scales. *Metallurgical Transactions A-physical Metallurgy and Materials Science*, 15(5):765–782, 1984.

[62] F. S. Pettit. Oxidation mechanisms for nickel-aluminum alloys at temperatures between 900°C and 1300°C. *Transactions of the Metallurgical Society of AIME*, 239(9):1296–1305, 1967.

[63] C. S. Giggins and F. S. Pettit. Oxidation of Ni-Cr-Al alloys between 1000°C and 1200°C. *Journal of the Electrochemical Society*, 118(11):1782–1790, 1971.

[64] Carl Wagner. Passivity and inhibition during the oxidation of metals at elevated temperatures. *Corrosion Science*, 5(11):751–764, 1965.

[65] P. Kofstad. *Nonstoichiometry, diffusion and electrical conductivity in binary metal oxides*. Wiley-Interscience, Chichester, Sussex, UK, 1972.

[66] N. Birks, G. H. Meier, and F. S. Pettit. Forming continuous alumina scales to protect superalloys. *JOM*, 46(12):42–46, 1994.

[67] A. D. Cetel and D. N. Duhi. Second-generation nickel-base sinlge crystal superalloy. In S. Reichman, D. N. Duhl, S. Maurer, S. Antolovich, and C. lund, editors, *Superalloys 1988*, pages 235–244, Warrendale, PA, USA, 1988. The Metallurgical Society.

[68] J. H. W. de Wit. High temperature oxidation of metals. *Journal of Materials Education*, 3:343, 1981.

[69] B. A. Pint, J. R. Martin, and L. W. Hobbs. The oxidation mechanism of θ-Al_2O_3 scales. *Solid State Ionics*, 78:99–107, 1995.

[70] A. Sato, Y. L. Chiu, and R. C. Reed. Oxidation of nickel-based single-crystal superalloys for industrial gas turbine applications. *Acta Materialia*, 59(1):225–240, 2011.

[71] K. Harris, G. L. Erickson, W. D. Brentnall, J. M. Aurrecoechea, S. L. Sikkenga, and K. G. Kubarych. Development of the rhenium containing superalloys CMSX-4(R) and CM 186 LC(R) for single-crystal blade and directionally solidified vane applications in advanced turbine-engines. In S.D. Antolovich, R.A. Stusrud, R.W. abd Mackay, D.L. Anton, T. Khan, and R.D. Kissinger, editors, *Superalloys 1992*, pages 297–306, 1992.

[72] Y. Koizumi, T. Kobayashi, T. Yokokawa, J. X. Zhang, M. Osawa, H. Harada, Y. Aoki, and M. Arai. Development of next-generation Ni-base single crystal superalloys. In K. A. Green, T. M. Pollock, H. Harada, T. E. Howson, R. C. Reed, J. J. Schirra, and S. Walston, editors, *Superalloys 2004*, pages 35–43, Warrendale, PA, USA, 2004.

[73] S. Walston, A. Cetel, R. MacKay, K. O'Hara, D. Duhl, and R. Dreshfield. Joint development of a fourth generation single crystal superalloy. In K. A. Green, T. M. Pollock, H. Harada, T. E. Howson, R. C. Reed, J. J. Schirra, and S. Walston, editors, *Superalloys 2004*, pages 15–24, Warrendale, PA, USA, 2004. Minerals, Metals & Materials Soc.

[74] R. C. Reed, T. Tao, and N. Warnken. Alloys-By-Design: Application to nickel-based single crystal superalloys. *Acta Materialia*, 57(19):5898–5913, 2009.

[75] M. McLean. Nickel-base superalloys - current status and potential. *Philosophical Transactions of the Royal Society of London, Series A: Mathematical, Physical and Engineering Sciences*, 351(1697):419–433, 1995.

[76] H. C. Basoalto, J. W. Brooks, and I. Di Martino. Multiscale microstructure modelling for nickel based superalloys. *Materials Science and Technology*, 25(2):221–227, 2009.

[77] M. S. A. Karunaratne and R. C. Reed. Interdiffusion of the platinum-group metals in nickel at elevated temperatures. *Acta Materialia*, 51(10):2905–2919, 2003.

[78] C. M. F. Rae and R. C. Reed. Primary creep in single crystal superalloys: Origins, mechanisms and effects. *Acta Materialia*, 55(3):1067–1081, 2007.

[79] L. Muller, U. Glatzel, and M. Feller-Kniepmeier. Calculation of the internal stresses and strains in the microstructure of a single crystal nickel-base superalloy during creep. *Acta Metallurgica Et Materialia*, 41(12):3401–3411, 1993.

[80] J. Friedel. *Dislocations*. Pergamon Press, New York, 1964.

[81] T. M. Pollock and A. S. Argon. Directional coarsening in nickel-base single-crystals with high-volume fractions of coherent precipitates. *Acta Metallurgica Et Materialia*, 42(6):1859–1874, 1994.

[82] C. E. Campbell, W. J. Boettinger, and U. R. Kattner. Development of a diffusion mobility database for Ni-base superalloys. *Acta Materialia*, 50(4):775–792, 2002.

[83] M. S. A. Karunaratne, P. Carter, and R. C. Reed. Interdiffusion in the face-centred cubic phase of the Ni-Re, Ni-Ta and Ni-W systems between 900 and 1300°C. *Materials Science and Engineering A*, 281(1-2):229–233, 2000.

[84] M. S. A. Karunaratne and R. C. Reed. Interdiffusion of niobium and molybdenum in nickel between 900-1300°C. In M. Danielewski, R. Filipek, R. Kozubs, W. Kucza, P. Zieba, and Z. Zurek, editors, *Diffusion in Materials: Dimat 2004, Pts 1 and 2*, volume 237-240, pages 420–425. Trans Tech Publications Ltd, Stafa-Zurich, 2005.

[85] R. C. Reed, D. C. Cox, and C. M. F. Rae. Kinetics of rafting in a single crystal superalloy: effects of residual microsegregation. *Materials Science and Technology*, 23(8):893–902, 2007.

[86] Y. Koizumi, T. Kobayashi, T. Yokokawa, M. Osawa, H. Harada, Y. Aoki, and M. Arai. Effects of alloying additions on the creep strength of a fourth generation single-crystal superalloy. *Journal of the Japan Institute of Metals*, 68(3):206–209, 2004.

[87] T. Kobayashi, H. Harada, M. Osawa, and A. Sato. Creep strength of Co-free Ni-base single crystal superalloys. *Journal of the Japan Institute of Metals*, 69(8):707–710, 2005.

[88] F. R. N. Nabarro. Rafting in superalloys. *Metallurgical and Materials Transactions A-Physical Metallurgy and Materials Science*, 27(3):513–530, 1996.

[89] R. Schmidt and M. Feller-Kniepmeier. Phase chemistry of a nickel-base superalloy after creep experiments. *Scripta Metall. Mater.*, 29(8):1079–84, October 1993.

[90] A. Epishin, T. Link, M. Nazmy, M. Staubli, H. Klingelhoffer, and G. Nolze. Microstructural degradation of CMSX-4: Kinetics and effect on mechanical properties. In R. C. Reed, K. A. Green, P Caron, T. P. Gabb, M. G. Fahrmann, and E. S. Huron, editors, *Superalloys 2008*, pages 725–731, Warrendale, PA, USA, 2008. Minerals, Metals & Materials Soc.

[91] M. Morinaga, Y. Murata, and H. Yukawa. Recent progress in the new PHACOMP approach. In *Materials Design Approaches and Experiences. Proceedings of Symposium*, pages 15–27, Warrendale, PA, USA, 2001. TMS - Miner., Metals & Mater. Soc.

[92] Z. Zhu, H. Basoalto, N. Warnken, and R.C. Reed. A model for the creep deformation behaviour of nickel-based single crystal superalloys. *Acta Materialia*, 60(12):4888–4900, July 2012.

[93] K. Onal, M.C. Maris-Sida, G.H. Meier, and F.S. Pettit. The effects of water vapor on the oxidation of nickel-base superalloys and V coatings at temperatures from 700°C to 1100°C. In K. A. Green, T. M. Pollock, H. Harada, T. E. Howson, R. C. Reed, J. J. Schirra, and S. Walston, editors, *Superalloys 2004*, pages 607–615, Warrendale, PA, USA, 2004. Minerals, Metals and Materials Society.

[94] K. Kawagishi, A. Sato, T. Kobayashi, and H. Harada. Oxidation properties for 2nd-5th generation Ni-base single-crystal superalloys at 1023, 1173 and 1373 K. *Journal of the Japan Institute of Metals*, 71(3):313–19, March 2007.

[95] A. Akhtar, M.S. Hook, and R.C. Reed. On the oxidation of the third-generation single-crystal superalloy CMSX-10. *Metallurgical and Materials Transactions A*, 36(11):3001–3017, 2005.

[96] S. Mrowec, T. Werber, and M. Zastawnik. The mechanism of high temperature sulphur corrosion of nickel-chromium alloys. *Corrosion Science*, 6(2):47–68, 1966.

[97] B. Gleeson. *Corrosion and Environmental Degradation*. Wiley-VCH, 2008.

[98] A. Ma, D. Dye, and R. C. Reed. A model for the creep deformation behaviour of single-crystal superalloy CMSX-4. *Acta Materialia*, 56(8):1657–1670, 2008.

[99] T. Hino, T. Kobayashi, Y. Koizumi, H. Harada, and T. Yamagata. Development of a new single crystal superalloy for industrial gas turbines. In T.M. Pollock, R.D. Kissinger, R.R. Bowman, K.A. Green, M. McLean, S.L. Olson, and J.J. Schirra, editors, *Superalloys 2000*, pages 729–736, Warrendale, PA, USA, 2000. Minerals, Metals & Materials Soc.

[100] Atsushi Sato, Johan Moverare, Magnus Hasselqvist, and Roger Reed. On the mechanical behavior of a new single-crystal superalloy for industrial gas turbine applications. *Metallurgical and Materials Transactions A: Physical Metallurgy and Materials Science*, 43(7):2302–2315, 2012.

[101] M. Morinaga, Y. Murata, and H. Yukawa. New PHACOMP and its application to alloy design. In M. Gell, C.S. Kortovich, R.H. Bricknell, W.B. Kent, and J.F. Radavich, editors, *Superalloys 1984*, pages 523–532, Warrendale, PA, USA, 1984. Minerals, Metals and Materials Society.

[102] B. Seiser, R. Drautz, and D. G. Pettifor. TCP phase predictions in Ni-based superalloys: Structure maps revisited. *Acta Materialia*, 59(2):749–763, 2011.

[103] B. Seiser. *Topologically close-packed phase prediction in Ni-based superalloys: phenomenological structure maps and bond-order potential theory.* PhD thesis, University of Oxford, 2011.

[104] R. A. MacKay, T. P. Gabb, J. L. Smialek, and M. V. Nathal. A new approach of designing superalloys for low density. *JOM*, 62(1):48–54, January 2010.

[105] M. Sakamoto, H. Harada, T. Yokokawa, Y. Koizumi, T. Kobayashi, H. Zhou, J. X. Zhang, and N. Miyamoto. Assessment on the thermo-mechanical fatigue properties of 98 Ni-base single crystal superalloys. In R. C. Reed, K. A. Green, P Caron, T. P. Gabb, M. G. Fahrmann, and E. S. Huron, editors, *Superalloys 2008*, pages 521–526, Warrendale, PA, USA, 2008. Minerals, Metals & Materials Soc.

[106] G.B. Olson and C.J. Kuehmann. Materials genomics: From CALPHAD to flight. *Scripta Materialia*, 70(0):25–30, January 2014.

[107] L. Kaufman and J. Ågren. CALPHAD, first and second generation - Birth of the materials genome. *Scripta Materialia*, 70(0):3–6, January 2014.

[108] J. O. Andersson, T. Helander, L. H. Hoglund, P. F. Shi, and B. Sundman. THERMO-CALC & DICTRA, computational tools for materials science. *Calphad*, 26(2):273–312, June 2002.

[109] TCNI6, Thermodynamic Database, Thermo-Calc Software AB, Stockholm, 2013.